



Mathematisch-Naturwissenschaftliche Fakultät  
Universität zu Köln

$\gamma$ -ray spectroscopy of  $^{33}\text{P}$  and  $^{33}\text{S}$   
&  
Upgrade and Commissioning of the  
Lund-York-Cologne CALorimeter

**Inaugural-Dissertation**

zur

Erlangung des Doktorgrades

der Mathematisch-Naturwissenschaftlichen Fakultät

der Universität zu Köln

vorgelegt von

**Bo Fu**

aus Hebei, China

Köln - 2018

Berichterstatter:  
(Gutachter)

Prof. Dr. Peter Reiter  
Prof. Dr. Andreas Zilges

Tag der mündlichen Prüfung: 05.03.2018



*Mathematics began to seem too much like puzzle solving. Physics is puzzle solving, too, but of puzzles created by nature, not by the mind of man.*

- MARIA GOEPPERT-MAYER



# Abstract

The neutron-rich nuclei  $^{33}\text{P}$  and  $^{33}\text{S}$  in the upper  $sd$ -shell were investigated by means of the  $^{26}\text{Mg}(^{13}\text{C},\text{np}\alpha)$  and  $^{26}\text{Mg}(^{13}\text{C},2\text{n}\alpha)$  fusion-evaporation reactions. Excited states with intermediate and high spins have been populated. The level schemes of both nuclei have been considerably extended. Utilizing the  $\gamma\gamma$  angular correlation method the spin-parity assignment of the new excited states in  $^{33}\text{P}$  has been investigated. The experimentally determined energy levels as well as the known reduced transition probabilities (i.e.  $B(M1)$  and  $B(E2)$  values) from both nuclei were compared to  $0\hbar\omega$  and  $1\hbar\omega$  truncated  $p$ - $sd$ - $pf$  shell-model calculations using the PS-DPF interaction. For the energy levels a very good agreement between experiment and theory was shown for both  $^{33}\text{P}$  and  $^{33}\text{S}$ . However, for  $B(M1)$  and  $B(E2)$  values the calculated values cannot reproduce the experimental results with satisfying agreement for all transitions. In some places the discrepancy between experiment and theory is even large, which requires further experimental as well as theoretical investigation of this thesis for these nuclei.

The second part was focused on the upgrade and commissioning tests of the Lund-York-Cologne CAlorimeter (LYCCA). As a key device of the High resolution In-flight SPECtroscopy (HISPEC) campaign of the FAIR/NUSTAR collaboration, LYCCA was designed to identify the reaction products after the secondary target, as well as to track the particle trajectory event by event. After the successful employment of the precursor LYCCA-0 in the PreSPEC campaign, the electronic as well as mechanic components of the LYCCA system were upgraded by STFC Daresbury Laboratory. Using the high integrated AIDA Front-End electronics with ASICs the signals from more than thousand DSSSD-channels were pre-amplified and processed. Since 2016, the new LYCCA setup is located at the Cologne tandem accelerator. Triple-Alpha tests and in-beam experiments of elastic scattering were carried out to check the specifications of the system after the upgrade. The obtained results allow first important conclusions about energy resolution and efficiency of the calorimeter at low energies for future NUSTAR experiments.



# Kurzzusammenfassung

Die neutronenreichen Kerne  $^{33}\text{P}$  und  $^{33}\text{S}$  in der oberen *sd*-Schale wurden mittels der Fusionsverdampfungsreaktionen  $^{26}\text{Mg}(^{13}\text{C}, \text{n}\alpha)$  und  $^{26}\text{Mg}(^{13}\text{C}, 2\text{n}\alpha)$  untersucht. Angeregte Zustände mit mittleren und hohen Spins wurden bevölkert. Die Niveauschemata beider Kerne wurden erheblich erweitert. Mittels der  $\gamma\gamma$ -Winkelkorrelationsmethode wurde die Zuordnung der Spin und Parität der neuen angeregten Zustände in  $^{33}\text{P}$  untersucht. Die experimentell bestimmten Energieniveaus sowie die bekannten reduzierten Übergangsstärke ( $B(M1)$ - und  $B(E2)$ -Werte) von beiden Kernen wurden mit den  $0\hbar\omega$  und  $1\hbar\omega$  verkürzten p-sd-pf Schalenmodellberechnungen unter der Verwendung der PSDPF-Wechselwirkung verglichen. Für die Energieniveaus wurde eine sehr gute Übereinstimmung zwischen Experiment und Theorie gezeigt sowohl für  $^{33}\text{P}$  als auch für  $^{33}\text{S}$ . Jedoch können die berechneten  $B(M1)$ - und  $B(E2)$ -Werte die experimentellen Ergebnisse nicht zufriedenstellend für alle Übergänge reproduzieren. An einigen Stellen ist die Diskrepanz zwischen Experiment und Theorie sogar sehr groß, was weitere experimentelle sowie theoretische Untersuchungen für diese Kerne erfordert.

Im zweiten Teil dieser Arbeit wurde Upgrade und Inbetriebnahme des Lund-York-Cologne CALorimeters (LYCCA) untersucht. LYCCA wird als ein Schlüsselinstrument für die High resolution In-flight SPECTroscopy (HISPEC)-Kampagne der FAIR/NUSTAR-Kollaboration entwickelt, um die Reaktionsprodukte hinter dem sekundären Target zu identifizieren und die Teilchentrajektorien Event-für-Event zu verfolgen. Nach dem ersten erfolgreichen Einsatz des Vorläufers LYCCA-0 während der PreSPEC-Kampagne wurde ein Upgrade der Elektronik sowie der mechanischen Komponenten des LYCCA-Systems vom STFC Daresbury Laboratory durchgeführt. Hochintegrierte AIDA Front-End-Elektronik Module mit ASICs werden dabei eingesetzt, um die Signale von mehr als tausend DSSSD-Kanälen zu verstärken, und zu verarbeiten. Seit 2016 befindet sich der neue LYCCA-Setup am Kölner Tandembeschleuniger. Messungen mit einer Tripel-Alpha-Quelle und In-beam-Experimente zur elastischen Streuung von schweren Ionen wurden durchgeführt um die Spezifikationen des Systems nach dem Upgrade zu überprüfen. Die erzielten Ergebnisse erlauben wichtige

Rückschlüsse auf Energieauflösung und Effizienz des Kalorimeters bei niedrigen Energien für zukünftige NUSTAR-Experimente.

# Contents

<b>I. <math>\gamma</math>-ray spectroscopy of <math>^{33}\text{P}</math> and <math>^{33}\text{S}</math></b>	<b>13</b>
<b>1. Nuclear Shell Model for <math>sd</math>-shell nuclei</b>	<b>15</b>
1.1. The Nuclear Shell Model . . . . .	15
1.2. The universal $sd$ interaction - USD . . . . .	22
1.3. Effective $sd$ - $pf$ shell-model interactions . . . . .	25
1.4. The PSDPF interaction . . . . .	28
1.5. The $A = 33$ isotopes $^{33}\text{P}$ and $^{33}\text{S}$ . . . . .	31
<b>2. <math>\gamma</math>-ray spectroscopy of <math>^{33}\text{P}</math> and <math>^{33}\text{S}</math></b>	<b>35</b>
2.1. The fusion-evaporation reaction $^{13}\text{C} + ^{26}\text{Mg}$ . . . . .	35
2.2. Level scheme of $^{33}\text{P}$ . . . . .	37
2.3. Level Scheme of $^{33}\text{S}$ . . . . .	42
2.4. $\gamma\gamma$ angular-correlation analysis . . . . .	47
2.4.1. Properties of $\gamma$ radiation . . . . .	47
2.4.2. $\gamma\gamma$ angular correlation in in-beam experiments . . . . .	49
2.4.3. Determination of level spins in $^{33}\text{P}$ . . . . .	52
<b>3. Shell-Model Calculations</b>	<b>59</b>
3.1. Calculations for $^{33}\text{P}$ . . . . .	59
3.1.1. Level Scheme of $^{33}\text{P}$ . . . . .	59
3.1.2. Transition Strength . . . . .	63
3.2. Calculations for $^{33}\text{S}$ . . . . .	65
3.2.1. Level Scheme of $^{33}\text{S}$ . . . . .	65
3.2.2. Transition Strength . . . . .	67
3.3. Summary . . . . .	68

<b>II. Upgrade and Commissioning of the Lund-York-Cologne</b>	
<b>    CAlorimeter</b>	<b>73</b>
<b>4. Introduction</b>	<b>75</b>
4.1. HISPEC Campaign . . . . .	77
4.2. LYCCA . . . . .	78
<b>5. Upgrade of LYCCA</b>	<b>81</b>
5.1. Detectors . . . . .	81
5.1.1. Functionality of the detectors . . . . .	81
5.1.2. DSSSD . . . . .	83
5.1.3. Caesium iodide (CsI) scintillators . . . . .	86
5.1.4. LYCCA $\Delta E - E$ telescope . . . . .	91
5.2. Electronics . . . . .	92
5.2.1. Application Specific Integrated Circuit (ASIC) . . . . .	93
5.2.2. Front End Electronics (FEE) . . . . .	96
5.2.3. Adapter Box . . . . .	98
5.2.4. Electronics System . . . . .	99
5.3. Mechanics . . . . .	102
<b>6. Commissioning of LYCCA</b>	<b>106</b>
6.1. Test of ASICs . . . . .	106
6.2. Triple-alpha measurement with DSSSD . . . . .	112
6.2.1. Energy Resolution . . . . .	112
6.2.2. Energy correlations . . . . .	118
6.3. In-beam experiment . . . . .	120
6.3.1. Elastic Scattering of $^{12}\text{C} + ^{197}\text{Au}$ . . . . .	120
6.3.2. Elastic and inelastic scattering of $^{12}\text{C} + ^{12}\text{C}$ . . . . .	129
6.4. Summary . . . . .	132
<b>7. Outlook</b>	<b>134</b>
<b>A. Shell Model Calculations</b>	<b>137</b>
A.1. Level Energies . . . . .	137
A.2. Transition Strength $B(L)$ . . . . .	140
<b>B. Mapping and technical drawing of LYCCA FEE-mezzanine</b>	<b>145</b>
<b>List of tables</b>	<b>153</b>



## *Contents*

List of Figures	155
Bibliography	158



## Part I.

$\gamma$ -ray spectroscopy of  $^{33}\text{P}$  and  $^{33}\text{S}$



# 1. Nuclear Shell Model for *sd*-shell nuclei

## 1.1. The Nuclear Shell Model

Atomic nuclei with  $Z$  protons and  $N$  neutrons are complicated many-body systems, which are driven by two quantum-mechanical interactions: the strong nucleon-nucleon (NN) interaction, and the electromagnetic interaction. The NN-interaction provides the main contribution for the nuclei to form and has the following properties (nucleon separation  $r = |\vec{r}_i - \vec{r}_j|$ ):

- Short range: attractive at  $r \approx 1\text{-}2$  fm;
- Vanishes at larger distances  $r \geq 10$  fm;
- Repulsive at very small distances  $r < 0.5$  fm;
- Charge independent;
- Spin and momentum dependent.

A schematic illustration of the nucleon-nucleon interaction is shown in Fig. 1.1. The Hamiltonian for a nucleus with the mass number  $A = Z + N$  can be written as the sum of the kinetic energy  $T_i$  of the nucleus and their potential energies in the NN-potentials  $V_{ij}$  formed by the  $A$  interacting nucleons:

$$H = \sum_i^A T_i + \frac{1}{2} \sum_{i \neq j}^A V_{ij} \quad (1.1)$$

In modern experimental and theoretical approaches even 3-body (NNN) forces haven't been proven to exist [2–5]. To solve this many-body problem a simplification of the theoretical description is needed. Based on the experimental evidence that atomic nuclei with certain proton and neutron numbers 2, 8, 20, 28, 50, 82 and 126 (the so called "magic numbers") were observed, which appeared to be comparatively stable, the nuclear shell model was suggested. Similar to electrons orbiting around the nucleus, the nucleons experience an average central, spherical potential  $U(r)$  and move independently in well-defined orbits.

## 1. Nuclear Shell Model for *sd*-shell nuclei

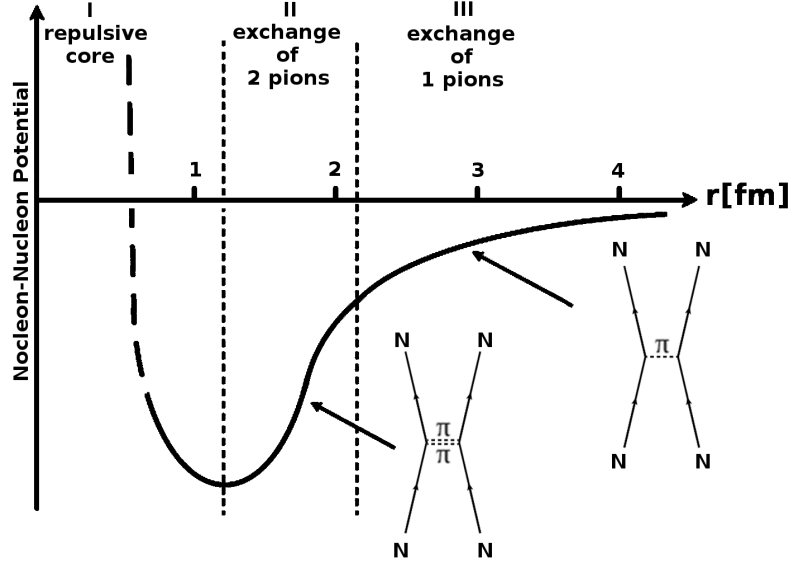


Figure 1.1.: Schematic illustration of the nucleon-nucleon potential as a function of distance  $r = |\vec{r}_i - \vec{r}_j|$  ( $r$  given in units of fm). At  $r$  around a few fm the nucleon-nucleon interaction is weakly attractive, determined by one-pion exchange (region III). In region II the interaction is determined by two-pion exchange. For short distances (region I), a repulsive hard-core potential prevents nucleons merging. Modified from [1].

In the shell-model approach the systematic general Hamiltonian is transformed to:

$$H = \sum_i^A (T_i + U_i) + \left( \frac{1}{2} \sum_{i \neq j}^A V_{ij} - \sum_i^A U_i \right) = \sum_i^A H_0(i) + V_{res} \quad (1.2)$$

where  $H_0(i)$  describes the movement of one nucleon in an average single-particle potential  $U(r)$  determined by all nucleons. For a properly chosen potential  $U(r)$  the residual interaction  $V_{res.}$  can be treated as perturbation. Two typical spherical potentials used in shell-model calculations are the harmonic-oscillator potential:

$$U(r) = U_0 + \frac{1}{2} m \omega^2 r^2 \quad (1.3)$$

and the Woods-Saxon potential:

$$U(r) = \frac{U_0}{1 + \exp((r - R)/a)} \quad (1.4)$$

(see Fig. 1.2) where  $\omega$  is the harmonic oscillator frequency, deduced from the mean nuclear radii:  $\hbar\omega \approx 40A^{-1/3}$  MeV. For the Woods-Saxon potential the typical values for the parameters are given by the nuclear radius  $R = r_0 A^{1/3}$  with  $r_0 = 1.2$  fm, the

### 1. Nuclear Shell Model for *sd*-shell nuclei

potential depth  $U_0$  and  $a$ , a length representing the surface thickness of the nucleus. The typical values of the parameters are  $U_0 = -50$  MeV and  $a = 0.5$  fm.

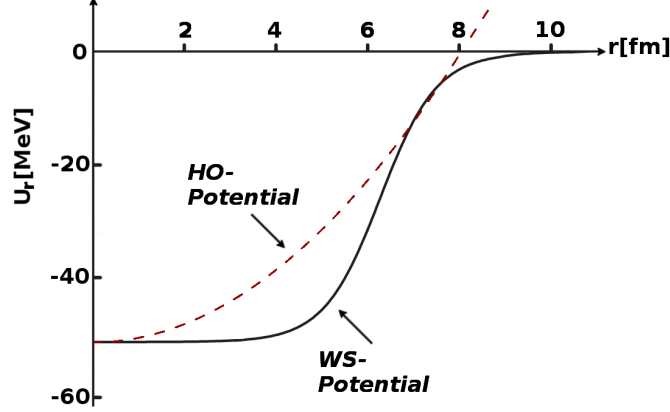


Figure 1.2.: Sketch of harmonic oscillator potential (dashed line) and Woods-Saxon potential (solid line) as a function of  $r$ .

Using the harmonic-oscillator potential many analytical results can be calculated. However, the quick rise to infinity with increasing  $r$  is in contradiction with the NN-potential shown in Fig. 1.1. Hence, the harmonic-oscillator potential can only describe the deeply bound states well but can not reproduce the magic numbers over 20. The correct explanation of all magic numbers was given in 1949 by O. HAXEL, J. H. D. JENSEN, H. E. SUESS [7] and independently by M. GOEPPERT-MAYER [8], using the Woods-Saxon potential plus the strong spin-orbit coupling in the NN-interaction. Figure 1.3 shows the comparison of the single-particle states calculated using (A) a harmonic-oscillator potential  $V_H$ , (B) a Woods-Saxon potential  $V_{WS}$  and (C) a Woods-Saxon potential with strong spin-orbit coupling  $V_{WS} + V_{LS}$ . Considering the spin-orbit interaction  $\vec{l} \cdot \vec{s}$  every level splits into two orbits with total angular momenta  $j_{\pm} = l \pm 1/2$ . For each  $j$ , the orbit degenerates into  $2j + 1$  magnetic substates with  $-j \leq m \leq j$ . According to the Pauli principle each state can be occupied by maximum two protons (or neutrons), so that the total occupation number was obtained and characterized as "magic number". For the proton states the level energies are influenced by the Coulomb interaction and therefore are slightly different to the respective neutron states.

Several experimental observations can be explained by the nuclear shell model, which will be briefly discussed in the following paragraphs.

**Nuclear masses and binding energies:** Figure 1.4 shows experimentally determined nuclear masses and calculated nuclear masses using the finite-range droplet model (FRDM) from P. MÖLLER *et. al.* [9], as a function of the neutron numbers.

# 1. Nuclear Shell Model for *sd*-shell nuclei

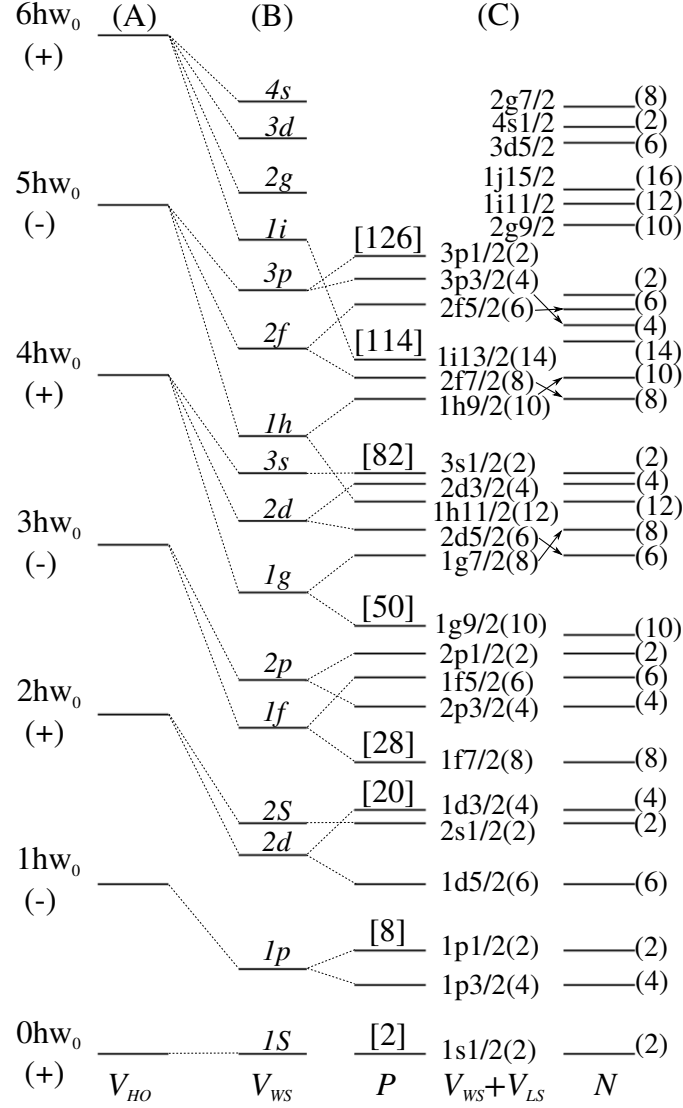


Figure 1.3.: Single-particle states in the shell model for (A) harmonic-oscillator potential  $V_{HO}$ , (B) Woods-Saxon potential  $V_{WS}$  and (C) Woods-Saxon potential plus spin-orbit coupling for protons ( $P$ ) and neutrons ( $N$ ), respectively. The numbers in brackets give the total occupation number of each state. The magic numbers describe the respective shell closure (Modified from [6]).

Nuclei nearby the shell closures have enhanced binding energies and therefore the nuclear masses are reduced, giving rise to the observation of the magic numbers.

**Two-neutron separation energies:** According to the shell model the separation of nucleons from nuclei with closed shells requires more energy. The two-neutron separation energy  $S_{2n}$  is defined as the binding-energy difference of  ${}^A_ZX_N$  and  ${}^{A-2}_ZX_{N-2}$ :  $S_{2n} = B(Z, N) - B(Z, N - 2)$ . As shown in Fig. 1.5 the  $S_{2n}$  drops significantly from  $N = 50$  to 52, which is a clear indication of the shell closure at  $N = 50$ .



### 1. Nuclear Shell Model for $sd$ -shell nuclei

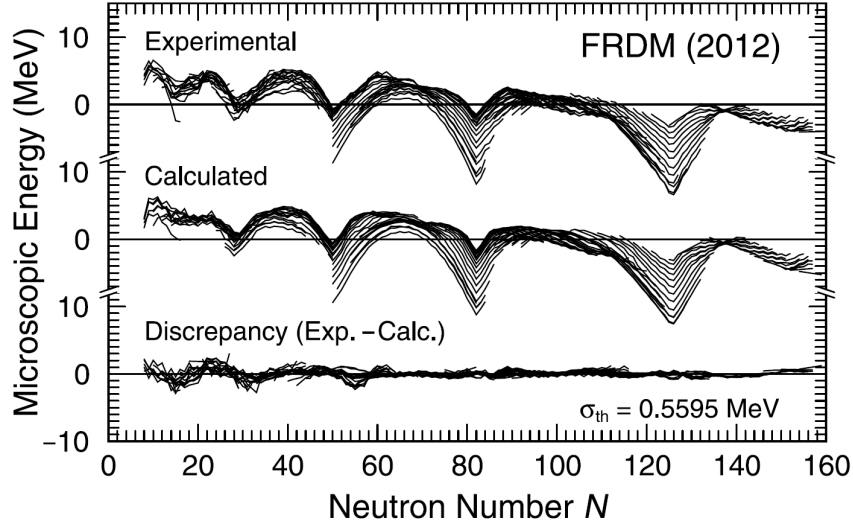
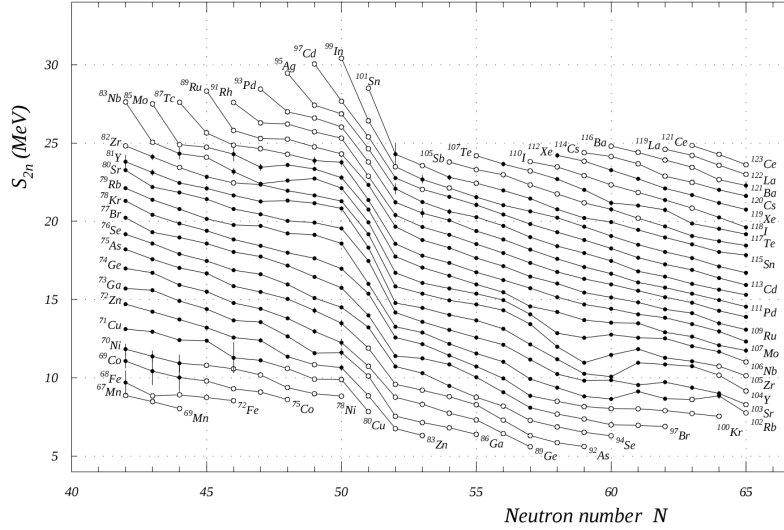


Figure 1.4.: Comparison of experimental to calculated microscopic energies corresponding to the FRDM [9], as a function of the neutron number  $N$  (taken from [10]).



### 1. Nuclear Shell Model for $sd$ -shell nuclei

excited state  $J^\pi = 0^+$  with excitation energy  $E_x = 6.05$  MeV cannot be explained by general shell model calculations. Using a microscopic  $^{12}\text{C}+\alpha$  cluster-coupling model the first excited  $0^+$  state was reproduced by Y. SUZUKI [12]). For  $^{15}\text{N}$  and its mirror nucleus  $^{15}\text{O}$  with exchanged number of  $Z$  and  $N$  the ground states are characterized as the one-hole state  $\pi p_{1/2}^{-1}$  and  $\nu p_{1/2}^{-1}$ , respectively. The excitation of both nuclei need to cross the large shell gap between the  $p_{1/2}$  and  $d_{5/2}$  shell, therefore the excitation energies of the first excited states are above 5 MeV. For  $^{17}\text{O}$  and  $^{17}\text{F}$  the major  $p$ -shell for protons and neutrons is fully occupied, and the ground states are characterized as the one-particle state  $\nu d_{5/2}^{+1}$  and  $\pi d_{5/2}^{+1}$ , respectively. The excitation of the valence neutron ( $^{17}\text{O}$ ) (or proton ( $^{17}\text{F}$ )) to the next open  $\nu s_{1/2}$  ( $\pi s_{1/2}$ ) orbital does not require much additional energy, thus, the excitation energies are 0.87 MeV for  $^{17}\text{O}$  and 0.5 MeV for  $^{17}\text{F}$ .

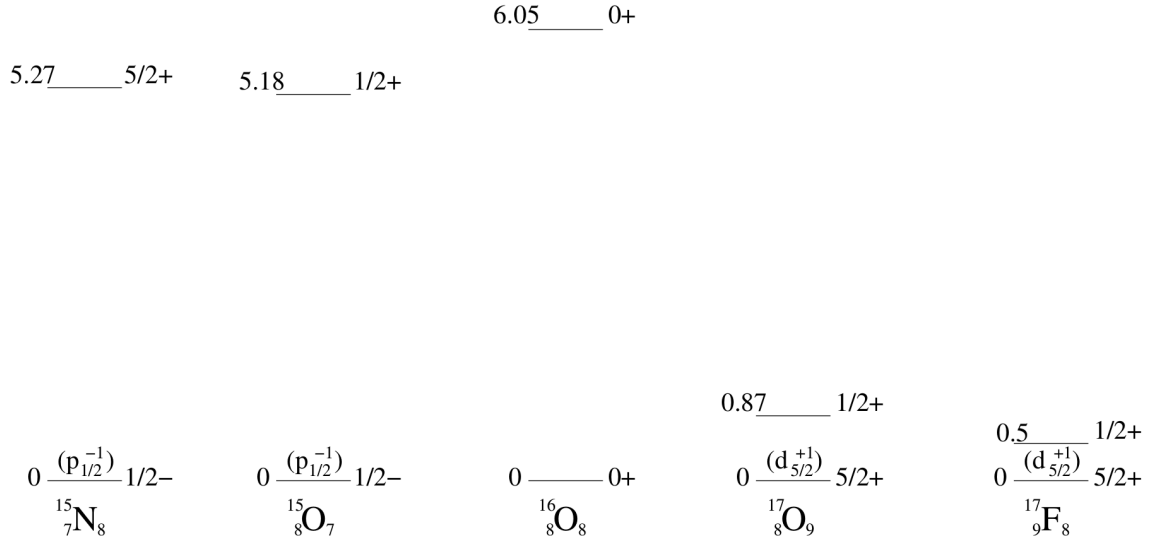


Figure 1.6.: Comparison of the one-particle and one-hole states in nuclei around  $^{16}\text{O}$ . Information of spin, parity and excitation energy are taken from [13].

Since the nuclear shell model assumes the nuclei to be spherical symmetric, it is mostly useful to describe: (i) the light nuclei, which have good spherical form, (ii) the doubly-magic nuclei, as well as (iii) the nuclei nearby the major shell closures, which have just a few valence nucleons or holes. However, there are still many properties of nuclei such as semi-magic numbers (e.g.  $N = 16$  [14]) and  $\alpha$ -cluster structures [15], which using nuclear shell model cannot be explained satisfied. Also for very deformed and exotic nuclei with very large  $N/Z$  ratios the shell-model calculations have striking deviation from experimental results.

Since shell-model calculations do not provide consistent results for all nuclei, alternative theories and methods have been developed. In 1974 Arima and Iachello [16] invented the interacting boson model (IBM) to describe the collective nuclear states

## 1. Nuclear Shell Model for *sd*-shell nuclei

in intermediate and heavy atomic nuclei. In IBM nucleons pair up, and act as a single particle with boson properties, occupying angular momentum of 0, 2 or 4. There are two types of IBM, so called the IBM1 and IBM2, which both are restricted to describe nuclei with even number of protons and neutrons. Based on isospin symmetry IBM1 treats both protons and neutrons the same and considers only the pairs of nucleons, which are coupled to total angular momentum of 0 (*s*-boson) and 2 (*d*-boson), while in IBM2 protons and neutrons are treated separately. By prediction of vibrational and rotational modes of non-spherical nuclei the IBM is very successful [17].

*ab initio* method is another way to describe atomic nucleus by solving the non-relativistic Schrödinger equation for all component nucleons and interactions. Compared to nuclear shell model, the *ab initio* method is a more fundamental approach. Previously this treatment was limited to very light nuclei, recently by means of the enhanced computing power heavier nuclei such as even oxygen isotopes (up to  $^{24}\text{O}$ ) can be treated [18].

Although the nuclear shell model has its limitation, it is still a well developed and successful method to predict the characteristics of atomic nuclei. To describe the properties of a nucleus with several nucleons (protons or neutrons) outside a closed shell (valence particle) or holes inside a closed shell (valence hole), the residual interaction  $V_{res}$  should also be considered. The effective Hamiltonian of the valence nucleons can be written as:

$$H_{eff} = \sum_i H_0(i) + V_{res} \quad (1.5)$$

In shell-model calculations the effective Hamiltonian can be approximated with only one-particle and two-particle operators. Considering a relative simple system with two valence nucleons the two-particle wave function can be written as:

$$\psi(j_1(1)j_2(2); JM, TT_z)$$

where  $j_i$  designate the single-particle angular momentum of the respective particles 1 and 2.  $J$  and  $T$  are the total angular momentum coupling and total isospin, respectively.  $M$  and  $T_z$  are the projection of  $J$  and  $T$ , respectively. The Schrödinger equation to describe the nuclear excited states can be solved:

$$\langle H_{eff.} \rangle = \sum_i \varepsilon_{j_i} + \langle j_1 j_2; JM, TT_z | V(1, 2) | j_3 j_4; JM, TT_z \rangle \quad (1.6)$$

### 1. Nuclear Shell Model for *sd*-shell nuclei

The first term of the right hand side of the equation,  $\varepsilon_{ji}$ , denoted as One-Body Matrix Element or Single Particle Energy (SPE), is understood as the binding energy of a single nucleon in the valence orbit with angular momentum  $j$  to the shell-model core. The second term, denoted as Two-Body Matrix Element (TBME), describes the perturbed energy splitting caused by the residual nucleon-nucleon interaction  $V(1, 2)$ . To determine the SPE and TBME of a realistic nucleonic system, an appropriate nucleon-nucleon interaction and model space, including all orbits which can be occupied by the valence nucleons, has to be chosen.

A calculation with realistic interactions, which start from the free nucleon-nucleon interaction incorporating necessary modifications induced by the nuclear medium is always difficult. As an approximation some schematic interactions (e.g. exponential potential, Woods-Saxon potential and delta potential) can be chosen to solve the problem analytically [19]. There is also another approach that the SPE and TBME are taken as free parameters to describe the nuclear excited states. Based on a set of experimental data the final effective TBME and SPE can be fitted using the iterative least-squares method. Due to enhanced capability of modern computing forms the last approach has been extensively applied to describe the nuclei in various shells.

In the next sections the discussion of the shell-model calculations is focussed on *sd*-shell nuclei, i.e. nuclei with  $8 \leq Z \leq 20$  and  $8 \leq N \leq 20$ .

## 1.2. The universal *sd* interaction - USD

The sub-shells  $1d_{5/2}$ ,  $2s_{1/2}$  and  $1d_{3/2}$  between the magic number 8 and 20 form the *sd* shell. Considering a model space which includes the full *sd* space, three SPE are needed as parameters:  $\varepsilon_{1d_{5/2}}$ ,  $\varepsilon_{2s_{1/2}}$  and  $\varepsilon_{1d_{3/2}}$ . For the TBME there are two kinds of nucleon-nucleon configurations required: (i) the configurations of two identical particles like proton-proton or neutron-neutron, with total isospin  $T = 1$ , and (ii) the proton-neutron configurations with total isospin  $T = 0$ . For the two-proton (or two-neutron) configurations there are 14 diagonal and 16 off-diagonal TBME to be determined. For the proton-neutron configurations there are 14 diagonal and 19 off-diagonal TBME. Therefore, 63 matrix elements and three single-particle energies need to be known to total, in order to describe the *sd*-shell.

In the 1980s B. H. WILDENTHAL and B. A. BROWN constructed a model-independent effective Hamiltonians, the so called universal *sd* interaction (USD) for *sd*-shell nuclei [20, 21], using the above mentioned approach that the SPE and TBME relative to the  $^{16}\text{O}$  core are treated as parameters in a least-square fit of experimentally determined ground-state binding energies and excited energies. The three SPE given

### 1. Nuclear Shell Model for *sd*-shell nuclei

by USD are independent of mass. On the other hand there is no mass-independent set of TBME in the USD, which can fit the experimental data of all *sd*-shell nuclei with good agreement. Therefore, based on the determined TBME of *sd*-shell nuclei with mass  $A = 18$ , the TBME for all other masses can be derived by the empirical formula [20]:

$$TBME(A) = TBME(A = 18) \times (18/A)^{0.3} \quad (1.7)$$

Assuming that the radius of a nucleus is proportional to  $A^{1/3}$  the approach of A-dependent BTMEs can be explained as that the increasing of nuclear size has an effect on the matrix elements of the nucleon-nucleon interaction.

Using the least-squares fit to 380 experimentally determined energy data of 66 *sd*-shell nuclei the USD Hamiltonian was obtained. The Root-Mean-Square (RMS) deviation between experimental and theoretical energies amount to around 150 keV for the final fit solution. However, as shown in Fig. 1.7, experimental data for the middle *sd*-shell nuclei were only sparsely included in the fit, although many energy states were already known. Due to the limited computational power in the 1980s, the times required to construct and diagonalize the energy matrices for nuclei located in the middle of the *sd*-shell with about 3 – 9 valence particles or holes were simply too large. In the last decades even more experimental data for the neutron-rich nuclei were obtained, and modern, more powerful computers provided the opportunity to improve the USD Hamiltonian by incorporating additional data sets, especially for the mid-shell nuclei. In 2006 B. A. BROWN and W. A. RICHTER derived the new USD Hamiltonians USDA/USDB [22], which considered 608 energy states of 77 nuclei distributed over the whole *sd* shell as shown in Fig. 1.8. Energy information on excited states of nuclei inside the so-called *island of inversion* with  $N = 19 - 20$  and  $Z = 10 - 12$ , which are known to deviate from the expected *sd*-shell characteristics [23–25], were not included in the fit. In the USDA and USDB Hamiltonians the SPE are treated to be A-independent and TBME are varied with the A-dependent factor  $(18/A)^{0.3}$  as for USD. Using 30 varied linear combinations the constrained Hamiltonian USDA was obtained. The RMS deviations between experimental values and the USDA calculations are around 160 keV. By varying 56 linear combinations of parameters the USDB Hamiltonian was derived, which gives a better fit of the data, with RMS deviations around 130 keV. The remaining deviation between experiment and theory might result from missing three-body forces, which were not considered in USD and USDA/B.

Figure 1.9 shows the comparison of experimental and theoretical ground-state binding energies for *sd*-shell nuclei. For the neutron-rich isotope  $^{27}\text{F}$  the signifi-

### 1. Nuclear Shell Model for *sd*-shell nuclei

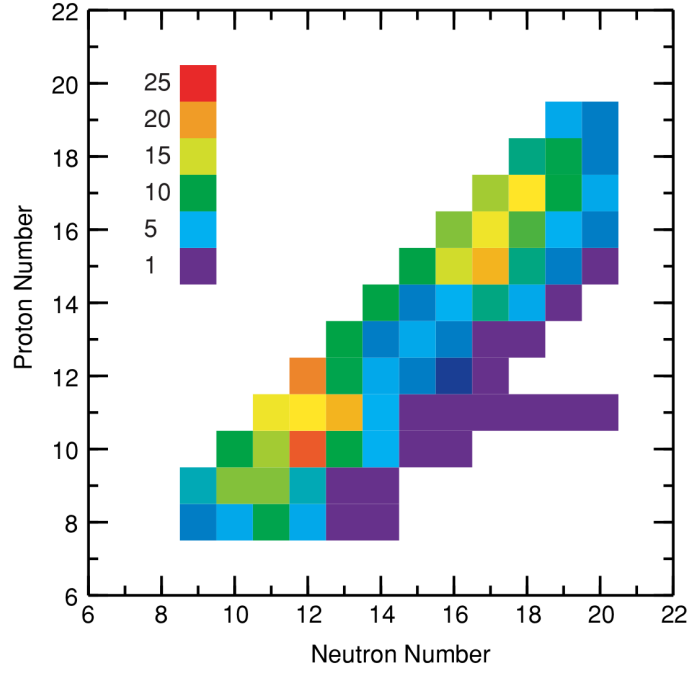


Figure 1.7.: Number of experimentally determined energy states used to fit the USD Hamiltonian for each nucleus. The maximum numbers of states are taken from nuclei around  $N = Z = 12$  and  $N = Z = 17$ , whilst nuclei around mid-shell are underrepresented (taken from [22]).

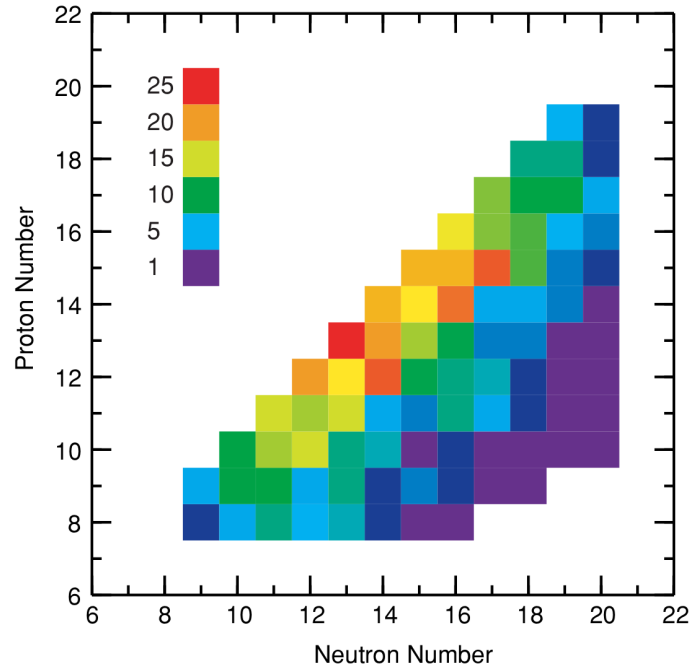


Figure 1.8.: Number of experimentally determined energy states used to fit the USDA and USDB Hamiltonian for each nucleus (Diagram taken from [22]).

## 1. Nuclear Shell Model for $sd$ -shell nuclei

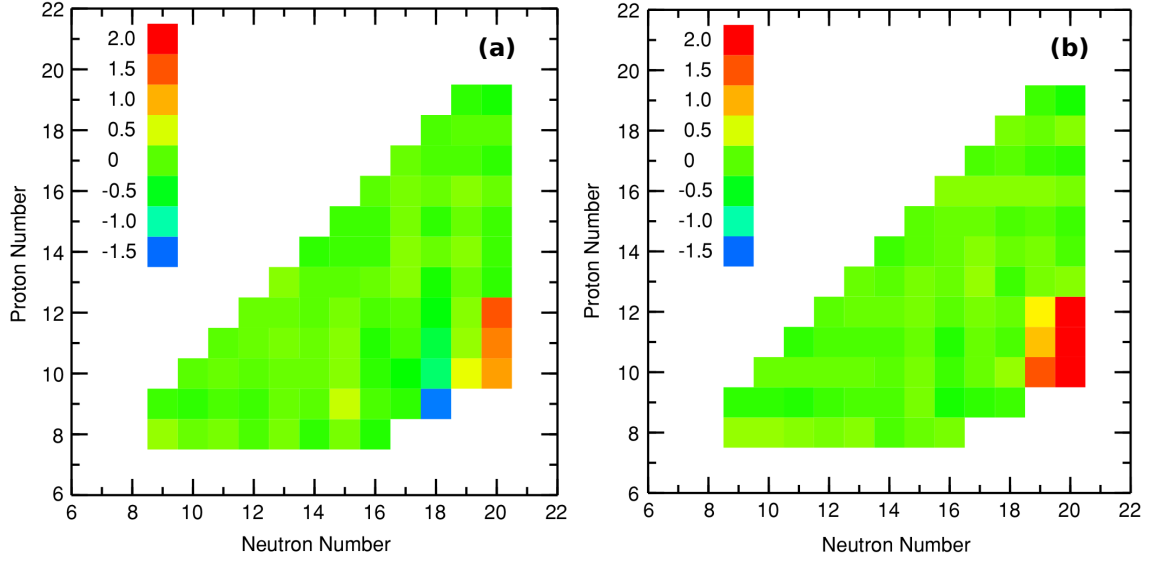


Figure 1.9.: Comparison of experimental and theoretical ground-state binding energies of  $sd$ -shell nuclei for (a) USD and (b) USDB. Colors represent the energy scale in MeV. A negative value indicates that a nucleus is more bound in theory than in experiment (adopted from [22]).

cant discrepancy between experimental and USD value around 1.5 MeV (cf. blue square in diagram (a)) has been improved in USDB. Both, USD and USDB, cannot reproduce the ground-state binding energies for the nuclei inside the island of inversion. Furthermore the USD and USDA/B Hamiltonians took only the pure  $sd$ -model space into consideration and omitted the  $p$ - $sd$  and  $sd$ - $pf$  cross-shell effects. Thus, the USD and USDA/B can primarily describe the  $0\hbar\omega$  low-lying positive-parity states of  $sd$ -shell nuclei with good agreement. For high excitation energies usually above  $E_x > 6$  MeV, the experimental level density becomes suddenly larger than the theoretical level density. Also the negative-parity excited states cannot be reproduced by USD or USDA/B. In order to understand these intruder states new Hamiltonians with extended model space are required.

### 1.3. Effective $sd$ - $pf$ shell-model interactions

To build a Hamiltonian which includes a model space larger than one major shell, truncations of the model space need to be done to reduce the  $J$ -dimension of the shell-model calculation. For neutron rich  $sd$ -shell nuclei the usual approach is to limit the valence protons in the  $sd$ -shell and to allow some neutrons to be excited from the  $sd$  shell into the  $pf$  shell or, in case of neutron-rich nuclei with  $N > 20$ , to have valence neutrons in the  $pf$  shell. This approach is based also on the fact

### 1. Nuclear Shell Model for *sd*-shell nuclei

that for proton excitations of neutron-rich *sd*-shell nuclei the energy gap between the  $1d$  and  $1f$  orbits is very large, therefore the *sd-pf* excitations for proton can be neglected.

Based on the successful USD interaction E. K. WARBURTON, J. A. BECKER and B. A. BROWN constructed the WBMB interaction to describe the  $A = 29 - 44$  nuclei with  $Z = 8 - 20$  and  $N = 18 - 25$  [26], which is also denoted as SDPFMW interaction and gives the first explanation for the island of inversion. The SDPFMW interaction for shell-model calculations in the *sd-pf* model space is derived from an effective one-body plus two-body Hamiltonian and is composed of three parts:

- *Wildenthal's USD interaction.* As described in section 1.2 the parameters of USD consist of three mass-independent SPEs and 63 mass-dependent TBMEs relative to the  $^{16}\text{O}$  core.

- *McGrory's  $fp$  interaction* [27]. To describe the  $(1f, 2p)$  interaction there are four SPEs and 195 TBMEs relative to the  $^{40}\text{Ca}$  core, which were assumed to be mass independent. The relative SPEs were set to 0, 2.1, 3.9 and 6.5 MeV for the  $1f_{7/2}$ ,  $2p_{3/2}$ ,  $2p_{1/2}$  and  $1f_{5/2}$  orbits, respectively.

- *The cross-shell interaction.* Connecting the *sd-pf* shells the cross-shell interaction was generated from the nucleon-nucleon potential of the Millener-Kurath particle-hole interaction [28]. There are 510 TBMEs needed to describe the interaction.

Based on the fact that the TBME of the USD interaction is  $A$ -dependent while the McGrory interaction is  $A$ -independent, the three interactions were connected with the  $A^{-0.3}$  dependence for  $A \leq 40$  nuclei for all three interactions, while for  $A \geq 40$  nuclei the TBMEs of the McGrory and Millener-Kurath interactions were fixed at their  $A = 40$  values. Using the SDPFMW interaction E. K. WARBURTON, J. A. BECKER and B. A. BROWN investigated the nuclei inside the island of inversion with the configurations of  $n\hbar\omega$  excitations ( $n = 0 - 4$ ). The anomaly of the ground-state binding energy for nuclei inside the island of inversion was explained by the deformed  $2\hbar\omega$  configurations to be energetically favoured over the spherical  $0\hbar\omega$  configurations.

Figure 1.10 shows the schematic diagram of the neutron structures of  $^{30}\text{Mg}$  ( $N = 18$ ) and  $^{32}\text{Mg}$  ( $N = 20$ ). Two neutrons additional on the  $^{30}\text{Mg}$  can form the  $J^\pi = 0^+$  state in  $^{32}\text{Mg}$  with neutron close-shell structure (A) ( $0\hbar\omega$ -excitation) and open-shell structure (B) ( $2\hbar\omega$ -excitation). Theoretically near the shell gaps the configuration (B) appears usually as excited state and the excitation energy is lower than twice the shell gap due to the pairing between the particles and between the holes. In recent experiment K. WIMMER *et al.* [29] confirmed that in  $^{32}\text{Mg}$  the excited



### 1. Nuclear Shell Model for $sd$ -shell nuclei

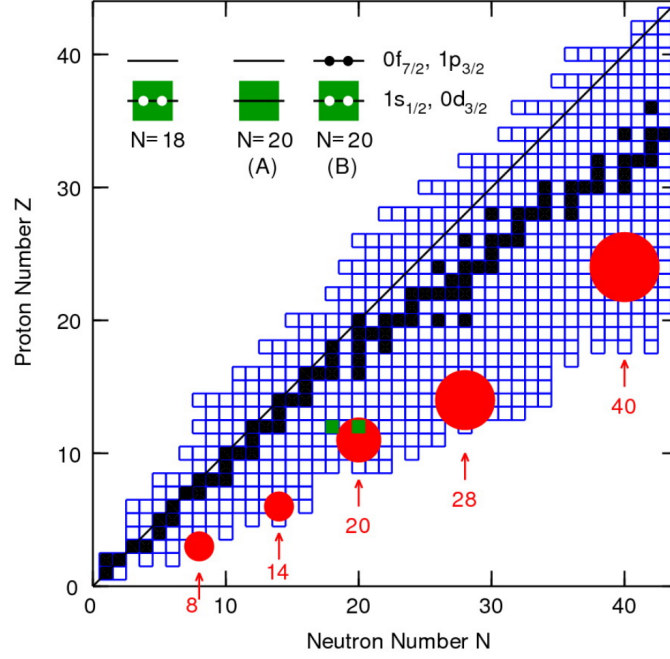


Figure 1.10.: The nuclear chart with stable nuclei (black squares) and unstable nuclei inside the proton and neutron drip lines (open blue squares). The areas marked by red circle indicate the regions with possibly altered shell closures. The shell model structure for neutrons of  $^{30}\text{Mg}$  ( $N = 18$ ) and  $^{32}\text{Mg}$  ( $N = 20$ ) are shown in green (Modified from [24]).

$0_2^+$  state locates above the  $0_1^+$  ground state with excitation energy about 1.06 MeV. Here the configuration (B) becomes the ground state. The inversion of  $2\hbar\omega$  relative to  $0\hbar\omega$  is caused by three important mechanisms: the reduction in the single-particle energy gap, the increase in the pairing-energy  $E_{nn}$ , and the increase in the  $Z$ -dependent proton-neutron interaction  $E_{pn}$ . In  $^{32}\text{Mg}$  the low excitation energy of  $0_2^+$ -state (1.06 MeV) cannot be reproduced by theoretical predictions. Understanding the reason for the disagreement with experiments is required to improve the many-body models in neutron-rich nuclei.

Besides the SDPFMW another mixed  $sd$ - $pf$  interaction is the SDPF-NR interaction, which was developed by J. RETAMOSA, E. CAURIER, F. NOWACKI and A. POVES [30–32]. The valence space of SDPF-NR consists of the full  $sd$  shell for  $Z - 8$  protons and the full  $pf$  shell for  $N - 20$  neutrons to describe neutron-rich nuclei with  $14 \leq Z \leq 20$  and  $N \geq 20$ . Similar to the SDPFMW interaction the SDPF-NR consists of three parts, including WILDENTHAL's USD interaction as starting point for particles in the  $sd$  shell. For particles in the  $pf$  shell a modified version of the Kuo-Brown interaction (denoted KB' in Ref [33]) is used to determine the TBMEs. As third part the  $G$  matrix of LEE, KAHANNA and SCOTT (LKS) [34] is taken to

### 1. Nuclear Shell Model for *sd*-shell nuclei

describe the cross-shell interaction, including mass-dependent TBMEs:

$$V = \left\{ \left( \frac{A_0}{A} \right) \left[ 1 - \zeta \left( \frac{N-Z}{A} \right)^{1/2} \right] \right\}^{1/3} V_0 \quad (1.8)$$

with  $\zeta = 0.42$  and  $A_0 = 40$ . For the characterization of electromagnetic transitions standard effective charges  $e_\pi = 1.5$  (for protons) and  $e_\nu = 0.5$  (for neutrons) are used.

Using large-scale shell-model calculations with the SDPF-NR interaction the nuclei around the shell closures  $N = 20$  and  $N = 28$  were investigated. Neutron-rich Ne, Na, and Mg isotopes around  $N = 20$  could successfully identified to belong to the island of inversion, indicating the breakdown of the  $N = 20$  shell closure. for Mg isotopes the deformation of the nuclei is predicted even for the neutron magic number  $N = 28$ . Therefore, according to the SDPF-NR calculations  $N = 28$  is not a closed shell for  $Z = 12$ . In a recent work by CRAWFORD *et al.* [35]  $^{40}\text{Mg}$  was produced via a two-proton knockout reaction of  $^{42}\text{Si}$  and the first structural information on the  $N = 28$  isotone was provided. This measurement provides support for the interpretation that the ground state of  $^{40}\text{Mg}$  is prolate deformed.

## 1.4. The PSDPF interaction

The abovementioned shell-model interactions SDPFMW and SDPF-NR (including the more recent version SDPF-U [36]) describe the energy levels of neutron-rich isotopes with  $Z = 8 - 20$  and  $N = 18 - 28$  very nicely. However, they do not describe successfully the odd- $A$  *sd*-shell nuclei. In particular for the first negative-parity intruder states the calculated energies are generally too high. Sometimes the ordering of the spins of negative-parity states cannot be reproduced. In order to resolve this issue, the PSDPF interaction was derived by BOUHELAL *et al.* [37].

Figure 1.11 shows the chart of *sd*-shell nuclei with an overall number of about 400 known negative-parity states, which emerge from  $1\hbar\omega$  excitation of one nucleon from the  $p$  to the  $sd$  or from the  $sd$  to the  $pf$  shell. The inclusion of the  $p$  and the  $pf$  shells to shell-model calculations required the treatment of  $p$ - $sd$  excitation for negative-parity states at the beginning of the *sd*-shell, and  $sd$ - $pf$  excitation for negative-parity states at the end of the *sd*-shell. To realize the shell-model description of the  $1p - 1h$  intruder states throughout the *sd*-shell, the model space must be extended to the full  $p$ - $sd$ - $pf$  space, which is based on a  $^4\text{He}$  core and allowing one nucleon jump from  $p$  to  $sd$  or  $sd$  to  $pf$ . As a consequence of the model-space extension the dimensions of the J-scheme matrix are so large, that all of these negative-parity

### 1. Nuclear Shell Model for *sd*-shell nuclei

[illegible]

Figure 1.11.: Chart of  $sd$ -shell nuclei with known negative-parity states until 2011 (Diagram modified from [37]).

states cannot be involved in the fitting procedure of the shell-model codes ANTOINE and NATHAN [38–40], especially for the nuclei located in the middle of the  $sd$ -shell. In the actual fitting process most of the  $0\hbar\omega$  positive-parity states of  $sd$ -shell nuclei have been included in the fit. However, in the case of  $1\hbar\omega$  states nuclei between  $Z = 10 - 14$  and  $A = 22 - 33$  were not included in the fit. The nuclei taken into account in the  $1\hbar\omega$  fit are shown in Fig. 1.12. The construction of the PSDPF interaction is based on the primary interactions of each major shell: the interaction of COHEN and KURATH (denoted as CK) [41] for the  $p$  shell, USDB for the  $sd$  shell, SDPF-NR for the  $pf$  shell. The interactions for cross-shell configurations are PSDT [42] for  $p$ - $sd$  and SDPF-NR for  $sd$ - $pf$ . The mass-dependence of  $(18/A)^{0.3}$  applied in the USD interaction was used for all TBMEs.

The final SPEs of the PSDPF interaction are presented in Table 1.1. The calculated energy gaps for doubly-magic nuclei, i.e.  $^{16}\text{O}$  and  $^{40}\text{Ca}$ , are a sensible test of the PSDPF interaction. For proton and neutron shells the energy gaps can be calculated [37]:

$$\begin{aligned} G_p &= 2BE(Z, N) - BE(Z + 1, N) - BE(Z - 1, N), \\ G_n &= 2BE(Z, N) - BE(Z, N + 1) - BE(Z, N - 1) \end{aligned}$$

where  $BE(N, Z)$  is the binding energy of nucleus  $(N, Z)$ . In the PSDPF interaction the Coulomb energy was not taken into account, thus the binding energies of mirror nuclei  $(Z, N + 1)$  and  $(Z + 1, N)$  are identical:  $G_p = G_n = G$ . Using the PSDPF in-

## 1. Nuclear Shell Model for $sd$ -shell nuclei

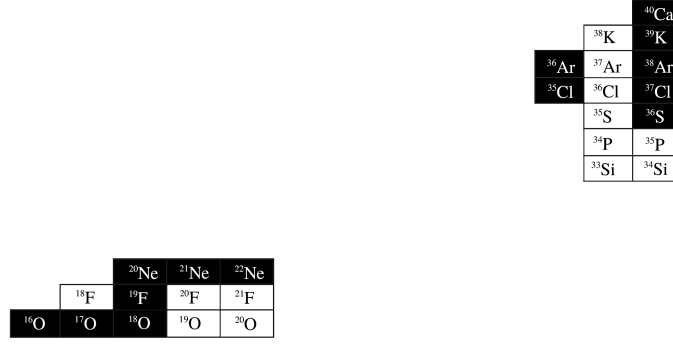


Figure 1.12.: Chart of  $sd$ -shell nuclei included in the fit of  $1\hbar\omega$  states. There are two regions of nuclei at both ends of  $sd$ -shell, which are treated in the fitting procedure separately. near  $^{16}\text{O}$  the  $1\hbar\omega$  configuration described as  $p^{-1}sd^1$ , while near  $^{40}\text{Ca}$  is  $sd^{-1}pf^1$ . Please note, that both nuclei of interest,  $^{33}\text{P}$  and  $^{33}\text{S}$ , are not part of the fitting basis for the PSDPF interaction. (Diagram modified from [37]).

teraction the energy gaps between the  $1p_{1/2}$  and  $1d_{5/2}$  orbitals of  $^{16}\text{O}$  was obtained as  $G = 11.26$  MeV [37], which is very close to the experimental value of 11.5 MeV [37]. In the case of  $^{40}\text{Ca}$ , the calculated energy gap between the  $1d_{3/2}$  and  $1f_{7/2}$  orbitals amounts to 7.24 MeV using the PSDPF interaction [37], while the experimental gaps for proton and neutron shells in  $^{40}\text{Ca}$  are 7.2 and 7.3 MeV, respectively [37]. Thus, the  $1p_{1/2} - 1d_{5/2}$  and  $1d_{3/2} - 1f_{7/2}$  energy gaps of the doubly-magic nuclei  $^{16}\text{O}$  and  $^{40}\text{Ca}$  is in a good agreement with PSDPF calculations.

Table 1.1.: Single Particle Energies (SPE) in MeV for the PSDPF interaction.

	$1d_{5/2}$	$2s_{1/2}$	$1d_{3/2}$	$1f_{7/2}$	$2p_{3/2}$	$1f_{5/2}$	$2p_{1/2}$
PSDPF	4.945	2.334	7.698	15.310	16.010	18.810	15.910

All  $0\hbar\omega$  and  $1\hbar\omega$  energy states up to 7 MeV in the  $sd$ -shell nuclei from  $^{16}\text{O}$  to  $^{40}\text{Ca}$  were calculated using the PSDPF interaction. For the nuclei, which were included in the  $0\hbar\omega$  and  $1\hbar\omega$  fitting procedure, the RMS deviation for positive-parity  $0\hbar\omega$  states yields 145 keV, while for the USDB interaction the value is 151 keV [22, 37]. For the negative-parity  $1\hbar\omega$  states PSDPF calculations give a RMS deviation of about 407 keV. For the mid-shell nuclei, which could not be included in the  $1\hbar\omega$  fitting procedure, the RMS deviation from PSDPF calculations for the negative-parity states amounts to 488 keV. The reduced accuracy of PSDPF calculations can be explained by the fact, that due to the extremely large dimensions of the J-scheme matrices, around 185 negative-parity states of  $sd$  mid-shell nuclei were not included in the fit.

## 1. Nuclear Shell Model for $sd$ -shell nuclei

Generally, the calculated results using the PSDPF interaction are in good agreement with experimental data for all  $sd$ -shell nuclei, especially for nuclei at the beginning and the end of the shell [43–45]. Figure 1.13 demonstrates the evolution of the first excited negative-parity  $3^-$  (a) and  $7/2^-$  (b) states in  $N = 18$  and 19 isotones. The good agreement in  $7/2^-$  allows further comparisons of PSDPF calculations and

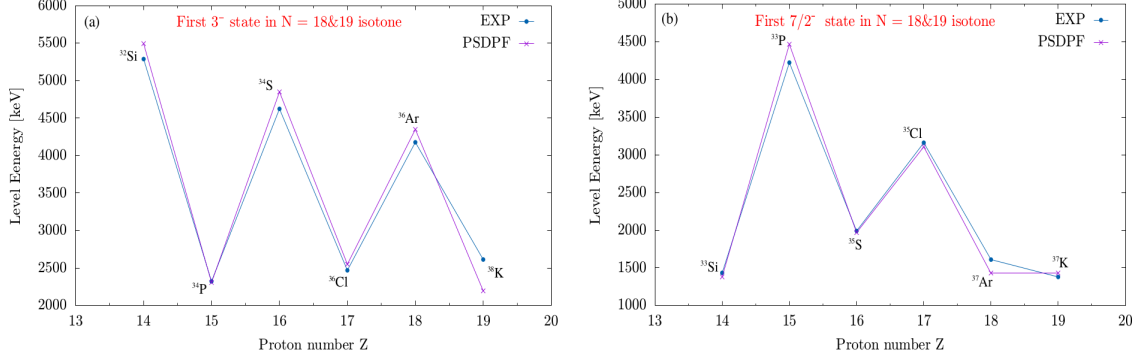


Figure 1.13.: Comparison of experimental and calculated excitation energies in  $N = 18$  and 19 isotones using the PSDPF interaction. (a) In the even-A isotones the  $3^-$  state is the first negative-parity state in the even-A isotones (except for odd-odd  $^{34}\text{P}$  and  $^{36}\text{Cl}$ ); (b) In odd-A nuclei of the upper  $sd$ -shell the  $7/2^-$  state is the first negative-parity state (Diagram modified from [46]).

known experimental data even by excited states with higher spin order and energies.

However, in the case of  $sd$  mid-shell nuclei, the wave functions of the intruder states can be massively mixed and sensitive to the kind of the  $1p - 1h$  excitations, i.e. competition of excitations from the  $p$  to the  $sd$  shell or the  $sd$  to the  $pf$  shell. To obtain a more satisfying description for  $1\hbar\omega$  configurations of the  $sd$  mid-nuclei, the current interaction would require new fitting procedures. For nuclei approaching the  $N$  and  $Z \sim 20$  shell gaps multi-particle multi-hole ( $n\hbar\omega$ ,  $n > 1$ ) excitations contribute more to the wave functions even at low excitation energies, which are also not included in the current PSDPF interaction.

### 1.5. The $A = 33$ isotopes $^{33}\text{P}$ and $^{33}\text{S}$

In the case of  $^{33}\text{P}$ , experimental investigations started in the 1970s. The level scheme of  $^{33}\text{P}$  up to 8 MeV was established using transfer reactions [47–50] as well as fusion-evaporation reaction [51]. The known states with high excitation energies up to 10.12 MeV were determined by DAVIS and NELSON using the  $^{30}\text{Si}(\alpha, p)^{33}\text{P}$  reaction [52]. Utilizing the Doppler-Shift Attenuation Method (DSAM) CURRIE *et*

### 1. Nuclear Shell Model for $sd$ -shell nuclei

*al.* [53], CARR *et al.* [54], POLETTI *et al.* [55] and WAGNER *et al.* [56] measured lifetimes of some low-lying states.

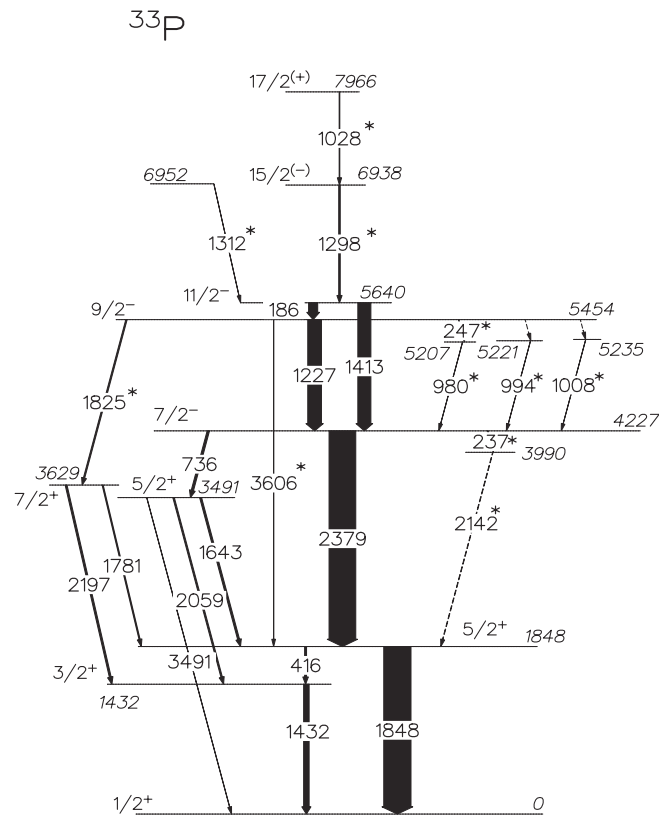


Figure 1.14.: Level scheme of  $^{33}\text{P}$  given by Ref. [51].

In a previous investigation of the level structure of  $^{33}\text{P}$  from Chakrabarti *et al.* [51] the level scheme of  $^{33}\text{P}$  was established up to 8 MeV using the fusion-evaporation reaction  $^{18}\text{O}(^{18}\text{O}, 2pn)^{33}\text{P}$  at 34 MeV. They reported new  $\gamma$ -ray transitions at 1028, 1298, 2142 and 3605 keV. Multipolarities of the respective transitions were investigated using DCO ratios, giving rise to first spin and parity assignments of the de-populated states and their places in the level scheme.

As previously reported, Chakrabarti *et al.* placed newly found  $\gamma$ -ray transitions at 1028, 1298, 2142, and 3605 keV in the level scheme, as shown in Fig. 1.14 [51]. With the amount of  $\gamma\gamma$  coincidences collected in the present experiment the former experimental indication for the allocation of these  $\gamma$ -ray transitions in the level scheme of  $^{33}\text{P}$  should easily be improved and extended to higher excitation energies. Indeed, the previously reported  $\gamma$ -ray transitions at 1028, 1298, 2142, and 3605 keV were confirmed to belong to  $^{33}\text{P}$  in the present analysis.

In  $^{33}\text{S}$ , by the means of particle spectroscopy the excitation energies were determined up to 17 MeV [57–59]. Using particle- $\gamma$  coincidences [60–62] as well as a

### 1. Nuclear Shell Model for *sd*-shell nuclei

fusion-evaporation reaction [63] the level scheme was established up to 7.9 MeV. CARR *et al.* determined the lifetime in  $^{33}\text{S}$  for states with energies up to 5.3 MeV utilizing the reaction  $^{30}\text{Si}(\alpha, n\gamma)^{33}\text{S}$  and DSAM. In a recent work Bisoi *et al.* reported two high-spin states of  $11/2^+$  at 7180 keV, and  $15/2^-$  at 7820 keV, using the fusion-evaporation reaction  $^{27}\text{Al}(^{12}\text{C}, \alpha pn)^{33}\text{S}$ . Similar to  $^{33}\text{P}$ , the previously reported  $\gamma$ -ray transitions at 2313 and 2952 keV [63] were also confirmed to belong to  $^{33}\text{S}$  in the present work.

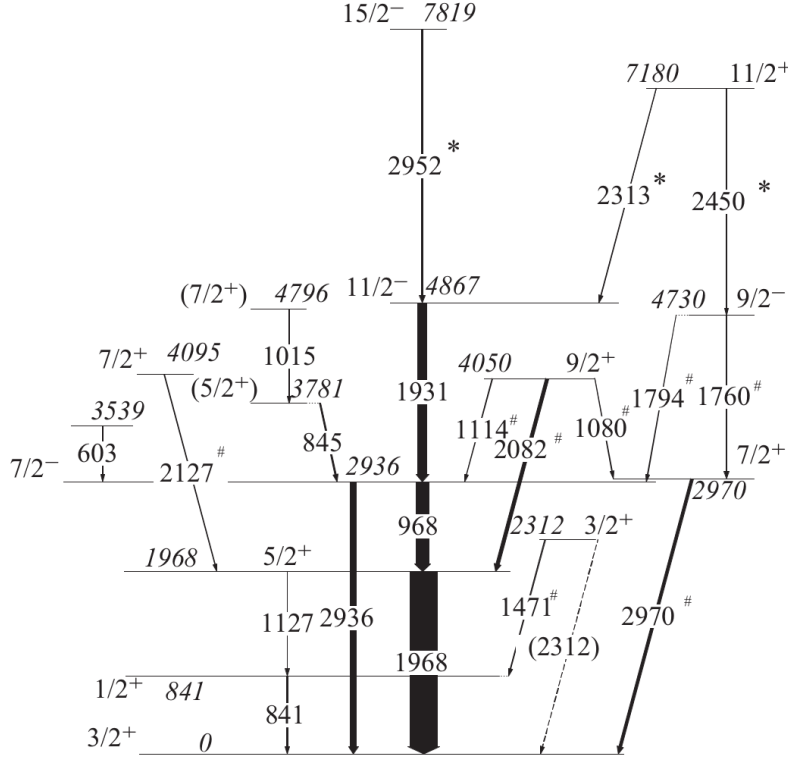


Figure 1.15.: Level scheme of  $^{33}\text{S}$  reported by Bisoi *et al.* [63]. In this work newly assigned  $\gamma$ -ray transitions are indicated by \*, and known  $\gamma$ -ray transitions observed in light-ion-induced transitions are indicated by #.

In both nuclei, the most interest of present work focused on the extension of level scheme to higher excitation energies. By means of  $\gamma\gamma$  angular correlation spin and parity assignments for newly determined states will be suggested, and compared to theoretical calculations. Note that in PSDPF calculations the Coulomb interaction is not taken into account, thus, the calculated energy spectra of mirror nuclei are identical [37]. Although this approximate treatment the theoretical prediction is still interesting for mirror nuclei  $^{33}\text{Ar}$  (for  $^{33}\text{P}$ ) and  $^{33}\text{Cl}$  (for  $^{33}\text{S}$ ). In the neutron deficient  $^{33}\text{Ar}$ , only 7 positive excited states with excitation energy up to 3.8 MeV are known [13]. There are no negative parity states reported. In  $^{33}\text{Cl}$ , the first experimental determined negative parity state is  $(5/2^-)$  at energy of 2.68 MeV, and

### *1. Nuclear Shell Model for $sd$ -shell nuclei*

the first  $7/2^-$  state is reported at energy of 4.78 MeV [13], while PSDPF calculations give the prediction of  $7/2_1^-$  state at 2.85 MeV and  $5/2_1^-$  state at 4.58 MeV (see chapter Shell-Model Calculations). This significant discrepancy requires further experimental and theoretical investigations.



## 2. $\gamma$ -ray spectroscopy of $^{33}\text{P}$ and $^{33}\text{S}$

### 2.1. The fusion-evaporation reaction $^{13}\text{C} + ^{26}\text{Mg}$

Excited states of the  $A = 33$  isotopes  $^{33}\text{P}$  and  $^{33}\text{S}$  have been populated by the fusion-evaporation reactions  $^{26}\text{Mg}(^{13}\text{C},pn\alpha)^{33}\text{P}$  and  $^{26}\text{Mg}(^{13}\text{C},2n\alpha)^{33}\text{S}$ , respectively. The  $^{13}\text{C}$  beam was delivered by the 10 MV FN tandem accelerator located at the Institute of Nuclear Physics in Cologne with a beam energy of 46 MeV and an average intensity of 1 pnA. For the population of the  $pn\alpha$  ( $^{33}\text{P}$ ) reaction channel the programs CASCADE [64] and LISE-PACE4 [65] yielded cross sections of around 120 mb and 188 mb, respectively, while for the  $2n\alpha$  ( $^{33}\text{S}$ ) reaction channel the cross sections were calculated to be around 246 mb and 366 mb, respectively. Although there is a discrepancy of the calculated production yields of both programs, the relative ratio  $\sigma_{33P}/\sigma_{33S} \sim 1/2$  of the cross sections is almost identical. The  $^{26}\text{Mg}$  target with a thickness of  $0.22 \frac{\text{mg}}{\text{cm}^2}$  was evaporated on a  $66 \frac{\text{mg}}{\text{cm}^2}$  thick  $^{209}\text{Bi}$  backing. The recoiling residual nuclei should be stopped after the reaction inside the backing material. Behind the  $^{209}\text{Bi}$  backing there is an additional  $1 \frac{\text{mg}}{\text{cm}^2}$  thin In layer plus an  $108 \frac{\text{mg}}{\text{cm}^2}$  thick Cu layer for improved heat dissipation.

De-excitation  $\gamma$  rays were detected by the High-efficiency Observatory for  $\gamma$ -Ray Unique Spectroscopy (HORUS) [66]. Figure 2.1 shows a schematic drawing of the HORUS  $\gamma$ -ray spectrometer. 14 high-purity germanium (HPGe) detectors were mounted around the target chamber at distances of approximately 10 cm to the target position, where BGO anti-Compton shields were mounted on 6 HPGe-detectors. The geometry of the HORUS-array allows measurements at five different angles  $\theta$  relative to the beam axis, i.e. at  $35^\circ$  (detectors 12 and 13),  $45^\circ$  (detectors 7 and 8),  $90^\circ$  (detectors 0 to 5),  $135^\circ$  (detectors 6 and 9) and  $145^\circ$  (detectors 10 and 11). The solid-angle coverage of the array is about 40% of  $4\pi$ . The  $\gamma$ -ray energies and the relative efficiency were calibrated using a  $^{226}\text{Ra}$  source. The count rate of each individual HPGe crystal during the experiment was maintained between 9 kHz and 12 kHz. The XIA Digital Gamma Finder (DGF) data-acquisition system [67, 68] was

## 2. $\gamma$ -ray spectroscopy of $^{33}\text{P}$ and $^{33}\text{S}$

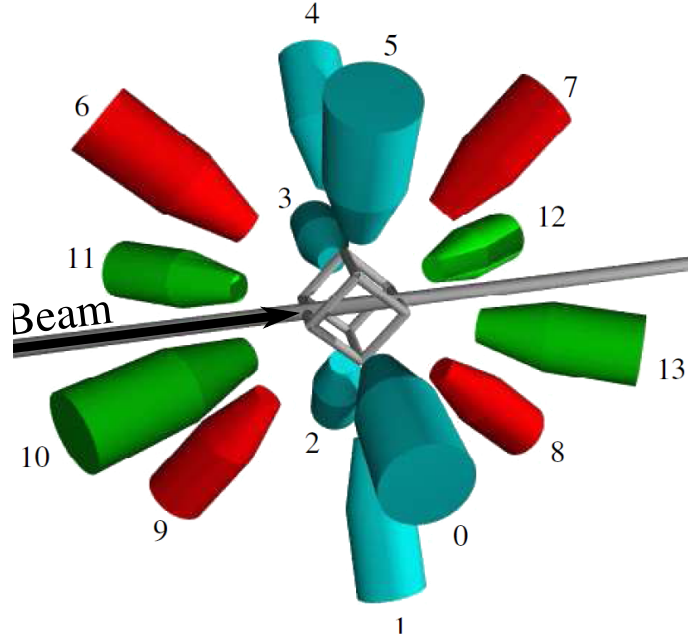


Figure 2.1.: Schematic drawing of the HORUS  $\gamma$ -ray spectrometer. The 14 HPGe detectors are mounted on the 6 faces and 8 corners of a cube geometry (Figure taken from [66]).

used to record  $\gamma\gamma$  coincidences. With a trigger condition of two detected  $\gamma$ -rays a total number of  $2.0 \times 10^9$  prompt coincident  $\gamma$ -ray events were recorded. Subsequently, data were sorted using the program SOCO [69] into three kinds of  $\gamma\gamma$ -coincidence matrices:

- (i) a symmetrical general matrix to study  $\gamma\gamma$ -coincidence relations;
- (ii) five matrices according to the angle  $\theta$  to determine level lifetimes using DSAM;
- (iii) 17 angular-correlation group matrices, which correspond to the relative angles  $\theta_{ij}$  and  $\phi$  between all detector pairs, to determine the spin- and parity-assumptions of the observed levels.

Isotopes populated in this experiment were identified by their prompt  $\gamma$ -ray emission observed in the projection spectra. Figure 2.2 shows the projection spectrum of the symmetric general  $\gamma\gamma$  matrix from the reaction. De-excitation  $\gamma$ -rays of  $^{30}\text{Si}$ ,  $^{33}\text{P}$ ,  $^{32,33,34}\text{S}$ ,  $^{34,35,36}\text{Cl}$  and  $^{37}\text{Ar}$  can be identified.  $^{21}\text{Ne}$  and  $^{23}\text{Na}$  formed in side reactions of  $^{13}\text{C}+^{16}\text{O}$  were also detected. The x-ray transitions from  $^{209}\text{Bi}$  (77 keV-KL<sub>2</sub>, 86 keV-KM<sub>3</sub>) and Coulex of  $^{13}\text{C}$  (169 keV:  $5/2^+ \rightarrow 3/2^-$ ) were identified. To investigate the nuclear structure of  $^{33}\text{P}$  and  $^{33}\text{S}$   $\gamma\gamma$ -coincidence spectra were obtained, allowing the identification of  $\gamma$ -ray transitions and their location in the level scheme up to high excitation energies.

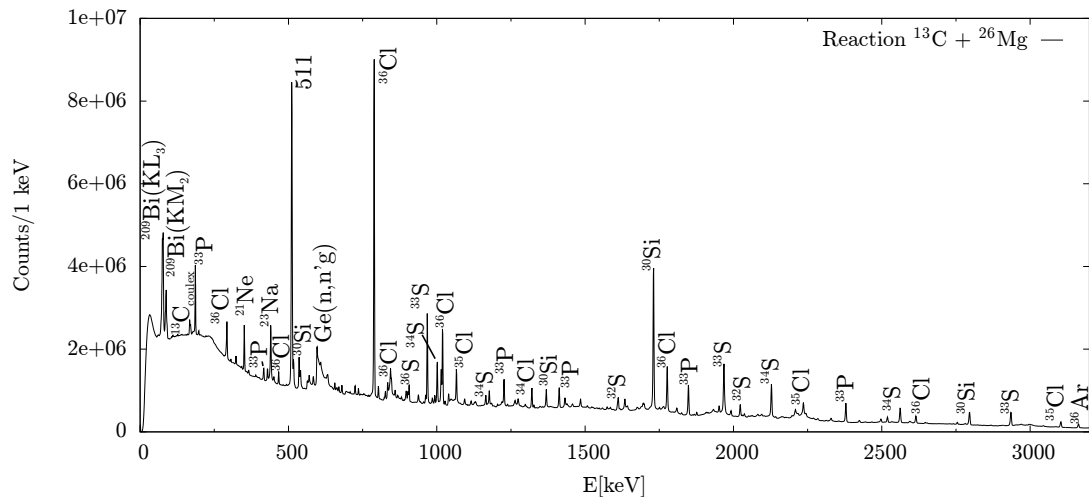


Figure 2.2.: Projection spectrum of the  $^{13}\text{C} + ^{26}\text{Mg}$  fusion-evaporation reaction at beam energy of 46 MeV. Populated reaction products are indicated of their characteristic  $\gamma$ -ray transitions.

## 2.2. Level scheme of $^{33}\text{P}$

Figure 2.3(a) shows the  $\gamma\gamma$ -coincidence spectrum with a gate set on the 1298 keV  $\gamma$ -ray transition in  $^{33}\text{P}$ . There are unambiguous coincidences between the 1298 keV transition and known  $\gamma$ -ray transitions in  $^{33}\text{P}$ . Moreover, a new  $\gamma$ -ray transition with an energy of 3169 keV was detected which also belongs to  $^{33}\text{P}$ . Chakrabarti *et al.* assigned 2142 keV transition as a weak depopulating transition from a newly introduced state at 3990 keV to a well-known  $5/2^+$  state at 1848 keV. Thus, the strong coincidence between 1298 keV and 2142 keV observed in the present work was unexpected. To clarify the location of the 2142 keV transition, its coincidence relations were investigated. As shown in Fig. 2.3(b) the 2142 keV  $\gamma$ -ray transition is obviously coincident with the transitions at 1028, 1298, 1412, 1848 and 2378 keV, and thus it cannot be in parallel to any of these transitions. Instead the 2142 keV transition should be the de-exciting  $\gamma$ -ray transition from a new state at 9078 keV in  $^{33}\text{P}$ . With a coincidence gate on the 1028 keV transition (see Fig. 2.3(c)) new  $\gamma$ -ray transitions at 1168, 1349, 1535, 2090, 2271, 2581, 2762 and 3440 keV were placed in the level scheme according to the observed  $\gamma\gamma$ -coincidence relations, intensity balances, and energy sums [cf. Fig. 2.4].

The energy sums of the 1028- plus 2142-keV transitions and of the 1298- plus 2142-keV transitions matched the energies of the 3169- and 3440-keV transitions, respectively. Hence, the 2142-keV transition had to be placed between the de-exciting 1028- and 1298-keV transitions, including new energy levels at 9078 and 10106 keV. The energy levels at 3990 keV and 7966 keV introduced by Chakrabati

## 2. $\gamma$ -ray spectroscopy of $^{33}\text{P}$ and $^{33}\text{S}$

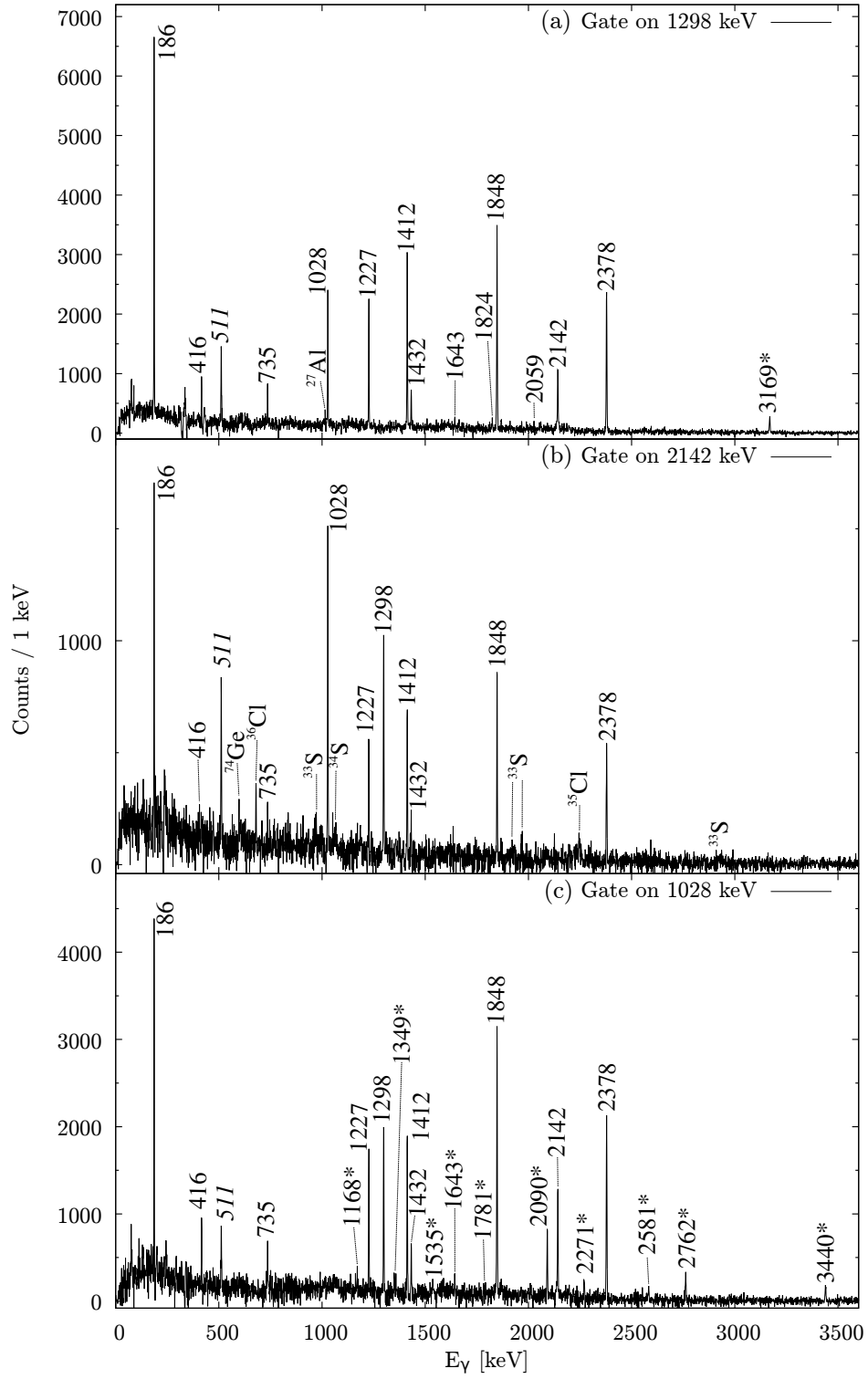


Figure 2.3.:  $\gamma\gamma$ -coincidence spectra in  $^{33}\text{P}$  with gates set on  $\gamma$ -ray transitions at (a) 1298, (b) 2142, and (c) 1028 keV, respectively. The newly detected  $\gamma$ -rays are indicated with an asterisk.

## 2. $\gamma$ -ray spectroscopy of $^{33}\text{P}$ and $^{33}\text{S}$

*et al.* cannot be confirmed in the present work. Moreover, the newly established energy level at 9078 keV is de-excited by three more  $\gamma$ -ray transitions at 2090, 2271 and 3440 keV. Due to  $\gamma\gamma$ -coincidence relations and energy sums of the 2090-keV transition and the  $\gamma$ -ray transitions at 186, 1227, 1349, 1535 and 2762 keV, another energy level was firmly established at 6807 and 6988 keV. The known energy level at 6936 keV was found to be de-excited by an additional 1484-keV transition to the  $9/2^-$  level. A new energy level at 6807 keV was introduced due to the observation of a 2271-keV populating transition and two weak de-exciting  $\gamma$ -ray transitions at 1168 keV and 2581 keV. The  $\gamma\gamma$ -coincidence analysis showed that the  $\gamma$ -ray events detected at 1356 keV, correspond only to the double-escape events of the 2378-keV transition, and not a possible transition between the 6807-keV and the 5453-keV levels. The newly found  $\gamma$ -ray transitions at 880 keV, 3587 keV, and 4467 keV were identified as new de-excitation paths off the 10106-keV level, with the cascade 880-3587 keV proceeding via a new level at 6518 keV (see Fig. 2.4).

The experimentally deduced energies, spins and parities of the levels as well as the relative intensities of the de-exciting  $\gamma$ -ray transitions are summarized in Table 2.1. The spin-assignments of the new energy states were determined by means of  $\gamma\gamma$  angular correlations. Details of this method is discussed in the following paragraphs.

## 2. $\gamma$ -ray spectroscopy of $^{33}\text{P}$ and $^{33}\text{S}$

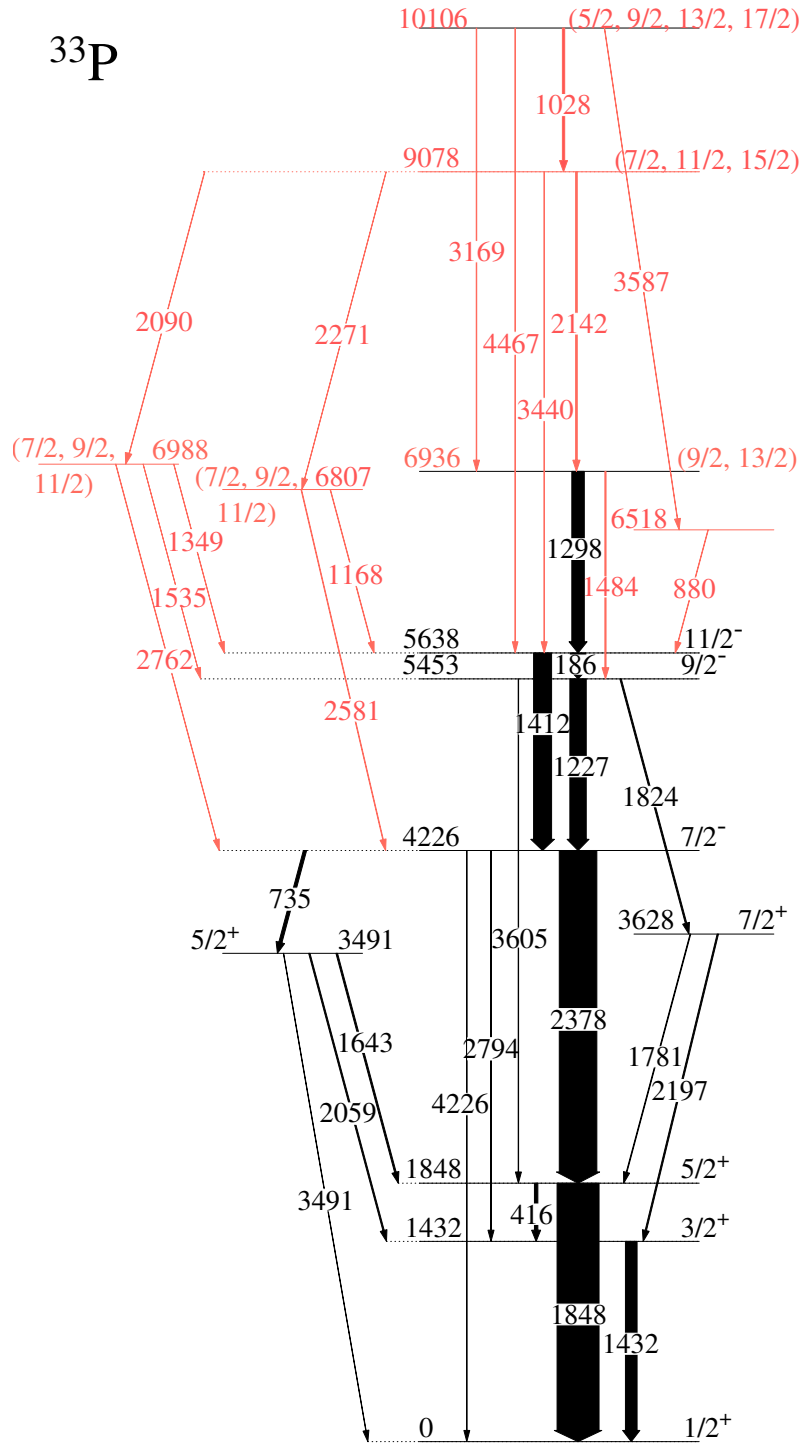


Figure 2.4.: Partial level scheme of  $^{33}\text{P}$ , as observed in the current experiment. New energy levels and assigned  $\gamma$ -ray transitions are marked in red. The widths of the arrows correspond to the relative intensities of the observed  $\gamma$ -ray transitions.

## 2. $\gamma$ -ray spectroscopy of $^{33}\text{P}$ and $^{33}\text{S}$

Table 2.1.: Level energies, spin-parity assignments,  $\gamma$ -ray transition energies, branching ratios and multiplicities for  $^{33}\text{P}$ . The energies of  $\gamma$ -ray transitions, branching ratios and level spin-parity assignments are determined from the present experiment. The transition multiplicities are taken from National Nuclear Data Center (NNDC) [13].

$E_i$ [keV]	$E_f$ [keV]	$J_i^\pi$	$J_f^\pi$	$E_\gamma$ [keV]	Branching ratios (%)	Multiplicity
$^{33}\text{P}$						
1432	0	$3/2^+$	$1/2^+$	1431.6 (3)	100.0 (10)	M1+E2
1848	0	$5/2^+$	$1/2^+$	1847.5 (3)	100.0 (5)	E2+M3
	1432	$5/2^+$	$3/2^+$	415.9 (2)	7.0 (1)	M1+E2
3491	0	$5/2^+$	$1/2^+$	3490.1 (10)	13.4 (15)	E2(+M3)
	1432	$5/2^+$	$3/2^+$	2058.5 (8)	73.6 (25)	(M1+E2)
	1848	$5/2^+$	$5/2^+$	1642.6 (4)	100.0 (22)	M1(+E2)
3628	1432	$7/2^+$	$3/2^+$	2196.0 (8)	100.0 (48)	E2
	1848	$7/2^+$	$5/2^+$	1780.1 (6)	44.5 (45)	M1(+E2)
4226	1432	$7/2^-$	$3/2^+$	2794.1 (13)	1.2 (2)	(M2)
	1848	$7/2^-$	$5/2^+$	2378.2 (5)	100.0 (4)	E1(+M2)
	3491	$7/2^-$	$5/2^+$	735.6 (3)	8.9 (2)	E1
5453	1848	$9/2^-$	$5/2^+$	3604.5 (15)	1.3 (4)	(M2)
	3628	$9/2^-$	$7/2^+$	1824.4 (4)	8.7 (2)	(E1)
	4226	$9/2^-$	$7/2^-$	1226.3 (3)	100.0 (3)	M1+E2
5638	5453	$11/2^-$	$9/2^-$	185.6 (3)	79.9 (18)	M1
	4226	$11/2^-$	$7/2^-$	1411.9 (4)	100.0 (23)	E2
6518	5638		$11/2^-$	880.3 (12)	100.0 (70)	
6807	4226	( $7/2, 9/2, 11/2$ )	$7/2^-$	2581.6 (10)	19.6 (50)	
	5638	( $7/2, 9/2, 11/2$ )	$11/2^-$	1168.6 (8)	100 (11)	
6936	5453	( $9/2, 13/2$ )	$9/2^-$	1484.2 (9)	13.8 (29)	
	5638	( $9/2, 13/2$ )	$11/2^-$	1297.9 (4)	100.0 (31)	(Q)
6988	4226	( $7/2, 9/2, 11/2$ )	$7/2^-$	2761.0 (11)	100 (11)	
	5453	( $7/2, 9/2, 11/2$ )	$9/2^-$	1535.4 (11)	36.3 (71)	
	5638	( $7/2, 9/2, 11/2$ )	$11/2^-$	1349.4 (10)	49 (10)	
9078	5638	( $7/2, 11/2, 15/2$ )	$11/2^-$	3440 (2)	25.3 (25)	
	6807	( $7/2, 11/2, 15/2$ )	( $7/2, 9/2, 11/2$ )	2269.8 (12)	18.9 (29)	
	6936	( $7/2, 11/2, 15/2$ )	( $9/2, 13/2$ )	2141.8 (7)	100.0 (35)	
	6988	( $7/2, 11/2, 15/2$ )	( $7/2, 9/2, 11/2$ )	2090.6 (5)	50.3 (29)	
10106	5638	( $5/2, 9/2, 13/2, 17/2$ )	$11/2^-$	4468 (3)	5.7 (11)	
	6518	( $5/2, 9/2, 13/2, 17/2$ )		3587 (2)	13.4 (17)	
	6936	( $5/2, 9/2, 13/2, 17/2$ )	( $9/2, 13/2$ )	3169.4 (12)	19.4 (15)	
	9078	( $5/2, 9/2, 13/2, 17/2$ )	( $7/2, 11/2, 15/2$ )	1027.6 (3)	100.0 (18)	(D)

### 2.3. Level Scheme of $^{33}\text{S}$

In a recent work from Bisoi *et al.* [63] the level scheme of  $^{33}\text{S}$  was extended up to 7.8 MeV, with high-spin states up to  $J^\pi = 15/2^-$ . In the present work several new  $\gamma$ -ray transitions were found to de-excite states at excitation energies up to 10 MeV in  $^{33}\text{S}$ , and were analysed for their  $\gamma\gamma$ -coincidence relations, energy sums and intensity balances. Figure 2.5(a) shows the  $\gamma\gamma$ -coincidence spectrum with a gate set on the 1761-keV transition. The newly detected  $\gamma$ -ray events at 1063, 1173, 1641, 2270 and 2848 keV are all de-exciting transitions of previously unknown energy levels.

Additional new  $\gamma$ -ray transitions in  $^{33}\text{S}$  were detected at 1520, 2133, 2511, 2545 and 2951 keV in coincidence with the 1641-keV transition (cf. Fig. 2.5(b)). The new  $\gamma$ -ray transition observed at 2951 keV is in coincidence with  $\gamma$  rays at 1079, 1967, 2081, and 2969 keV. The latter transitions are known as part of the de-excitation cascade of the  $9/2^+$  state at 4049 keV. Thus, the 2951-keV transition was placed on top of the  $9/2^+$  state, de-populating a level at 7000 keV. Additionally, the level at 7000 keV is connected to the known  $7/2^+$  state at 4095 keV, to the  $9/2^-$  state at 4730 keV, and to the  $11/2^-$  state at 4867 keV via the  $\gamma$ -ray transitions with energies of 2905, 2270, and 2133 keV, respectively. All de-exciting  $\gamma$ -ray transitions of the 7000-keV level were observed without significant Doppler broadening. Hence, with a typical stopping time  $\Delta t_{\text{stop}} \sim 1.3$  ps of the  $^{33}\text{S}$  recoils in the  $^{209}\text{Bi}$ -backing of the target, a lifetime  $\tau > 1$  ps for the 7000-keV state is expected. Another de-excitation path was found via the 1520-keV transition feeding a new state at 5480 keV, which de-excites via the newly observed  $\gamma$ -ray transitions at 2511 and 2545 keV to the  $7/2^+$  and  $7/2^-$  states, respectively. The  $\gamma\gamma$ -coincidence spectrum with a gate set on the 1520-keV transition is shown in Fig. 2.5(c).

The state at 5480 keV cannot be the  $1/2^+$  state, previously reported at the same energy in  $(n, \gamma)$  [62],  $(^3\text{He}, p\gamma)$  [70], and  $(^3\text{He}, \alpha\gamma)$  reactions [61], as the direct  $\gamma$ -ray transitions to the ground and lowest-lying states, observed with a dominant branching in the afore mentioned experiments, were missing in the present experiment. However, Dubios *et al.* observed additional weak  $\gamma$ -ray transitions at energies of 1.95, 2.53, and 2.95 MeV in  $^{34}\text{S}(^3\text{He}, \alpha\gamma)^{33}\text{S}$  reactions [61], which are within the resolution of the formerly used NaI(Tl) crystals consistent with the  $\gamma$ -ray decay of the newly proposed level at 5480 keV. In coincidence with all transitions depopulating the 7000-keV state a strong  $\gamma$ -ray transition was observed at 1641 keV and was assigned to be a feeding transition to the 7000-keV level, thus introducing a new level with an excitation energy of 8641 keV. Due to observed Doppler-shift attenuation effects of the measured 1641-keV transition, the lifetime of the 8641-keV level should be  $< 1$  ps. Another weak decay branch of this level was observed



## 2. $\gamma$ -ray spectroscopy of $^{33}\text{P}$ and $^{33}\text{S}$

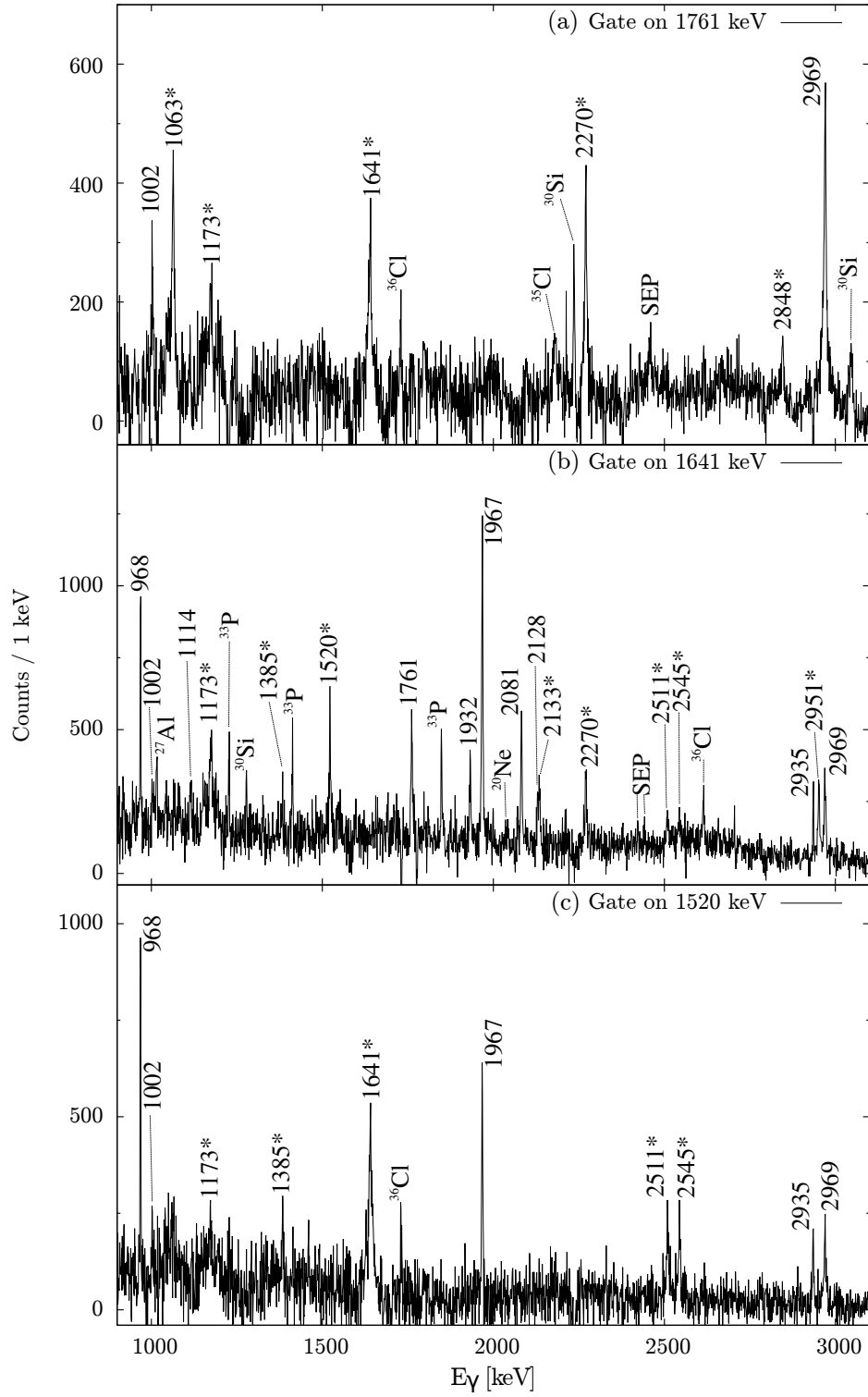


Figure 2.5.:  $\gamma\gamma$ -coincidence spectra in  $^{33}\text{S}$  with gates set on  $\gamma$ -ray transitions at (a) 1761, (b) 1641, and (c) 1520 keV, respectively. The newly detected  $\gamma$ -rays are indicated with an asterisk.

## 2. $\gamma$ -ray spectroscopy of $^{33}\text{P}$ and $^{33}\text{S}$

via the 2848-keV  $\gamma$  ray, which populates a new level at 5793 keV. In a previous work Raman *et al.* reported a  $1/2^+$  state at 8640 keV, using the  $^{32}\text{S}(n, \gamma)^{33}\text{S}$  reaction [70]. However, the strong de-exciting  $\gamma$ -ray transitions of this  $1/2^+$  state at 2930 and 5420 keV, were not observed in the present experiment. Thus, the newly introduced 8641-keV level is not assigned to the known  $1/2^+$  state at 8640 keV. Furthermore, a high-lying state with excitation energy of 9814 keV was determined to be connected by a 1173-keV transition to the 8641-keV state. Additionally,  $\gamma$ -ray decays of the short-lived ( $11/2^+$ ) and  $15/2^-$  states at 7180 and 7820 keV, respectively, reported recently by Biosi *et al.* [63], were observed. However, the proposed 2450-keV transition de-exciting the ( $11/2^+$ ) state could not be confirmed in the present experiment.

In summary the newly detected  $\gamma$ -ray transitions were placed in the level scheme of  $^{33}\text{S}$ , as shown in Fig. 2.6 and listed in Table 2.2. Within the present experiment it was not possible to perform  $\gamma\gamma$  angular-correlation analysis for  $^{33}\text{S}$  due to the limited statistics. Thus, the spin and parity of the newly determined energy levels were not assigned, while the spins and parities of the known states were taken from Refs. [13, 63].

## 2. $\gamma$ -ray spectroscopy of $^{33}\text{P}$ and $^{33}\text{S}$

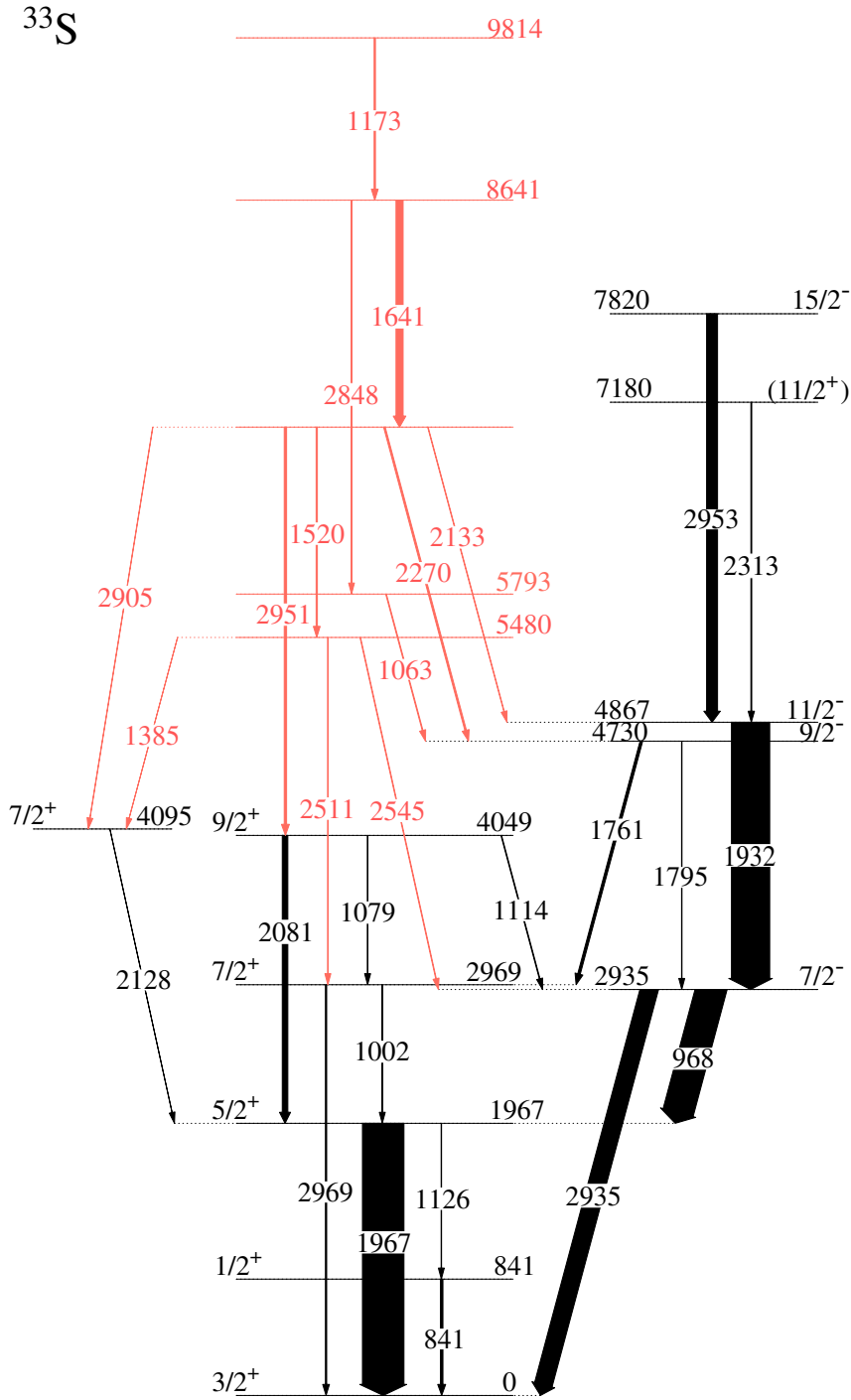


Figure 2.6.: Partial level scheme of  $^{33}\text{S}$ , as observed in the present work. New energy levels and assigned  $\gamma$ -ray transitions are marked in red. The widths of the arrows correspond to the relative intensities of the observed  $\gamma$ -ray transitions.

## 2. $\gamma$ -ray spectroscopy of $^{33}\text{P}$ and $^{33}\text{S}$

Table 2.2.: Level energies, spin-parity assignments,  $\gamma$ -ray transition energies, branching ratios and multiplicities for  $^{33}\text{S}$ . The energies of  $\gamma$ -ray transitions, and branching ratios are determined from the present experiment. The transition multiplicities are taken from National Nuclear Data Center (NNDC) [13].

$E_i$ [keV]	$E_f$ [keV]	$J_i^\pi$	$J_f^\pi$	$E_\gamma$ [keV]	Branching ratios (%)	Multiplicity
$^{33}\text{S}$						
841	0	$1/2^+$	$3/2^+$	840.6 (6)	100 (4)	M1+E2
1967	0	$5/2^+$	$3/2^+$	1966.9 (4)	100.0 (2)	M1+E2
	841	$5/2^+$	$1/2^+$	1126.3 (7)	1.5 (1)	E2
2935	0	$7/2^-$	$3/2^+$	2934.4 (8)	90.1 (11)	(M2+E3)
	1967	$7/2^-$	$5/2^+$	967.5 (4)	100.0 (7)	E1(M2)
2969	0	$7/2^+$	$3/2^+$	2968.9 (12)	100.0 (22)	E2
	1967	$7/2^+$	$5/2^+$	1002.0 (8)	13.1 (18)	M1(+E2)
4049	1967	$9/2^+$	$5/2^+$	2081.5 (6)	100.0 (31)	E2(+M3)
	2935	$9/2^+$	$7/2^-$	1113.6 (10)	6.1 (1.9)	E1
	2969	$9/2^+$	$7/2^+$	1079.5 (8)	32.8 (25)	(M1+E2)
4095	1967	$7/2^+$	$5/2^+$	2128.2 (11)	100 (9)	(M1+E2)
4730	2935	$9/2^-$	$7/2^-$	1795 (2)	20.3 (29)	M1+E2
	2969	$9/2^-$	$7/2^+$	1760.9 (11)	100.0 (39)	E1(+M2)
4867	2935	$11/2^-$	$7/2^-$	1932.1 (10)	100 (8)	(E2(+M3))
5480	2935		$7/2^-$	2545 (2)	70.1 (72)	
	2969		$7/2^+$	2510.5 (12)	100 (8)	
	4095		$7/2^+$	1383.7 (10)	29.2 (61)	
5793	4730		$9/2^-$	1063.4 (8)	100 (5)	
7000	4049		$9/2^+$	2951.3 (12)	100 (6)	
	4730		$9/2^-$	2269.9 (10)	84.4 (61)	
	4867		$11/2^-$	2133.2 (11)	71.5 (68)	
	5480		$1/2^+$	1520.3 (8)	82.3 (58)	
7180	4867	$(11/2^+)$	$11/2^-$	2313 (2)	100 (8)	
7820	4867	$15/2^-$	$11/2^-$	2954 (3)	100 (7)	(M1+E2)
8641	5793			2847 (3)	6.9 (28)	
	7000			1641.4 (16)	100 (6)	
9814	8641			1173.2 (8)	100 (7)	

## 2.4. $\gamma\gamma$ angular-correlation analysis

The investigation of emitted  $\gamma$ -rays after nuclear reactions can provide key information to characterize excited nuclear states. For example, employing lifetime measurements (e.g. electronic fast timing, recoil-distance Doppler-shift, Doppler-shift attenuation method) the transition strength can be determined. Using analysis of directional correlations de-exciting oriented states (DCO-ratio) the dipole or quadrupole nature of  $\gamma$ -ray transitions can be distinguished. Utilising linear-polarisation measurements the electric or magnetic character of  $\gamma$ -radiation can be identified. Investigating  $\gamma\gamma$  angular correlation unknown spins of excited states can be determined. In the following paragraphs the method of  $\gamma\gamma$  angular correlation is explicated.

### 2.4.1. Properties of $\gamma$ radiation

A measurement of  $\gamma\gamma$  angular correlation is based on the properties of  $\gamma$ -ray emission, i.e. of electromagnetic radiation. In spherical coordinates the wave function  $\psi(r, \theta, \phi)$  of the emitted  $\vec{E}$ - and  $\vec{B}$ -field can be written as:

$$\psi(r, \theta, \phi) = \frac{U(r)}{r} \cdot P(\cos \theta) \cdot Q(\phi) \quad (2.1)$$

where  $U(r)$  is the radial function depends only on radial distance  $r$ ,  $P(\cos \theta)$  depends on polar angle  $\theta$ , and  $Q(\phi)$  depends on azimuthal angle  $\phi$ . Introducing differential equations in spherical coordinates, the corresponding Legendre polynomials as solutions are obtained as a function of  $\theta$ :

$$P_l^m(\cos \theta) = \frac{(-1)^m}{2^l l!} (1 - \cos^2 \theta)^{m/2} \frac{d^{l+m}}{d(\cos \theta)^{l+m}} (\cos^2 \theta - 1)^l, \quad (2.2)$$

with  $l = 0, 1, 2, \dots$  and  $m = 0, \pm 1, \dots \pm l$ . The  $\phi$ -dependent solutions are then given by:

$$Q(\phi) = e^{im\phi} \quad (2.3)$$

For the study of angular distributions the radial dependence of the wave function is not relevant. The angular terms for the solutions of  $\theta$  and  $\phi$  can be combined as:

$$Y_{lm}(\theta, \phi) = \sqrt{\frac{2l+1}{4\pi} \cdot \frac{(l-m)!}{(l+m)!}} \cdot P_l^m(\cos \theta) \cdot e^{im\phi} \quad (2.4)$$

## 2. $\gamma$ -ray spectroscopy of $^{33}\text{P}$ and $^{33}\text{S}$

Considering a  $\gamma$ -ray transition with angular momentum  $\vec{l}$  between two states, the eigenfunction can be written as:

$$\vec{X}_l^m(\theta, \phi) = \frac{\vec{l}}{\sqrt{l(l+1)}} \cdot Y_l^m(\theta, \phi) \quad (2.5)$$

Due to the conservation of the total angular momentum the transition from an initial state  $J_i^\pi$  to a final state  $J_f^\pi$ , must fullfill the equation:

$$\vec{J}_i + \vec{l} = \vec{J}_f \quad (2.6)$$

The possible quantum number of  $l$  is therefore restricted by:

$$|J_i - J_f| \leq l \leq J_i + J_f, \quad \text{with } m = m_i - m_f \quad \text{and } |m| \leq l, \quad (2.7)$$

A transition  $0^+ \rightarrow 0^+$  with  $l = 0$  is forbidden since the photon has an intrinsic spin of 1. Considering the parity transformation this leads to:

$$\pi_i \cdot \pi_f = (-1)^l \quad \text{for an electric transition } El \quad (2.8)$$

$$\pi_i \cdot \pi_f = (-1)^{l+1} \quad \text{for a magnetic transition } Ml \quad (2.9)$$

For the electric and magnetic transitions the transition strengths can be written as:

$$\lambda^{(E)}(l, m) = \frac{8\pi k^{2l+1}}{\hbar[(2l+1)!!]^2} \left( \frac{l+1}{l} \right) |\langle f|Q_{lm}|i\rangle + \langle f|Q'_{lm}|i\rangle|^2, \quad (2.10)$$

and

$$\lambda^{(M)}(l, m) = \frac{8\pi k^{2l+1}}{\hbar[(2l+1)!!]^2} \left( \frac{l+1}{l} \right) |\langle f|M_{lm}|i\rangle + \langle f|M'_{lm}|i\rangle|^2, \quad (2.11)$$

with  $k = E_\gamma/(\hbar c)$ .  $Q_{lm}$  and  $M_{lm}$  are the multipole moments for electric transitions and magnetic transitions, respectively. The terms  $|\langle f|Q_{lm}|i\rangle + \langle f|Q'_{lm}|i\rangle|^2$  and  $|\langle f|M_{lm}|i\rangle + \langle f|M'_{lm}|i\rangle|^2$  are generally called the reduced transition strengths  $B(El)$  and  $B(Ml)$ , respectively. Using the Weisskopf estimate for a single-particle transition [71] the reduced electric transition strength  $B(El)$  and the reduced magnetic

## 2. $\gamma$ -ray spectroscopy of $^{33}\text{P}$ and $^{33}\text{S}$

transition strength  $B(Ml)$  are defined as:

$$B(El, J_i \rightarrow J_{g.s.}) = \frac{(r_0)^{2l}}{4\pi} \left( \frac{3}{l+3} \right)^2 A^{2l/3} e^2 (fm)^{2l} \quad (2.12)$$

$$B(Ml, J_i \rightarrow J_{g.s.}) = \frac{10}{4\pi} (r_0)^{2l-2} \left( \frac{3}{l+3} \right)^2 A^{(2l-2)/3} \mu_N^2 (fm)^{2l-2} \quad (2.13)$$

It can be shown that transitions with low values of  $l$  are typically favoured over higher multipole orders. Furthermore, comparing the electric and magnetic transition strengths of the same multipole order  $l$ , the electric transition strength is typically a factor  $10^2$  larger than the magnetic transition strength.

For a transition with mixed electric and magnetic multipole character the multipole mixing ratio  $\delta$  is defined as:

$$\delta(J_i \rightarrow J_f) \sim \frac{\langle J_f || B(E, l+1) || J_i \rangle}{\langle J_f || B(M, l) || J_i \rangle} \quad (2.14)$$

The extreme values of the multipole mixing ratio  $\delta$  are summarised in Table 2.3.

Table 2.3.: Limit values of the multipole mixing ratio  $\delta$  for electric and magnetic transitions up to multipole order 3, based on the electromagnetic selection rule.

$ J_i - J_f $	$\pi_i \pi_f$	multipole character	$ \delta  = 0$	$ \delta  = \infty$
0	+1	$E2/M1$	$M1$	$E2$
	-1	$M2/E1$	$E1$	$M2$
1	+1	$E2/M1$	$M1$	$E2$
	-1	$M2/E1$	$E1$	$M2$
2	+1	$M3/E2$	$E2$	$M3$
	-1	$E3/M2$	$M2$	$E3$

### 2.4.2. $\gamma\gamma$ angular correlation in in-beam experiments

For  $\gamma\gamma$  angular-correlation measurements the most important observable is the measured  $\gamma$ -ray intensity at a certain angle, which can be described via the Poynting vector:

$$I = |\vec{S}| = \varepsilon_0 c E^2 \propto |X_l^m(\theta, \phi)|^2 \quad (2.15)$$

## 2. $\gamma$ -ray spectroscopy of $^{33}\text{P}$ and $^{33}\text{S}$

Considering a transition based on the  $J_i = 1 \rightarrow J_f = 0$  cascade, the solutions for  $l = 1$  and  $m = 0, \pm 1$  are:

$$|X_1^0|^2 = \frac{3}{8\pi} \cdot \sin^2 \theta; \quad \text{and} \quad |X_1^{\pm 1}|^2 = \frac{3}{16\pi} \cdot (1 + \cos^2 \theta) \quad (2.16)$$

A schematic plot of the solutions in a polar diagram is shown in Fig. 2.7. The sum of

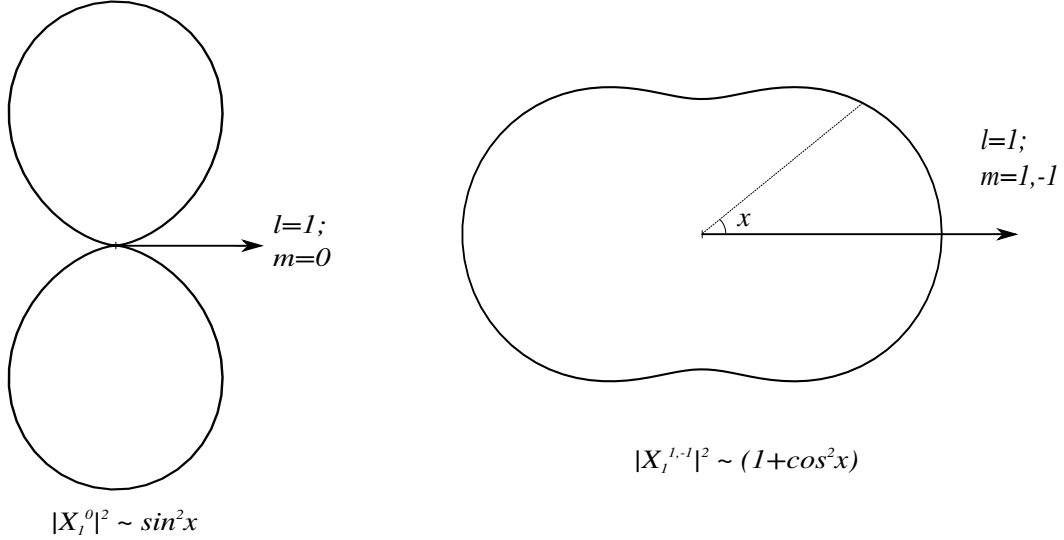


Figure 2.7.: Angular distribution of the vertical spherical function. Left:  $|X_1^0(\theta)|^2$ ; Right:  $|X_1^{\pm 1}(\theta)|^2$ .

the angular distribution of  $m = 0, \pm 1$  is proportional to a constant, yielding in this case a completely isotropic distribution of  $\gamma$  rays. Thus, if the  $m$ -substates of  $l$  are degenerate and equally populated in an ensemble of nuclei, the  $\gamma$  rays emitted by this ensemble will have an isotropic distribution in the laboratory frame. Hence, the intensity of the  $\gamma$ -rays is also isotropic over the angle  $\theta$ . Only if the occupation of the  $m$  substates is not equal, the emitted  $\gamma$  rays will have an anisotropic distribution and a measurement of the angular distribution can be performed. Employing  $\gamma\gamma$  coincidences the anisotropic distribution can be detected. When an excited nucleus decays by emitting multiple  $\gamma$  rays, an anisotropy is generally found in the spatial distribution of the second  $\gamma$  ray with respect to the first one. If the first  $\gamma$  ray is defined to be along the  $z$ -axis, the intermediate state should have an unequal population of its  $m$  substates. In this way the angular distribution of the second  $\gamma$  ray can be measured.

Recoil nuclei produced in in-beam experiments generally have a spatial orientation with respect to the momentum of the incoming particles. In the classical description the angular momentum is perpendicular to the beam axis. In the frame of quantum mechanics this means the substate  $m = 0$  is occupied. However, for statistical



## 2. $\gamma$ -ray spectroscopy of $^{33}\text{P}$ and $^{33}\text{S}$

reasons the orientation of angular momentum is not completely perpendicular to the beam-axis, rather belongs to a Gaussian distribution with a width  $\sigma$ , which has the value experimentally between 2 – 4, and must be taken into account in the determination of the angular distribution. Furthermore, the angular distribution is dependent on the level spins, the multipolarity of the two  $\gamma$ -ray transitions and, optionally, the multipole mixing ratio. The decay cascade is recorded by detector pairing, which is dependent on the angles  $\theta_1$ ,  $\theta_2$  and  $\phi$  (cf. Fig. 2.8 for definitions). Using the phase convention of KRANE, STEFFEN and WHEELER [72, 73] the angular

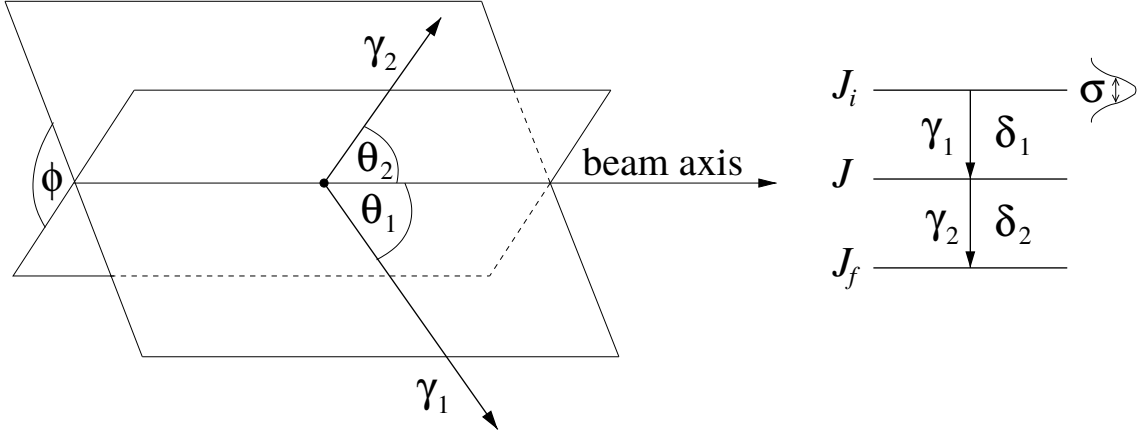


Figure 2.8.: Schematic illustration of angular correlation of two coincident  $\gamma$  rays. The  $\gamma$ -ray transitions are characterized by the level spins  $J$  and the multipole mixing ratio  $\delta$ . The width of the alignment distribution is tagged with  $\sigma$  (Modified from Ref. [72]).

distribution  $W(\theta_1, \theta_2, \phi)$  of two  $\gamma$  rays emitted in coincidence by the recoil nucleus can be written as:

$$W(\theta_1, \theta_2, \phi) = \sum_{k, k_1 k_2} B_{k_1}(J_i) A_k^{k_1 k_2}(\gamma_1) A_{k_2}(\gamma_2) H_{k k_1 k_2}(\theta_1, \theta_2, \phi) \quad (2.17)$$

The statistical tensor  $B_{k_1}(J_i)$  describes the initial orientation of the recoiling nucleus:

$$B_{k_1}(J_i) = \sqrt{2J_i + 1} \sum_m (-1)^{J_i + m} \cdot \langle J_i - m J_i m | k_1 0 \rangle Q(m), \quad (2.18)$$

where  $Q(m)$  is above mentioned Gaussian distribution of  $m = 0$  substate with the width  $\sigma$ :

$$Q(m) = \frac{1}{\sum_{m'=-J_i}^{J_i} e^{\frac{-m'^2}{2\sigma^2}}} \cdot e^{\frac{-m^2}{2\sigma^2}} \quad (2.19)$$

## 2. $\gamma$ -ray spectroscopy of $^{33}\text{P}$ and $^{33}\text{S}$

The coefficients  $A_k^{k_1 k_2}(\gamma_1)$  and  $A_{k_2}(\gamma_2)$  describe the general relations of the two coincident  $\gamma$  rays, and represent the reorientation via the emission of  $\gamma_1$ :

$$A_k^{k_1 k_2}(\gamma_1) = \frac{F_k^{k_1 k_2}(l_1 l_1 J_i J_f) + 2\delta_1 F_k^{k_1 k_2}(l_1 l'_1 J_i J_f) + \delta_1^2 F_k^{k_1 k_2}(l'_1 l'_1 J_i J_f)}{1 + \delta_1^2}, \quad (2.20)$$

$$A_{k_2}(\gamma_2) = \frac{F_{k_2}(l_2 l_2 J_i J_f) + 2\delta_2 F_{k_2}(l_2 l'_2 J_i J_f) + \delta_2^2 F_{k_2}(l'_2 l'_2 J_i J_f)}{1 + \delta_2^2} \quad (2.21)$$

where the generalized coefficients  $F_k$  are functions of the multiplicities of the  $\gamma$  ray, mixing ratios, as well as the level spins involved:

$$F_k = (-1)^{J_f - J_i - 1} \sqrt{(2l_1 + 1)(2l_2 + 1)(2J_i + 1)} \langle l_1 l_2 - 1 | k 0 \rangle S(J_i J_i l_1 l_2, k J_f) \quad (2.22)$$

where  $S(J_i J_i l_1 l_2, k J_f)$  is the Racah coefficients.

The last term of formula 2.17, the angular function  $H_{k k_1 k_2}(\theta_1, \theta_2, \phi)$  is defined as:

$$H_{k k_1 k_2}(\theta_1, \theta_2, \phi) = \sum_{q=0}^{k'} \frac{4\pi}{2k_2 + 1} \langle k_1 0 k q | k_2 q \rangle Y_{kq}(\theta_1, 0) Y_{k_2 q}^*(\theta_2, \phi) \quad (2.23)$$

The limit of the summation is  $k' = \min(k, k_2)$ . for  $k' = 0$ , one obtained the Legendre polynomial.

As was previously mentioned, the angular correlation coefficients are dependent on the spin assignments of the initial, intermediate and final states in the cascade, the multipolarity of the two  $\gamma$  rays, and the mixing ratio for mixed transitions. The values of these coefficients are one approach to determine the spins of nuclear states. Although there has so far no direct mention about parities, and the angular correlations do not strictly depend on the parity assignments of the levels, parities can often be deduced by combining the multiplicities of the transitions with the selection rules.

### 2.4.3. Determination of level spins in $^{33}\text{P}$

In present work regarding to the angles, all possible combinations of detector pairing of the HORUS array (cf. Fig. 2.1) were arranged in 17 angular-correlation groups, each one characterized by its values of  $\theta_1$ ,  $\theta_2$ , and  $\phi$  (see Table 2.4). Using the analysis-program CORLEONE [74], the angular distribution function  $W(\theta_1, \theta_2, \phi)$  of two coincident  $\gamma$ -ray transitions can be fitted to the measured  $\gamma$ -ray intensities in the  $\gamma\gamma$  matrix of the corresponding correlation group. A  $^{226}\text{Ra}$  source was used to perform the individual efficiency calibration of each HPGe-detector. To produce a

## 2. $\gamma$ -ray spectroscopy of $^{33}\text{P}$ and $^{33}\text{S}$

sensible analysis of angular correlation the same gate-window was applied to generate the coincidence spectrum for each correlation group.

Table 2.4.: All 17 possible  $\gamma\gamma$  angular-correlation groups by HORUS spectrometer, with 14 HPGe-detectors in use.

Group	$\theta_1$	$\theta_2$	$\Phi$	#	Detector combinations					
1	90	90	55	16	(0,1)	(0,2)	(0,4)	(0,5)	(1,0)	(1,3)
					(2,0)	(2,3)	(3,1)	(3,2)	(3,4)	(3,5)
					(4,0)	(4,3)	(5,0)	(5,3)		
2	90	90	180	6	(0,3)	(1,4)	(2,5)	(3,0)	(4,1)	(5,2)
3	90	135	270	8	(0,6)	(0,7)	(0,8)	(0,9)	(3,6)	(3,7)
					(3,8)	(3,9)				
4	90	145	0	8	(0,10)	(0,11)	(0,12)	(0,13)	(3,10)	(3,11)
					(3,12)	(3,13)				
5	90	90	70	8	(1,2)	(1,5)	(2,1)	(2,4)	(4,2)	(4,5)
					(5,1)	(5,4)				
6	90	135	215	16	(1,6)	(1,7)	(1,8)	(1,9)	(2,6)	(2,7)
					(2,8)	(2,9)	(4,6)	(4,7)	(4,8)	(4,9)
					(5,6)	(5,7)	(5,8)	(5,9)		
7	90	145	-55	16	(1,10)	(1,11)	(1,12)	(1,13)	(2,10)	(2,11)
					(2,12)	(2,13)	(4,10)	(4,11)	(4,12)	(4,13)
					(5,10)	(5,11)	(5,12)	(5,13)		
8	135	90	-270	8	(6,0)	(6,3)	(7,0)	(7,3)	(8,0)	(8,3)
					(9,0)	(9,3)				
9	135	90	-215	16	(6,1)	(6,2)	(6,4)	(6,5)	(7,1)	(7,2)
					(7,4)	(7,5)	(8,1)	(8,2)	(8,4)	(8,5)
					(9,1)	(9,2)	(9,4)	(9,5)		
10	135	45	0	8	(6,7)	(6,9)	(7,6)	(7,8)	(8,7)	(8,9)
					(9,6)	(9,8)				
11	135	45	-180	4	(6,8)	(7,9)	(8,6)	(9,7)		
12	135	145	-270	16	(6,10)	(6,11)	(6,12)	(6,13)	(7,10)	(7,11)
					(7,12)	(7,13)	(8,10)	(8,11)	(8,12)	(8,13)
					(9,10)	(9,11)	(9,12)	(9,13)		
13	145	90	0	8	(10,0)	(10,3)	(11,0)	(11,3)	(12,0)	(12,3)
					(13,0)	(13,3)				
14	145	90	55	16	(10,1)	(10,2)	(10,4)	(10,5)	(11,1)	(11,2)
					(11,4)	(11,5)	(12,1)	(12,2)	(12,4)	(12,5)
					(13,1)	(13,2)	(13,4)	(13,5)		
15	145	135	270	16	(10,6)	(10,7)	(10,8)	(10,9)	(11,6)	(11,7)
					(11,8)	(11,9)	(12,6)	(12,7)	(12,8)	(12,9)
					(13,6)	(13,7)	(13,8)	(13,9)		
16	145	145	180	8	(10,11)	(10,13)	(11,10)	(11,12)	(12,11)	(12,13)
					(13,10)	(13,12)				
17	145	35	180	4	(10,12)	(11,13)	(12,10)	(13,11)		

## 2. $\gamma$ -ray spectroscopy of $^{33}\text{P}$ and $^{33}\text{S}$

To proof the accuracy of the angular correlation using CORLEONE, experimental data of  $4226 \text{ keV} \rightarrow 1848 \text{ keV} \rightarrow g.s.$  cascade with known spins and parities in  $^{33}\text{P}$  were compared to calculations of this program. In Fig. 2.9 the dashed line shows the fitting result for pure  $E1$  (2378 keV) and  $E2$  (1848 keV) transitions with mixing ratios  $\delta_1 = \delta_2 = 0$ ; the solid line shows the best fit with varied mixing ratios. The from CORLEONE obtained mixing ratios  $\delta_1 = -0.02(3)$  and  $\delta_2 = 0.05(9)$  reproduced the NNDC-values ( $\delta_1 = 0.01(6)$ ,  $\delta_2 = -0.03(3)$ ) successfully. Using this method spins and parities of the yrast band built on the  $1/2^+$  ground state were confirmed up to the  $11/2^-$  state (cf. Fig. 2.10(a) and (b)).

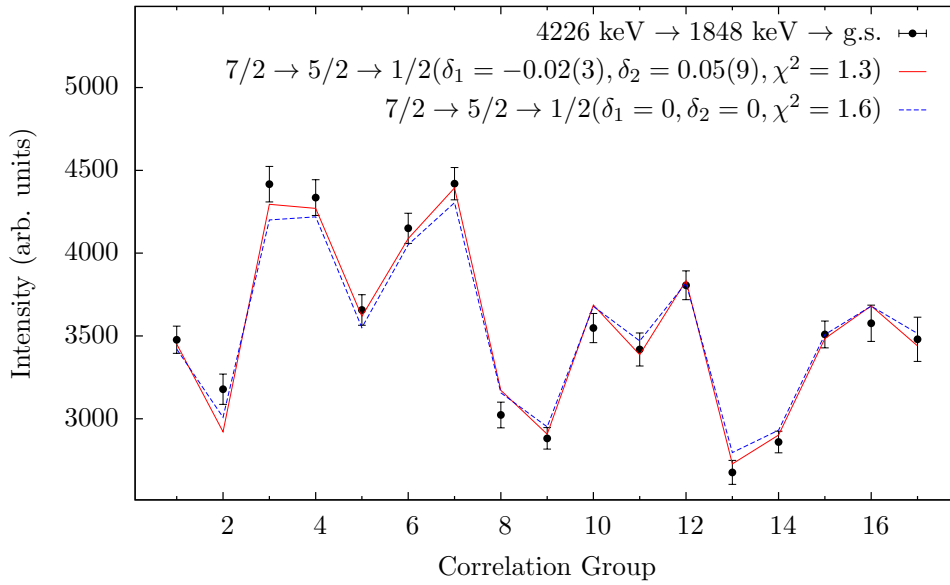


Figure 2.9.:  $\gamma\gamma$  angular correlation for  $7/2^- \rightarrow 5/2^+ \rightarrow 1/2^+$  cascade in  $^{33}\text{P}$ . Solid line shows the best fit of experimental data with varied mixing ratios  $\delta_1$  and  $\delta_2$ ; Dashed line shows the fit with fixed mixing ratios  $\delta_1 = \delta_2 = 0$ .

For high-lying levels Chakrabati *et al.* showed that the 1028- and 1298-keV transitions are of dipole and quadrupole nature, respectively, employing a DCO-Ratio measurement [51]. However, in that previous work the spin and parity assignments of the corresponding energy states were given only tentatively: ( $15/2^-$ ) for the 6936-keV energy level (de-excited via a 1298-keV  $\gamma$ -ray transition) and ( $17/2^+$ ) for the 7966-keV energy level (de-excited via a 1028-keV  $\gamma$ -ray transition). Figures 2.11(a) and 2.11(b) indicate the experimentally derived intensity distribution for the coincident  $\gamma$ -ray transitions at 1298 and 1412 keV, measured in the present work, compared to calculated values for different scenarios of the spin and parity of the 6936-keV level. As shown in Fig. 2.11(a), obviously a pure  $E2$  transition with 1298 keV does not fit the experimental data, which excludes both the possibility of

## 2. $\gamma$ -ray spectroscopy of $^{33}\text{P}$ and $^{33}\text{S}$

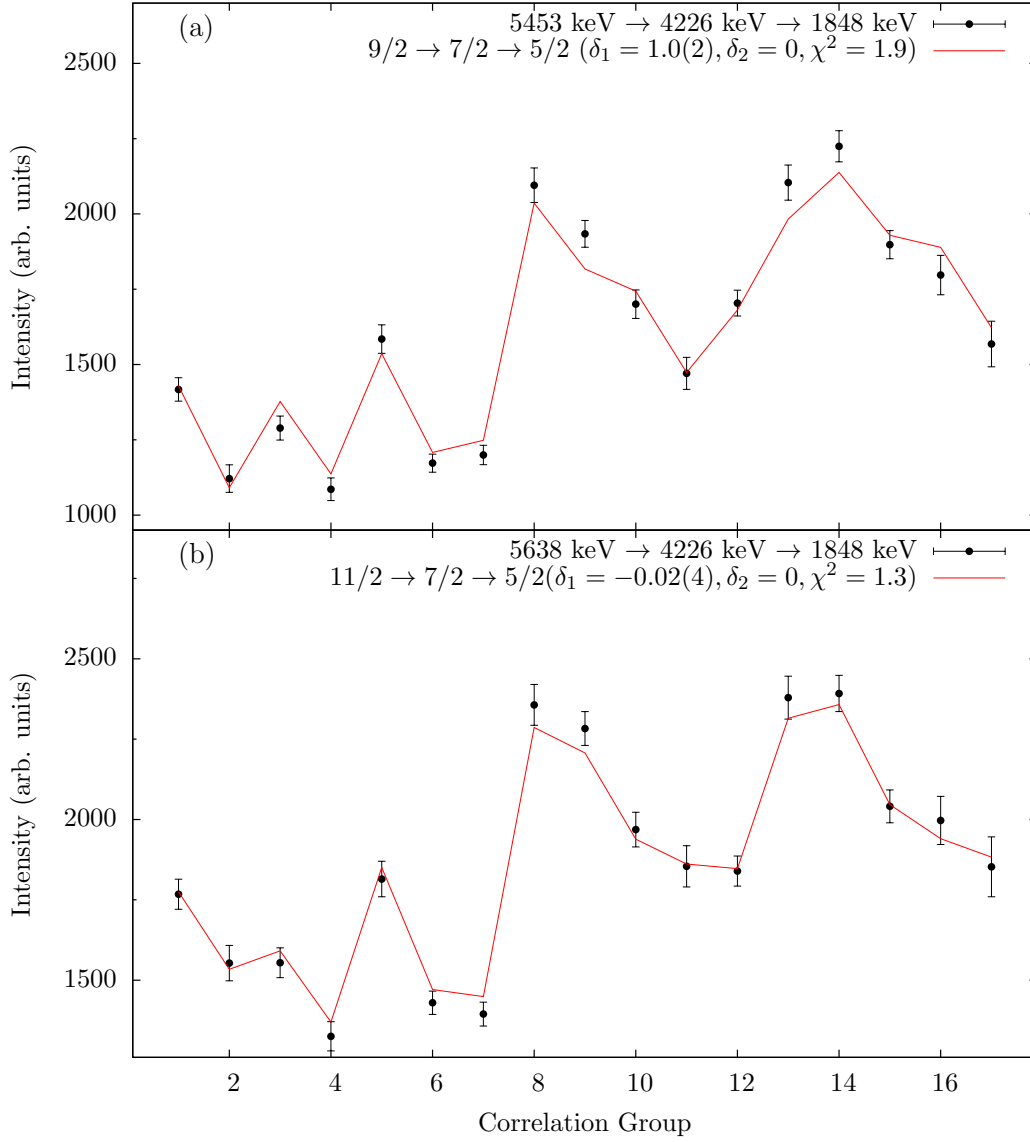


Figure 2.10.:  $\gamma\gamma$  angular correlations for coincident  $\gamma$  rays in  $^{33}\text{P}$ . Panel (a) shows the result for  $9/2^- \rightarrow 7/2^- \rightarrow 5/2^+$  cascade; Panel (b) shows the result for  $11/2^- \rightarrow 7/2^- \rightarrow 5/2^+$  cascade. In both cases the known mixing ratios were reproduced.

the a  $7/2^-$  and a  $15/2^-$  for the state at 6936 keV. Based on the present experimental data, whether the 1298-keV transition is parity changing or not, cannot be determined. As shown in Fig. 2.11(b), the angular correlation including multipole mixing fits the experimental data well, supporting  $9/2$  or  $13/2$  spin for the 6936-keV state. The hypothesis of a  $9/2$  spin state provides the best fit results with a dominating quadrupole contribution ( $\delta = 9.9(42)$ ) for the  $9/2 \rightarrow 11/2^-$  transition, while a  $13/2$  spin state yields a mixing ratio of  $\delta = -18(10)$ .

## 2. $\gamma$ -ray spectroscopy of $^{33}\text{P}$ and $^{33}\text{S}$

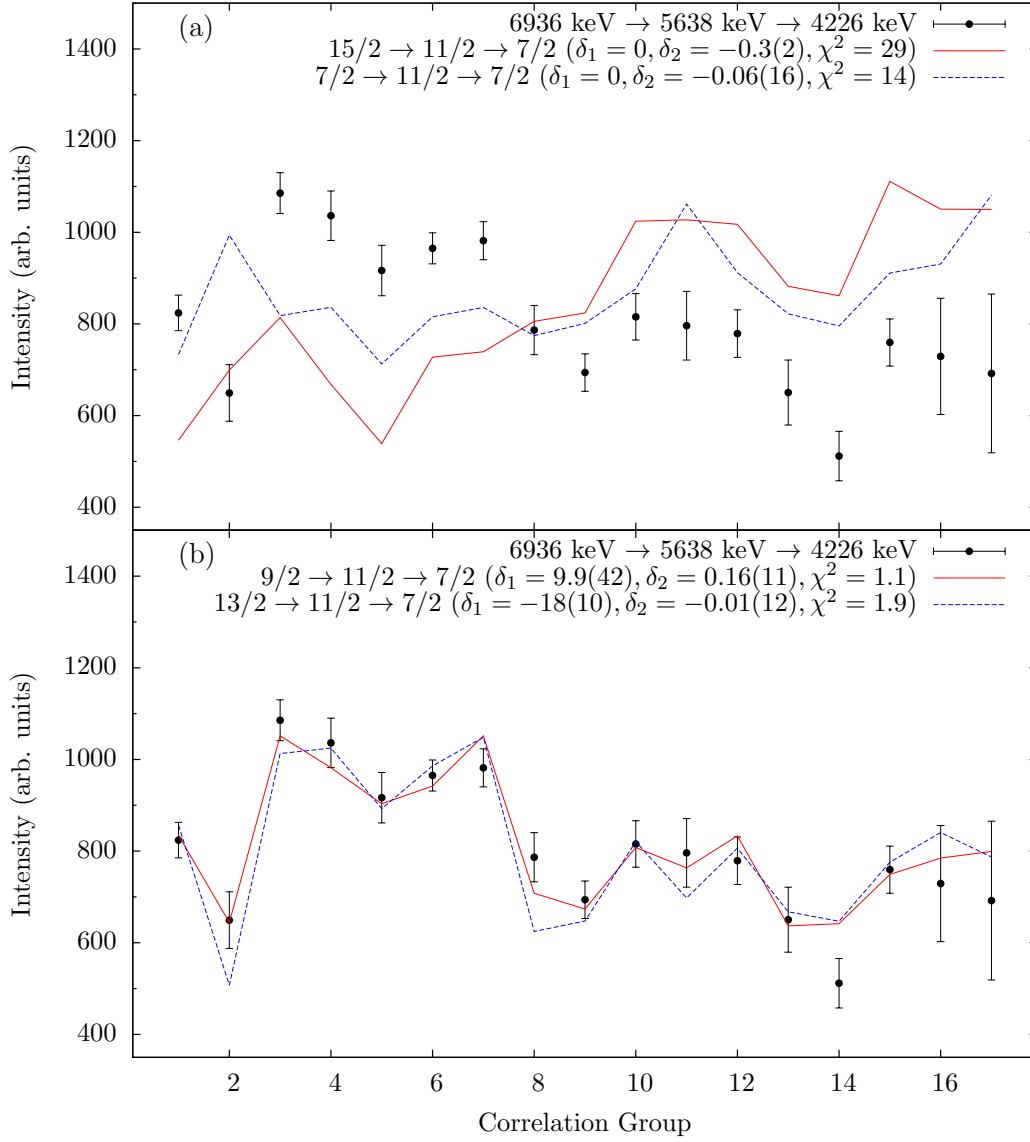


Figure 2.11.:  $\gamma\gamma$  angular correlations for 6936-keV energy level in  $^{33}\text{P}$ . Panel (a) shows the results of a pure  $E2$  transition from 6936-keV state with  $15/2 \rightarrow 11/2^- \rightarrow 7/2^-$  cascade (solid line), and  $7/2 \rightarrow 11/2^- \rightarrow 7/2^-$  cascade (dashed line). These calculations cannot reproduce the experimental data. Panel (b) shows the results of  $9/2$  (solid line) and  $13/2$  (dashed line) spin-assignments for 6936-keV state, where multipole mixing for the 1298-keV transition is included, with a dominating quadrupole term.

Obviously, there is no reason to exclude one of the both spin assignments of the 6936-keV state, therefore we need to keep the  $9/2$  and  $13/2$  as possible spin states to continue  $\gamma\gamma$  angular correlations for higher energy levels. Regarding the results for 6936-keV state, in  $\gamma\gamma$  angular correlations for 9078-keV state the mixing ratios need to be set free, and the calculated  $\delta_2$  should match the known values from

## 2. $\gamma$ -ray spectroscopy of $^{33}\text{P}$ and $^{33}\text{S}$

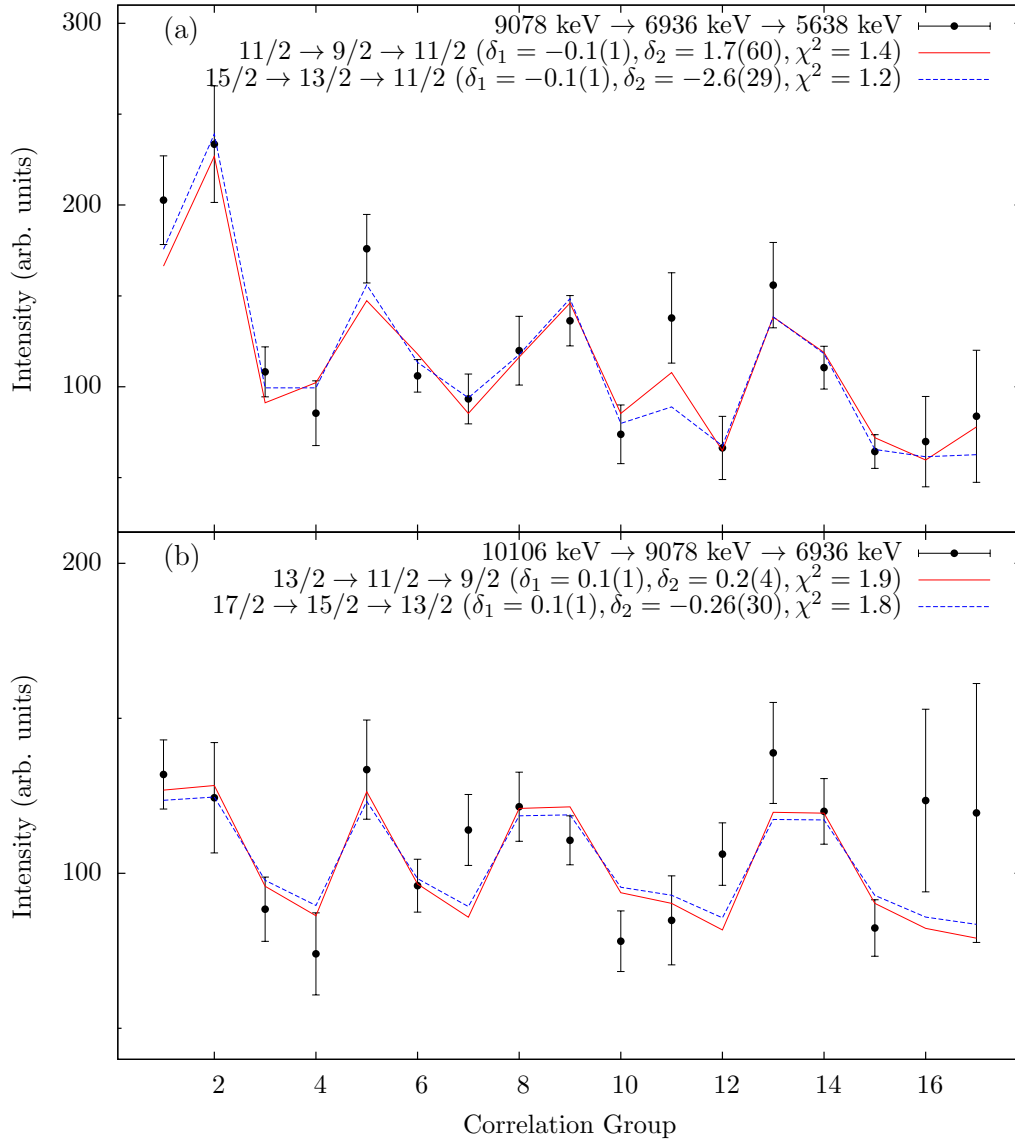


Figure 2.12.:  $\gamma\gamma$  angular correlations for high-lying states at 9078 keV and 10106 keV. Panel (a) shows results of  $11/2^- \rightarrow 9/2^- \rightarrow 11/2^-$  cascade (solid line) and  $15/2^- \rightarrow 13/2^- \rightarrow 11/2^-$  cascade (dashed line) for 9078-keV state. Calculations for the 10106-keV state are shown in panel (b), with results for spin assignments of  $13/2^-$  (solid line) and  $17/2^-$  (dashed line).

previous analysis. The calculations for the higher-lying state at 9078 keV are shown in Fig. 2.12(a). The solid line shows the result for a  $11/2^- \rightarrow 9/2^- \rightarrow 11/2^-$  cascade, with calculated mixing ratio for 1298-keV  $\delta_2 = 1.7(60)$ , which matches the previous result  $\delta = 9.9(42)$ . In this way the result for a  $15/2^- \rightarrow 13/2^- \rightarrow 11/2^-$  cascade was calculated (dashed line), with mixing ratio  $\delta_2 = -2.6(29)$ , which matches the previous value  $\delta = -18(10)$ . The calculated multipole mixing  $\delta_1 = -0.1(1)$  for

## 2. $\gamma$ -ray spectroscopy of $^{33}\text{P}$ and $^{33}\text{S}$

both cases denotes that the 2142-keV transition has a dipole character. Using the same method, the spins of the newly established excited state at 10106 keV were also determined [cf. Fig. 2.12(b)]. For both calculations with  $J = 11/2$  and  $15/2$  for the 9078-keV state, the obtained multipole mixing  $\delta_1 = 0.1(1)$  for the 1028-keV transition reproduced the result from Chakrabarti *et al.* [51], that this transition has a dipole nature. Finally, the with a spin assignment of  $J = 9/2$  for the 6936-keV state, the spins of the 9078- and 10106-keV states are limited to  $(7/2, 11/2)$  and  $(5/2, 9/2, 13/2)$ , respectively. With  $J = 13/2$  for the 6936-keV state, the spins of the 9078- and 10106-keV states are limited to  $(11/2, 15/2)$  and  $(9/2, 13/2, 17/2)$ , respectively. Therefore, the merged possibilities for the spin assignments of the high-lying states at 9078 keV and 10106 keV based on the present analysis are  $J = (7/2, 11/2, 15/2)$  and  $J = (5/2, 9/2, 13/2, 17/2)$ , respectively.

For the weakly populated excited states at 6518, 6807 and 6988 keV, due to limited statistics there is no possibility to perform an accurate analysis of the  $\gamma\gamma$  angular correlations. However, the spin of the 6988-keV state could be limited to  $(7/2, 9/2, 11/2)$ , due to the three observed de-exciting  $\gamma$ -ray transitions populating the well known  $7/2^-$ ,  $9/2^-$  and  $11/2^-$  states. Applying the same argument to the 6807-keV state, which is depopulated to the  $7/2^-$  and  $11/2^-$  states, the spins could be restricted to  $(7/2, 9/2, 11/2)$ . Therefore, the 6807-keV state is excluded to be the  $5/2^+$  state, reported by Khan *et al.* at an energy of 6820(60) keV, for which an  $E3$  transition to the known  $11/2^-$  state should be in competition with an  $E1$  transition to the  $7/2^-$  state.

There is an energy level at 6940(150) keV with spin  $J = (5/2, 7/2)$ , reported by Davis and Nelson [52], cannot be located clearly to a energy level observed in the present work. On the other hand, Davis and Nelson [52] have reported an excited state at 10120(150) keV, with a spin hypothesis of  $(1/2 \text{ to } 13/2)$ , which is identical with the newly established state at 10106 keV with spin  $J = (5/2, 9/2, 13/2, 17/2)$ .



## 3. Shell-Model Calculations

Using the PSDPF [37] interaction, the newly established level schemes of  $^{33}\text{P}$  and  $^{33}\text{S}$  are compared to  $p$ - $sd$ - $pf$  shell-model calculations. To describe the  $0\hbar\omega$  and  $1\hbar\omega$  states in the full  $p$ - $sd$ - $pf$  model space based on a  $^4\text{He}$  core, the PSDPF interaction was constructed starting from primary interactions. For the nuclei nearby the upper  $sd$ -shell closure, USDB interaction [22] was taken for  $sd$  major-shell and SDPF-NR interaction [30, 32] was taken for  $pf$ -shell and  $sd$ - $pf$  cross-shell terms. Furthermore, the matrix elements were adjusted to reproduce experimentally determined excitation energies.

### 3.1. Calculations for $^{33}\text{P}$

#### 3.1.1. Level Scheme of $^{33}\text{P}$

As a reference  $sd$ - $pf$  shell-model calculations using the SDPF-NR interaction were performed for  $^{33}\text{P}$  [75]. Allowing the neutron-excitation up to  $3\hbar\omega$ , SDPF-NR reproduces the low-lying positive-parity states. However, SDPF-NR can not reproduce the negative-parity states. The using SDPF-NR calculated first negative-parity state  $7/2^-$  is at energy of 6.7 MeV, with a difference to experimental value around 2.4 MeV, while the difference by PSDPF is around 200 keV. Even using the SDPFMW interaction [26], the calculations with  $1\hbar\omega$  excitation also failed to generate the first  $7/2^-$  state. As reported by Chakrabarti *et al.* [51], the calculated energy is higher than the experimental value by several MeV.

In table 3.1 experimentally determined states up to around 7 MeV with known spins and parities [13] are compared to the  $p$ - $sd$ - $pf$  shell-model calculations. Additionally, a detailed comparison between experimental and shell-model states is shown in Fig. 3.1, where all possible experimental spin values from the present data analysis are listed. The Energy differences between the experimental and calculated levels are small, and generally vary up to around 300 keV. By the PSDPF calculation the  $0\hbar\omega$  positive-parity states are reproduced with correct spin order and very small energy differences (cf. Table 3.1). For  $Z = 15$  isotopes of phosphorus, the energy gap of 1.43 MeV between the  $1/2^+$  ground state and the first excited  $3/2^+$

### 3. Shell-Model Calculations

Table 3.1.: Comparison between experimentally known states and calculated states up to 7.1 MeV in  $^{33}\text{P}$ .

Experiment		PSDPF		$E_{exp.} - E_{theo.}$
$E_x$ [keV]	$J^\pi$	$E_x$ [keV]	$J^\pi$	$\Delta E$ [keV]
$^{33}\text{P}$				
0	$1/2_{g.s.}^+$	0	$1/2_{g.s.}^+$	-
1432	$3/2^+$	1441	$3/2_1^+$	-9
1848	$5/2^+$	1905	$5/2_1^+$	-57
2538	$3/2^+$	2679	$3/2_2^+$	-141
3275	$3/2^+$	3433	$3/2_3^+$	-158
3490	$5/2^+$	3508	$5/2_2^+$	-18
3628	$7/2^+$	3778	$7/2_1^+$	-150
4048	$5/2^+$	3971	$5/2_3^+$	77
4226	$7/2^-$	4470	$7/2_1^-$	-244
5049	$5/2^+$	5012	$5/2_4^+$	37
5453	$9/2^-$	5696	$9/2_1^-$	-244
5638	$11/2^-$	5812	$11/2_1^-$	-180
5674	$1/2^+$	5830	$1/2_3^+$	-156
6432	$5/2^+$	6535	$5/2_5^+$	-100
6820	$5/2^+$	6721	$5/2_6^+$	99
		6858	$5/2_7^+$	-38
6936	$(9/2, 13/2)$	6720	$9/2_3^-$	216
		7109	$9/2_3^+$	-173
		7222	$13/2_1^-$	-286
7146	$5/2^+$	7172	$5/2_8^+$	-26

state of  $^{33}\text{P}$  ( $N = 18$ ) is larger than for the  $N = 16$  isotope  $^{31}\text{P}$  (1.27 MeV), but significantly smaller than for  $N = 20$  isotope  $^{35}\text{P}$  (2.39 MeV). The shell gaps between the  $1/2_{g.s.}^+$  and  $3/2_1^+$  states are nicely reproduced by the PSDPF interactions, therefore fitting the systematics towards the completely occupied neutron shell [45].

The intruder negative-parity states are described very good by the  $1\hbar\omega$  shell-model calculations, not only in  $^{33}\text{P}$ , but also for the  $N = 18$  isotones  $^{35}\text{Cl}$  and  $^{37}\text{K}$  [46]. Furthermore, in  $^{33}\text{P}$  the PSDPF calculation reproduces the high-spin states very nicely. Based on the good description of experimental states by the  $p$ - $sd$ - $pf$  shell-model calculations, shell-model arguments can also be employed to address the possible spin-parity assignments of specific states. The level at 6936 keV was previously assigned to be  $J^\pi = (15/2^-)$  [51], while in the present work the spin assignment of this state was changed by  $\gamma\gamma$  angular correlation to  $(9/2, 13/2)$ . An important argument supporting the  $13/2$  spin-state more against the  $9/2$  spin-state is that the fusion-evaporation reactions used in the present work populate most probably highly

### 3. Shell-Model Calculations

excited states of intermediate or high spins. Furthermore, the PSDPF calculation predicts a nearby  $13/2_1^-$  state at 7222 keV, while the calculated  $15/2_1^-$  state lies much higher (at 9094 keV), which also support the present experimental results.

For the state at 9078 keV, the experimental spin assignment was limited by  $\gamma\gamma$  angular-correlation analysis to  $(7/2, 11/2, 15/2)$ . Using the same argument that fusion-evaporation reactions populate most likely intermediate and high spins, corresponding states with  $J = 11/2$  and  $15/2$  are expected to be found in the results of PSDPF calculations. The calculated states of  $J^\pi = (11/2_2^+, 15/2_{1,2}^-)$  are at energies of (9442, 9094, 9488 keV), one of them could correspond to the experimentally observed state (cf. Fig. 3.1).

For the high-lying state at 10106 keV, the PSDPF calculates nearby states  $J^\pi = (13/2_2^+, 17/2_1^-)$  at energies (10554, 11239 keV). Combining the  $\gamma\gamma$  angular-correlation analysis, the fusion-evaporation mechanism, and the report of Davis and Nelson [52] about an excited state at 10120(150) keV with a spin assignment of  $(1/2 \text{ to } 13/2)$ , this may limit the spin of the 10106-keV state to only  $13/2$ .

The 6518-keV state was populated very weakly in the present experiment, therefore the angular-correlation analysis of the de-exciting  $\gamma$ -ray transitions was not possible. On the other hand, considering the populating and depopulating transitions of this state, the range of spins could be expected approximately from  $7/2$  to  $15/2$ . The PSDPF calculations suggest several theoretical analog states in this energy range with spins  $7/2^+$ ,  $9/2^\pm$ , and  $11/2^-$  (see Fig. 3.1). The newly observed states at 6807 and 6988 keV were also weakly populated in the present experiment. However, due to their de-excitation model their spins could be confined to  $(7/2, 9/2, 11/2)$ . As shown in Fig. 3.1, the shell-model calculations predict several close-lying states of positive and negative parity with respective spin values.

### 3. Shell-Model Calculations

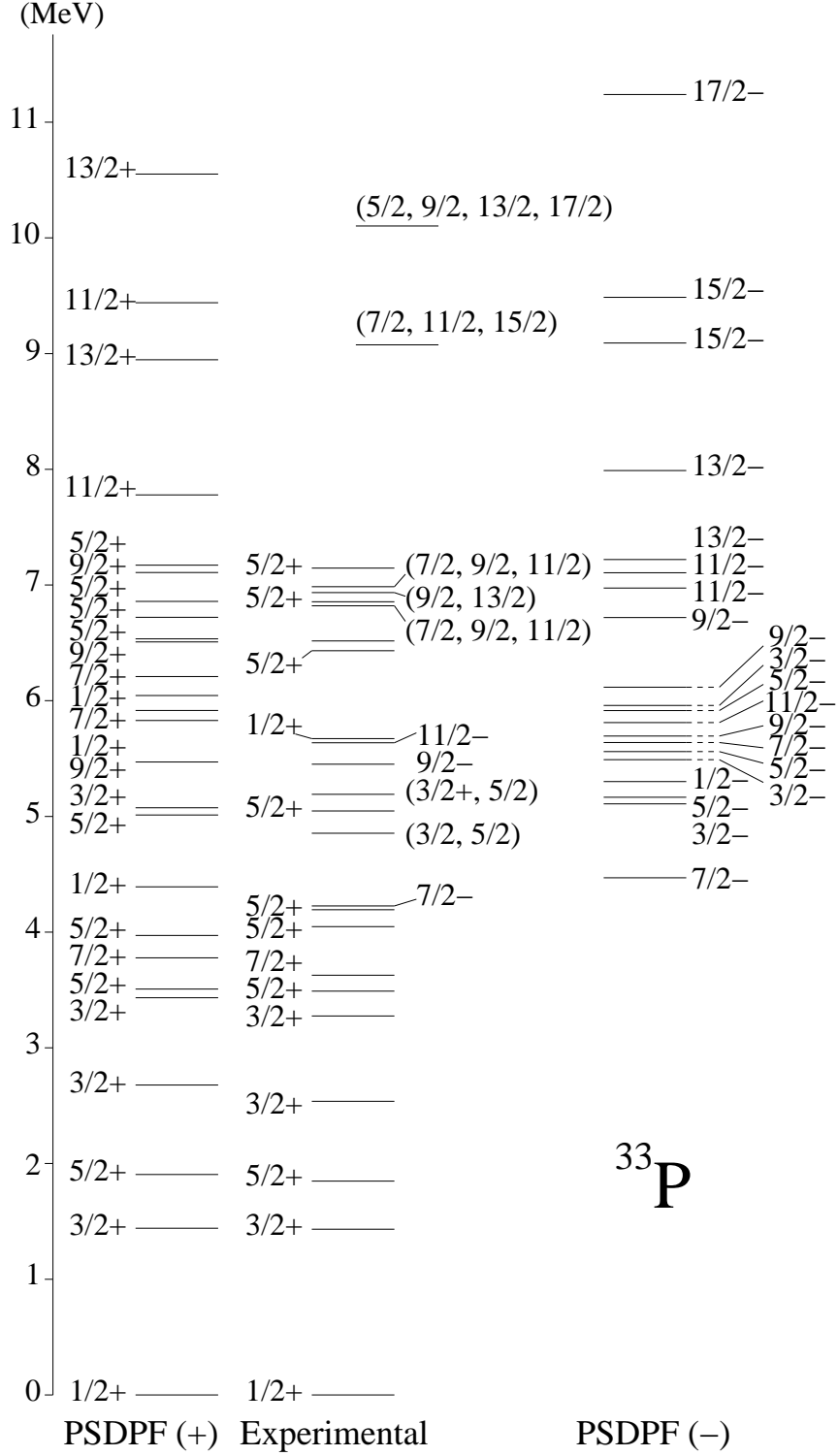


Figure 3.1.: Detailed comparison between experimental and calculated levels in  $^{33}\text{P}$ .

#### 3.1.2. Transition Strength

The transition strength is another sensitive candidate to test the validity of shell model calculations. Utilizing Doppler shift attenuation method (DSAM) the lifetimes of low-lying excited states (up to  $E_x \sim 4.2$  MeV) in  $^{33}\text{P}$  were measured by Currie *et al.* [53] and Carr *et al.* [54], using the  $^{30}\text{Si}(\alpha, p\gamma)^{33}\text{P}$  reaction, as well as Poletti *et al.* [55] and Wagner *et al.* [56], using the  $^{31}\text{P}(t, p\gamma)$  reaction, respectively. Using Recoil Distance Method (RDM) Nixon *et al.* [76] measured the lifetimes of 5453-keV ( $35 \pm 7$  ps) and the 5638-keV ( $14 \pm 2$  ps) states, by means of the reaction  $^{30}\text{Si}(\alpha, p\gamma)^{33}\text{P}$ . Comparing to the experimental results, shell-model calculations for reduced transition strengths ( $B(M1)$  and  $B(E2)$ ) in  $^{33}\text{P}$  were carried out. The USD, USDA, SDPF-NR [75] and PSDPF [77] calculations are undertaken to obtain the theoretical results. The for *sd*-shell nuclei optimized parameters (effective  $g$  factors and effective charges) from the reference [78] are considered. USD and USDA interactions are used for pure *sd* model space, and transitions from excited states up to 6.6 MeV are calculated, while for *sd-pf* model space PSDPF interaction with allowed excitation up to  $1\hbar\omega$ , and SDPF-NR interaction with allowed excitation up to  $3\hbar\omega$  are used also for negative-parity states. The calculated results and the comparison to experimental results in detailed are shown in Table 3.2.

**B( $M1$ )** - The experimental  $B(M1)$  values of transitions  $3/2_1^+ \rightarrow 1/2_{g.s.}^+$ ,  $5/2_3^+ \rightarrow 3/2_3^+$  and  $5/2_3^+ \rightarrow 3/2_1^+$  cannot be reproduced by shell-model calculations. For  $3/2_1^+ \rightarrow 1/2_1^+$ , the theoretical values are at least with factor two smaller than the experimental value. For other two transitions the theoretical values are too large. The experimental  $B(M1)$  values of other transitions between positive states are reproduced at least by USDA interaction, considering the large error of experiments. Generally the calculated results of USDA interaction has the better agreement than other three interactions. For transitions between negative parity states, the experimental  $B(M1)$  value of  $11/2_1^- \rightarrow 9/2_1^-$  is well reproduced by both PSDPF and SDPF-NR calculations. However, for  $9/2_1^- \rightarrow 7/2_1^-$  transition the theoretical  $B(M1)$  of PSDPF are with factor ten larger than experimental result, while  $B(M1)$  of SDPF-NR is even larger than PSDPF.

**B( $E2$ )** - For  $3/2_1^+ \rightarrow 1/2_{g.s.}^+$ ,  $5/2_1^+ \rightarrow 1/2_{g.s.}^+$  and  $7/2_1^+ \rightarrow 3/2_1^+$  transitions the theoretical values of  $B(E2)$  from all four calculations are consistent, and reproduce the experimental  $B(E2)$  in good agreement. For  $3/2_2^+ \rightarrow 1/2_{g.s.}^+$  and  $5/2_3^+ \rightarrow 3/2_1^+$  transitions, the experimental  $B(E2)$  values with relative big error (more than 50%) can still be reproduced by theoretical  $B(E2)$ , although there are discrepancy be-

### 3. *Shell-Model Calculations*

tween them, where the PSDPF values are with factor two larger than USDA values. For  $3/2_3^+ \rightarrow 1/2_{g.s.}^+$  and  $5/2_2^+ \rightarrow 1/2_{g.s.}^+$  transitions the experimental  $B(E2)$  cannot be reproduced, where the calculated values are either too large (for  $5/2_2^+ \rightarrow 1/2_{g.s.}^+$ ), or too small (for  $3/2_3^+ \rightarrow 1/2_{g.s.}^+$ ). For transitions between negative-parity states the theoretical  $B(E2)$  values from PSDPF and SDPF-NR interactions have significant discrepancies. For  $9/2_1^- \rightarrow 7/2_1^-$  transition the  $B(E2)$  from SDPF-NR reproduces the experimental value, while the PSDPF value is too large. For  $11/2_1^- \rightarrow 7/2_1^-$  transition the experimental  $B(E2)$  can be reproduced by PSDPF with good agreement, while the SDPF-NR value is too large.

## 3.2. Calculations for $^{33}\text{S}$

### 3.2.1. Level Scheme of $^{33}\text{S}$

The stable nucleus  $^{33}\text{S}$  has been studied intensively and many informations of their level energies, spins and parities are well known [13]. However, most of the high-lying states with energy up to 12 MeV have been investigated in light-particle transfer reactions, which mainly populate low-spin states [13]. Consequently, the in present experiment newly determined high-lying states populating in the fusion-evaporation reaction, do not necessarily correspond to the above-mentioned known low-spin states, although they have sometimes similar energies. Comparing the newly determined states to the PSDPF calculations in the following, possible spin and parity assignments have been suggested.

In a recent work Bisoi *et al.* [63] have compared experimental and calculated energy levels for  $^{33}\text{S}$ , using the SDPFMW interaction [26]. As shown in table 3.3 and Fig. 3.2, the using PSDPF calculated results, show good agreement with the experimental values, and reproduce the level energies generally better than SDPFMW [63]. In contrast to the SDPFMW interaction, the PSDPF interaction reproduces the correct spin order of the first  $9/2^-$  and  $11/2^-$  states. The high-spin states  $11/2^+$  at 7180 keV and  $15/2^-$  at 7820 keV reported by Bisoi *et al.* [63], are also reproduced by the PSDPF calculation very nicely (cf. Table 3.3 and Fig. 3.2). For the spin and parity assignments of the newly determined states, the PSDPF calculation suggests also possible candidates. The experimental state of 5480 keV has two corresponding states: the calculated  $9/2_2^-$  state at 5208 keV or the  $9/2_2^+$  state at 5778 keV. The PSDPF  $9/2_2^+$  (5778 keV) state or the  $11/2_2^-$  state at 6375 keV, could be the candidate for the weakly populated experimental 5793-keV state. Since the experimental state at 7000 keV is de-excited by transitions populating  $9/2^-$  and  $11/2^-$  states, the possible shell-model analog state could be the PSDPF  $11/2_1^+$  state at 6634 keV, or the  $13/2_1^-$  state at 6748 keV. For the newly observed high-lying states at 8641 and 9814 keV, the PSDPF calculation suggests possible spins and parities of  $(13/2_1^+, 15/2_2^-)$  and  $(13/2_2^+, 17/2_1^-)$ , respectively (see Fig. 3.2).

### 3. Shell-Model Calculations

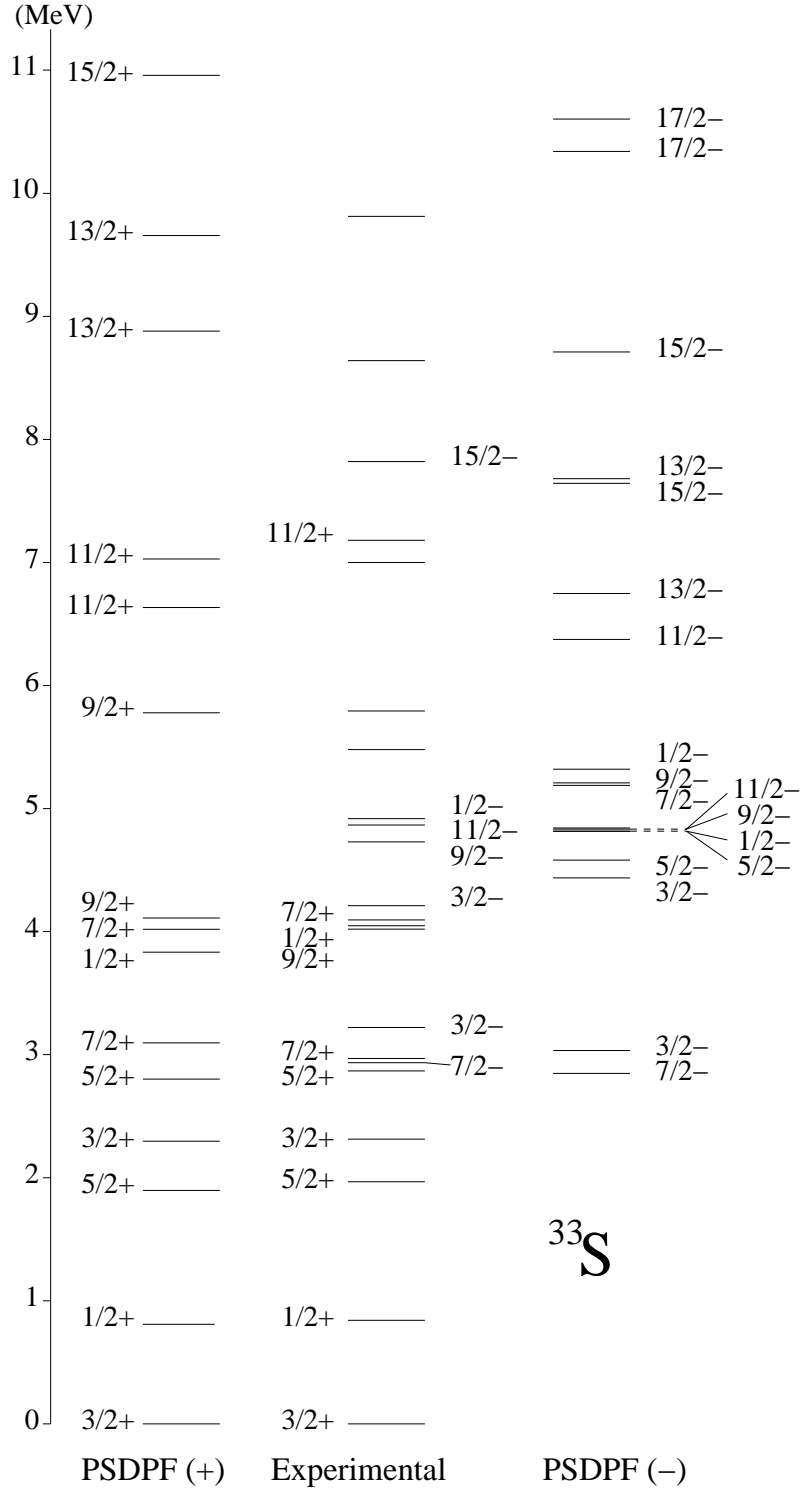


Figure 3.2.: Detailed comparison between experimental and calculated levels in  $^{33}\text{S}$ .



### 3.2.2. Transition Strength

Utilizing DSAM the lifetimes of excited states with energy up to 5.3 MeV in  $^{33}\text{S}$  were measured by Cummings *et al.* [79] and Carr *et al.* [54], using  $^{32}\text{S}(d, p\gamma)^{33}\text{S}$  and  $^{30}\text{Si}(\alpha, n\gamma)^{33}\text{S}$  reactions, respectively. Comparing to the experimental results the PSDPF interaction is taken to calculate reduced transition strength  $B(M1)$  and  $B(E2)$  in  $^{33}\text{S}$ , with parameters from reference [78]. As shown in Table 3.4, experimental and theoretical  $B(M1)$  and  $B(E2)$  values of transitions from excited states up to  $J^\pi = 11/2_1^-$  have been compared.

**B( $M1$ )** - The experimental  $B(M1)$  of  $7/2_1^+ \rightarrow 5/2_1^+$  and  $9/2_1^- \rightarrow 7/2_1^-$  transitions can be reproduced by PSDPF calculations with good agreement, considering the experimental errors. For  $5/2_2^+ \rightarrow 3/2_{g.s.}^+$  and  $7/2_2^+ \rightarrow 5/2_1^+$  transitions the theoretical  $B(M1)$  are with factor two larger than experimental values. For  $1/2_1^+ \rightarrow 3/2_{g.s.}^+$ ,  $5/2_1^+ \rightarrow 3/2_{g.s.}^+$  and  $5/2_3^+ \rightarrow 3/2_{g.s.}^+$  transitions the theoretical  $B(M1)$  are smaller than experimental values with factor two to three. For  $3/2_2^+ \rightarrow 3/2_{g.s.}^+$  and  $9/2_1^+ \rightarrow 7/2_1^-$  transitions the PSDPF values are around an order of magnitude smaller than experimental values.

**B( $E2$ )** - For transitions  $5/2_1^+ \rightarrow 3/2_{g.s.}^+$ ,  $5/2_2^+ \rightarrow 1/2_1^+$ ,  $7/2_1^+ \rightarrow 3/2_{g.s.}^+$ ,  $5/2_3^+ \rightarrow 3/2_{g.s.}^+$ ,  $9/2_1^+ \rightarrow 5/2_1^+$  and  $9/2_1^- \rightarrow 7/2_1^-$  the experimental  $B(E2)$  values can be reproduced by PSDPF calculations with good agreement. For  $1/2_1^+ \rightarrow 3/2_{g.s.}^+$ ,  $5/2_2^+ \rightarrow 3/2_{g.s.}^+$ ,  $7/2_2^+ \rightarrow 5/2_1^+$ ,  $9/2_1^+ \rightarrow 7/2_1^+$  and  $11/2_1^- \rightarrow 7/2_1^-$  transitions the theoretical  $B(E2)$  values are not far away from the experimental results, considering the relative big error of experiment. There are still three transitions, whose experimental  $B(E2)$  values cannot be reproduced by PSDPF: for  $5/2_1^+ \rightarrow 1/2_1^+$  the PSDPF value is an order of magnitude smaller than experimental result, while for  $3/2_2^+ \rightarrow 3/2_{g.s.}^+$  the PSDPF value is an order of magnitude larger than experimental value; for  $7/2_2^+ \rightarrow 3/2_{g.s.}^+$  the PSDPF value is larger than experimental result with factor about five.

## 3.3. Summary

In the present work fusion-evaporation reactions were used to study excited states in upper *sd*-shell nuclei  $^{33}\text{P}$  and  $^{33}\text{S}$ . Employing the  $\gamma\gamma$ -coincidence and  $\gamma\gamma$  angular-correlation analysis the level schemes of  $^{33}\text{P}$  and  $^{33}\text{S}$  were extended to excitation energy around 10 MeV. Tentative spin-parity assignments for several states were adjusted. Completely 15 new  $\gamma$ -ray transitions were observed and 4 new excited states were determined in  $^{33}\text{P}$ . In  $^{33}\text{S}$  13 new  $\gamma$ -ray transitions were observed and 5 new energy levels were determined.

The experimental determined level schemes of  $^{33}\text{P}$  and  $^{33}\text{S}$  were compared to large-scale shell-model calculations using the PSDPF interaction. In both investigations of  $^{33}\text{P}$  and  $^{33}\text{S}$ , the PSDPF calculations reproduce the known positive- and negative-parity states very well. The agreement of PSDPF is clearly better than previous calculations. It underlines the necessity to take the full *p-sd-pf* model space into account to describe  $0\hbar\omega$  positive-parity states, as well as  $1\hbar\omega$  negative-parity intruder states. The satisfying quality of the PSDPF calculation provided useful indications to discuss the experimental results and suggested possible spin-parity assignments of newly determined states.

Based on the known lifetimes of excited states in  $^{33}\text{P}$  and  $^{33}\text{S}$  from NNDC [13], comparison between experimental and theoretical values of  $B(M1)$  and  $B(E2)$  are carried out. For  $^{33}\text{P}$ , theoretical calculations using USD, USDA, PSDPF and SDPF-NR interactions are taken. The USDA calculations indicate generally better agreement with experimental  $B(M1)$  and  $B(E2)$  values of transitions between positive-parity states. For transitions between negative-parity states, both PSDPF and SDPF-NR calculations can only reproduce part of the experimental values. For  $^{33}\text{S}$ , PSDPF calculations for reduced transition strength are undertaken to compare with experimental  $B(M1)$  and  $B(E2)$  values. PSDPF calculations can reproduce the experimental results of transitions between negative-parity states with good agreement. However, for the transitions between positive-parity states the theoretical values from PSDPF are unsatisfied. Especially for the comparison of  $B(M1)$  values, the discrepancy in some places are very large.

Note that the experimental results were mostly obtained around 40 years ago, and with more than 25% uncertainty. Recently Bisoi *et al.* [63] also measured the lifetimes in  $^{33}\text{S}$  utilizing DSAM. They reported lifetimes of five states with excitation energy from 4.1 MeV to 7.8 MeV. However, there are no new lifetimes of low-lying states in  $^{33}\text{S}$  reported. In present work, due to  $\gamma$ -rays from contaminants there are no reasonable lifetimes of low-lying states in  $^{33}\text{S}$  evaluated. For  $^{33}\text{P}$ , because the compound nuclei are very high excited and the de-excitation way need to pass through

### *3. Shell-Model Calculations*

the two states with lifetime larger than 10 ps, so that there are no more Doppler shifts of low-lying states to observe. In the future, new lifetime measurements are required to improve the accuracy of data for a refined investigation.

### 3. Shell-Model Calculations

Table 3.2.: Comparison between known experimental and theoretical values of  $B(M1)$  and  $B(E2)$  in  $^{33}\text{P}$ . The experimental values are adopted from NNDC [13], where weighted average of available results from  $(t, p\gamma)$  and/or  $(\alpha, p\gamma)$  reactions are taken. Theoretical values are calculated with the parameters from the reference [78]. For  $M1$  transitions, effective  $g$  factors, and for  $E2$  transitions effective charge:  $e_p = 1.36$  and  $e_n = 0.45$  are taken. All values are in Weisskopf unit (W.U.).

Transition Strength				B(M1)				B(E2)					
$E_i$	$J_i^\pi$	$E_j$	$J_j^\pi$	Exp.	USD	USDA	PSDPF	SDPF-NR	Exp.	USD	USDA	PSDPF	SDPF-NR
1432	$3/2_1^+$	0	$1/2_{g.s.}^+$	0.013(3)	0.0077	0.0063	0.0023	0.0026	10(4)	6.55	7.15	6.08	6.50
1848	$5/2_1^+$	1432	$3/2_1^+$	0.025(5)	0.026	0.025	0.0027	0.0077	-	-	-	-	-
2538	$3/2_2^+$	0	$1/2_{g.s.}^+$	-	-	-	-	-	5.1(8)	5.33	5.46	5.62	5.67
		1432	$3/2_1^+$	0.037(15)	0.055	0.045	0.072	0.082	-	-	-	-	-
		0	$1/2_{g.s.}^+$	0.032(16)	0.045	0.046	0.052	0.044	0.5(4)	0.25	0.42	1.04	0.49
3275	$3/2_3^+$	0	$1/2_{g.s.}^+$	0.0020(6)	0.0026	0.0011	0.0038	0.0039	0.80(20)	0.12	0.12	0.16	0.064
3490	$5/2_2^+$	1432	$3/2_1^+$	0.017(4)	0.061	0.028	0.064	0.074	-	-	-	-	-
		0	$1/2_{g.s.}^+$	-	-	-	-	-	0.12(7)	1.0	0.88	1.03	0.90
3628	$7/2_1^+$	1848	$5/2_1^+$	0.0077(19)	0.0038	0.0052	0.00014	0.00022	-	-	-	-	-
		1432	$3/2_1^+$	-	-	-	-	-	8.1(19)	8.68	9.12	9.27	8.79
4048	$5/2_3^+$	3275	$3/2_3^+$	0.05(3)	0.13	0.16	0.15	0.14	-	-	-	-	-
		2538	$3/2_2^+$	0.010(6)	0.028	0.011	0.043	0.045	-	-	-	-	-
		1432	$3/2_1^+$	0.014(5)	0.043	0.051	0.059	0.063	0.29(16)	0.72	0.44	0.83	0.57
		0	$1/2_{g.s.}^+$	-	-	-	-	-	0.06(5)	0.17	0.43	0.12	0.12
5453	$9/2_1^-$	4226	$7/2_1^-$	0.00025(6)	-	-	0.0025	0.0093	0.55(14)	-	-	3.0	0.36
5638	$11/2_1^-$	5453	$9/2_1^-$	0.16(3)	-	-	0.13	0.13	-	-	-	-	-
		4226	$7/2_1^-$	-	-	-	-	-	0.9(1)	-	-	0.83	2.64

### 3. Shell-Model Calculations

Table 3.3.: Comparison between experimentally known states and calculated states up to 7.8 MeV in  $^{33}\text{S}$ .

Experiment		PSDPF		$E_{exp.} - E_{theo.}$
$E_x$ [keV]	$J^\pi$	$E_x$ [keV]	$J^\pi$	$\Delta E$ [keV]
$^{33}\text{S}$				
0	$3/2_{g.s.}^+$	0	$3/2_{g.s.}^+$	-
841	$1/2^+$	809	$1/2_1^+$	32
1967	$5/2^+$	1897	$5/2_1^+$	70
2313	$3/2^+$	2297	$3/2_2^+$	16
2868	$5/2^+$	2801	$5/2_2^+$	67
2935	$7/2^-$	2848	$7/2_1^-$	87
2969	$7/2^+$	3096	$7/2_1^+$	-127
3221	$3/2^-$	3034	$3/2_1^-$	187
3832	$5/2^+$	3690	$5/2_3^+$	142
3935	$3/2^+$	3617	$3/2_3^+$	318
4048	$9/2^+$	4111	$9/2_1^+$	-63
4055	$1/2^+$	3850	$1/2_2^+$	205
4095	$7/2^+$	4019	$7/2_2^+$	75
4211	$3/2^-$	4437	$3/2_2^-$	-226
4375	$1/2^+$	4404	$1/2_3^+$	-26
4729	$9/2^-$	4823	$9/2_1^-$	-94
4866	$11/2^-$	4842	$11/2_1^-$	24
4918	$1/2^-$	4816	$1/2_1^-$	102
4942	$5/2^-, 7/2^-$	4815	$5/2_2^-$	127
		5189	$7/2_2^-$	-247
5480	$1/2^+$	5398	$1/2_5^+$	82
5621	$1/2^+$	5982	$1/2_6^+$	-361
5711	$1/2^-$	5320	$1/2_2^-$	391
5888	$3/2^-$	5760	$3/2_4^-$	128
6363	$5/2^+$	6495	$5/2_8^+$	-132
7180	$11/2^+$	7028	$11/2_2^+$	152
7820	$15/2^-$	7643	$15/2_1^-$	177

### 3. Shell-Model Calculations

Table 3.4.: Comparison between experimental and theoretical values of  $B(M1)$  and  $B(E2)$  in  $^{33}\text{S}$ . The experimental values are adopted from NNDC [13], where weighted average of available results from  $(d, p\gamma)$  and/or  $(\alpha, n\gamma)$  reactions are taken. Theoretical values are calculated with the parameters from the reference [78]. For  $E2$  transitions, effective charge:  $e_p = 1.36$  and  $e_n = 0.45$ , and for  $M1$  transitions, effective  $g$  factors are taken. All values are in Weisskopf unit (W.U.).

Transition Strength				B( $M1$ )		B( $E2$ )	
$E_i$	$J_i^\pi$	$E_j$	$J_j^\pi$	Exp.	PSDPF	Exp.	PSDPF
841	$1/2_1^+$	0	$3/2_{g.s.}^+$	0.031(4)	0.018	6(4)	2.69
1967	$5/2_1^+$	841	$1/2_1^+$	-	-	37(8)	3.99
		0	$3/2_{g.s.}^+$	0.021(4)	0.0075	8(3)	8.31
2313	$3/2_2^+$	0	$3/2_{g.s.}^+$	0.0043(8)	0.00037	0.26(13)	3.28
2868	$5/2_2^+$	841	$1/2_1^+$	-	-	3.6(13)	5.48
		0	$3/2_{g.s.}^+$	0.08(3)	0.17	0.6(5)	1.43
2969	$7/2_1^+$	1967	$5/2_1^+$	0.034(8)	0.028	-	-
		0	$3/2_{g.s.}^+$	-	-	5.5(9)	5.12
3832	$5/2_3^+$	0	$3/2_{g.s.}^+$	0.0061(18)	0.0016	0.25(9)	0.35
4048	$9/2_1^+$	2969	$7/2_1^+$	0.0068(19)	0.00038	2.6(10)	4.92
		1967	$5/2_1^+$	-	-	8.7(23)	8.77
4095	$7/2_2^+$	1967	$5/2_1^+$	0.046(14)	0.089	1.5(5)	3.90
		0	$3/2_{g.s.}^+$	-	-	0.09(4)	0.42
4729	$9/2_1^-$	2935	$7/2_1^-$	0.0060(25)	0.0051	8(3)	7.01
4866	$11/2_1^-$	2935	$7/2_1^-$	-	-	13(4)	8.45

## Part II.

# Upgrade and Commissioning of the Lund-York-Cologne CAlorimeter





## 4. Introduction

Nuclear physics is concerned with investigating the properties of nuclei such as mass and radius, level energies, spins and parities of excited states, lifetimes, decay models and relative abundances. However, the investigation of atomic nuclei is often a rather difficult work, since not all nuclei are stable or at least long-lived enough to be easily examined. Looking at the chart of nuclides in Fig. 4.1, one can see that just a small number of nuclei are stable and found in nature. The rest decay to other nuclei within a characteristic lifetime. The nuclei far off the line of stability are experimentally very difficult to populate and so far mostly unknown. Accordingly,

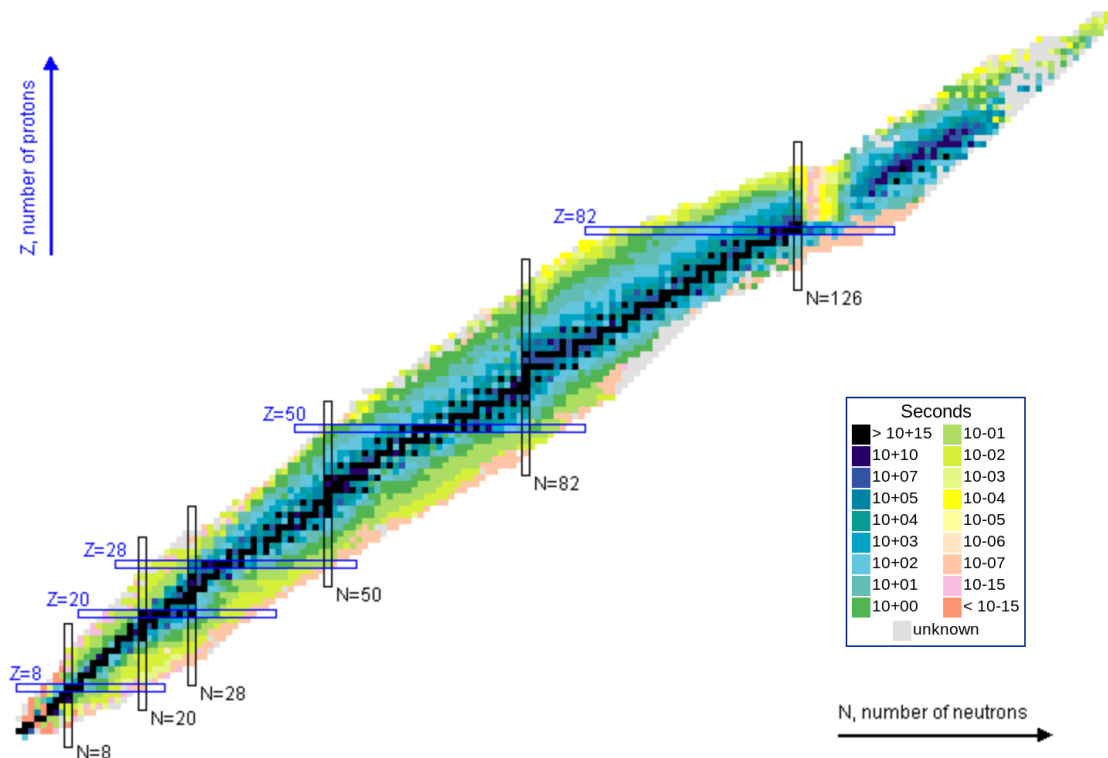


Figure 4.1.: Chart of Nuclides. As shown in the table of lifetime, different colors represent the half lives of elements. Stable elements are marked with black. Taken from [80].

one of the major objects of nuclear physics is to create exotic nuclei far from the line of stability and determine their physical properties. The studies are intended

#### 4. Introduction

to answer fundamental questions:

How does the strong interaction work, and change for different  $Z/N$  ratios?

What is the origin of the elements?

What is the nature of nuclear matter?

In order to study these questions a new generation of accelerators and advanced high-resolution detectors are required to produce and identify the nuclei from fragmentation reactions. In such experiments each nucleus of interest must be selected from other nuclei of similar mass in order to ensure that the measured nuclear properties correlate with the right nucleus. These conditions will be provided at the future Facility for Antiproton and Ion Research (FAIR), which is currently under construction at Gesellschaft für Schwerionenforschung (GSI) in Darmstadt, Germany. NUClear Structure, Astrophysics and Reactions (NUSTAR) is one of the main collaborations that will use the new facility. NUSTAR is focused on experiments mainly using Radioactive Ion Beams (RIB), selected with the Superconducting FRagment Separator (Super-FRS) (structure shown in Fig. 4.2). Using the in-flight separa-

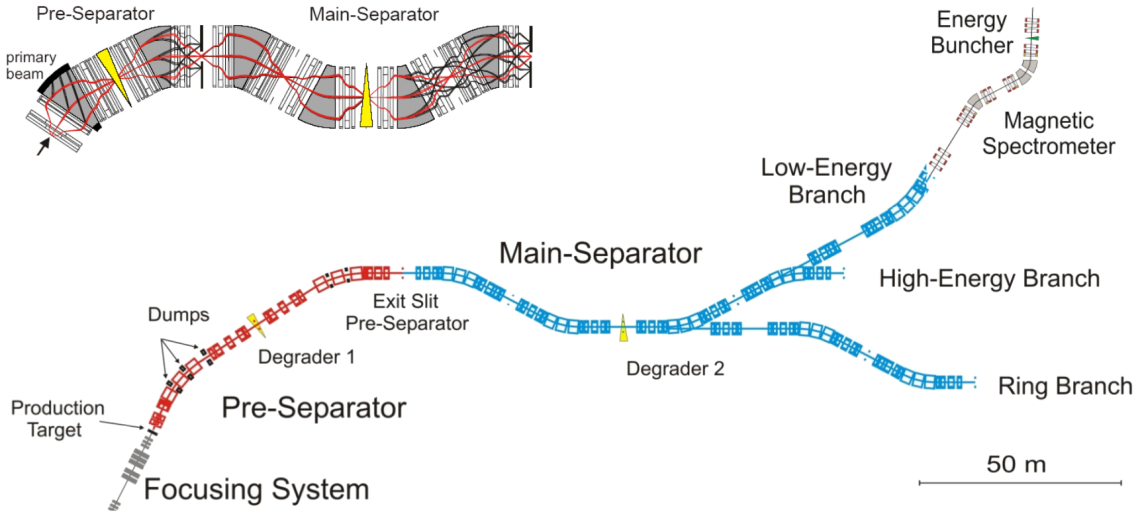


Figure 4.2.: Illustration of the Superconducting FRagment Separator. Three energy branches are supplied: high-energy branch of 300 – 1500 MeV/u, low-energy branch up to 300 MeV/u, and ring branch. Adopted from [81].

tor, rare nuclei can be produced and separated, supplying high currents of beams of exotic nuclei up to uranium at relativistic energies. At NUSTAR three energy branches of RIB will be provided: the high-energy branch with relativistic energies of 300 – 1500 MeV/u, the low-energy branch with beam energies up to 300 MeV/u, and the ring branch.

### 4.1. HISPEC Campaign

One part of the NUSTAR collaboration is the HISPEC (High resolution In-flight SPECtroscopy) campaign, which will be conducted at the low-energy branch to investigate the expected changes in nuclear structure predicted in very neutron or proton rich nuclei, using high-resolution  $\gamma$ -ray spectroscopy. As the continuation of the successful RISING (Rare ISotope INvestigations at GSI) campaign, HISPEC will employ beam energies of around 100 MeV/u to study the evolution of the shell structure nearby the shell closure, nuclear shapes, as well as transition probabilities of exotic nuclei [82]. The goal of HISPEC is to use Coulomb excitation as well as fragmentation reactions to answer fundamental questions of nuclear physics concerning among others the location of the neutron dripline, new forms of collective movement in nuclei far from stability, and the symmetries in nuclei close to the driplines. To realize these investigations high-efficiency  $\gamma$ -ray spectroscopy should be undertaken. During the HISPEC campaign the new-generation Advanced GAMMA-ray Tracking Array (AGATA) (see Fig. 4.3) surrounding the secondary target will be employed. The complete setup of AGATA will be a  $4\pi$  array, including 180 segmented hexag-

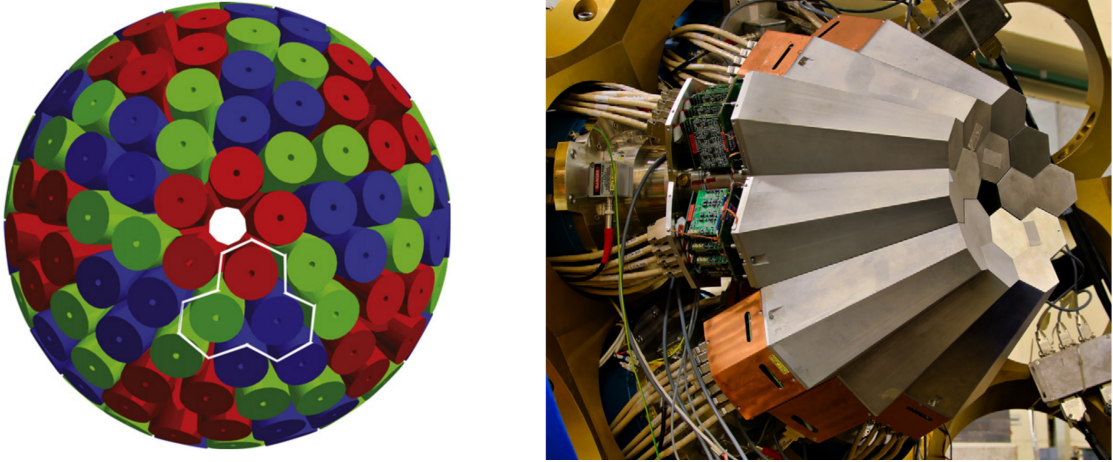


Figure 4.3.: AGATA detector. Left: Simulated AGATA design of the spherical construction with 180 crystals. Right: Photograph of the setup with five AGATA triple-cluster detectors installed at LNL in Italy. Adopted from [83].

onal high-purity Germanium crystals. Each crystal comprises a 6-fold sector-wise segmentation and a 6-fold longitudinal segmentation, which allows the tracking and reconstruction of the full scattering path of the  $\gamma$  events [83].

To ensure the good quality of data from AGATA, the reaction products after the secondary target should be tracked and identified event by event, so that the precise information about the position, trajectory as well as velocity of the particles can

be used to perform a sensible Doppler correction. For this reason, the Lund-York-Cologne CALorimeter (LYCCA) was developed. The LYCCA detector system is a key device designed for the NUSTAR collaboration consisting of time-of-flight (ToF) and  $\Delta E - E$  detectors, which will be employed flexibly to comply with individual requirements of different experiments. For light nuclei, LYCCA is required to identify  $A \approx 20$  for energies up to 200 MeV/u as well as, for heavy nuclei, up to  $A = 200$  with energies of around 100 MeV/u.

## 4.2. LYCCA

The LYCCA detector is a improved design of the  $\Delta E - E$  telescope CATE (CALorimeter Telescope), which was employed for charged-particle identification during the RISING campaign [84]. CATE consisted of Double-Sided Silicon Strip Detectors (DSSSDs) and CsI crystals, which measured the energy loss ( $\Delta E$ ) and residual energy ( $E_{res.}$ ) of the indicated particles, respectively. However, exact velocity measure-

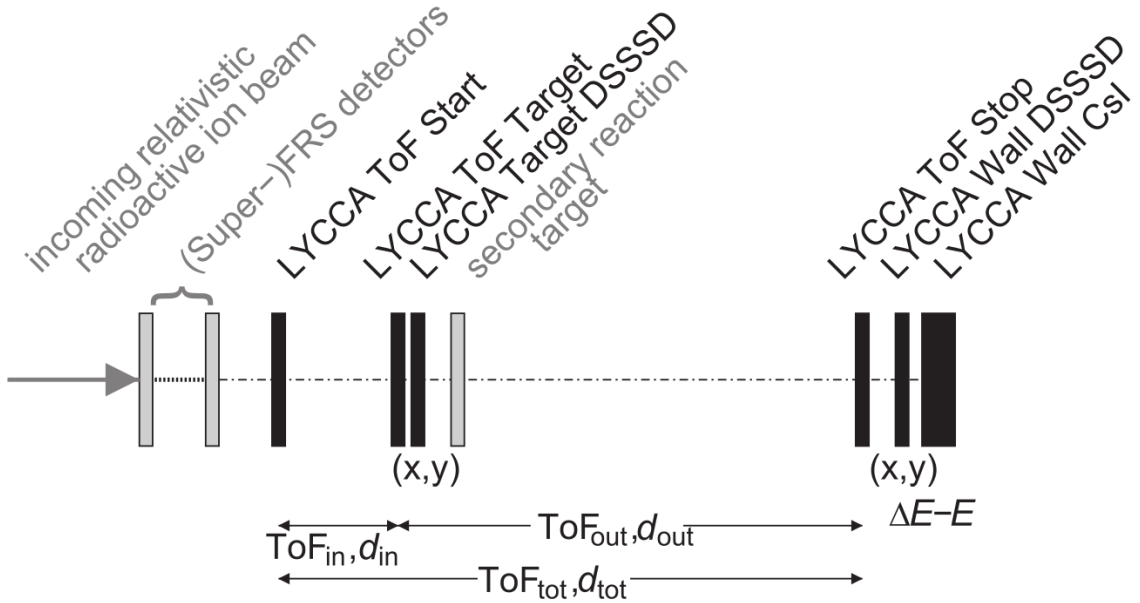


Figure 4.4.: Sketch of the detection principle of the LYCCA detector system, which are marked in black. Adopted from [85].

ments are hindered by energy straggling in thick secondary targets. To overcome this problem, in addition to DSSSDs and CsI detectors LYCCA uses ToF detectors (fast plastic scintillators) to reduce velocity uncertainties. Figure 4.4 shows the sketch of the LYCCA detector system, which will be located at the end of the (Super-)FRS. The ToF measurements are performed using different ToF detector combinations.  $\text{ToF}_{in}$  for incoming particles is measured by the ToF-Start and ToF-Target detectors,

#### 4. Introduction

while  $\text{ToF}_{out}$  for outgoing particles is measured by the ToF-Target and ToF-Stop detectors (cf. Fig.4.4). The trajectory tracking of the reaction products after the secondary target is supplied by the LYCCA Target DSSSD together with the LYCCA Wall DSSSD, which is positioned at the end of the beam line, around 3 m behind the secondary target [85]. In addition, the LYCCA Wall DSSSD measures the energy loss  $\Delta E$  of the reaction products, while the LYCCA Wall CsI detector determines the residual energy  $E_{res}$ . The charge number  $Z$  of the reaction products can be determined through the  $\Delta E - E$  technique. The mass number  $A$  of the reaction products can be determined through  $\text{ToF}_{out}$  together with  $E_{res}$ . Via the identification of  $Z$  and  $A$ , the reaction channel of interest will be selected, and the unwanted nuclear reactions contributing to the measured background should be gated out. To perform an acceptable Doppler correction, the tracked particle trajectory and position sensitive Germanium detectors (like AGATA) are needed to precisely determine the angle  $\theta_\gamma$  between the outgoing particle and the  $\gamma$ -ray.

The precursor of LYCCA, known as LYCCA-0, using 12  $\Delta E - E$  telescopes and analog electronics was employed in the PreSPEC campaign from 2009 to 2014 [86]. As shown in Fig. 4.5, the LYCCA setup was used together with the EUROBALL cluster and the HECTOR array during the PreSPEC beamtime to identify and investigate rare nuclei, as well as with the AGATA demonstrator to perform the commissioning test. Analysing the measured data, the tracking of particles event by event was successfully tested. The resolution of charge number by  $Z = 33$  [87] and  $Z = 36$  [88] was determined to be  $\Delta Z/Z = 0.21\sigma$  ( $\sigma$  expresses the statistic distribution). For a mass number  $A$  around 100 the resolution  $\Delta A/A$  was determined to be  $0.47\sigma$  (for  $A = 104$ ) [89]. Afterwards, the electronics and mechanics of LYCCA system were upgraded. Since 2016 the new LYCCA set-up is located at the Cologne tandem accelerator. This thesis focuses on the detailed upgrade and the commissioning test of LYCCA.



#### 4. Introduction

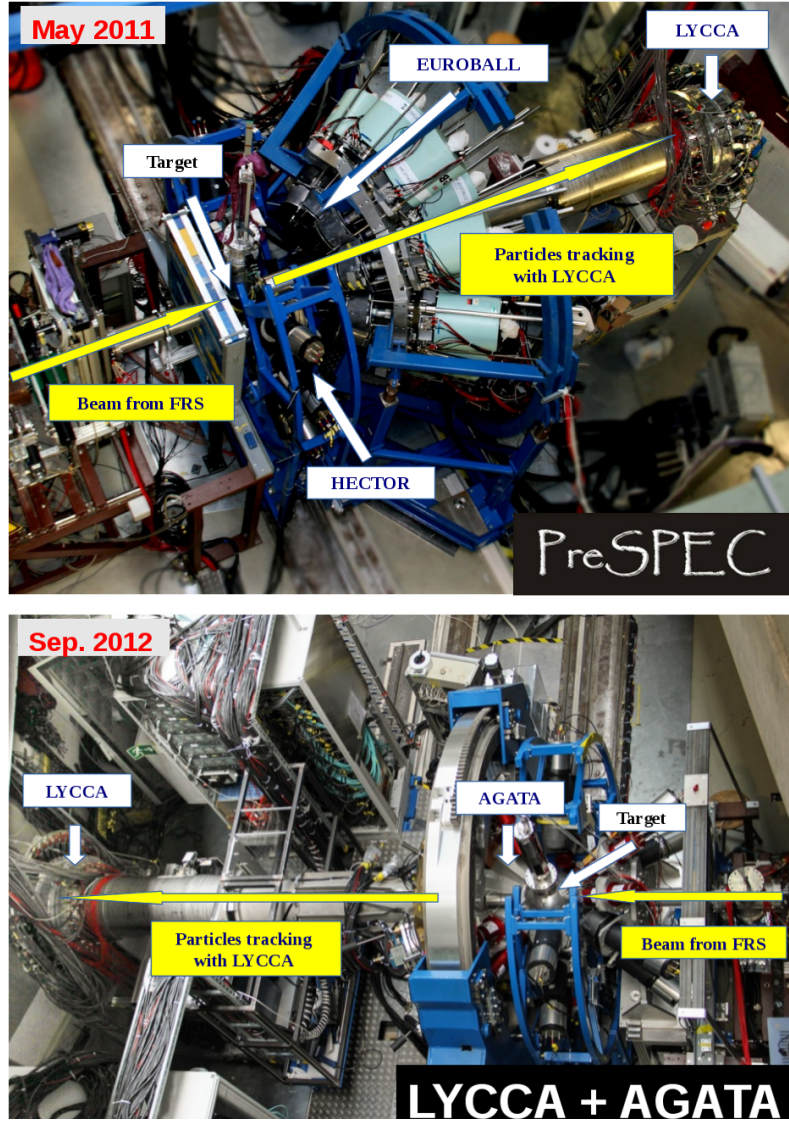


Figure 4.5.: Top: LYCCA setup together with the EUROBALL cluster detectors and the HECTOR array during the PreSPEC beamtime. Bottom: LYCCA setup with the AGATA demonstrator during the commissioning phase.

# 5. Upgrade of LYCCA

## 5.1. Detectors

In this section the features of the DSSSD and CsI detectors as well as their underlying detection principles are described.

### 5.1.1. Functionality of the detectors

The LYCCA detectors aim to detect and identify heavy ions, whose mass is equal to or larger than that of a proton ( $m_p = 938 \text{ MeV}/c^2$ ). During the flight through matter, heavy ions interact with the atoms in a material and lose their energy mainly by the following two processes:

- elastic scattering from the nuclei, and
- inelastic scattering from the electrons, i.e. excitation or ionization,

where the second process dominates the energy loss. In each inelastic scattering an ion loses only a very small part of its energy, so that a large number of events is required to stop the ions. The differential energy loss per unit of path length, also known as stopping power, is defined as  $(-dE/dx)_e$ . For high-energetic ions ( $v \gg v_0$ ; Bohr velocity  $v_0 \approx \frac{c}{137}$ ),  $(-dE/dx)_e$  can be described by the Bethe-Bloch formula:

$$\left(-\frac{dE}{dx}\right)_e = \frac{4\pi e^4 z^2 N Z}{m_e \beta^2 c^2} \cdot \left[ \ln \left( \frac{2m_e c^2 \beta^2}{I} \right) + \ln \frac{1}{1 - \beta^2} - \beta^2 \right] \quad (5.1)$$

where

- $E$ : ion energy
- $x$ : path length

## 5. Upgrade of LYCCA

- $\beta = v/c$ : relative velocity of ions
- $z$ : charge number of ions
- $Z$ : charge number of stopping material
- $N$ : electron density
- $m_e$ : electron mass
- $I$ : average excitation potential of the material

For a non-relativistic approximation  $\beta \ll 1$ , the formula is simplified to:

$$\left(-\frac{dE}{dx}\right)_e \approx \frac{4\pi e^4 z^2 N Z}{m_e \beta^2 c^2} \cdot \left[ \ln \left( \frac{2m_e c^2 \beta^2}{I} \right) \right] \quad (5.2)$$

Furthermore, the (non-relativistic) relationship of the energy loss in a thin  $\Delta E$  detector with the total kinetic energy  $T$  can be written as:

$$\Delta E = \frac{k \cdot z^2 \cdot M_i}{T} \quad (5.3)$$

where  $M_i$  is the ion mass, and  $k$ , a constant that depends on the material of the detectors. An example of such  $\Delta E$  to  $T$  plot is shown in Fig. 5.1. For different  $z$

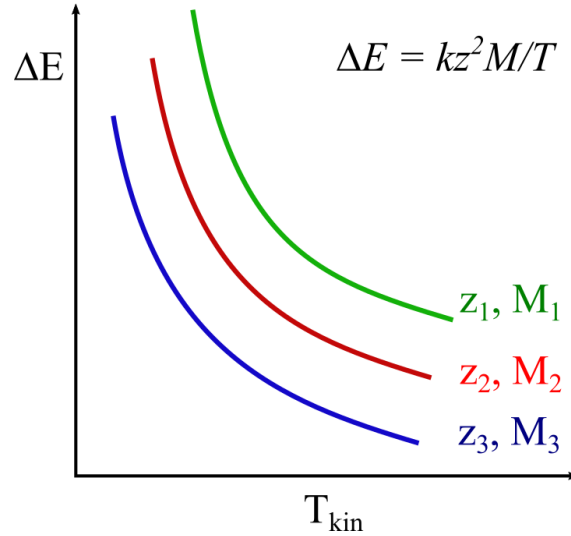


Figure 5.1.: The plot of energy loss  $\Delta E$  to total kinetic energy  $T$  for different  $z$  and  $M$ . Modified from [90].



## 5. Upgrade of LYCCA

and  $M$ , a group of hyperboles are produced, which are proportional to  $z^2 M$ .

If the energy of the ions to be observed is relativistic, the total energy  $T$  depends on the flight time (ToF) and the distance  $L$ . In this case the relativistic energy  $T$  should be described as:

$$T = Mc^2 \cdot \left( \frac{1}{\sqrt{1 - \left( \frac{L}{c \cdot t_{ToF}} \right)^2}} - 1 \right) \quad (5.4)$$

Here the most important criterion for the detectors of the ToF measurement is the timing resolution, which depends on the time required to form a signal after radioactive radiation has arrived. A good timing resolution is usually produced by a rapidly formed signal with a steeply rising edge. LYCCA employs two different types of timing detector, large-area CVD (Chemical Vapour Deposition) polycrystalline diamond detectors and fast plastic scintillators. The optimal timing resolution of both types of detectors is typically around 50 ps [91].

### 5.1.2. DSSSD

The Double-Sided Silicon Strip Detector (DSSSD) employed in LYCCA is a semiconductor device that measures both the position of incident ions in the  $x - y$  plane and the energy loss  $\Delta E$ . Around 30 years ago segmented silicon detectors were introduced to detect charged particles, and they have obtained a central role in nuclear and high-energy physics. As detector material silicon offers a number of advantages. Silicon can be operated even at room temperature, so no cooling or isolating system is required. Furthermore, this semiconductor is a crystal consisting of atoms with four valence electrons. Each electron forms a covalent bond with another electron from an adjacent atom. Thus all electrons are closely bound, the semiconductor has a fully occupied valence band and an empty conduction band. Between the two bands, there is a gap of forbidden energies only about 1 eV wide. This band gap is so small that thermal energies are sufficient to excite electrons into the conduction band, leaving holes in the valence band. In the semiconductor material incident-charged particles transport energies to the electrons, which may overcome the band gap and move into the conduction band, creating electron-hole pairs. In this way the energy loss to be measured is transformed to electronic signals.

An effective way to improve the conducting performance of a semiconductor is doping. There are two types, n-doping and p-doping. For n-doping small impurities

## 5. Upgrade of LYCCA

with five valence electrons are brought into the material on purpose. Four valence electrons of the n-dopant will be in the covalent band with electrons of the regular semiconductor atoms, while the fifth is just very loosely bound. Thus, only a little

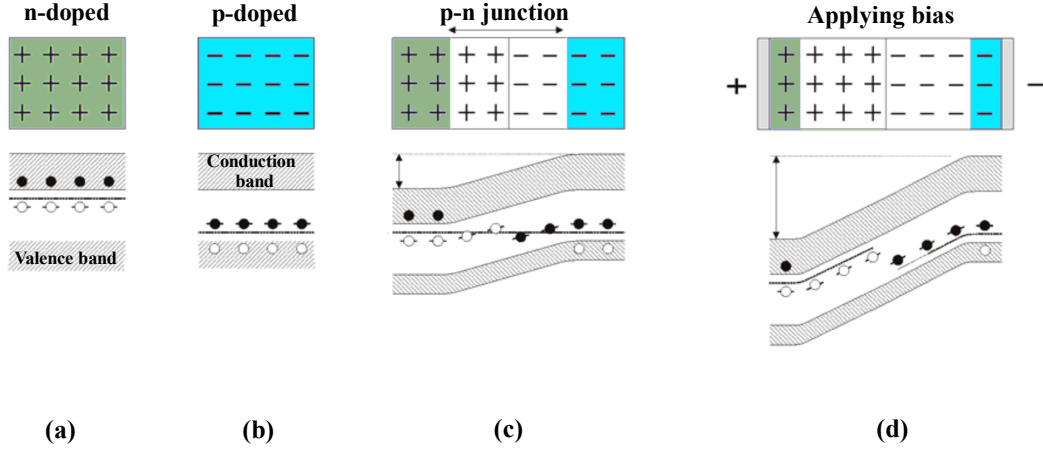


Figure 5.2.: (a) Band structure of a n-doped semiconductor. The donor states are close to the conduction band. (b) Band structure of a p-doped semiconductor. The acceptor states are just above the valence band. (c) Band structure of a p-n junction. Contacting the n-type and p-type semiconductors electrons from the n-side recombine with holes in the p-side, and an electric field is created. (d) Applying reverse bias, more electrons are forced into the p-side and the electric field is increased. Modified from [90].

energy is needed to excite this electron into the conduction band. This kind of dopant is called a donor, whose states are close to the conduction band (see Fig. 5.2(a)). Since there are negative charge carriers in excess, material with a donor is called n-doped.

When the dopant has only three valence electrons, one of the neighbouring electrons cannot form a covalent bond, so that there is an excess of positive charge carriers (holes). Such a kind of material is called p-doped, and the dopant (acceptor) will accept an electron easily. The acceptor states are close to the valence band, as shown in Fig. 5.2(b).

Bringing n- and p-doped semiconductor materials together, electrons from the n-side recombine with holes in the p-side. Consequently the n-side becomes positively charged while the p-side becomes negatively charged, and between both sides a depletion region without free charge carriers is created. The charges on both sides form then an electric field that blocks further electrons from moving across the junction (cf. Fig. 5.2(c)). Applying a reverse bias on the junction, more electrons can be forced to the p-side, so that the depletion region and the electric field

## 5. Upgrade of LYCCA

are increased (cf. Fig. 5.2(d)). Incident-charged particles ionize the atoms of the semiconductor and create electron-hole pairs. The number of electron-hole pairs depends on the energy of the incident ions. The electric field in the depletion region forces the electrons to move to the anode, the holes, to the cathode. Thus, electric signals that can be measured are created. Hence, the detection of incident ions is only possible in the depletion region, and a sufficient operating bias is required to enlarge the sensitive area of the detector as well as to improve the charge collection. However, the increase of the voltage is ultimately limited by the onset of avalanching. In sufficient high electric fields (higher than about  $10^5$  V/cm in Si) electrons obtain sufficient energy between collisions so that secondary electrons can be ejected, which may trigger ejecting secondary electrons, ultimately leading to a self-supporting charge avalanche. This phenomenon is called "breakdown" and can result in permanent damage to detectors [92]. Considering the thickness of LYCCA-DSSSD of around  $300\text{ }\mu\text{m}$ , the limit of the operating bias should be below 300 V. The typical operating voltage is  $50 - 70$  V in experiments.

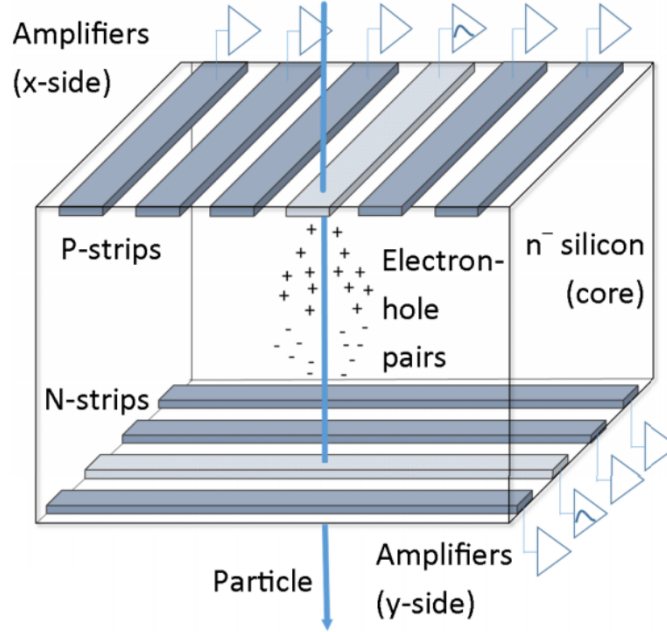


Figure 5.3.: Schematic of the double sided silicon strip detector. Taken from [93].

A double-sided silicon strip detector is segmented on both the p- and n-side into strips, which are placed perpendicular to each other. For  $N_f$  and  $N_b$  strips on the front (junction) and back (ohmic) sides, respectively, the detector provides information on  $N_f \times N_b$  pixels (overlap regions between front and back strips) by employing only  $N_f + N_b$  electronics channels. A schematic illustration of this kind of detector is depicted in Fig. 5.3. For ToF measurements and event tracking, an important

## 5. Upgrade of LYCCA

information is the exact impact position of ions on detectors. Obviously, a higher segmentation in certain detector areas improves the position resolution, which is limited by the width of the strips. However, the ion energy is not always completely deposited in one strip, but rather in two or more strips, especially when the ions fly through the detector not perpendicular but with a slope angle. Furthermore, there is always the effect of transverse diffusion and induced transmitsignals, which divides the charge on multi-strips by a Gaussian distribution (cf. Fig. 5.3) with a standard deviation  $\sigma = p/\sqrt{12}$  ( $p$  is the strip pitch in  $\sim\mu\text{m}$ ) [92]. Moreover, a charge can also be collected by the interstrip area on the p-side, thus an anomalous charge distribution may occur. This effect was observed and discussed by references [94–96]. Hence, to improve the position resolution in such cases, the charge distribution has to be evaluated.

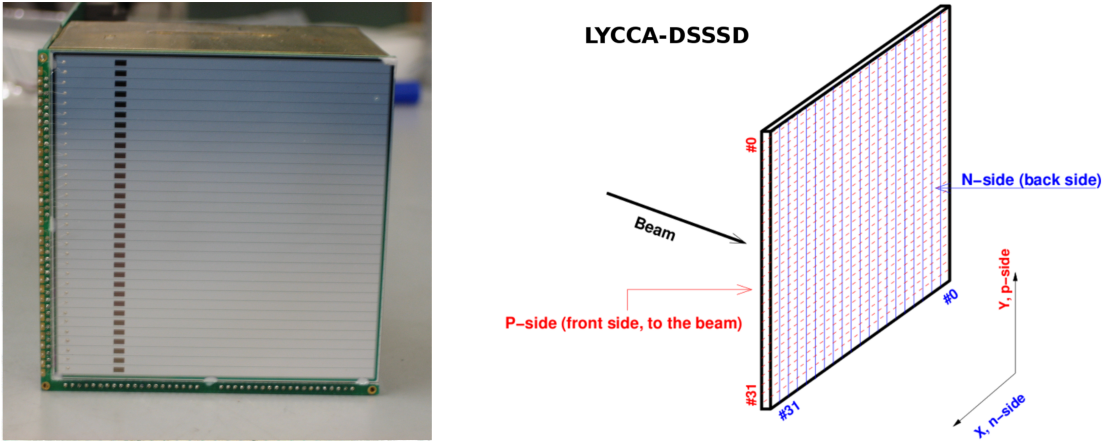


Figure 5.4.: Left: A view of the LYCCA-DSSSD from the p-side. The small rectangular marks on p-strips indicate the missing dead layer. Right: Drawing of strips on p- and n-side of LYCCA-DSSSD. The beam direction is indicated with the black arrow. Adopted from [97].

The LYCCA-DSSSDs are produced by RADCON Ltd., Zelenograd, Russia, and are bonded on custom-made printed circuit frames by University of Lund. Figure 5.4 shows the structure of the LYCCA-DSSSD. The characteristics of the DSSSDs are summarized in Table 5.1. The n-strips on the ohmic side are isolated from adjacent strips via a p-type zone. A layer of Aluminium is deposited on both p- and n-strips for signal read-out. The surfaces of the detector are passivated with silicon dioxide ( $\text{SiO}_2$ ), and the sensitive area is surrounded by guard rings.

### 5.1.3. Caesium iodide (CsI) scintillators

The total kinetic energy of implanted ions are measured by employing slightly hygroscopic inorganic CsI(Tl) scintillators, which originate from Kharkov, Ukraine [98].

## 5. Upgrade of LYCCA

Table 5.1.: Overview of LYCCA-DSSSD characteristics. Data taken from [98].

Wafer Dimension:	$(60.0 \pm 0.2) \times (60.0 \pm 0.2) \text{ mm}^2$
Active area:	$58.5 \times 58.5 \text{ mm}^2$
Thickness:	$(303 \pm 3) \text{ }\mu\text{m}$
Number of strips:	$32 \times 32$
Strip width:	1.80 mm on p-side 1.63 mm on n-side
Interstrip width:	30 $\mu\text{m}$ on p-side 200 $\mu\text{m}$ on n-side
Dead layers:	0.48 $\mu\text{m}$ on p-side 0.55 $\mu\text{m}$ on n-side
Full depletion voltage:	typical 40 V
Operating voltage:	50 – 70 V
Leakage current:	10 – 15 nA per strip
Capacity:	33 pF per strip
Resistivity:	6.3 k $\Omega\text{cm}$

The CsI detector in LYCCA telescopes consists of nine CsI crystals, which are placed in  $3 \times 3$  arrays and 10 mm behind the LYCCA-DSSSD (see Fig. 5.5).

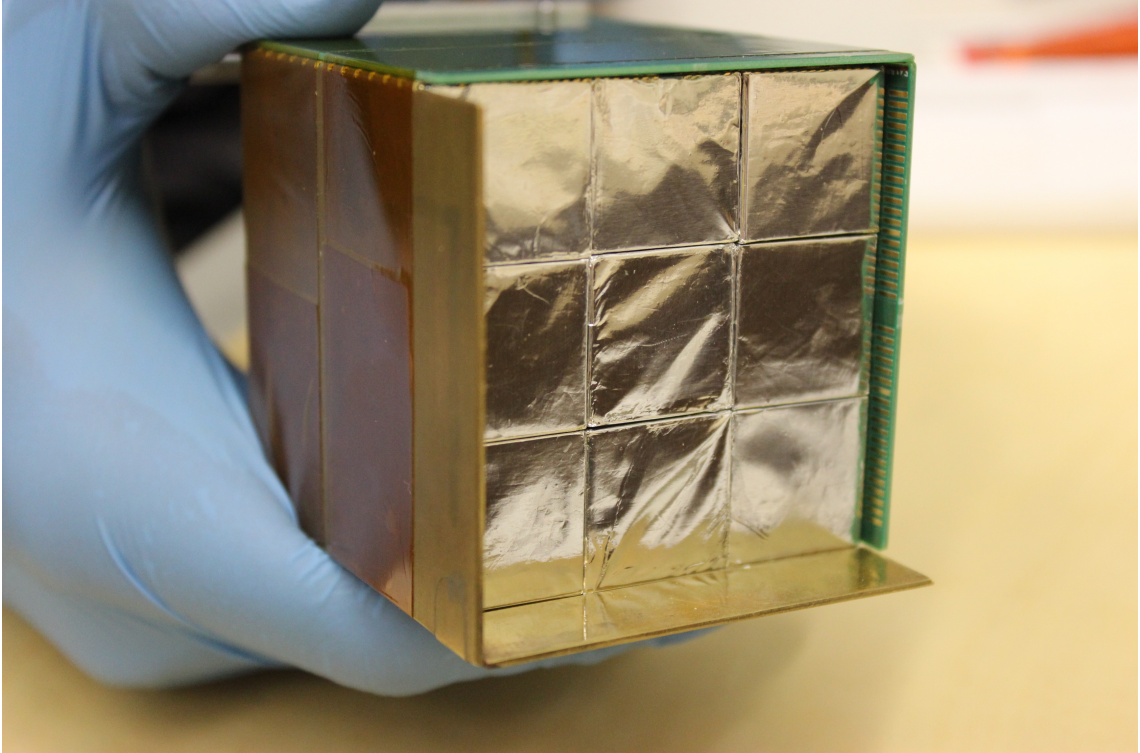


Figure 5.5.: A  $3 \times 3$  block of LYCCA-CsI scintillators with brass frame. Each single CsI crystal is wrapped in foil.

## 5. Upgrade of LYCCA

The material in a scintillation detector is an insulator with a crystal structure, which has a full valence band and an empty conduction band. The typical energy gap of a pure scintillator material is about 4 eV. When a scintillator is irradiated by ions with sufficient energy, the electrons of the crystal can be excited to the conduction band, leaving holes in the valence band. By ejecting photons with energies close to the band gap these electrons de-excite to the valence band again. The photons emitted by a pure crystal are often in the non-visible range of the light readout device, and are absorbed most likely by the crystal itself (self-absorption). This problem can be overcome by introducing small impurities into the crystal. In a CsI crystal thallium has been introduced as an activator. The energy required to ionize an electron in the activator is less than for an electron in the scintillator. Thus, the holes created by incident radiation will move to an activator state, while electrons in the conduction band move to an activator state, too, and neutralize the atom (see Fig. 5.6). Since the activators fit into the previously forbidden energy range, the

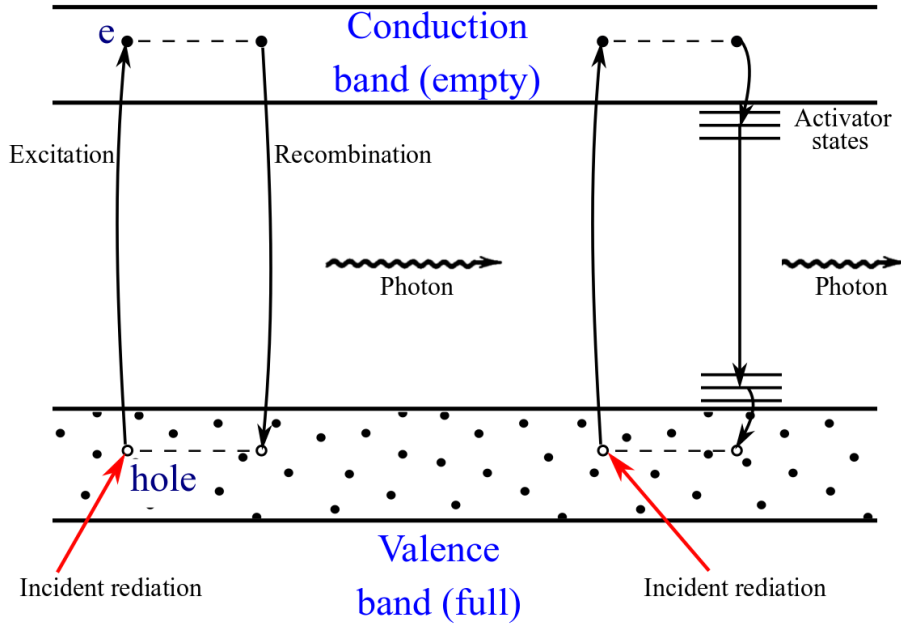


Figure 5.6.: Band structure in a scintillation crystal. The left processes of excitation and recombination occur in a pure crystal. The right process occurs in an activated crystal. The activator states lie within the band gap, and thus the energy of emitted photons are smaller than that in pure crystal. Modified from [90].

distances between the energy levels are smaller and photons are emitted in the visible range. Consequently, the self-absorption of photons can be significantly reduced.

The CsI crystals used in LYCCA telescopes are in cuboid form and have two different lengths, as shown in Fig. 5.7. All sides of the crystals are polished, and



## 5. Upgrade of LYCCA

a pyramidal lightguide is built at the end of the crystal. In order to increase the efficiency of light collection, all sides of the crystals (except front and end) are packed in 65  $\mu\text{m}$  VM2000 (ESR, Enhanced Specular Reflector) film. However, this film is transparent for scintillation light of certain wavelengths, therefore 12  $\mu\text{m}$  Aluminium foil is additionally used to wrap the crystals, ensuring optical isolation between adjacent crystals in a module [85]. The characteristics of LYCCA-CsI(Tl) crystals are summarized in Table 5.2.

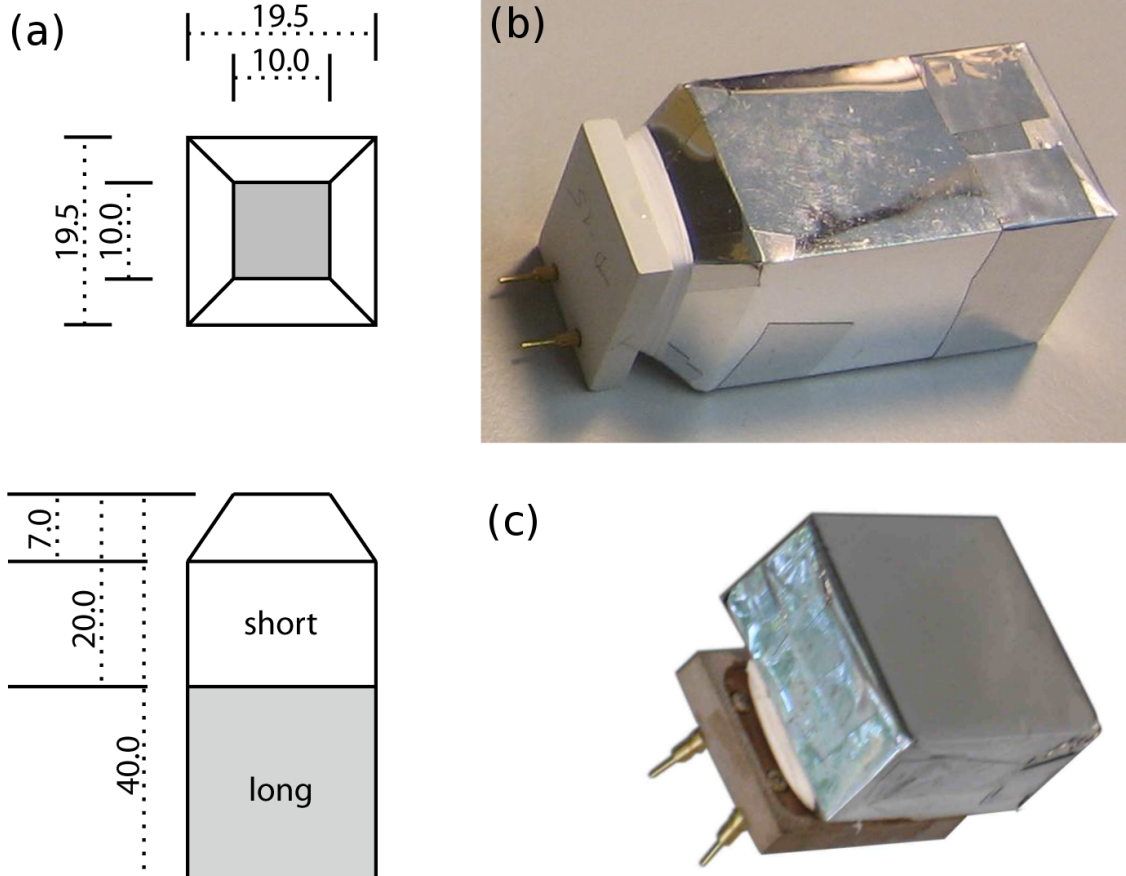


Figure 5.7.: (a) Schematic illustration of the different types of CsI scintillators. All lengths in mm. (b) Single CsI crystal in the big length. (c) Single CsI crystal in the small length. Taken from [99].

To read out the scintillation light, at the back side of each CsI crystal a photodiode is mounted, which is selected to have a good efficiency of around 85% at the wavelength of maximum emission for CsI(Tl) (about 560 nm). The photodiodes are PIN diodes, which consist of n-doped silicon with highly p-doped material on the front side and n-doped material on the back side, respectively. Via the photoelectric effect, scintillation photons from the p-side are absorbed by electrons in the depletion region, creating electron-hole pairs. Operating with reverse bias,

## 5. Upgrade of LYCCA

the charge carriers will be collected and processed by a charge sensitive preamplifier.

Table 5.2.: Overview of LYCCA-CsI(Tl) characteristics. Data taken from [98].

Density:	4.51 g/cm <sup>3</sup>
Front face:	19.5 × 19.5 mm <sup>2</sup>
Length (crystal+lightguide):	33 + 7 mm (long) 13 + 7 mm (short)
Thickness of Aluminium-wrapping:	12 µm
Thickness of VM2000-wrapping:	65 µm
Operating voltage:	50 V
Leakage current:	1 – 2 nA
Capacity:	40 pF
Max. emitted wavelength:	560 nm
Total light efficiency:	5.2 × 10 <sup>4</sup> photons/MeV



#### 5.1.4. LYCCA $\Delta E - E$ telescope

Figure 5.8 shows the technical drawing of a complete LYCCA  $\Delta E - E$  telescope. Each telescope consists of one DSSSD and a block of nine CsI scintillators. Two printed circuit boards are mounted perpendicular on the DSSSD to transport signals from the p- and n-side separately. 32-pin flat-ribbon cables are used to connect

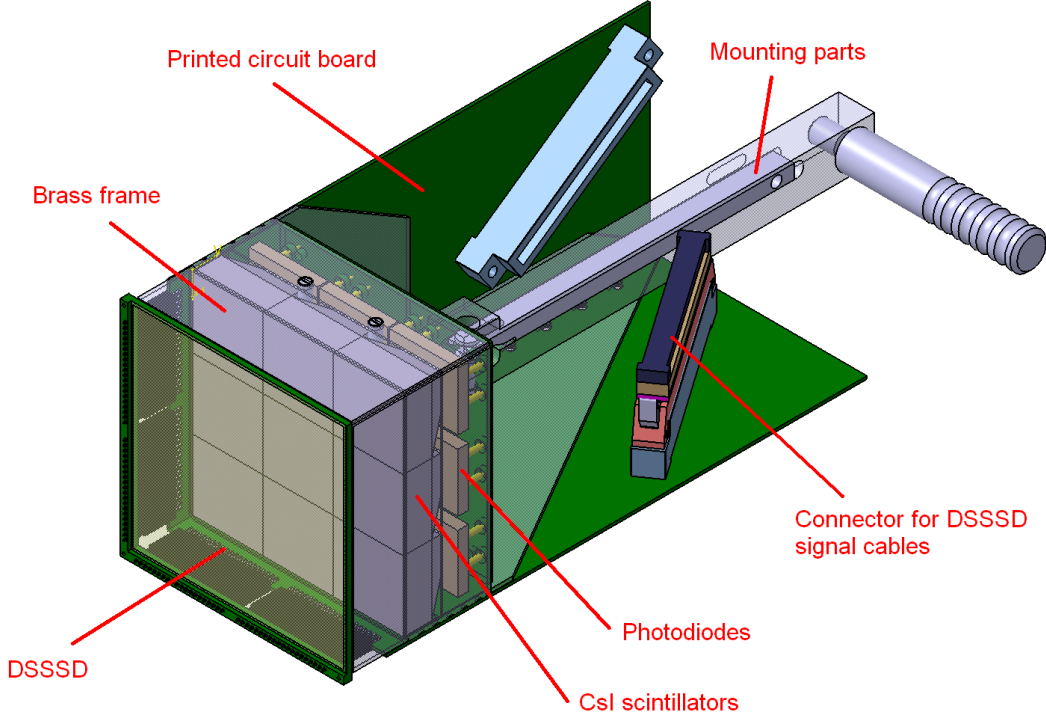


Figure 5.8.: Technical drawing of a LYCCA  $\Delta E - E$  telescope. Adopted from [85].

the electronics at the vacuum feedthroughs. The CsI block is located about 10 mm behind the DSSSD. A signal distribution board is mounted to the back nine photodiodes. For each photodiode a shielded coaxial cable is used for signal transportation. An additional signal distribution adapter is employed to connect the vacuum feedthrough. Each adapter of this kind (27 channels) can match cables from three CsI blocks. The connection is shown in Fig. 5.9. A mounting part is attached to the brass frame for locating the telescope inside the LYCCA chamber. All parts of the telescope can be tested, exchanged and repaired separately. The main design of the  $\Delta E - E$  telescope is chosen to obtain the highest solid-angle coverage under extreme forward angles, by achieving the telescopes in a wall. Furthermore, in order to keep maximal flexibility, all telescopes can be replaced individually to arrange the wall in different geometries. In the PreSPEC campaign 12  $\Delta E - E$  telescopes were employed [99]. In the future HISPEC campaign, the final LYCCA setup contains 26 telescopes.

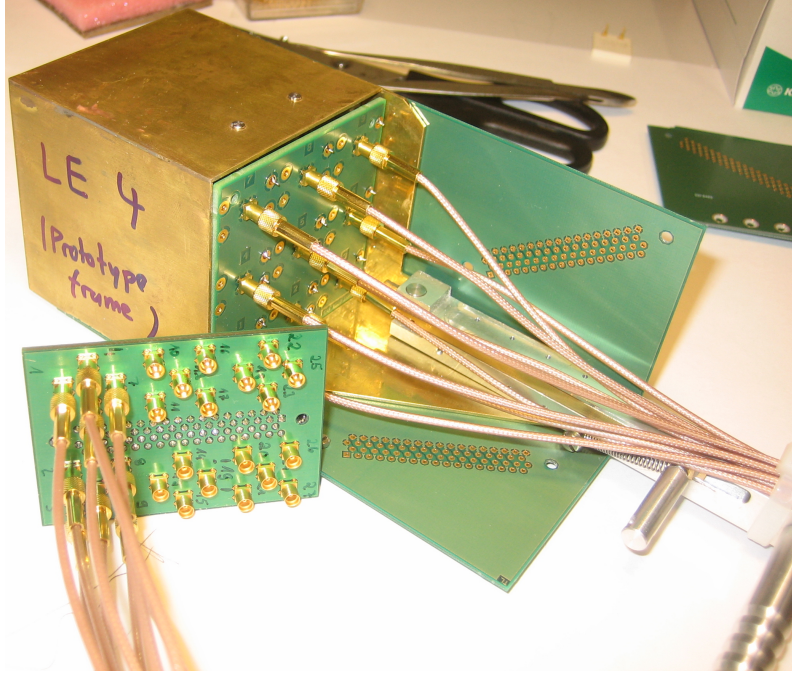


Figure 5.9.: CsI block with nine CsI crystals, connected with cables and adapter boards.

## 5.2. Electronics

During the PreSPEC campaign analog electronics were used to operate the detectors and acquire data. The CSP-32 series of highly compact charge-sensitive preamplifiers (see Fig. 5.10) was developed at the University of Cologne to cover a wide energy range of signals from both DSSDs and photodiodes. Each preamplifier can

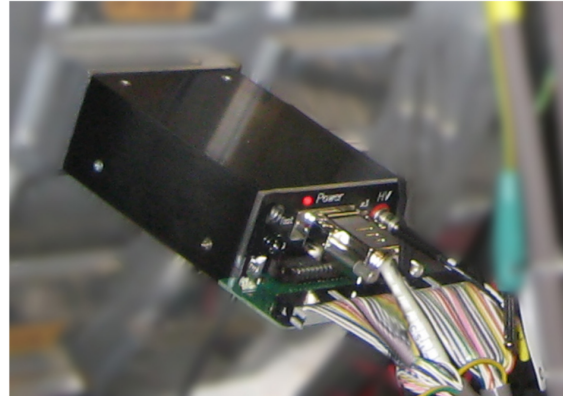
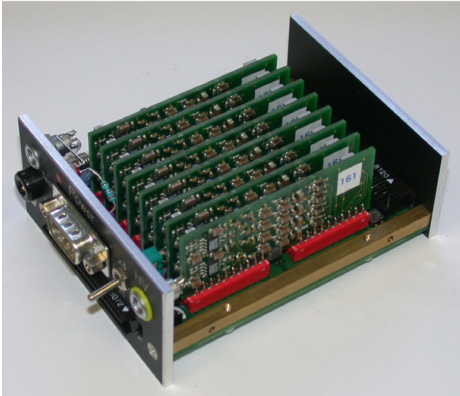


Figure 5.10.: View of the charge-sensitive preamplifier. Left: a prototype; Right: Final version mounted on the LYCCA chamber. Taken from [85].

operate max. 32 DSSSD channels or 27 CsI channels. The output signals can be directly digitized with two GSI-EE 16-channel FEBEX3 sampling ADC modules. More detailed specifications of the preamplifier can be found in reference [85].

## 5. Upgrade of LYCCA

In the future HISPEC campaign the complete LYCCA setup consists of 26  $\Delta E - E$  telescopes, which comprises signals from 1664 DSSSD channels and 234 CsI channels. In order to simplify the electronic assignment and data acquisition, new digital electronics are required. As a solution, the highly integrated FEE (Front End Electronics) modules with ASICs (Application Specific Integrated Circuits), developed for the Advanced Implantation Detector Array (AIDA) [100], will also be employed to operate LYCCA DSSSDs. This major upgrade from analog to digital electronics for LYCCA was carried out by STFC Daresbury Laboratory. The commissioning and optimization of the new electronics with LYCCA detectors at IKP Cologne is a main part of this work.

### 5.2.1. Application Specific Integrated Circuit (ASIC)

Attached to the very front end of each FEE module, four ASICs are wire-bonded to a mezzanine PCB, as shown in Fig. 5.11. In each ASIC, electronic components

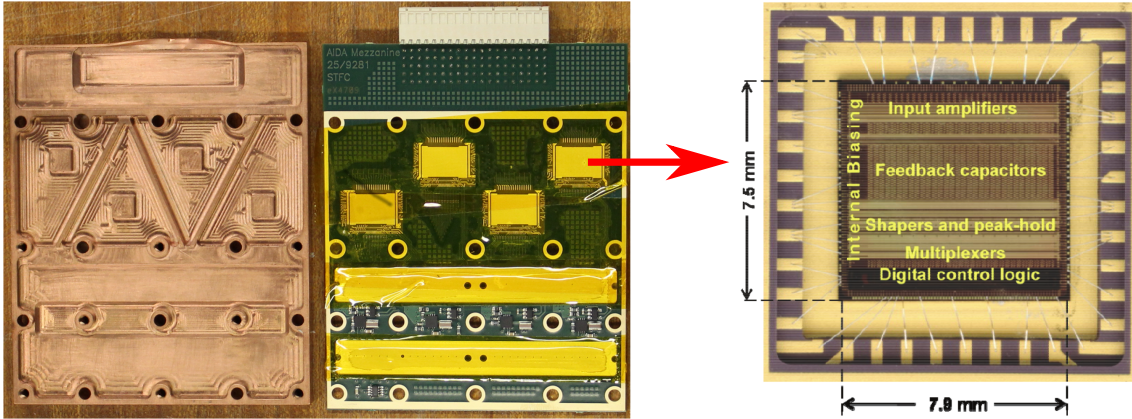


Figure 5.11.: View of the AIDA ASIC. Left: A mezzanine with four AIDA ASICs mounted, connecting to the detector using an ERNI 2mm pitch connector. The copper cover secures the AISCs and dissipates heat. Right: Picture of the ASIC structure. In one ASIC electronic components are integrated processing signals from 16 DSSSD channels. Modified from [101].

such as preamplifier, shaper, slow (fast) comparator, peak-hold and control logic are integrated to process signals from 16 DSSSD channels. Thus, each FEE module can operate all 64 channels of one LYCCA DSSSD. The most distinctive feature of the ASIC is that each of the 16 channels has two dedicated preamplifiers. One of them is directly connected to the input and has a selectable gain for the low/medium-energy ranges (low energy: up to 20 MeV; medium energy: up to 1 GeV), while the other has a much lower gain for the high-energy range (up to 20 GeV) and is connected

## 5. Upgrade of LYCCA

to the input node via a diode link. The initial idea of this design is that the AIDA ASIC should be able to measure both huge signals from unstable nuclei implanted into the detector as well as much smaller signals from subsequent radioactive decay. The preamplifiers are linked together by diodes and bypass transistors, which are normally switched off. As shown in Fig. 5.12, the arrival of a large signal creates a

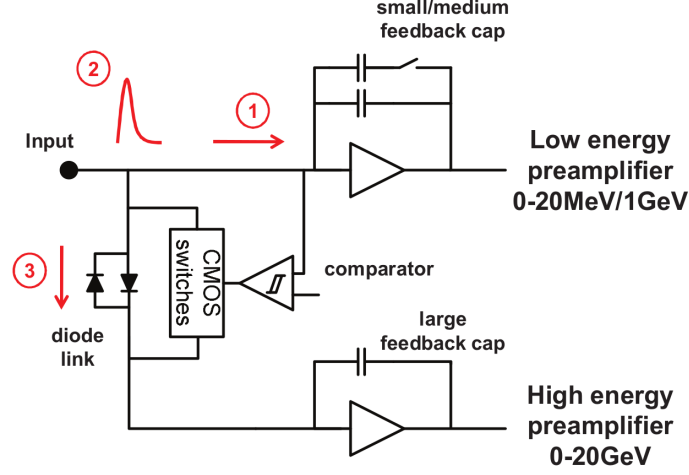


Figure 5.12.: Simplified diagram of the AIDA preamplifiers. Normally the low-energy preamplifier is the only one connected to the detector (1), when the deposited energy is over the input range, a saturation is caused (2) and the link to the high-energy preamplifier is activated (3). Taken from [101].

saturation of the low-energy amplifier and a fluctuation of the input voltage. The bypass transistors switch on, and the link diode is then biased to the high-energy amplifier, where the rest charge is integrated. The diode link between high-energy channel and low/medium-energy channel is bidirectional, so that the ASIC can operate with both input signal polarities for a flexible system.

The challenge for AIDA electronics is that after a few microseconds of the implantation the electronics should be reset and ready to record the decay events. However, this specification is not requested for the LYCCA setup in HISPEC. Thus, during LYCCA experiments a certain energy range of preamplifiers should be manually chosen and maintained in the control program.

The ASIC is optimized for a highly dynamic range with excellent linearity and noise performance. The schematic diagram of the functionality of a single AISC channel is shown in Fig. 5.13. The preamplifiers of high and low/medium gain differ in the feedback capacitor. The low-energy channel preamplifier has a selectable feedback capacitor of 0.7 pF or 35 pF for input range up to 20 MeV or 1 GeV,



## 5. Upgrade of LYCCA

respectively. The high-energy channel preamplifier has a 700 pF feedback capacitor for energies up to 20 GeV. Behind the preamplifiers, the shaper component is a CR-RC filter with selectable shaping time: from 0.5 to 8.5  $\mu$ s in 16 steps, which allows tracking of the optimum shaping time according to the ageing of the detector under radiation damage. Another feature of the ASIC is a special analogue output for each low/medium-energy channel. These outputs are intended for high-speed digitalization, bypassing the normal stages shaper  $\rightarrow$  peak-hold  $\rightarrow$  multiplexer. This way closely separated pulses on a single channel can be resolved. These outputs have high-speed buffers with a rise-time of about 10 ns, in order to preserve information about pulse shapes and timing. The link between the peak-hold and multiplexer circuits is managed by a control logic (cf. Fig. 5.13). Whenever a hit is detected and multiplexed to the analog output, the voltage stored in the peak-hold is accessed in sequence. The logic provides a 4-bit address of the hit channel and sets a flag to indicate the range of energy. Another function of the control logic is the handling of the reset of analogue circuits, which includes the CMOS bypass switches, preamplifier, shaper and peak-hold. The intention is to minimize the recovery time to a few microseconds.

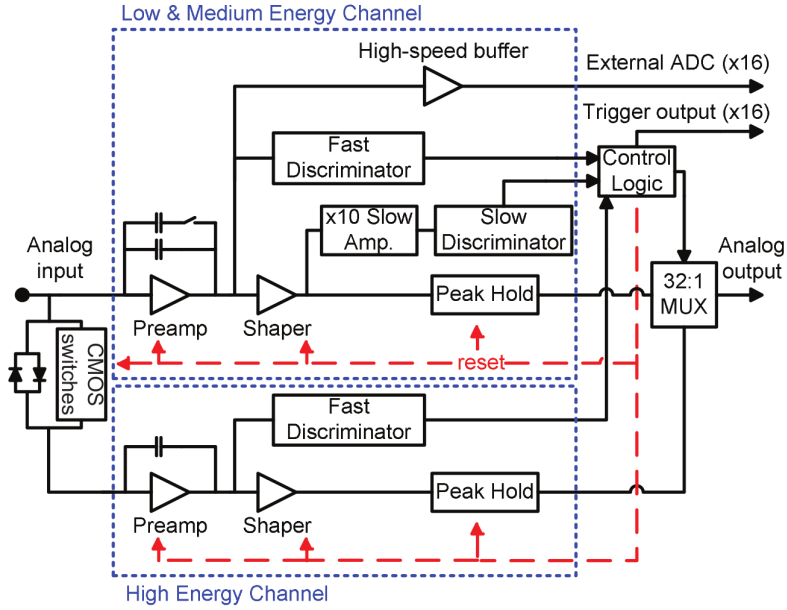


Figure 5.13.: Schematic diagram of the functionality of one ASIC channel. Taken from [101].

The ASIC has been fabricated in an AMS 0.35  $\mu$ m CMOS process. A considerable amount of the layout area is occupied by the feedback capacitors of the high-energy channel preamplifiers (700 pF per channel), where each capacitor has been laid out

## 5. Upgrade of LYCCA

as the sum of several smaller elements in parallel, with many contacts in place to improve the yield and reduce the equivalent series resistance.

### 5.2.2. Front End Electronics (FEE)

The FEE modules will interface the ASIC with the data acquisition software, providing facilities for control and event collection. The FEE consist of a number of unit modules. Each module contains sufficient equipment to support 4 ASICs and hence 64 detector channels. Signals from the ASIC are buffered and digitised by Analog Digital Converters (ADCs), and the digital data are processed by an Field Programmable Gate Array (FPGA). Data are transmitted from FEE by a Gbit Ethernet interface. The timing of events are based on the Bunch Timing System (BuTiS) distributed clock. A signal is provided for other parts of the experiment based on the "OR" for all channel discriminators within the ASICs. Communication with the FEE for data transfer and control use the Gbit Ethernet interface. The inputs to the FEE module comprise 64 connections to a LYCCA-DSSSD, while the outputs from the FEE module are blocks of time ordered events.

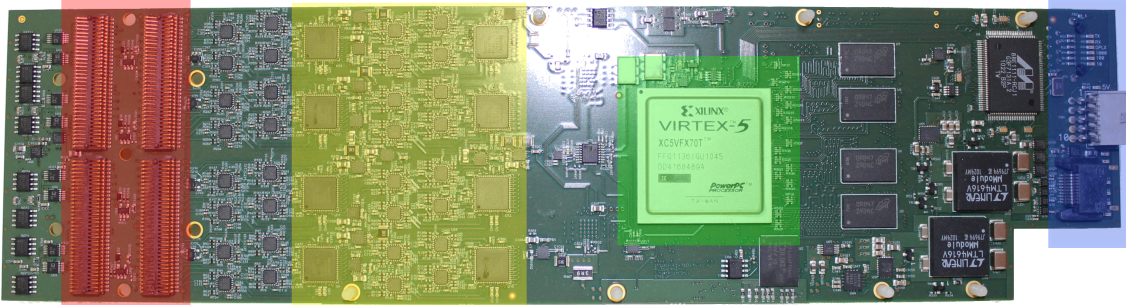


Figure 5.14.: View of a FPGA board. In red area four transition circuits are located, which connect to the mezzanine PCB of ASICs and transmit signals from ASIC to ADC. Eight octal 16-bit ADCs are located in the yellow area. In green area: Xilinx Virtex5 PowerPC for data processing. In blue area connectors are located at the end of FEE: HDMI (High Definition Multimedia Interface) connector (for Clock, SYNC and Reset), Power supply connector, Gbit Ethernet (for data transport) and JTAG (Join Test Action Group) connector (for DEBUG).

Figure 5.14 illustrates the inside view of a FPGA board, which occupies boards with an 8 cm maximum dimension at the interface with DSSSDs. The card is secured in a metal case and cooled with water. The FPGA board contains analogue buffers, ADCs, the clock interface, processor peripherals, connections for external interfaces and power supplies. One Xilinx Virtex5 PowerPC is used on each FEE module to

## 5. Upgrade of LYCCA

control and to collect events for four ASICs and to communicate with the acquisition computers. Each detector analogue readout channel is converted using an AD7686 16-bit ADC.

The FEE concept and ASIC to Data Acquisition (DAQ) block diagram are shown in Fig. 5.15. One ASIC acquisition and control unit requires 54 connections (cf. Fig. 5.15 left):

- I<sup>2</sup>C (Inter-Integrated Circuit) - bit serial register access route between FEE and ASIC. - 2 signals. Clock and bidirectional data.
- Channel discriminator output to create timestamps of activity. - 16 logic signals.
- Channel preamp outputs for digital signal processing. - 16 analogue signals with a single reference voltage.
- Discriminator OR - Low Voltage Differential Signaling (LVDS) to give 1 ns timing. - 2 signals.
- Multiplexed analogue - The output of the readout analog multiplexor. - 1 signal with reference.
- Readout information - Logic signals to indicate which channels on the multiplexed analogue allow handshaking between the ASIC control and the readout logic in the FPGA. 7 logic signals.
- Readout control - Controls the output of the multiplexed analogue. 4 signals including a RESET.
- Calibration register control - Logic signals to control the calibration connections in the ASIC. 3 logic and an analogue signal.

The data digitized by ADC will be transmitted to the PowerPC, where they are processed using VHDL (Very High Speed Integrated Circuit Hardware Description Language) functions (see right part of Fig. 5.15):

- MicroBlaze soft processor runs Linux to handle the data transfer to DAQ computers and for control of the FEE module.
- Detector analogue readout collects data from ASIC using the multiplexed analogue output and controls.
- Detector digital readout collects data from the waveforms digitized by the FADC for each channel and processes them using discriminator packages. Events are stored in intermediate memory and transferred to processor memory under control of a state machine.
- Timestamp is used to provide a time relationship between events, coordinated by the external clock system. Timestamps are queued in a FIFO (First In First Out) for each of the detector readout blocks and are used to generate event data.

## 5. Upgrade of LYCCA

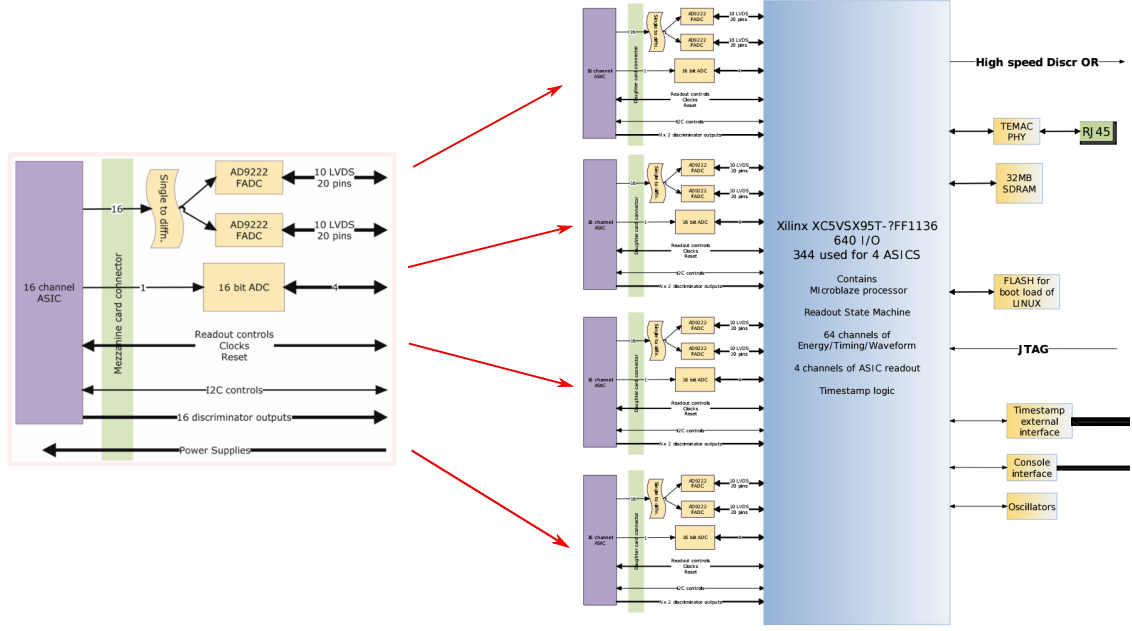


Figure 5.15.: Front End Electronics (FEE) concept. Left: Support connections and parts for one ASIC circuit; Right: ASIC to data acquisition block diagram for a complete FEE module. Taken from [102].

The Clock and SYNC (Synchronisation) signals are distributed using a HDMI cable format from a central resource module. The Discriminator OR signal from ASICs is sent using the same cable. Power supplies are derived from 24 V using a mixture of DC-DC converters and linear regulators. No high voltage on the module is required. Cooling of the FEE module is implemented using water-cooled metal and heat conducting material. The temperature of the FEE module should be maintained at 20°C to ensure moisture cannot condense on the electronics, and ASICs work under a safe temperature of up to 50°C.

### 5.2.3. Adapter Box

Since the FEE modules have a different interface and cannot directly connect to the vacuum feedthrough, adapter boards between them are required to transport signals from the p- and n-side of the DSSSD to the FEE module. As shown in Fig. 5.16, the adapter boards of the p- and n-side are connected through a cable bridge, which transports the signals from the DSSSD n-side to adapter board of the p-side, and then signals from the p- and n-side are fed into the four ASICs. Moreover, the adapter boards provide access to test signals, grounding as well as operating bias. Test signals (like generated pulser signals) can be given through the connections on p- and n-boards to check the performance of ASICs. The negative bias (HV)



## 5. Upgrade of LYCCA

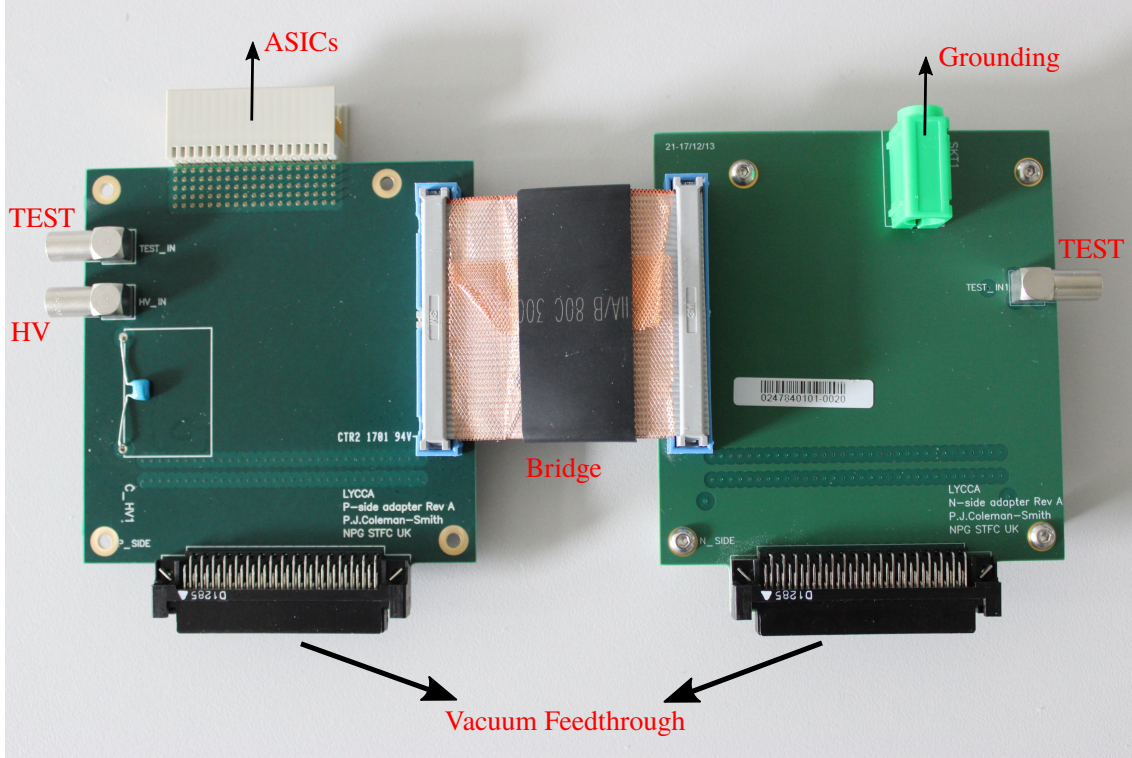


Figure 5.16.: Adapter boards of both p-side (left) and n-side (right).

is plugged on the connection of the p-board to operate the DSSSD. The bias and pulser signals are transported through LEMO cables. The green connection on the n-board provides individual grounding for each DSSSD.

### 5.2.4. Electronics System

The new electronic system for LYCCA was developed and tested in the STFC Daresbury Laboratory. Figure 5.17 illustrates the LYCCA setup in Daresbury. The FEE modules are installed through the adapter boxes on the LYCCA chamber. Cooling water is imported through the blue pipes and exported through the red pipes. On the right side, the main electronic control units are installed on a 19 inch rack server enclosure. The four power supply units (top), which support a maximum of 32 FEE modules, are controlled by a Relay unit (middle). A Raspberry Pi system connecting to the Relay unit through USB cable provides remote control via the web. Below the Relay unit there are MACB (Multi Application Correlation Box) NIM units. The purpose of the MACB is to allow a correlation with other DAQ systems and the LYCCA system to exchange signals to identify events as well as to distribute signals required by the FEE timestamping and to buffer the triggers from the ASICs.

## 5. Upgrade of LYCCA

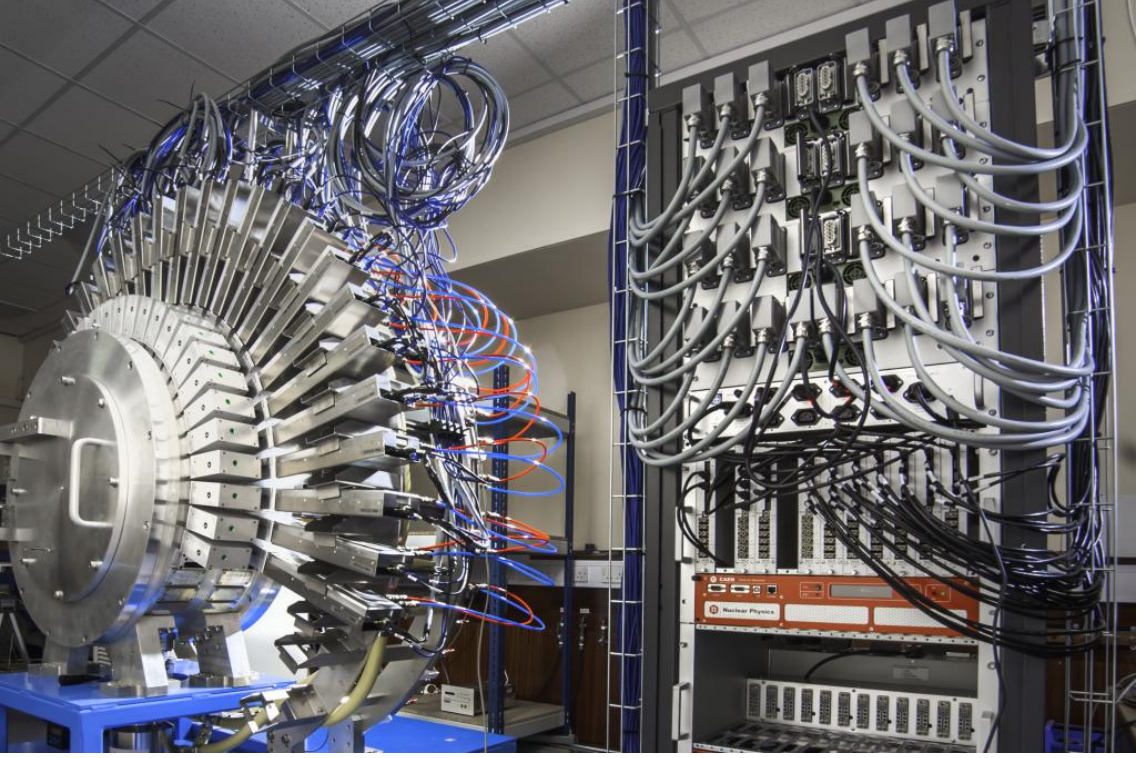


Figure 5.17.: View of LYCCA-electronic System in STFC Daresbury Laboratory.

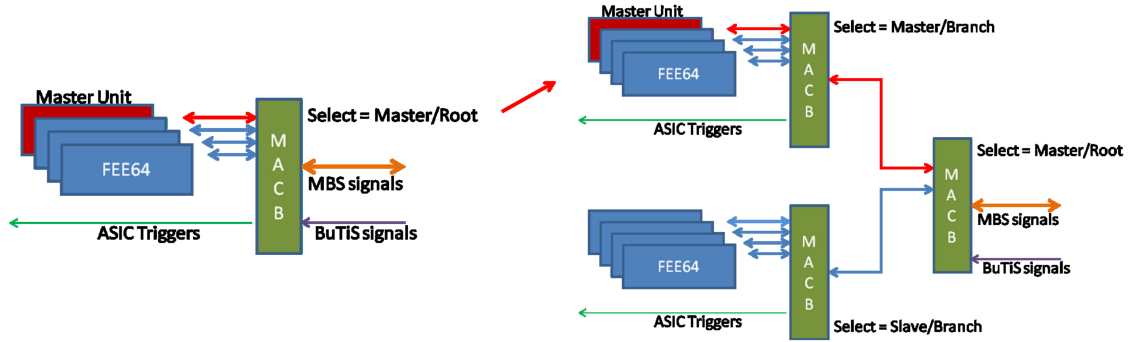


Figure 5.18.: Connection of MACB units. Left: Illustration shows the unit interconnections for four or less FEE modules; Right: Illustration shows the unit interconnections for five or more FEE modules. Note the master FEE module must always be connected through Port 1 of the Master selected MACB. Taken from [103].

The MACB unit can operate as an independent system generating its own 50 MHz clock or it can distribute an external clock. Furthermore, a MACB unit can operate not only as a stand-alone for a small number of FEEs, but also be extended as part of a gradation to operate with many FEEs. A MACB unit interfaces to up to 4 FEE modules as shown in Fig. 5.18 (left part). Larger numbers of FEE modules can be controlled by a branch structure of multiple MACB units interconnected by HDMI

## 5. Upgrade of LYCCA

type C cables (cf. Fig. 5.18 right part). Each MACB unit has 5 HDMI connectors, one of which connects to the next level up the gradation while the other four connect either to FEE modules or to MACB units lower in the gradation. Note that all FEE modules should be connected at the same level of gradation in order to match signal delays. The number of branches can be extended as far as necessary (in the LYCCA setup 3 levels were built to control up to 64 FEE modules). The MACB units can be configured in several different ways, depending on where they are in the gradation, whether they use the external clock or generate their own, and whether they are connected to an FEE Master or not.

An illustration of the front panel of MACB NIM unit is shown in Fig. 5.19. A 16 position rotary switch at the front panel determines the function of the module:

- Master/Slave for FEE Timestamping.
- External/MACB for Clock source.
- Root/Branch for the interconnection gradation.
- Correlation DAQ for the isolated Fast NIM signals.

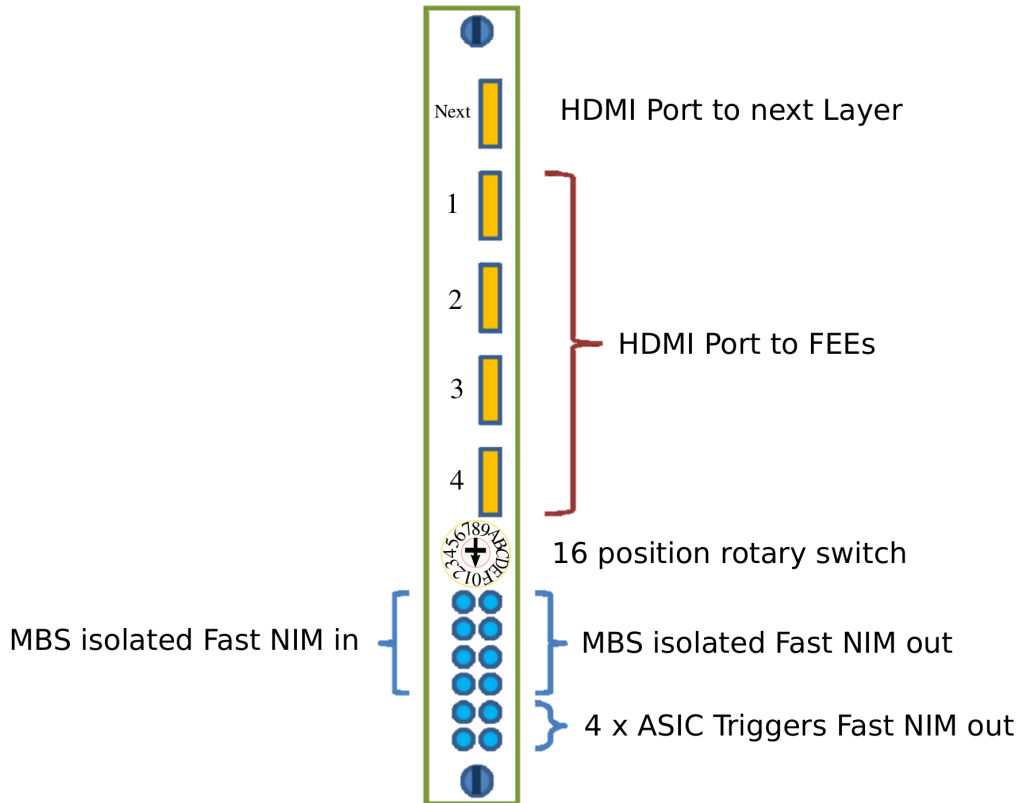


Figure 5.19.: Illustration of the front panel of the MACB NIM unit.

There are some important definitions used in the configurations:

## 5. Upgrade of LYCCA

**Master** - HDMI port 1 is connected to the Master FEE module, which generates SYNC pulses for the whole system, using the internal 50 MHz Clock. Port 1 FEE module generates the SYNC and receives it again at the same time.

**Slave** - Not operating in Master mode, so all 4 HDMI ports behave the same.

**Root** - Top level of gradation, provides all Clock and SYNC signals.

**Branch** - Lower level of gradation, receives and passes on all Clock and SYNC signals.

All FEE modules will be connected through Gbit Ethernet cables to LYCCA-Server, which uses the Multi-Instance Data-Acquisition System (MIDAS) to realize system control and DAQ. MIDAS also provides the functions hardware setup, FEE temperature monitoring, timestamp control, system-wide check, experiment control data merging and data storage. The stored data is sorted event by event and analysed using the data analysis framework ROOT.

### 5.3. Mechanics

In the PreSPEC campaign as well as the future HISPEC campaign the  $\Delta E - E$  telescopes are placed in the specially designed LYCCA chamber, which was developed and manufactured at the mechanical workshop of IKP, Cologne (see Fig. 5.20). The mechanical construction is compatible with the final LYCCA setup and can flexibly be placed at any suitable position along the Super-FRS and HISPEC beamlines. The LYCCA chamber is based on a cylindrical vacuum vessel, which has a diameter of 800 mm and a depth of 400 mm. The front side has an open circular entrance with a diameter of 450 mm for the incoming particles. The front flange is designed to house the plastic ToF stop detector, and to provide 64 feedthroughs for high voltage and signals of the photomultiplier tubes of the scintillator detector. Up to 72 vacuum feedthroughs for DSSSDs and CsI signal cables can be installed. In order to support a maximum of 26  $\Delta E - E$  telescopes, a holding structure was mounted inside the chamber (cf. Fig. 5.20 right), which can host the anticipated 26 telescopes in five rows of 4, 6, 6, 6 and 4 telescopes, respectively. The design of the holding structure allows the removal and replacement of single telescopes and offers the flexibility to place telescopes in different arrangements.

After the upgrade of the electronics in order to hold the heavy FEE modules and to supply the cooling water, a new holding structure in horseshoe form surrounding the LYCCA chamber was developed and manufactured at STFC Daresbury Laboratory, as shown in Fig. 5.21. The cooling water coming from a chiller will be cycled in the pipes to ensure that all FEE modules work below the safe temperature.



## 5. Upgrade of LYCCA

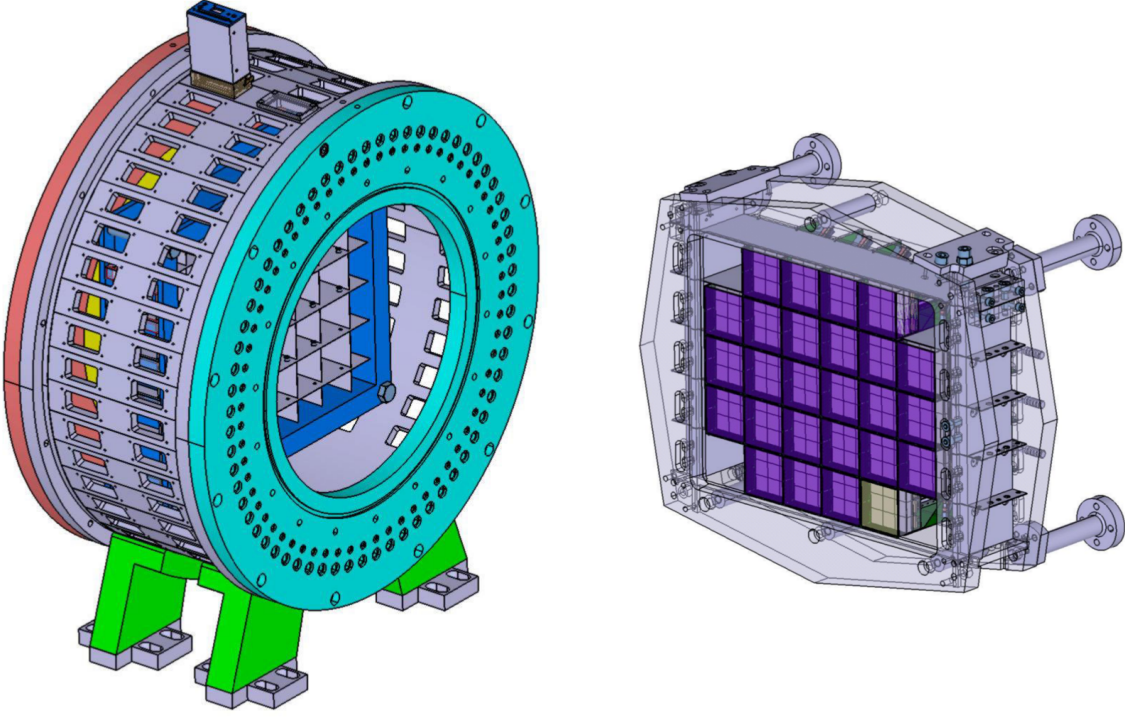


Figure 5.20.: Technical drawing of LYCCA chamber. Left: front view of LYCCA chamber with holding structure inside. Right: front view of holding structure equipped with detectors. Taken from [85].

Since 2016 the LYCCA setup is located at the Cologne tandem accelerator, preparing for the future HISPEC campaign in GSI. In order to match the accelerator and to do in-beam commissioning test, a new three-stage beam tube was built for LYCCA, which allows three different distances of 700 mm, 950 mm and 1200 mm between the target position and the DSSSD wall. Thus, the corresponding opening angles range from  $1.5^\circ$  to maximally  $14.5^\circ$ . The technical drawing of the new beam tube with LYCCA chamber is illustrated in Fig. 5.22. The three-stage beam tube and the LYCCA chamber contain a huge volume. In order to obtain a satisfying vacuum the volume is pumped by one tube molecular pump. After a sufficient pumping time the vacuum inside the chamber is measured to be better than  $2 \times 10^{-6}$  mbar. Currently 25 FEE modules and 14  $\Delta E - E$  telescopes are installed within the LYCCA chamber. The complete LYCCA setup at IKP Cologne is shown in Fig. 5.23.

## 5. Upgrade of LYCCA

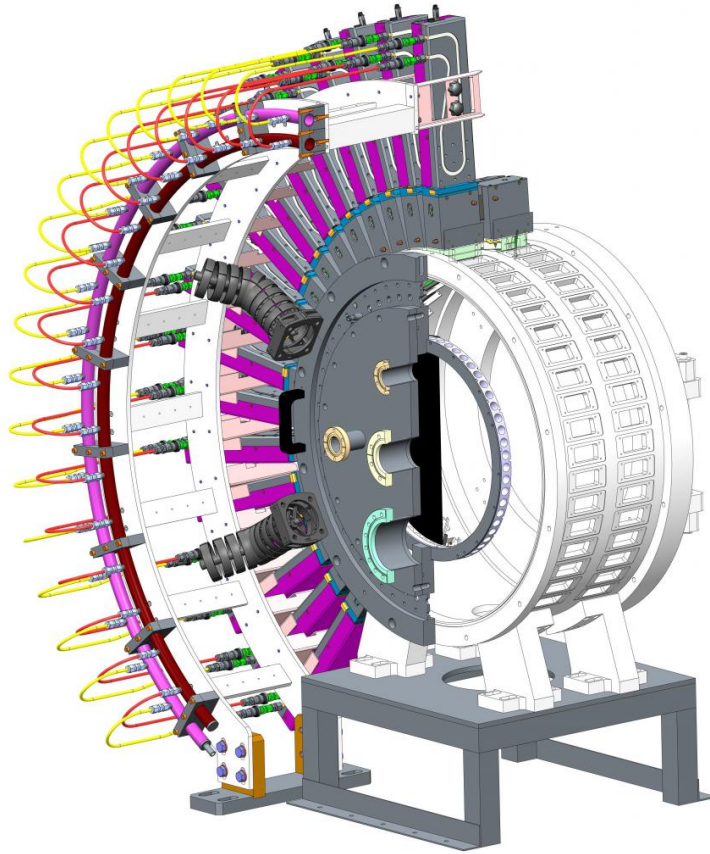


Figure 5.21.: Technical drawing of the new mechanical structure of the LYCCA chamber. The horseshoe-form structure hosts the FEE modules and provides cooling water to each FEE module. Taken from [104].

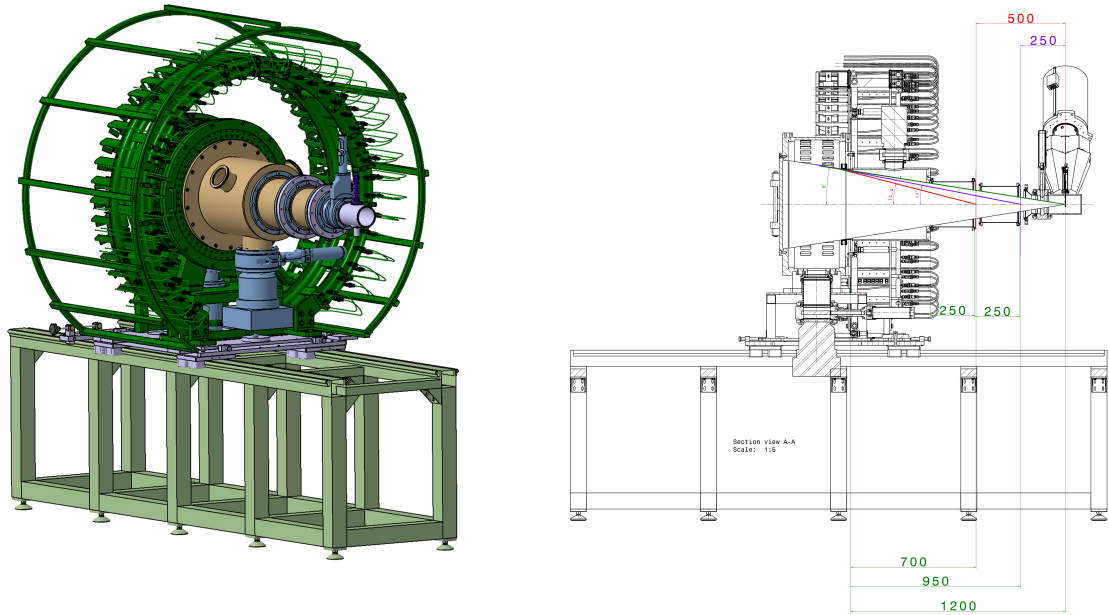


Figure 5.22.: Illustration of the LYCCA chamber with the new beam pipe. Left: front view; Right: side view. Taken from [104].

## 5. Upgrade of LYCCA

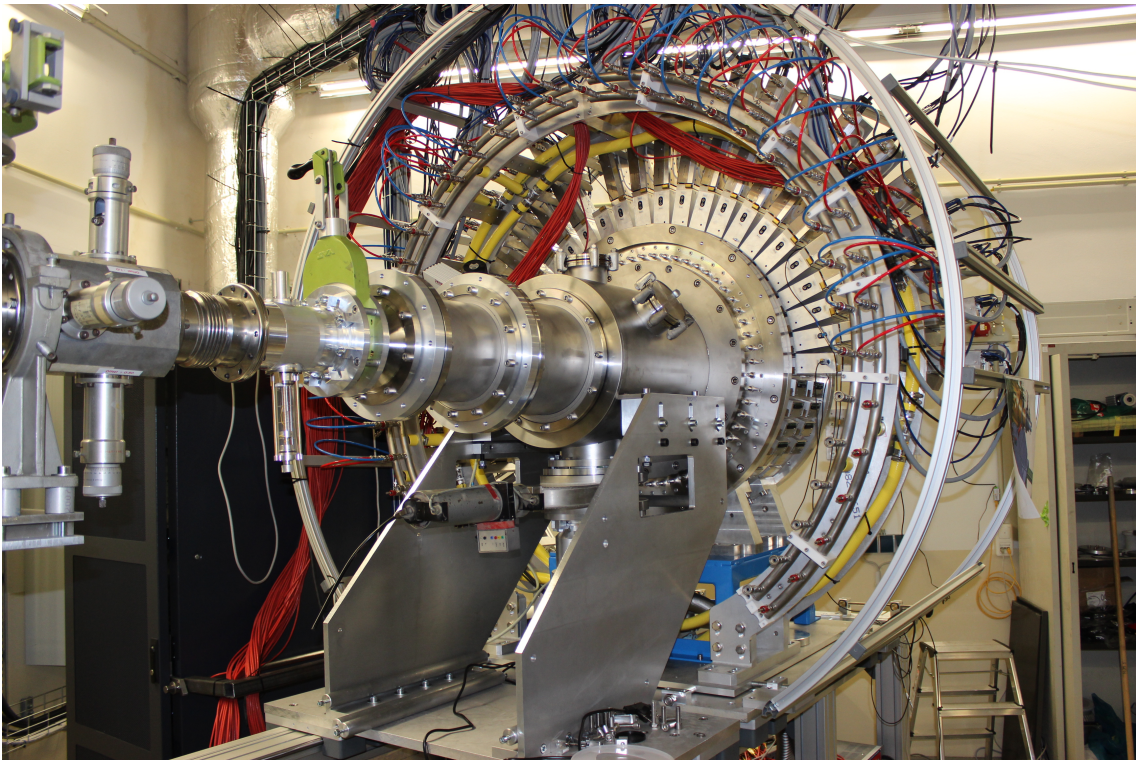


Figure 5.23.: Complete LYCCA setup at IKP Cologne.

## 6. Commissioning of LYCCA

### 6.1. Test of ASICs

After the mounting of the LYCCA system at IKP Cologne, a series of commissioning measurements were carried out to determine the performance of electronics and detectors.

To perform measurements, the control surface of LYCCA is called up in a web browser starting with the address: "localhost:8015". Using the Web Services Description Language (WSDL), the control surface provides numerous options to setup and control the LYCCA system. There are three major options to control a experi-



Figure 6.1.: LYCCA Experiment Control window.

ment, as shown in Fig. 6.1:

- AIDA Hardware Control, which contains comprehensive options to configure the hardware, to setup parameters, to monitor the system as well as to reload/reset the settings (see Fig. 6.2).
- Data Acquisition Run Control, where each FEE module (except Master FEE *nnlycca1*) can be individually chosen to join a test. Starting the DAQ Run Control, the Timestamp ReSYNC will also be checked. If the ReSYNC fails then, one can still use the option "Perform Timestamp ReSYNC" under "AIDA Hardware Control" to synchronize the timestamp (cf. Fig. 6.2).



## 6. Commissioning of LYCCA

- Histogram Browser, where the spectrum of each ASIC channel of an experiment is shown and analysed online.

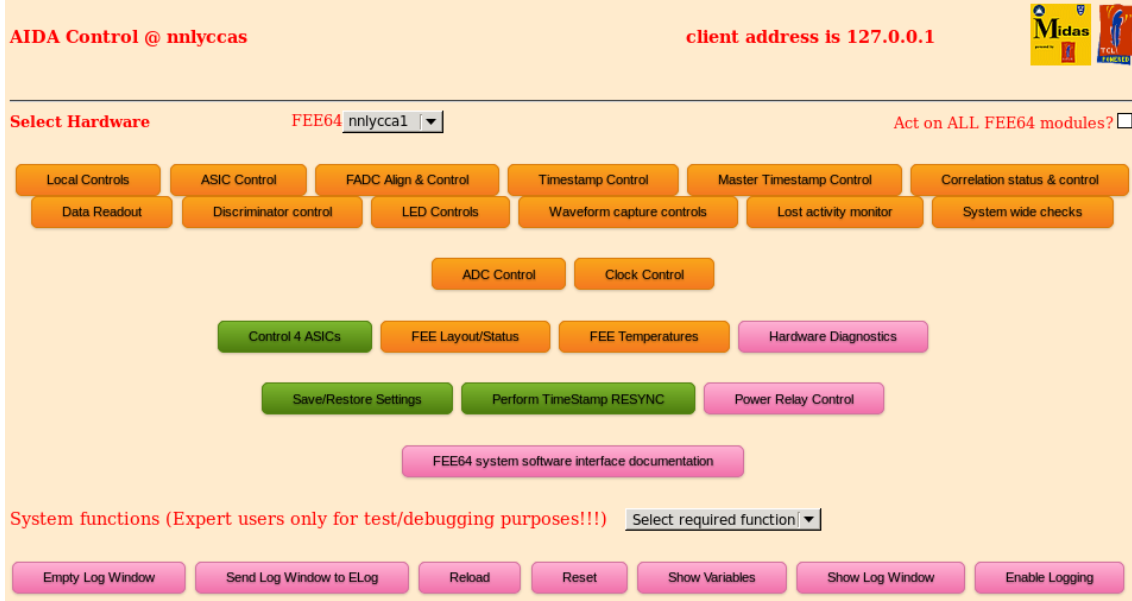


Figure 6.2.: Options under the AIDA Hardware Control. The most useful options are marked in green.

Starting the DAQ, first of all one has to ensure that the Clocks are synchronized for all FEE modules operated in the experiment, and the temperatures of the ASICs are in the safe range. To meet the first condition, the Master/Root signal from MACB should be always input in the previously designated Master FEE module (here called module *nnlycca1*), which needs to be operated by each experiment. Figure 6.3 shows the server states of a correctly started DAQ Run, operating 10 FEE modules. The information regarding the ReSYNC performance indicates, that the ReSYNC of timestamp for all FEE is successful. "H" next to the module number means that the histogram is enabled, while "X" means that the data transfer is enabled.

The hardware temperatures are monitored through the option "FEE Temperatures" under "AIDA Hardware Control". As shown in Fig. 6.4, the temperatures of the Virtex PowerPC, the Power Supply Unit (PSU) and the ASICs of each FEE module can be observed and plotted. If one of the three temperatures is 10% higher than the allowed maximum, this module will shut down automatically.

The next step is to carry out the configuration of the ASICs. Using the option "Control 4 ASICs" under "AIDA Hardware Control" (cf. Fig. 6.2), the parameters of ASICs will be set up, as demonstrated in Fig. 6.5. Firstly, the polarity of the preamplifier of the ASICs should be determined. Since ASIC1 and ASIC2 are connected to the n-side of DSSSD, while ASIC3 and ASIC4 are connected to the

## 6. Commissioning of LYCCA

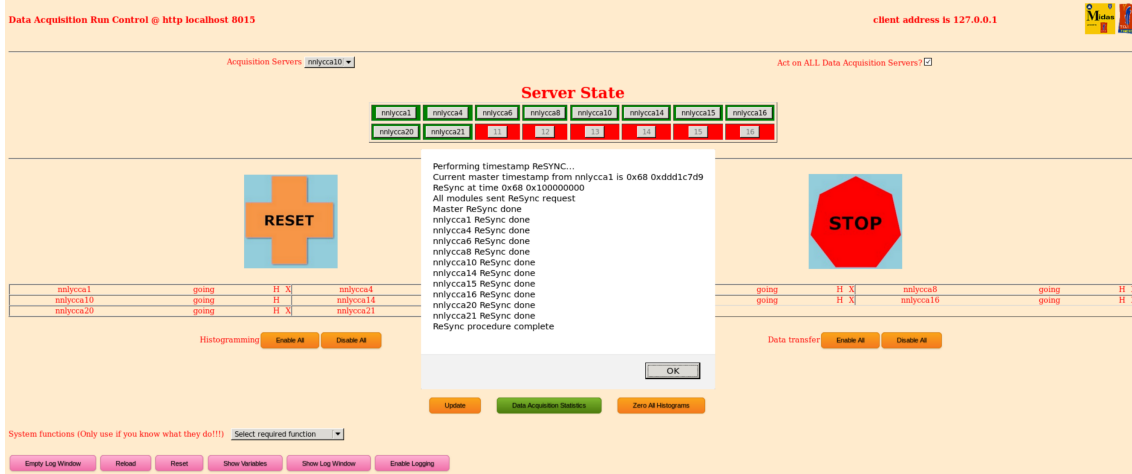


Figure 6.3.: Example of a correctly started DAQ Run. Each operated FEE module can be individually started/stopped, with or without Data transfer service.

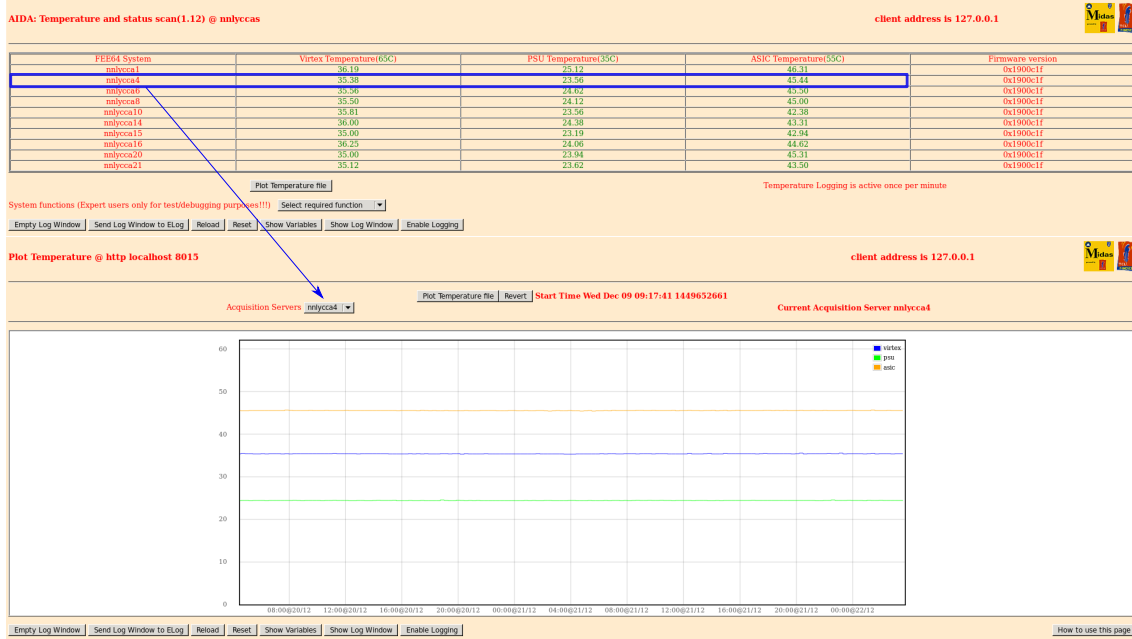


Figure 6.4.: Monitoring of hardware temperatures. The plot of temperatures based on the timeline can be performed for every FEE module. The spectrum in green indicates the temperature of Power Supply Unit (PSU), in blue the temperature of Virtex PowerPC, in yellow the temperature of ASICs.

p-side, in a measurement with detectors the polarity of ASIC1 and ASIC2 are set to "negative", while the polarity of ASIC3 and ASIC4 are set to "positive", to match the collection of charge carriers. In a test using a pulser signal without connection to DSSSDs, the polarity of all ASICs can be generally set to "positive" or "negative" to match the pulse polarity. Depending on the measurements the energy range of

## 6. Commissioning of LYCCA

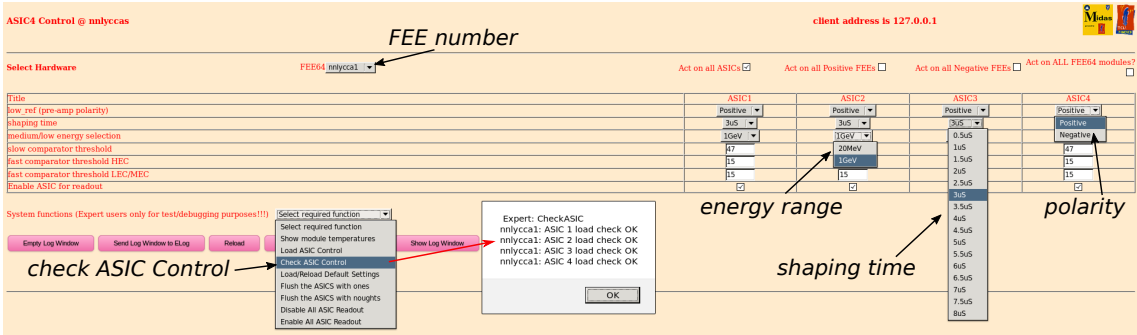


Figure 6.5.: View of the Configuration of ASICs. The polarity, energy range, shaping time as well as thresholds can be set up.

the preamplifiers has to set to low energy (up to 20 MeV) or medium energy (up to 1 GeV). Currently, the option for the high energy range (up to 20 GeV) is not active for LYCCA. For shaping time 16 values between 0.5  $\mu$ s and 8.0  $\mu$ s can be chosen. For certain experiments one needs to find the optimized shaping time. The values of slow/fast comparator threshold need also to be determined depending on the measurements to minimize the electrical noise. There are several system functions to control the ASICs. The most important function is "Check ASIC Control", which checks the status of each ASIC and gives a performance report. At the start of any measurement, the function "Check ASIC Control" should be carried out. If all of the ASIC channels are successfully checked, one can open the "Histogram Browser" to observe the online spectra of measurements. Opening the four statistics windows, as shown in Fig. 6.6, one can check the performance of all 4 ASICs of one FEE module. If some channels are missing, one needs to repeat the process "Check ASIC Control" to ensure that all ASIC channels are active in the measurement.

If one wants to store the measured data for later offline analysis, the options "MERGE Control" and "Tape Service" under the address "localhost:8115" should be called up. Figure 6.7 shows the control surface of the "MERGE" option, with 10 FEE modules active in DAQ. Every FEE module can be individually chosen to be included or excluded in the DAQ.

In order to check the performance of the FEE modules without connection to the DSSSDs, a Canberra 814FP Pulser was used to simulate the output signals from silicon detectors. The 814FP Pulser provides a tail pulse with a range of 0 to  $\pm 5$  volts terminated into 50 ohms, and a rise time smaller than 30 ns, which is in the same range as the time for charge collection in DSSSD. Combined with the exponentially decaying voltage, the waveform of the DSSSD signals will be reproduced in a good approximation. For the 1 GeV range of preamplifier, taking pulse signals from 1 to

## 6. Commissioning of LYCCA



Figure 6.6.: View of statistics of four ASICs with Pulser signal. In the top two windows the Hit and HitRate of each ASIC channel are indicated, where n-side signals correspond channel 0 – 15 from ASIC1 and 16 – 31 from ASIC2, while p-side signals correspond channel 32 – 47 from ASIC3 and 48 – 63 from ASIC4. The total Rate and Stat are shown in the two bottom windows. The empty areas correspond high energy range statistics, which are not active in the current LYCCA setup.

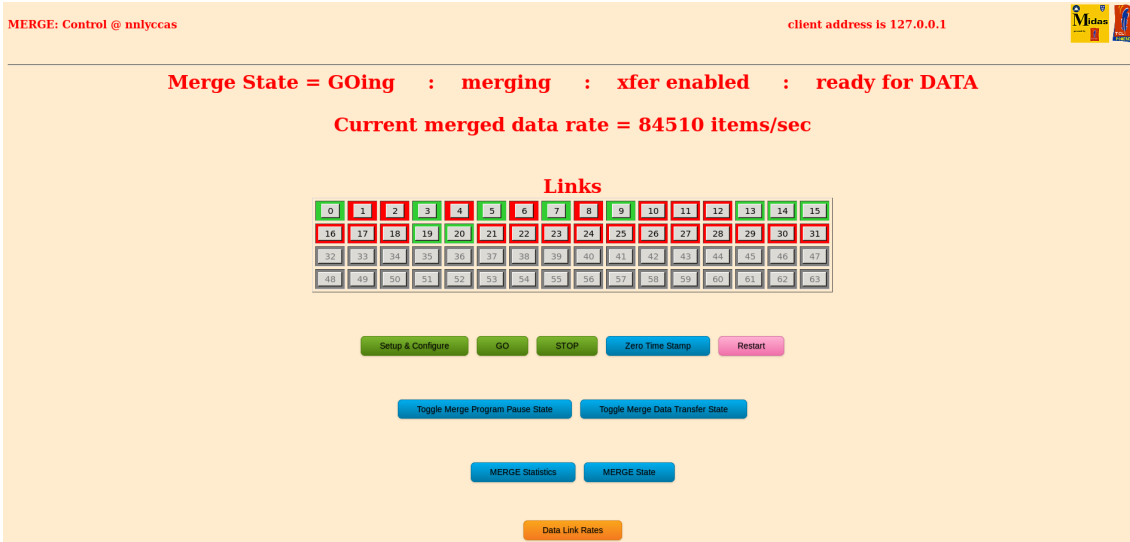


Figure 6.7.: View of MERGE Control for LYCCA setup. Module number in green means the FEE is active in DAQ. The "current merged data rate" indicates not only the measured data, but also the clock informations.

## 6. Commissioning of LYCCA

5 volt with 1 V step for both positive and negative polarities the test results are shown in Table 6.1 and Fig. 6.8.

Table 6.1.: Test result using pulse signal from +5 volt to −5 volt with 1 V step. The intensity and resolution are obtained using fitting with a Gauss function. Linearity is observed for positive as well as negative pulse signals.

Pulse Height [V]	Peak Position	Intensity	FWHM [chn.]
+5	30019	33089	7.47
+4	30538	32945	7.57
+3	31061	35593	7.64
+2	31594	33229	7.80
+1	32104	33107	7.86
−1	33106	32892	8.74
−2	33623	35028	8.67
−3	34154	35210	8.54
−4	34680	32813	8.50
−5	35196	35045	8.52

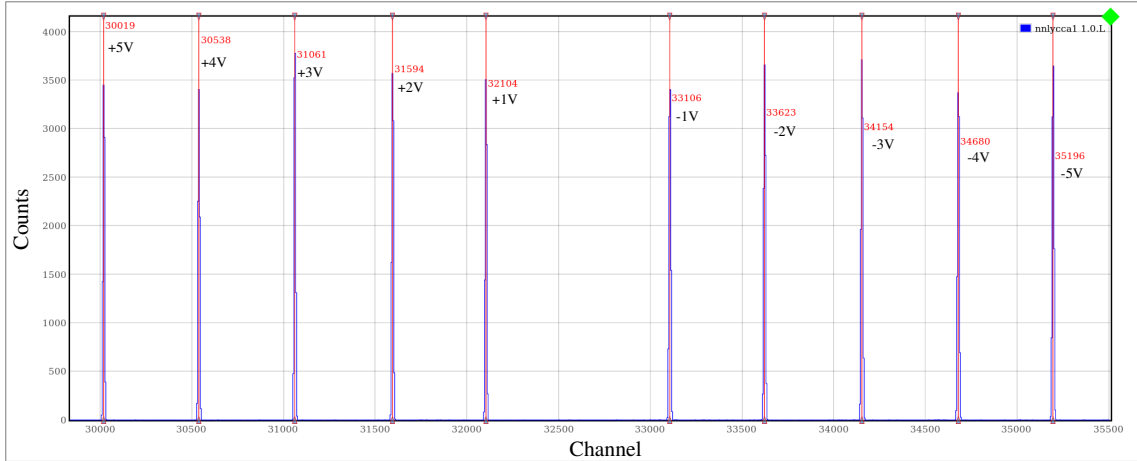


Figure 6.8.: Spectra of pulser test. Pulse signals from +5 volt to −5 volt with 1 V/step were measured for the 1 GeV energy range. The peak positions (in red) are determined using the "peak find" online function.

Note here the LYCCA spectrum service has a special structure of display. The X-axis range from 0 to 65535 corresponds to the incoming signals from positive maximum (around channel 0) to negative maximum (around channel 65535), with the zero "0" point on channel 32768, which can vary in different measurements. The result of the pulser measurement gives a linear channel assignment of the input voltage. Fitting the points with a linear function, one gets a slope of  $-1.92(3) \times 10^{-3}$  V/chn. The resolution of the electronics is obtained using Gauss-function, and the FWHM (Full Width at Half Maximum) is around 7.60 chn for the p-side (ASIC3 & ASIC4) and

8.50 chn for the n-side (ASIC1 & ASIC2). FWHM is generally improved for signals with increasing pulse height (cf. Table. 6.1). Using the same setup the resolution of all installed FEE modules were measured. The resolution (FWHM) is consistently around 7.60 chn for positive polarity and 8.50 chn for negative polarity electronic test pulses.

## 6.2. Triple-alpha measurement with DSSSD

### 6.2.1. Energy Resolution

In order to investigate the performance of the FEE modules working together with the DSSSDs, measurements with a triple-alpha source were carried out using the new LYCCA setup. The energies, activities and half-lives of the employed triple-alpha source are indicated in Table 6.2. For the triple-alpha measurement the high-gain preamplifier (up to 20 MeV) had to be used.

Table 6.2.: Information of the employed triple-alpha source.

Radionuclide	$\alpha$ Energy [MeV]	Intensity [%]	Half-life [yr]	Activity [100%]
$^{239}\text{Pu}$	5.105	11.5	$2.4 \times 10^4$	1
	5.143	15.1		
	5.155	73.4		
$^{241}\text{Am}$	5.388	1.4	432.20	0.92
	5.443	12.8		
	5.486	85.2		
$^{244}\text{Cm}$	5.763	23.3	18.1	0.78
	5.805	76.7		

In order to measure the triple-alpha spectrum using all installed 14 DSSSDs, the radioactive source was placed in a distance of around 20 cm centrally, with the source front side against the DSSSD-wall. The location of the 14 installed telescopes is illustrated in Fig. 6.9. With this setup the minimum incident angle of  $\alpha$  particles on telescopes  $T5$  and  $T24$  is about  $8.5^\circ$ , while the maximum incident angle on  $T13$  and  $T26$  is about  $45^\circ$ . Using the programs LISE++ [65] and SRIM [105] the range of alpha particles in Silicon detector was calculated. The alpha particles with kinetic energy of 5155, 5486 and 5805 keV are stopped in DSSSD at  $T5$  at a maximum after 24.94(21), 27.30(24) and 30.07(25)  $\mu\text{m}$ , respectively. The ranges of  $\alpha$  particles in DSSSD at  $T13$  was 18.01(53), 19.78(47) and 21.48(42)  $\mu\text{m}$ , respectively. Considering that the LYCCA-DSSSDs have a thickness of about 300  $\mu\text{m}$ , the range of alpha particles is smaller than 1/10 of the detector thickness. Since the charge

## 6. Commissioning of LYCCA

collection of electrons needs to go through the long drift distance to reach the n-side, the resolution of the n-side electronics (ASIC1 & ASIC2) is generally worse than the p-side (ASIC3 & ASIC4) due to the re-combination of charge carriers. To improve the resolution of the n-side the operating voltage of 65 V from Mesytec MHV-4 High Voltage Supply was set on all DSSSDs. During the measurement the leakage currents of DSSSDs were observed through MHV-4 modules. The minimum leakage current was observed on  $T2$  of  $0.4 \mu\text{A}$ , while the maximum leakage current was observed on  $T23$  of  $2.7 \mu\text{A}$ . The measured data were calibrated and analysed using the programs ROOT [106] and HDTV [107]. As an example the analysis for  $T5$  will be shown as follows.

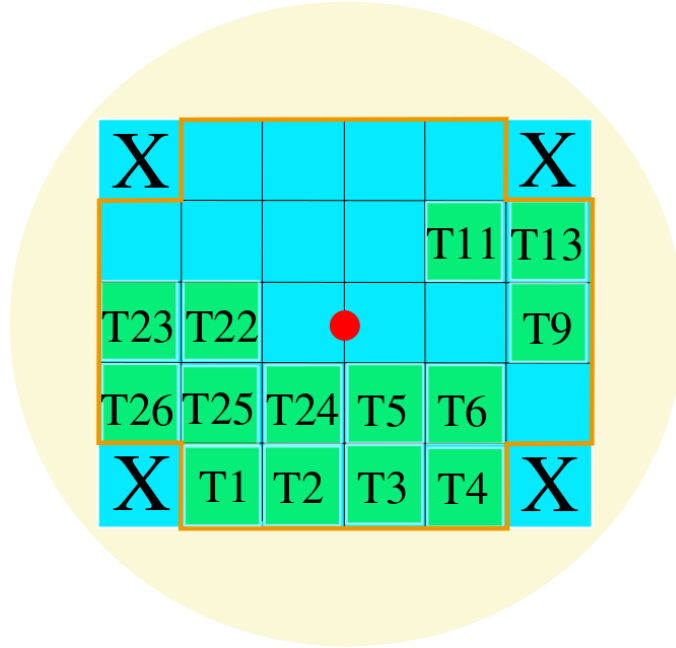


Figure 6.9.: Illustration of the location of the 14 installed telescopes inside the LYCCA chamber. A triple-alpha source is located 20 mm in front of the DSSSD-wall. The red point indicates the center of beam axis.

Figure 6.10 shows the calibrated energy spectra of DSSSD from a p-side strip (red) and n-side strip (blue) of DSSSD  $T5$  with the alpha source. At 5.8 MeV the energy resolution ( $\Delta E/E$ ) of p-side strips is about 1.12% (FWHM  $\sim 65$  keV), and of n-side strips, about 1.19% (FWHM  $\sim 70$  keV). This resolution was caused by the asymmetry of the peak form with a left tail, which corresponds to the multi-transitions of nuclei as shown in Table 6.2. To investigate the fine understructure the energy spectrum was fitted using the program HDTV under the condition that the double Gauss peaks have the same peak width and will be fitted simultaneously. The results of decomposition are shown in Table 6.3 and Fig. 6.11.

## 6. Commissioning of LYCCA

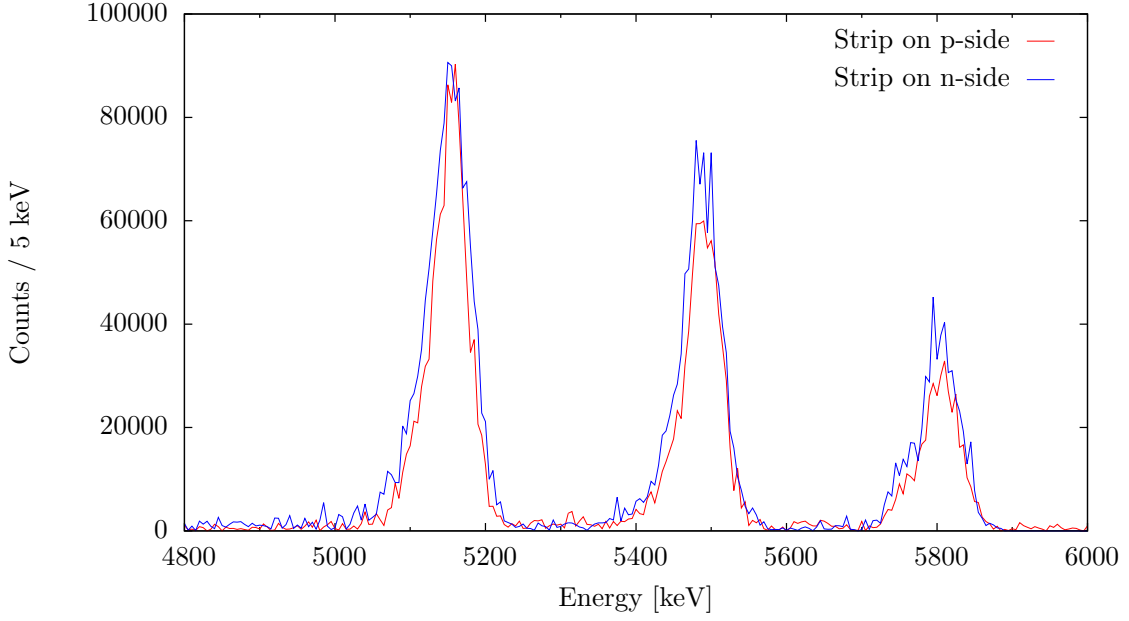


Figure 6.10.: Energy spectra of DSSSD from p-side strip (red) and n-side strip (blue) with a triple Alpha source ( $\frac{\Delta E}{E} \sim 1.1\%$  by 5.80 MeV).

Table 6.3.: Decomposition of the triple-alpha spectrum.

$\alpha$ Energy [keV]	Position [keV]	Volume [ $10^6$ ]	Int. ratio [%]	FWHM [keV]
5105	5102.38(12)	0.857(4)	13.68	54.52(5)
5155	5153.22(6)	6.263(7)	100	54.52(5)
5443	5417.28(32)	0.568(4)	11.05	56.23(6)
5486	5486.85(4)	5.142(6)	100	56.23(6)
5763	5759.35(11)	0.632(5)	29.65	49.33(10)
5805	5807.08(7)	2.131(6)	100	49.33(10)

For  $\alpha$  transitions of  $^{239}\text{Pu}$  the energies of  $\alpha$  particles at 5143 and 5155 keV are no longer separable due to the too small difference, thus HDTV fitted the two peaks as one. The intensity ratio for 5105 : 5155(+5143) of around 13.7% reproduced the literature ratio (13%) with good agreement. For  $\alpha$  transitions of  $^{244}\text{Cm}$ , the double-fit process has found the two peaks at the right positions. The intensity ratio of 5763 : 5805 reproduced the literature value of about 30%. However, the fitting process for  $\alpha$  transitions of  $^{241}\text{Am}$  was not satisfying: the peak position at 5443 keV cannot be found, and the error is more than 20 keV. Also the intensity ratio was not reproduced.

Using the double-fit process the fine understructure of the triple-alpha spectrum was decomposed. This way the energy resolution at 5.8 MeV was improved from 1.1% to about 0.8%. Compared to the other two fitting processes, the energy resolu-



## 6. Commissioning of LYCCA

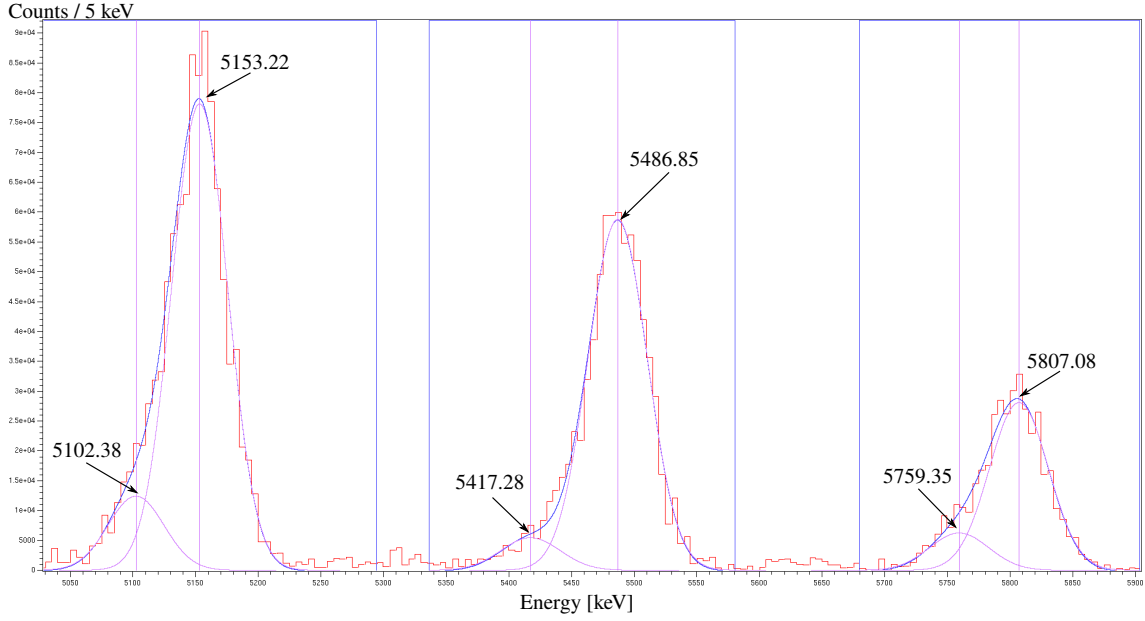


Figure 6.11.: Decomposition of the triple-alpha spectrum. Using the double-fit condition that the two peaks have the same FWHM, the triple-alpha peaks with left tail were decomposed into two Gauss peaks.

tion around 5.4 MeV is worse, while it should be better than the FWHM at 5.1 MeV. Repeating the same fitting process for all operated DSSSDs, the energy resolution and performance of every DSSSD strip as well as ASIC channel were investigated. A two-dimensional plot of  $\alpha$  energy to ASIC channel number, as shown in Fig. 6.12, illustrates the global overview of the results, where the combinations of 14 detector + FEE modules are indicated. Since currently for 25 installed FEE modules only 14 DSSSDs are available, during this measurement there are 9 not active FEE modules, which corresponds to the empty areas in the plot. The X-axis (channel number) is arranged according to FEE modules from *nnlycca1* to *nnlycca26* (module *nnlycca12* not installed), where the first 32 channels from ASIC1 & ASIC2 of each FEE module are connected to the n-side, and the second 32 channels from ASIC3 & ASIC4, to the p-side of DSSSD. Most of the operated DSSSDs and FEE modules worked normally as expected. Only the ASIC4 of module *nnlycca17* (*N17*) and several other single ASIC channels were during the measurement not working and the data readout was disabled. Overall 876 from total 896 ( $\sim 98\%$ ) DSSSD+FEE channels were tested successfully. The energy resolution of all tested channels at 5.8 MeV is consistent with FWHM  $\sim 65$  keV for the p-side and FWHM  $\sim 70$  keV for the n-side. Only the p-side of *nnlycca23* (*N23+T23*) showed that the resolutions are 10% worse than n-side. After changing the data cable of this p-side, this combination works as expected, too.

## 6. Commissioning of LYCCA

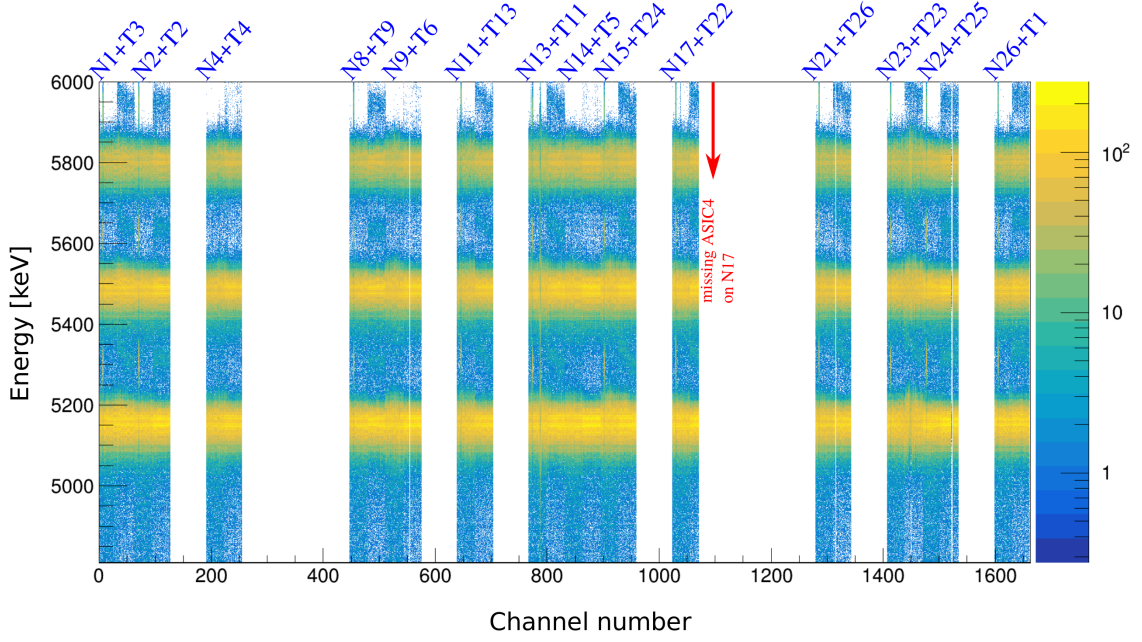


Figure 6.12.: Two-dimension plot of  $\alpha$  energy to ASIC channels. The combinations of DSSSD+FEE are indicated in blue (N: *nnlycca*; T: *telescope*). The channel number is arranged according to FEE modules (from *N1* to *N26*). The empty areas correspond to the FEE modules, which are not operated in this measurement. Around 98% channels are tested successfully. The ASIC4 of *N7* was crashed during the measurement.

Note that for most DSSSDs (11 from 14) events are detected on the p-side with energies higher than 5.8 MeV. This unusual effect is caused by the missing dead layer on the p-side surface of DSSSDs. If one takes a closer look at Fig. 5.4 and the datasheet (Table 5.1), the dark marks on the p-side correspond to the missing dead layer of  $\text{Al}_2\text{O}_3$  in a thickness of about  $0.55 \mu\text{m}$ . Using LISE++ [65] the energy loss of  $\alpha$  particles in  $0.55 \mu\text{m}$   $\text{Al}_2\text{O}_3$  can be calculated:  $\Delta E = 147 \text{ keV}$  ( $E_\alpha = 5155 \text{ keV}$ ),  $\Delta E = 140 \text{ keV}$  ( $E_\alpha = 5486 \text{ keV}$ ), and  $\Delta E = 134 \text{ keV}$  ( $E_\alpha = 5805 \text{ keV}$ ). In the dark areas incident  $\alpha$  particles deposit kinetic energy without additional energy loss in the dead layer. Since the energy calibration has been carried out for  $\alpha$  particles going through the dead layer, second peaks with higher energy are found. Figure 6.13 illustrates the double-peak structure on the p-side (Front5) and n-side (Back6 & Back7) strips. The area without dead layer on each p-side strip has a length of about 1.40 mm, corresponding to  $\sim 2\%$  of the total surface of the strip. On the n-side the area without dead layer corresponds to strip Back6 and Back7, with around 0.72 mm and 0.46 mm respectively, and the rest on the interstrip area. The location of this area without dead layer has been determined by means of the intensity ratio fitted from the double peaks (cf. Fig. 6.13).

## 6. Commissioning of LYCCA

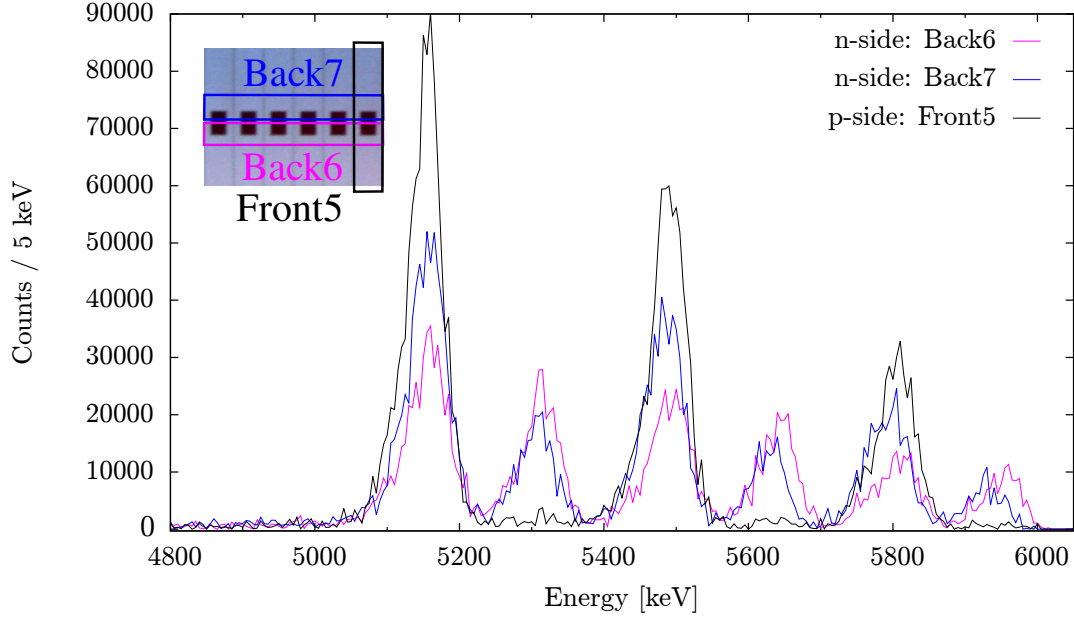


Figure 6.13.: Illustration of the double-peak structure on n-side strip Back6(in violet) and Back7 (in blue). As a comparison the p-side strip Front5 (in black) is plotted.

Although the area without dead layer on the p-side of DSSSD is only around 2% of the total surface, its influence cannot be ignored. For high energetic incident ions the energy loss in the dead layer is very small, so that these events will cause a right tail at the full energy peaks, which makes the resolution worse. Through a segment analysis the events in the dark area can be removed and one can get a spectrum without contribution from strip Back6 and Back7. The correction of the energy spectrum is shown in Fig. 6.14.

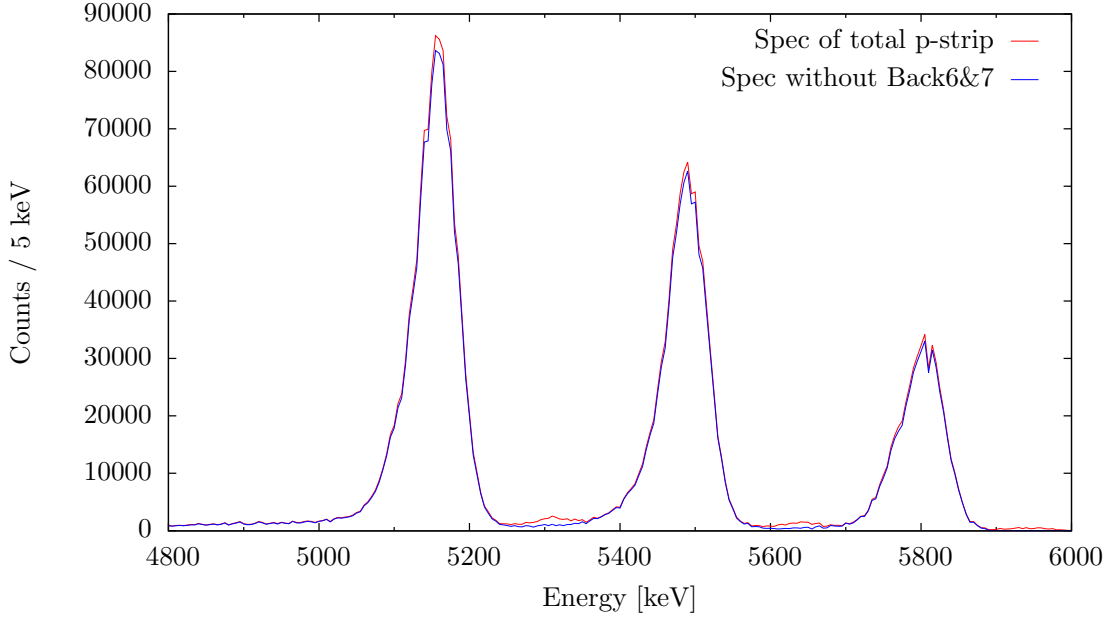


Figure 6.14.: Correction of spectrum for p-side strips.

### 6.2.2. Energy correlations

As discussed in the previous section the energy of alpha particles can be deposited in more than one segment of DSSSD, which corresponds to a multiplicity of events higher than 1. In order to study the energy distribution on the p- and n-side of the detectors two-dimensional energy correlations are investigated. As shown in Fig. 6.15 (top), if the fully deposited energies of alpha particles are distributed into two neighbouring strips, the result is three  $\alpha$ -lines, where the energy distribution is different but clearly correlated to the strips, while the deposited energy remains constant. Events below the three lines indicate that the energy of the alpha particles is not completely deposited into the two neighbouring strips, which means the incident alpha particles are located in the interstrip area. The situation on the p-side (cf. Fig. 6.15 (bottom)) is quite different than the n-side: there are no lines visible, but only rare points, which correspond to interstrip events on the p-side. This reflects the fact that on that DSSSD side the produced positive charge carriers (holes) will be collected quickly, and the energy of alpha particles has been deposited mostly in a single strip. On the other hand, the electrons moving towards the n-side have a long way to go. During this distance the electrons can drift transversely and will be collected by two or more n-side strips.

A further investigation of the correlations between both sides is shown in Fig. 6.16. Events in the four special regions *A*, *B*, *C* and *D* correspond to different correlations.

## 6. Commissioning of LYCCA

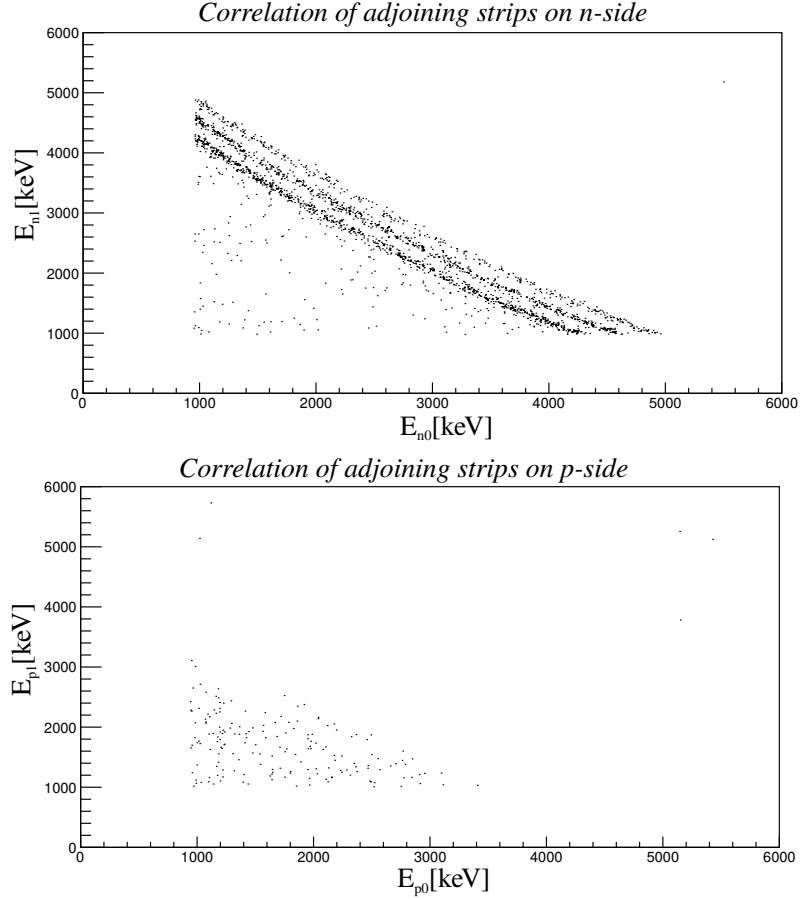


Figure 6.15.: Correlation of adjoining strips on DSSSD. Top: energy correlation between neighbouring n-side strips; Bottom: energy correlation between neighbouring p-side strips. Due to the set threshold, events with energy lower than 1000 keV haven been excluded.

*A:* In this region the appearance of the three accumulations indicates that the energies of alpha particles are completely deposited in DSSSD and detected by only one strip on both sides.

*B:* The diagonal corresponds to the events whose energy is incompletely deposited in one pixel. However, the same energy has been detected by p- and n-side strips.

*C:* The three vertical lines indicate the full energy deposition of alpha particles on p-side strips, while on the n-side strips the energy has been incompletely detected. This kind of energy distribution on n-side strips has been illustrated in Fig. 6.15.

*D:* The area indicates events that have been detected simultaneously in the interstrip area of p-side and n-side. As already reported by Torresi *et al.* [95], the

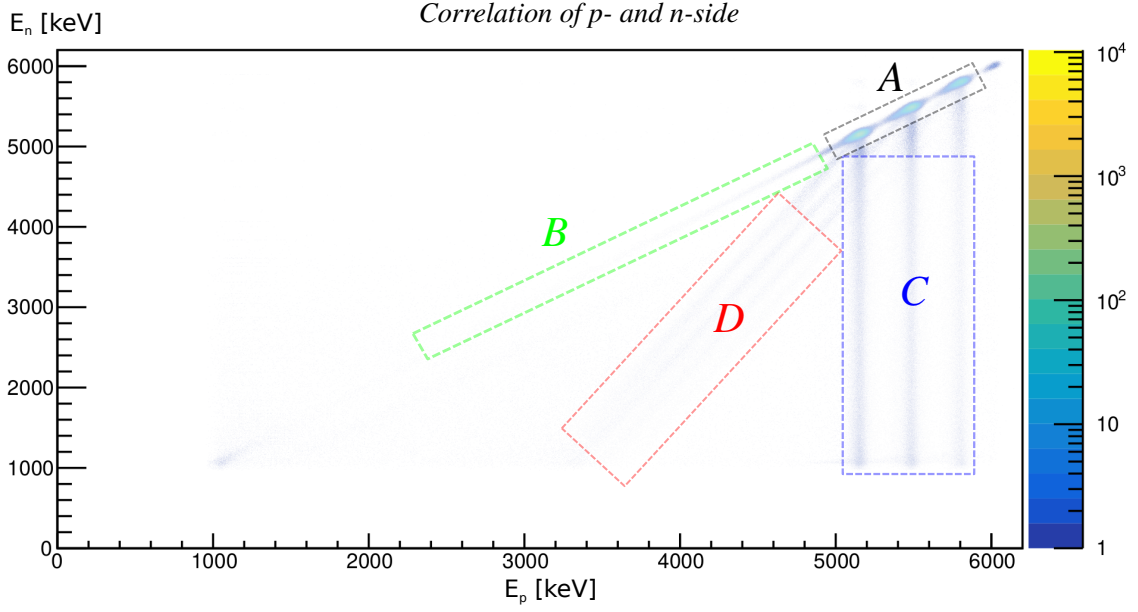


Figure 6.16.: Energy correlation of p- and n-side.

interstrip events influence the charge collection. Unlike the diagonal in region *B*, here the detected energies on p- and n-side are asymmetrical. P-side trips have generally more charge carriers collected than n-side strips. The reason is similar as for previously discussed energy distributions of n-side strips: even for interstrip events the electrons need to move a long distance to arrive at n-side strips, thus their transverse drift will be larger than that of holes at the p-side.

### 6.3. In-beam experiment

#### 6.3.1. Elastic Scattering of $^{12}\text{C} + ^{197}\text{Au}$

In order to test the medium-gain range (up to 1 GeV) of the LYCCA-FEE modules in-beam experiments were carried out in November 2016 for the first time. A  $^{12}\text{C}$  beam with energies of 50 MeV and 60 MeV was scattered on a  $^{197}\text{Au}$  target with a thickness of  $0.17 \frac{\text{mg}}{\text{cm}^2}$ , which is located at a distance of 1200 mm in front of the DSSSD-wall. In this in-beam experiment 10 DSSSDs and FEE-modules were employed. The location of DSSSDs in the LYCCA-chamber is illustrated in Fig. 6.17. With this setup a continuous scattering-angle coverage of  $1.5^\circ$  to  $10.5^\circ$  is obtained. With beam energies of 50 MeV and 60 MeV only Rutherford scattering on the gold target occurs. Accordingly, there are no reaction products to detect except for elastically scattered  $^{12}\text{C}$ -particles in DSSSD. In order to perform an individual energy calibration for each DSSSD channel, the energy loss of the  $^{12}\text{C}$ -beam has

## 6. Commissioning of LYCCA

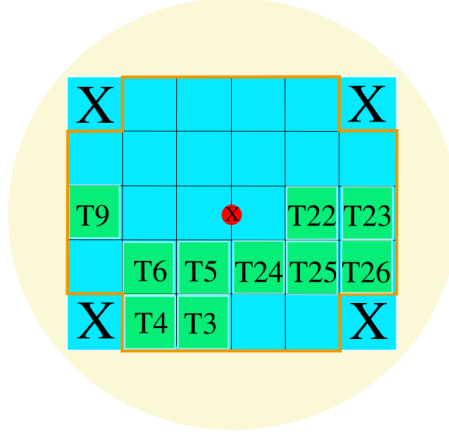


Figure 6.17.: Location of the 10 DSSSDs in the in-beam experiment, with the view along the beam direction.

been accurately calculated according to the scattering angle on each DSSSD pixel. Using LISE [65] the minimal and maximal energy losses of the 50 MeV  $^{12}\text{C}$ -beam are calculated as about 70 keV (at pixel *front0-back0* on *T24*) and 190 keV (at pixel *front31-back31* on *T26*), respectively.

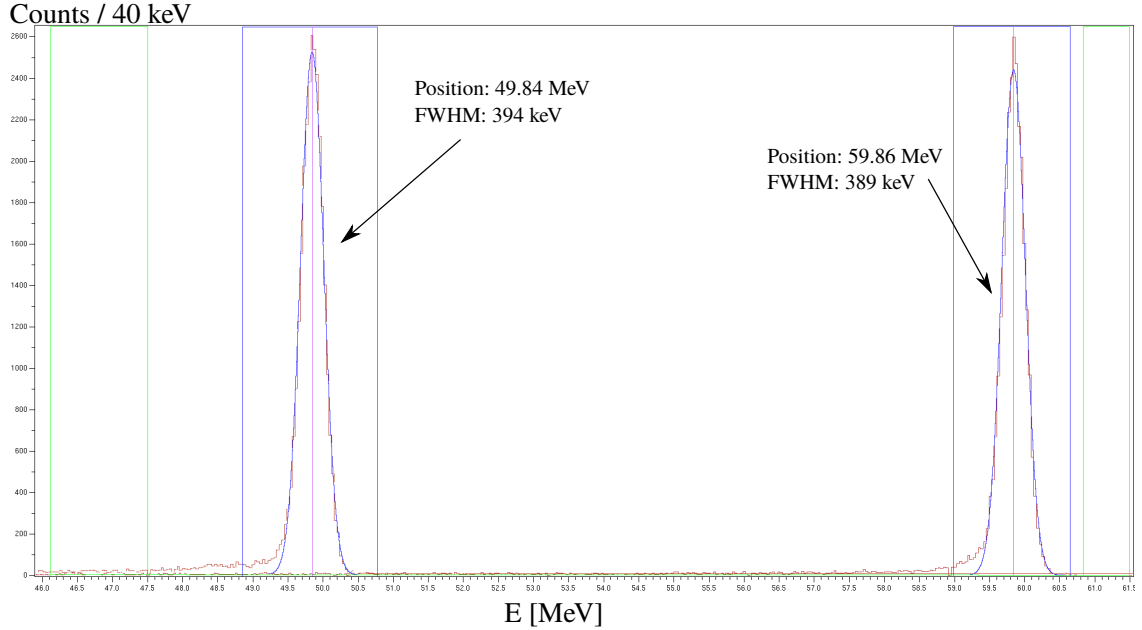


Figure 6.18.: Calibrated energy spectra of  $^{12}\text{C}$ -beam in one DSSSD pixel. The FWHM by energy around 50 MeV is about 394 keV and by 60 MeV is about 389 keV.

Figure 6.18 shows the calibrated energy spectra for  $^{12}\text{C}$ -beams with energies of 50 and 60 MeV, where the energies have been deposited in the DSSSD pixel *front15-back15* on *T26*. The FWHMs amount to about 394 keV at 50 MeV, and 389 keV

## 6. Commissioning of LYCCA

at 60 MeV, which corresponds to a energy resolution of around 0.79% and 0.65%, respectively. Considering the energy straggling of the  $^{12}\text{C}$ -beam in the gold target, the energy peaks will be broaden. The energy resolution of the LYCCA system could be even better, when the beam has been scattered off by a thinner gold target. The in-beam energy spectra of all DSSSD-channels from the operated 10 detectors were successfully calibrated.

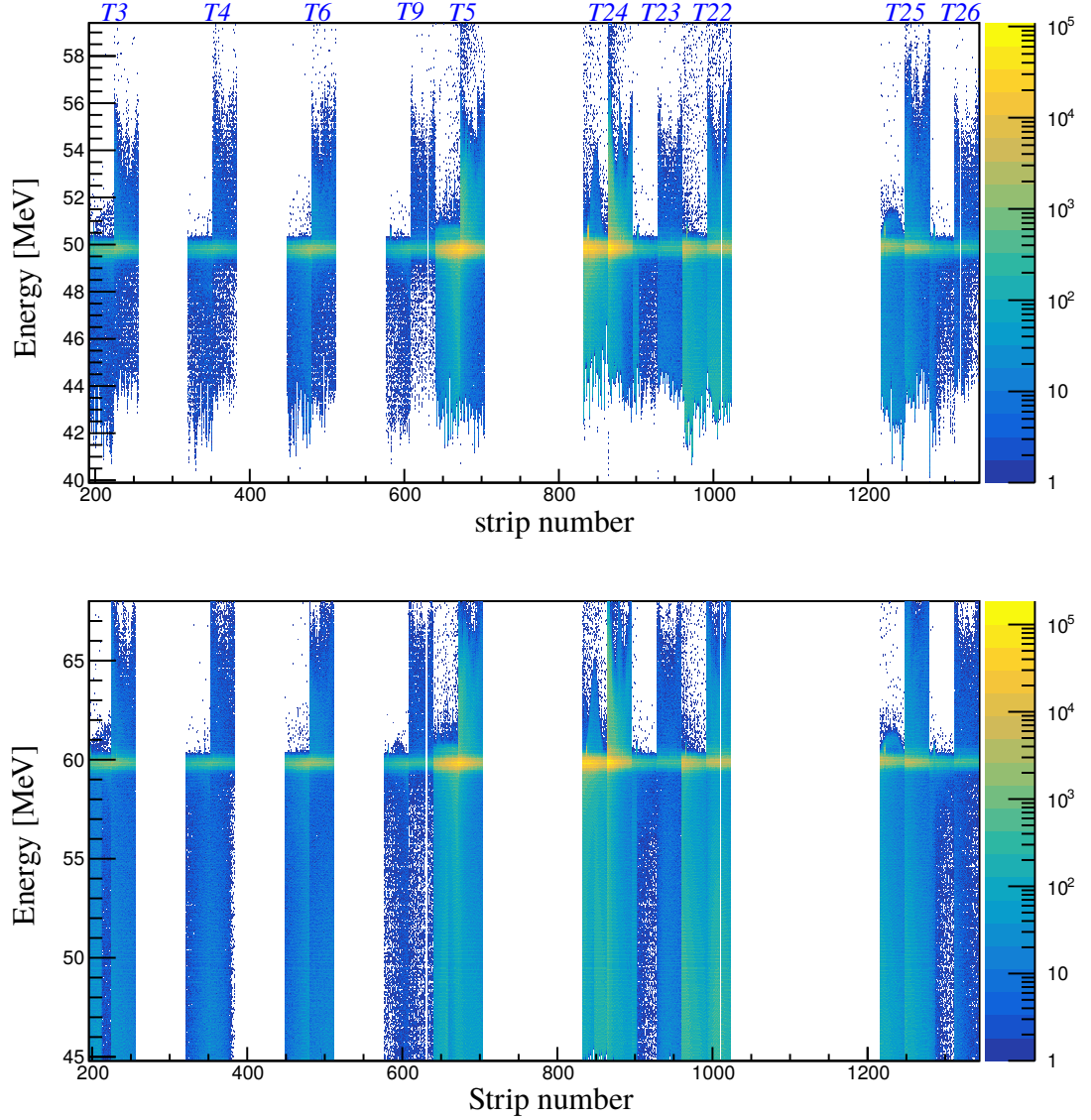


Figure 6.19.: Calibrated in-beam energy spectra of  $^{12}\text{C}+^{197}\text{Au}$  scattering. Top: 2-dimensional energy spectra of scattering with 50 MeV beam; Bottom: 2-dimensional energy spectra of scattering with 60 MeV beam. On each DSSSD the first 32 channels indicate the signals from the n-side, while the second 32 channels indicate the signals from the p-side.



## 6. Commissioning of LYCCA

Figure 6.19 shows the 2-dimensional energy spectra of  $^{12}\text{C}+^{197}\text{Au}$  scattering, with the beam energy of 50 MeV and 60 MeV. Because the threshold of all ASICs was set relative high during the measurements, events with energy lower than 40 MeV were not recorded. It is noticeable, that in both diagrams for each detector the energy structure of the p- and n-side are quite different. On the p-side of each DSSSD there are events with energy up to about 10 MeV higher than the beam energy observed, while on the n-side the most events were detected with energy up to the beam energy, except on the detectors *T5*, *T24* and *T25*, where the statistics are very high, and events were also detected with energy higher than the beam energy. Example for the energy spectra of the p-side and n-side strips have been shown in Fig. 6.20.

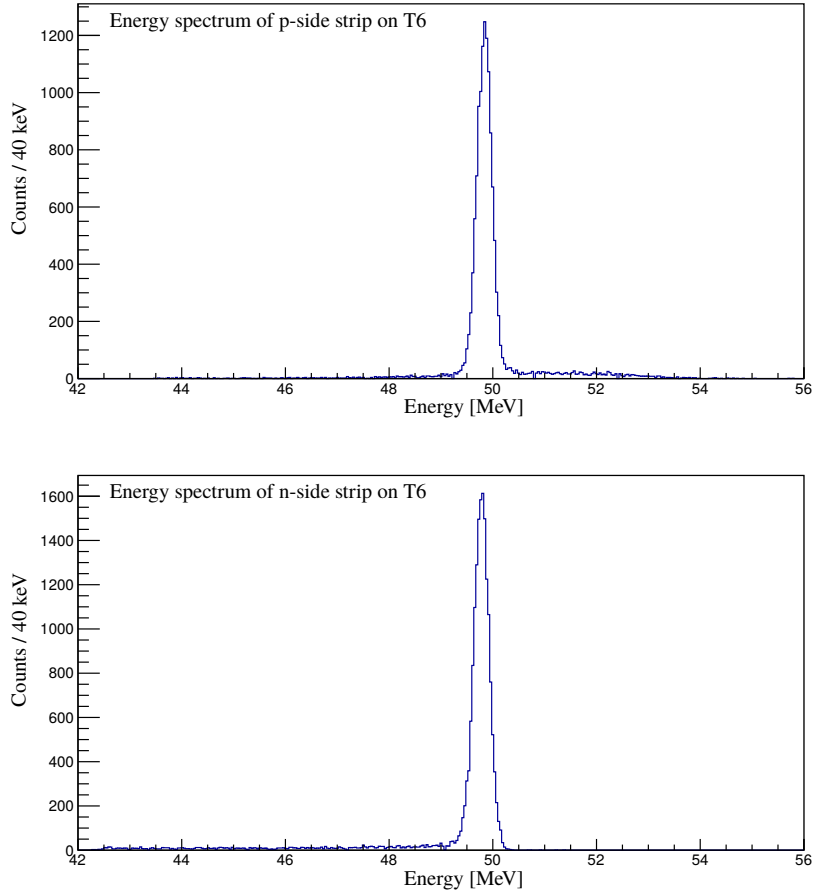


Figure 6.20.: Comparison of the 50 MeV energy spectra of the p-side strip (top) and the n-side strip (bottom).

In order to investigate this issue, energy correlations of the total p- and n-side were built up for all operated detectors based on the data of the  $^{12}\text{C}+^{197}\text{Au}$  @50 MeV

## 6. Commissioning of LYCCA

elastic scattering. The correlations have been sorted into three diagrams as shown in Fig. 6.21, 6.22 and 6.23, according to the respective statistics and scattering angles.

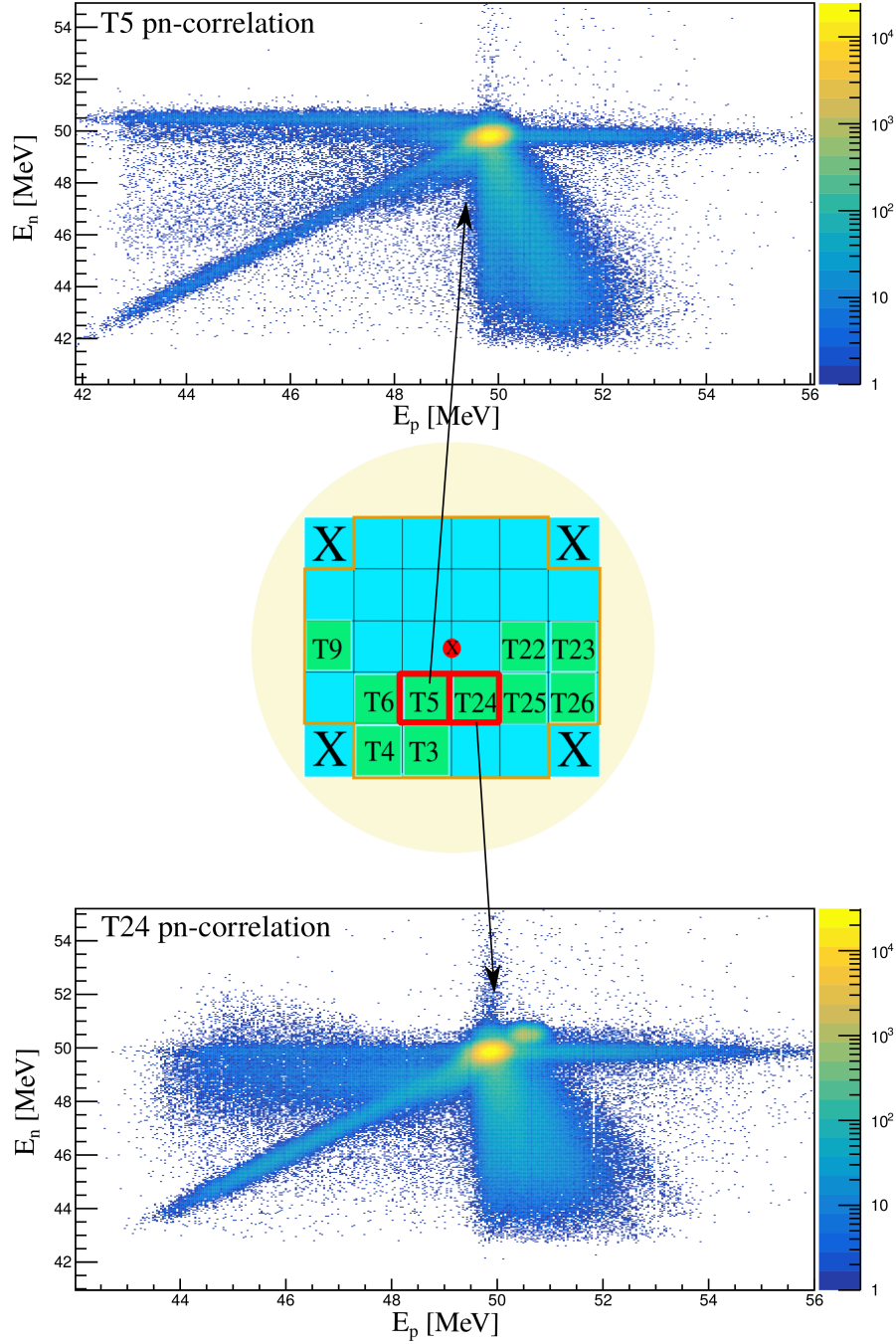


Figure 6.21.: PN-correlation of telescopes  $T5$  (top) and  $T24$  (bottom), which have the highest statistics.

## 6. Commissioning of LYCCA

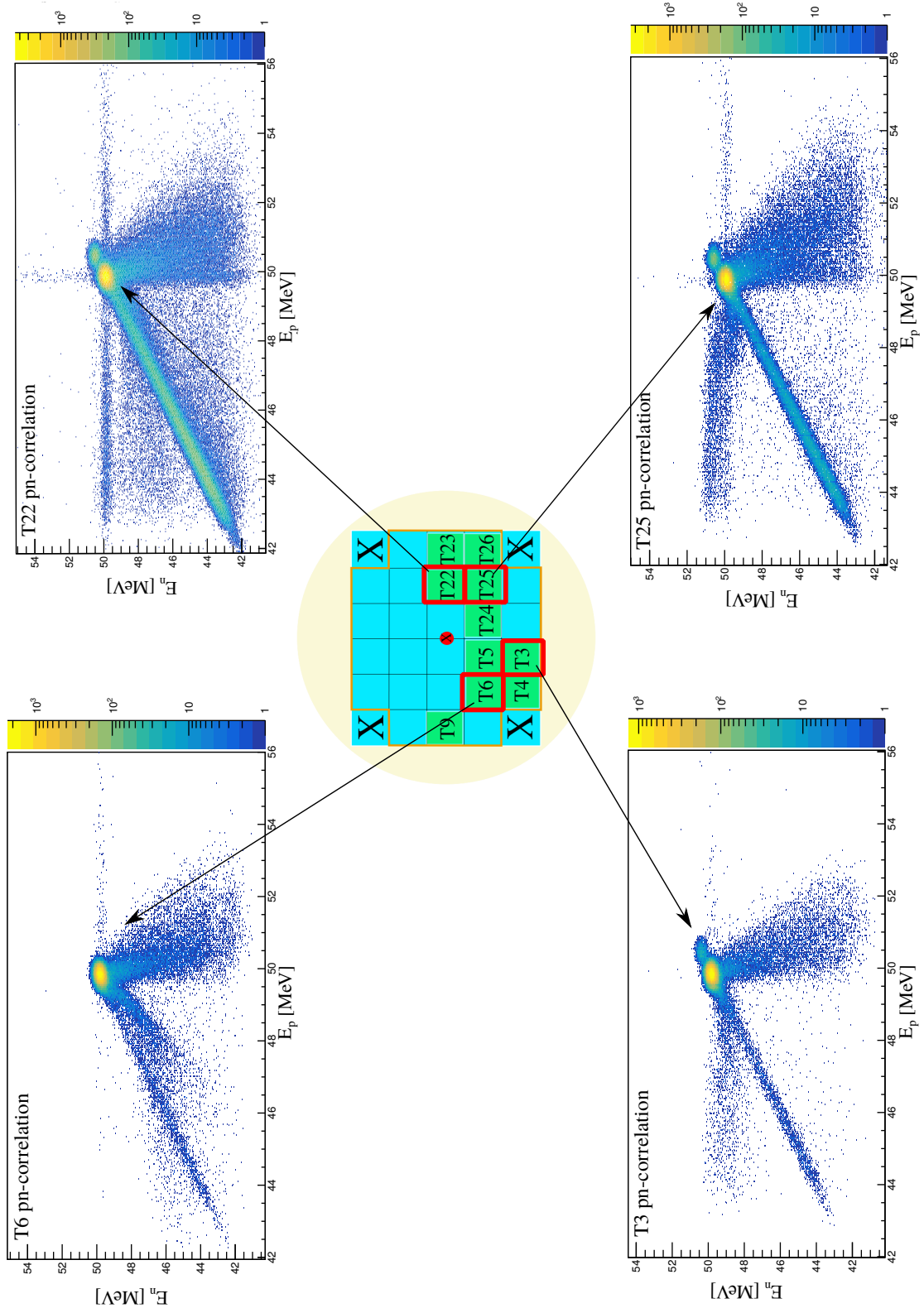


Figure 6.22.: PN-correlation of telescopes  $T3$ ,  $T6$ ,  $T22$  and  $T25$

## 6. Commissioning of LYCCA

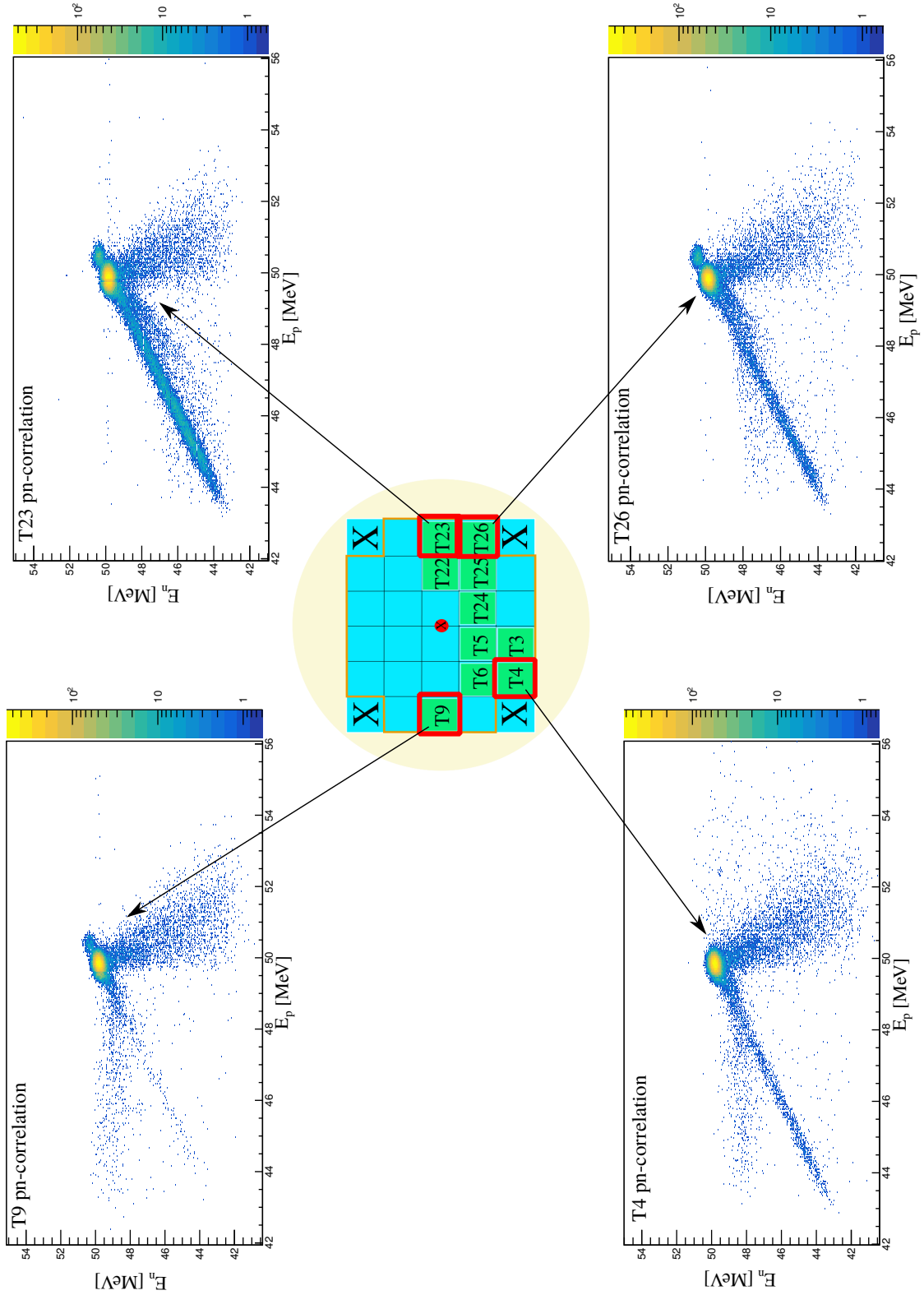


Figure 6.23.: PN-correlation of  $T_4$ ,  $T_9$ ,  $T_{23}$  and  $T_{26}$ , which locate at large scattering angle and collect low statistics.

## 6. Commissioning of LYCCA

There are three areas of events, which were observed in all pn-correlation patterns. (i) the expected main accumulation nearby the beam energy for both p- and n-side, which corresponds to the full energy deposition in a single pixel (forwards as well as backwards). (ii) the diagonal extending to low energies corresponds to the incomplete energy deposition in single pixel area, but the same energy has been recorded by pixels on p-side as well as on n-side. (iii) the triangle area below the main accumulation indicates the events, whose energy recorded by the p-side pixel is higher than the beam energy, but on the n-side, the recorded energy is lower than the beam energy. Furthermore, on the pn-correlation of detector *T5*, *T22*, *T24* and *T25* there is a horizontal line by n-side energy of about 50 MeV observed, which obviously depends on the recorded high statistics, and cannot be observed by other detectors with low statistics.

Such unusual phenomena was neither observed by the triple alpha experiments with the high-gain electronics (up to 20 MeV), nor by pulser tests with the medium gain electronics (up to 1 GeV). Physically there are no reason to build such unexpected events with energy higher than the beam energy, which were only recorded by the p-side strips. The structure and setup of the new LYCCA-FEEs for the p-side and n-side strips are almost identical. The only possible way to construct such kind of signals is that the charge collection of previous event by the p-side electrode has been delayed, and then combined with the next incoming event. The delay- and combination-process will happen most likely in the interstrip area, where the distribution of electric stream field lines is quite different than in the strip area, as shown by GRASSI with the simulation of potential maps [96]. There are several ways to check this hypothesis. The first one is to turn the DSSSDs with the n-side towards the beam direction in the future in-beam experiment, and to observe whether the unusual phenomena can still only be recorded by the n-side electronics. Another way is to shield the interstrip areas with a mask, and to compare the results with the current in-beam experiment.

There is another question to be explained: the unusual phenomena was not observed by triple-Alpha tests. A difference between the  $\alpha$ -particles and  $^{12}\text{C}$ -beam is the range of particles in the silicon detector. The range of  $^{12}\text{C}$ -beam with kinetic energy around 50 MeV is about 65  $\mu\text{m}$ , while by triple-Alpha source the maximum range of  $\alpha$ -particles is about 30  $\mu\text{m}$ . If the process of charge collection of previous event for  $\alpha$ -particles is quick enough, so that the combination with next incoming event will be avoided. In the future in-beam experiment  $^{12}\text{C}$ -beam with lower kinetic energy around 30 MeV can be used to check this assumption, which has an average range in silicon detector of about 32  $\mu\text{m}$ .

## 6. Commissioning of LYCCA

In order to investigate the angular distribution of the scattered  $^{12}\text{C}$ -particles, the number of counts per DSSSD-pixel has been analysed. Taking into account the data from 64 contiguous pixels *back31-front0* to *back31-front31* in telescopes *T5* and *T3*, a angular distribution covering a range of  $1.5^\circ$  to  $7.3^\circ$  has been obtained, as shown in Fig. 6.24. Compared to the differential Rutherford cross section, the data points for elastic scattering show very good agreement with the well known  $\sin^{-4}(\theta/2)$  dependency.

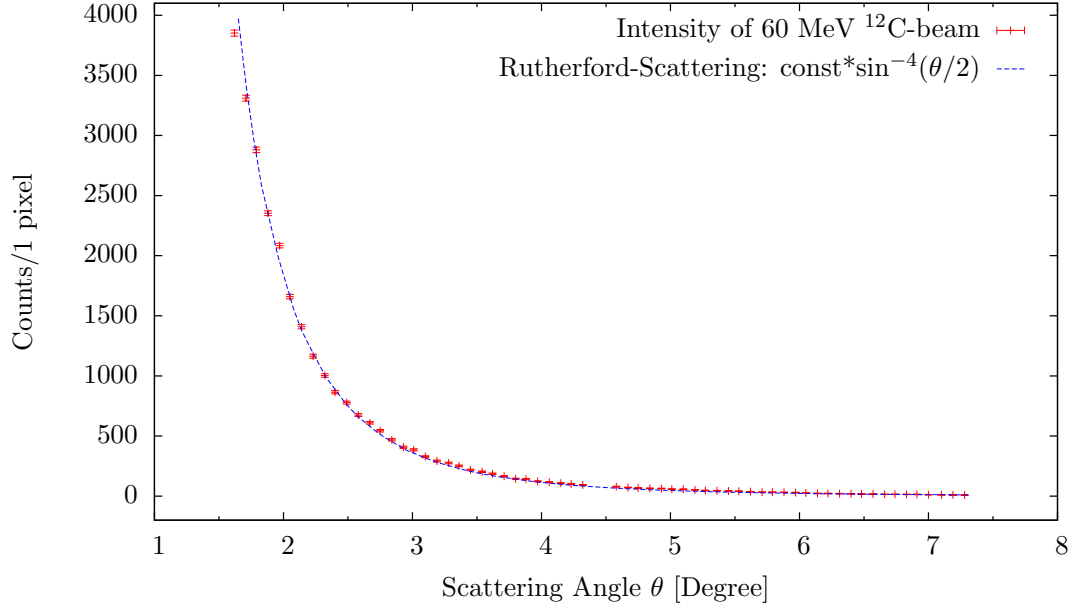


Figure 6.24.: The measured angular distribution of the elastically scattered  $^{12}\text{C}$ -particles on gold-target follows the expected distribution of the Rutherford scattering.

### 6.3.2. Elastic and inelastic scattering of $^{12}\text{C} + ^{12}\text{C}$

The elastic and inelastic scattering of the identical particles  $^{12}\text{C}$  by  $^{12}\text{C}$  is an interesting object and has been intensively studied since 1960s, using bombarding energies within a large range from about 0.5 MeV/u to around 90 MeV/u [108–118]. Measuring the interaction cross sections, the structure of angular distributions has revealed properties of the nucleus-nucleus potential. In elastic scattering the scattered projectile and backscattered recoil are staying in the ground state (marked as  $(0^+, 0^+)$ ), and their movement corresponds to the conservation of energy and momentum. For identical particles the angle between the directions of the two elastically scattered particles is  $90^\circ$ . For bombarding energies below the Coulomb barrier ( $E_{lab} \sim 18.9$  MeV) a clear interference of the differential cross section depending on the scattering angle can be observed [108]. For bombarding energies above the Coulomb barrier regular structures in the elastic excitation function were observed and interpreted by W. E. FRAHN [119] as diffraction patterns in the heavy-ion scattering. For bombarding energies above  $E_{lab} \sim 100$  MeV large cross sections of the elastic scattering at large angles were observed and can be interpreted as nuclear rainbow scattering [114–118]. The angular distributions of the elastic  $(0^+, 0^+)$  and inelastic  $(0^+, 2^+)$  scattering can be reproduced using the optical model calculations with Wood-Saxon and folded potentials [114].

Furthermore, in the inelastic scattering of  $^{12}\text{C}$  by  $^{12}\text{C}$  if a nucleus has been excited to the  $0_2^+$ -state at  $E_x = 7.65$  MeV, which is known as the Hoyle state [120], the direct  $3\alpha$  decay can occur with a small probability [121–123]. M. FREER *et al.* measured the branching ratio of direct  $3\alpha$  decay using the inelastic scattering of  $^{12}\text{C}$  by  $^{12}\text{C}$  at a beam energy of 58 MeV, and reported an upper limit of around 4% [121]. M. ITOH *et al.* measured the  $3\alpha$  decay using the  $^{12}\text{C}(^{12}\text{C}, 3\alpha)^{12}\text{C}$  reaction at beam energies of 110 MeV, and obtained an upper limit of only 0.2% [122]. Very recently L. MORELLI *et al.* reported as results of their measurement an upper limit of direct  $3\alpha$  decay of around  $1.1(\pm 0.4)\%$ , using the inelastic  $^{12}\text{C} + ^{12}\text{C}$  reaction at a beam energy of 95 MeV [123]. Since the various experimental results are inconsistent, further precise measurements of direct  $3\alpha$  decay are required to clarify this issue.

In the experiments mentioned above position-sensitive semiconductor detectors have been utilized as a key device to identify the scattered ions, to measure their energies, and determine the angular distribution of reaction cross sections. As highly segmented detectors LYCCA-DSSSDs are ideal for measurements of elastic and inelastic particle scattering. The 10 MV tandem accelerator at IKP Cologne can provide  $^{12}\text{C}$ -beams with kinetic energies up to 60 MeV. With such an energy the maximum range of  $^{12}\text{C}$  particles in a silicon detector is about 85  $\mu\text{m}$ , which corre-

## 6. Commissioning of LYCCA

sponds to around 1/3 of the total thickness of LYCCA-DSSSD. Since the incident  $^{12}\text{C}$ -particles cannot fly through the DSSSD and reach the CsI crystals, there is no  $\Delta E - E$  relation that can be used to identify the incoming particles. However, the measurements of  $^{12}\text{C} + ^{12}\text{C}$  scattering using the current LYCCA-setup have collected informations, which reflect the features of the DSSSDs as well as new electronics, and are meaningful for the commissioning phase.

The energy spectra of  $^{12}\text{C} + ^{12}\text{C}$  scattering with beam energy of 50 MeV is shown in Fig. 6.25. The data were taken from the 32 pixels of strip *back31* on the telescope *T5*, which is standing vertically under the center point of the LYCCA chamber. The peak around 49.5 MeV corresponds to the  $(0^+, 0^+)$  elastic scattering of  $^{12}\text{C}$  on  $^{12}\text{C}$ . The  $(2^+, 0^+)$  state of inelastic scattering is energetic 4.44 MeV less than  $(0^+, 0^+)$ , which was not observed in the current experiment. According to the previous investigations [111, 112] the cross section of the  $(2^+, 0^+)$  state is generally two orders of magnitude smaller than the  $(0^+, 0^+)$  state in  $^{12}\text{C} + ^{12}\text{C}$  scattering, and for higher order inelastic scattering like the  $(2^+, 2^+)$  state the cross sections are even smaller. Due to the short measuring time the statistics of the current experiment is not enough to produce visible peaks from inelastic scattering.

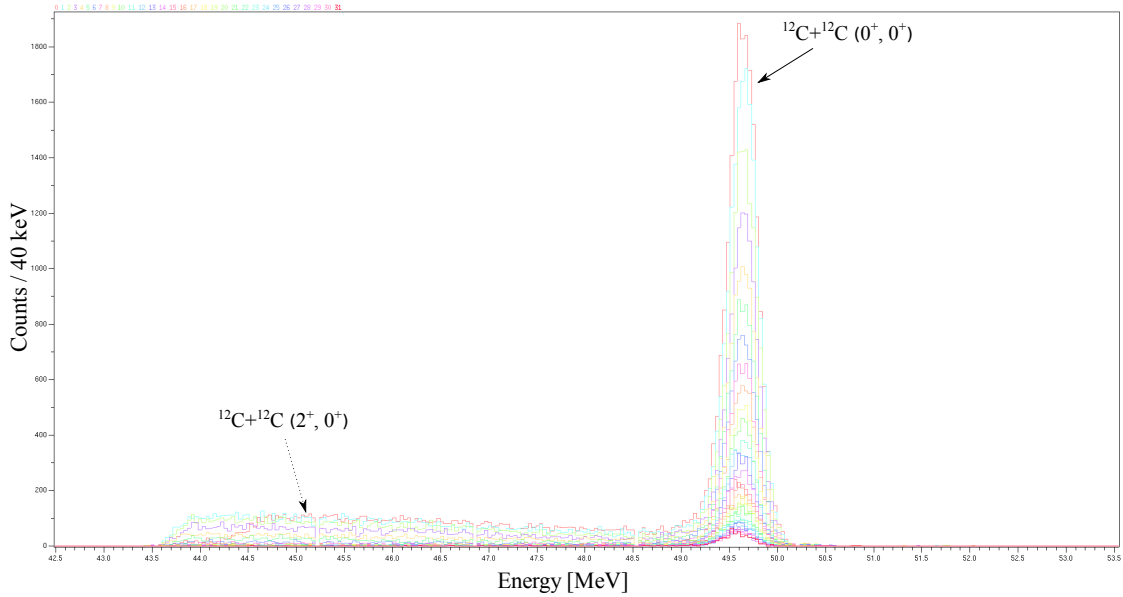


Figure 6.25.: Energy spectra of  $^{12}\text{C} + ^{12}\text{C}$  scattering from telescope *T5*. The data were taken from the 32 pixels of strip *back31*, which is standing vertically under the center point of the LYCCA chamber.

To study the angular distribution of  $(0^+, 0^+)$  elastic scattering the experimental data from telescopes *T5* and *T3* were investigated. As shown in Fig. 6.26 the analysis was carried out up to  $\theta_{lab} = 5.1^\circ$ , due to the limited statistics. In order to study the angular distribution at larger scattering angles, energy spectra of the n-side



## 6. Commissioning of LYCCA

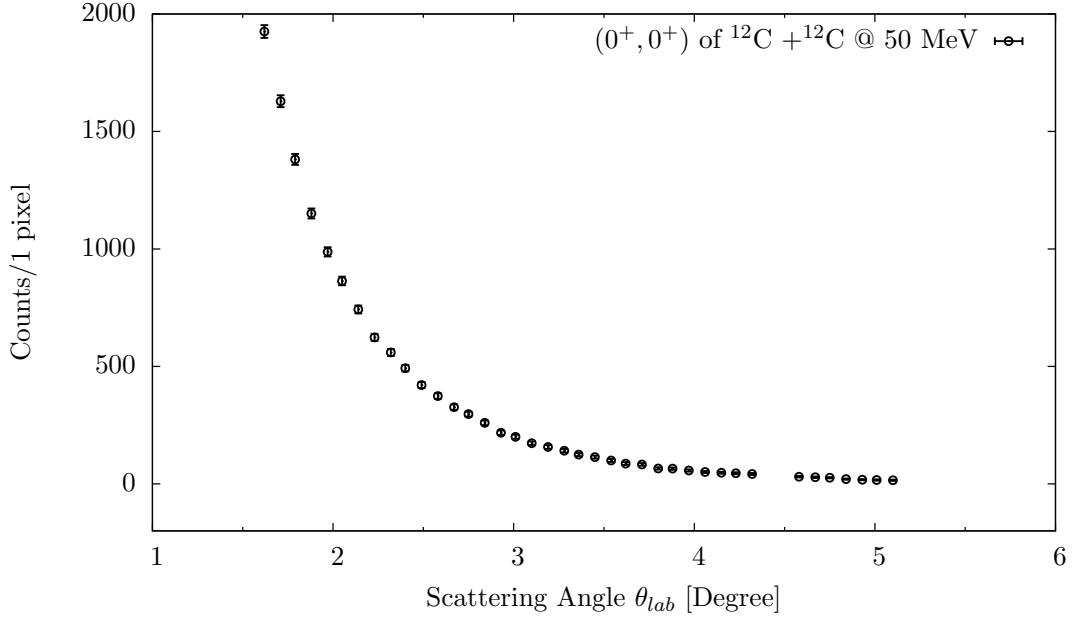


Figure 6.26.: Angular distribution of  $(0^+, 0^+)$  state of  $^{12}\text{C} + ^{12}\text{C}$  scattering, with the beam energy of 50 MeV.

strips of telescopes *T22* and *T23* were analysed, which are standing vertically on the right hand side of the center point, and covering the scattering angle  $\theta_{lab}$  from  $3.3^\circ$  to  $10.4^\circ$ . Unlike the energy spectra from *T5* (cf. Fig. 6.25), the energy spectra from *T22* and *T23* (strips *back0* to *back6*) show very strong background (cf. Fig. 6.27). The ratio of peak to total by *T22* and *T23* is around 11%, where by *T5* the ratio is clearly larger than 60%. The strong background was not observed on the spectra from strips *back7* to *back31* on *T23*. Furthermore, the total statistics of the first 7 n-side strips on *T23* (*back0* to *back6*) are much larger than the remaining 25 strips. Such unusual phenomena was neither observed on other telescopes by the  $^{12}\text{C} + ^{12}\text{C}$  scattering, nor by experiment of  $^{12}\text{C} + ^{197}\text{Au}$  scattering. Since the ASIC-setup throughout the measurement was not changed, the cause of the strong background is still unclear. In the future in-beam experiments a cross-check with different combinations of DSSSD and FEE-module is necessary to study, whether such phenomena will be reproduced, and to find the reasonable explanation.

## 6. Commissioning of LYCCA

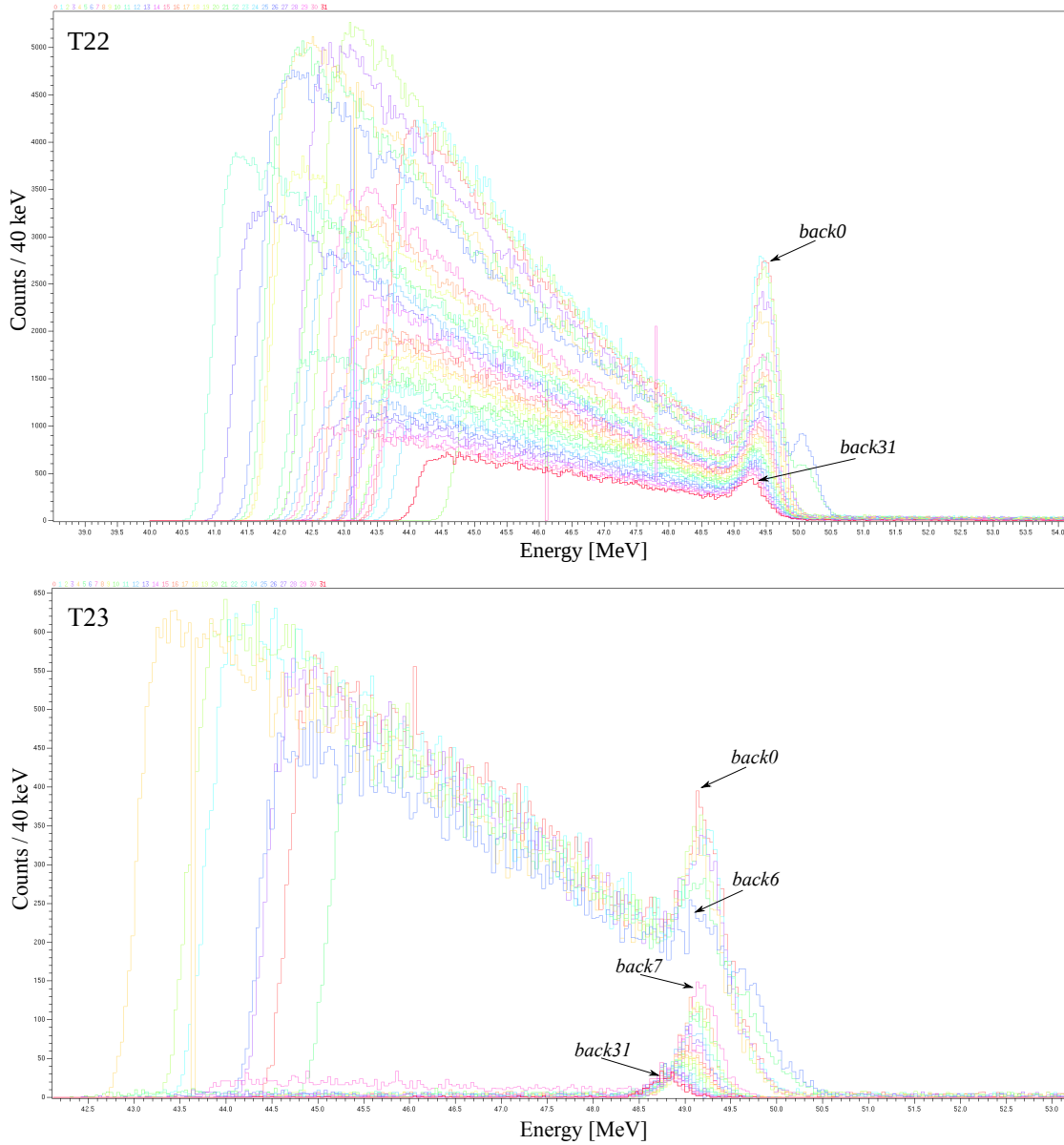


Figure 6.27.: Energy spectra of  $^{12}\text{C}+^{12}\text{C}$  scattering from telescopes  $T22$  (top) and  $T23$  (bottom). The data were taken from the backwards strips, which are standing vertically on the right hand side of the center point.

### 6.4. Summary

After the upgrade of the electronics for LYCCA, the new system was moved and set up at the Cologne tandem accelerator. Currently 25 FEE modules and 14  $\Delta E$ -E telescopes are installed on LYCCA chamber. A series of commissioning experiments were carried out to check the specifications and energy resolutions of the DSSSDs with the new digital FEE modules. Employing the Multi-Data-Acquisition System (MIDAS) experiment data were successfully stored, sorted event by event and

## 6. Commissioning of LYCCA

analysed using the data analysis framework ROOT. With the in-beam  $^{12}\text{C}$ -scattering experiments the first information about the 1 GeV range electronics was collected. To optimize the detector performance and electronic setup further measurements under different experiment conditions are required.

## 7. Outlook

The  $^{12}\text{C}$ -scattering experiments carried out with LYCCA will allow for different experiments with a new scattering chamber, because the original design of the LYCCA chamber limits the scattering-angle coverage. For further in-beam experiments of elastic and inelastic particle scattering at the Cologne tandem accelerator, a modified mechanical construction of the LYCCA chamber was realized by IKP's mechanics workshop.

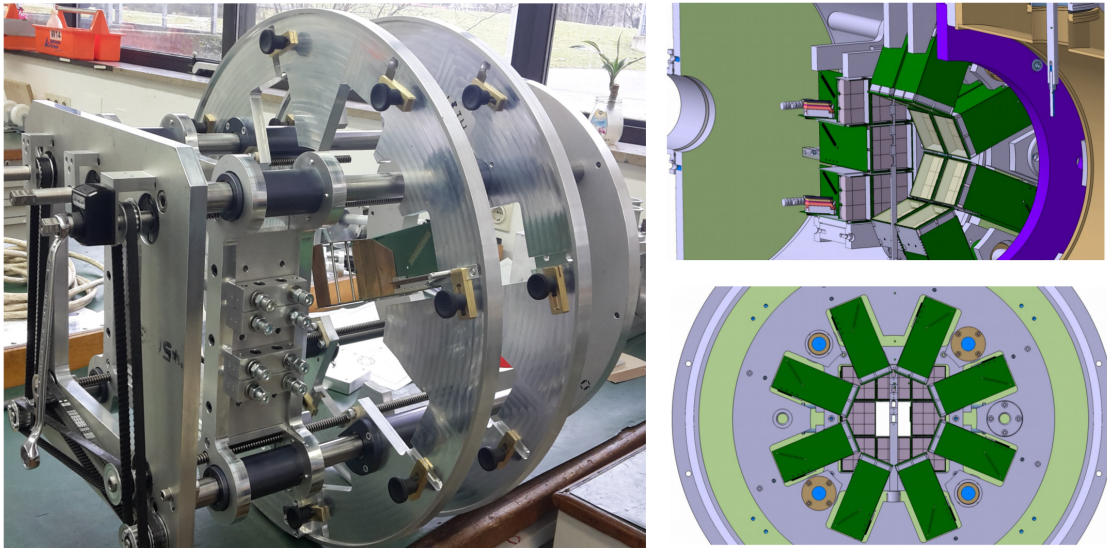


Figure 7.1.: New design of the LYCCA chamber. Left: Prototype of the octagon holder; Right (top): technical drawing (side view), bottom: front view.

As shown in Fig. 7.1 and 7.2, the new design consists of two octagon brackets and a back wall, which support up to 24  $\Delta E$ -E telescopes in operation. The target ladder is located between the octagon brackets. This new construction increases the scattering-angle coverage from a maximum of  $16^\circ$  to a maximum of about  $120^\circ$ , as well as the solid-angle coverage up to 60% of  $4\pi$  significantly. Especially with the new construction the high segmented LYCCA DSSDs provide an angular resolution generally better than  $1.27^\circ$ , so that a continuous angular distribution even at large scattering angles can be measured.



Figure 7.2.: New LYCCA chamber with DSSSDs installed. Top: view of 8 installed telescopes on the forward and backward brackets, with the target ladder in the middle. Bottom: complete setup with 8 installed telescopes on the backward bracket.



# A. Shell Model Calculations

## A.1. Level Energies

PSDPF calculations for level energies in  $^{33}\text{P}$ , using SM-code NATHAN [40] with maximum allowed excitation  $1\hbar\omega$ :

Table A.1.: PSDPF calculations for level scheme in  $^{33}\text{P}$  up to 12.5 MeV.

PSDPF for level scheme in $^{33}\text{P}$ , $E_{g.s.} = -274.24653$ MeV					
N,Z= 18 15	2*J= 1	N= 1	P= 0	E= -274.24653	EXC= 0.00000
N,Z= 18 15	2*J= 3	N= 1	P= 0	E= -272.80596	EXC= 1.44057
N,Z= 18 15	2*J= 5	N= 1	P= 0	E= -272.34161	EXC= 1.90493
N,Z= 18 15	2*J= 3	N= 2	P= 0	E= -271.56771	EXC= 2.67883
N,Z= 18 15	2*J= 3	N= 3	P= 0	E= -270.81378	EXC= 3.43276
N,Z= 18 15	2*J= 5	N= 2	P= 0	E= -270.73839	EXC= 3.50815
N,Z= 18 15	2*J= 7	N= 1	P= 0	E= -270.46867	EXC= 3.77787
N,Z= 18 15	2*J= 5	N= 3	P= 0	E= -270.27588	EXC= 3.97065
N,Z= 18 15	2*J= 1	N= 2	P= 0	E= -269.85522	EXC= 4.39132
N,Z= 18 15	2*J= 7	N= 1	P= 1	E= -269.77604	EXC= 4.47049
N,Z= 18 15	2*J= 5	N= 4	P= 0	E= -269.23443	EXC= 5.01211
N,Z= 18 15	2*J= 3	N= 4	P= 0	E= -269.17140	EXC= 5.07514
N,Z= 18 15	2*J= 3	N= 1	P= 1	E= -269.13627	EXC= 5.11027
N,Z= 18 15	2*J= 5	N= 1	P= 1	E= -269.07993	EXC= 5.16661
N,Z= 18 15	2*J= 1	N= 1	P= 1	E= -268.94589	EXC= 5.30064
N,Z= 18 15	2*J= 9	N= 1	P= 0	E= -268.77632	EXC= 5.47021
N,Z= 18 15	2*J= 1	N= 2	P= 1	E= -268.76471	EXC= 5.48182
N,Z= 18 15	2*J= 3	N= 2	P= 1	E= -268.75649	EXC= 5.49005
N,Z= 18 15	2*J= 5	N= 2	P= 1	E= -268.68642	EXC= 5.56011
N,Z= 18 15	2*J= 7	N= 2	P= 1	E= -268.60750	EXC= 5.63904
N,Z= 18 15	2*J= 9	N= 1	P= 1	E= -268.55062	EXC= 5.69591
N,Z= 18 15	2*J= 11	N= 1	P= 1	E= -268.43411	EXC= 5.81242
N,Z= 18 15	2*J= 1	N= 3	P= 0	E= -268.41647	EXC= 5.83006
N,Z= 18 15	2*J= 7	N= 2	P= 0	E= -268.33470	EXC= 5.91183
N,Z= 18 15	2*J= 5	N= 3	P= 1	E= -268.33137	EXC= 5.91517
N,Z= 18 15	2*J= 3	N= 3	P= 1	E= -268.28753	EXC= 5.95900
N,Z= 18 15	2*J= 1	N= 3	P= 1	E= -268.28455	EXC= 5.96199
N,Z= 18 15	2*J= 7	N= 3	P= 1	E= -268.25610	EXC= 5.99043
N,Z= 18 15	2*J= 1	N= 4	P= 0	E= -268.20140	EXC= 6.04513
N,Z= 18 15	2*J= 9	N= 2	P= 1	E= -268.12842	EXC= 6.11812
N,Z= 18 15	2*J= 3	N= 4	P= 1	E= -267.99931	EXC= 6.24722
N,Z= 18 15	2*J= 3	N= 5	P= 0	E= -267.88293	EXC= 6.36360
N,Z= 18 15	2*J= 9	N= 2	P= 0	E= -267.73695	EXC= 6.50959

Continued on following page

## A. Shell Model Calculations

Table A.1, continued

PSDPF for level scheme in $^{33}\text{P}$					
N,Z= 18 15	2*J= 5	N= 5	P= 0	E= -267.71108	EXC= 6.53546
N,Z= 18 15	2*J= 5	N= 6	P= 0	E= -267.52492	EXC= 6.72161
N,Z= 18 15	2*J= 3	N= 7	P= 0	E= -267.50659	EXC= 6.73994
N,Z= 18 15	2*J= 3	N= 6	P= 1	E= -267.48677	EXC= 6.75976
N,Z= 18 15	2*J= 5	N= 7	P= 0	E= -267.38811	EXC= 6.85842
N,Z= 18 15	2*J= 5	N= 7	P= 1	E= -267.30468	EXC= 6.94185
N,Z= 18 15	2*J= 7	N= 5	P= 0	E= -267.30463	EXC= 6.9419
N,Z= 18 15	2*J= 11	N= 2	P= 1	E= -267.27104	EXC= 6.97549
N,Z= 18 15	2*J= 3	N= 7	P= 1	E= -267.27089	EXC= 6.97564
N,Z= 18 15	2*J= 1	N= 5	P= 0	E= -267.26305	EXC= 6.98348
N,Z= 18 15	2*J= 3	N= 8	P= 0	E= -267.14484	EXC= 7.10169
N,Z= 18 15	2*J= 11	N= 3	P= 1	E= -267.13879	EXC= 7.10774
N,Z= 18 15	2*J= 9	N= 3	P= 0	E= -267.13757	EXC= 7.10896
N,Z= 18 15	2*J= 5	N= 8	P= 1	E= -267.1224	EXC= 7.12413
N,Z= 18 15	2*J= 5	N= 8	P= 0	E= -267.07407	EXC= 7.17246
N,Z= 18 15	2*J= 3	N= 8	P= 1	E= -267.05348	EXC= 7.19305
N,Z= 18 15	2*J= 13	N= 1	P= 1	E= -267.02414	EXC= 7.22239
N,Z= 18 15	2*J= 5	N= 9	P= 0	E= -266.80887	EXC= 7.43766
N,Z= 18 15	2*J= 3	N= 9	P= 0	E= -266.68457	EXC= 7.56196
N,Z= 18 15	2*J= 3	N= 10	P= 0	E= -266.55404	EXC= 7.69249
N,Z= 18 15	2*J= 11	N= 1	P= 0	E= -266.46653	EXC= 7.78
N,Z= 18 15	2*J= 1	N= 6	P= 0	E= -266.46409	EXC= 7.78244
N,Z= 18 15	2*J= 9	N= 4	P= 0	E= -266.41455	EXC= 7.83198
N,Z= 18 15	2*J= 1	N= 7	P= 0	E= -266.37288	EXC= 7.87365
N,Z= 18 15	2*J= 9	N= 5	P= 0	E= -266.30323	EXC= 7.9433
N,Z= 18 15	2*J= 13	N= 2	P= 1	E= -266.25548	EXC= 7.99105
N,Z= 18 15	2*J= 5	N= 10	P= 0	E= -266.25163	EXC= 7.9949
N,Z= 18 15	2*J= 3	N= 11	P= 0	E= -266.09609	EXC= 8.15044
N,Z= 18 15	2*J= 5	N= 11	P= 0	E= -265.98229	EXC= 8.26424
N,Z= 18 15	2*J= 3	N= 12	P= 0	E= -265.68472	EXC= 8.56181
N,Z= 18 15	2*J= 5	N= 12	P= 0	E= -266.17681	EXC= 8.06972
N,Z= 18 15	2*J= 5	N= 13	P= 0	E= -265.46924	EXC= 8.77729
N,Z= 18 15	2*J= 13	N= 1	P= 0	E= -265.29728	EXC= 8.94925
N,Z= 18 15	2*J= 5	N= 14	P= 0	E= -265.21331	EXC= 9.03322
N,Z= 18 15	2*J= 15	N= 1	P= 1	E= -265.1523	EXC= 9.09423
N,Z= 18 15	2*J= 5	N= 15	P= 0	E= -265.02201	EXC= 9.22452
N,Z= 18 15	2*J= 11	N= 2	P= 0	E= -264.80403	EXC= 9.4425
N,Z= 18 15	2*J= 5	N= 16	P= 0	E= -264.7596	EXC= 9.48693
N,Z= 18 15	2*J= 15	N= 2	P= 1	E= -264.75869	EXC= 9.48784
N,Z= 18 15	2*J= 5	N= 17	P= 0	E= -264.65139	EXC= 9.59514
N,Z= 18 15	2*J= 5	N= 18	P= 0	E= -264.58948	EXC= 9.65705
N,Z= 18 15	2*J= 15	N= 3	P= 1	E= -264.04823	EXC= 10.1983
N,Z= 18 15	2*J= 13	N= 2	P= 0	E= -263.69259	EXC= 10.55394
N,Z= 18 15	2*J= 17	N= 1	P= 1	E= -263.0071	EXC= 11.23943
N,Z= 18 15	2*J= 17	N= 2	P= 1	E= -262.61205	EXC= 11.63448
N,Z= 18 15	2*J= 15	N= 1	P= 0	E= -261.76874	EXC= 12.47779



## A. Shell Model Calculations

**PSDPF calculations for level energies in  $^{33}\text{S}$ , using SM-code NATHAN [40]**  
with maximum allowed excitation  $1\hbar\omega$ :

Table A.2.: PSDPF calculations for level scheme in  $^{33}\text{S}$  up to 10.3 MeV.

PSDPF for level scheme in $^{33}\text{S}$ , $E_{g.s.} = -279.43800$ MeV					
N,Z= 17 16	2*J= 3	N= 1	P= 0	E= -279.43800	EXC= 0.00000
N,Z= 17 16	2*J= 1	N= 1	P= 0	E= -278.62944	EXC= 0.80856
N,Z= 17 16	2*J= 5	N= 1	P= 0	E= -277.54141	EXC= 1.89658
N,Z= 17 16	2*J= 3	N= 2	P= 0	E= -277.14068	EXC= 2.29732
N,Z= 17 16	2*J= 5	N= 2	P= 0	E= -276.63744	EXC= 2.80056
N,Z= 17 16	2*J= 7	N= 1	P= 1	E= -276.58970	EXC= 2.84830
N,Z= 17 16	2*J= 3	N= 1	P= 1	E= -276.40386	EXC= 3.03414
N,Z= 17 16	2*J= 7	N= 1	P= 0	E= -276.34230	EXC= 3.09570
N,Z= 17 16	2*J= 3	N= 3	P= 0	E= -275.82103	EXC= 3.61696
N,Z= 17 16	2*J= 5	N= 3	P= 0	E= -275.74816	EXC= 3.68984
N,Z= 17 16	2*J= 1	N= 2	P= 0	E= -275.58785	EXC= 3.85015
N,Z= 17 16	2*J= 7	N= 2	P= 0	E= -275.41874	EXC= 4.01926
N,Z= 17 16	2*J= 9	N= 1	P= 0	E= -275.32738	EXC= 4.11061
N,Z= 17 16	2*J= 1	N= 3	P= 0	E= -275.03401	EXC= 4.40399
N,Z= 17 16	2*J= 3	N= 4	P= 0	E= -275.01483	EXC= 4.42317
N,Z= 17 16	2*J= 3	N= 2	P= 1	E= -275.00030	EXC= 4.43770
N,Z= 17 16	2*J= 5	N= 1	P= 1	E= -274.85603	EXC= 4.58197
N,Z= 17 16	2*J= 5	N= 4	P= 0	E= -274.84477	EXC= 4.59323
N,Z= 17 16	2*J= 1	N= 1	P= 1	E= -274.62180	EXC= 4.81620
N,Z= 17 16	2*J= 9	N= 1	P= 1	E= -274.61489	EXC= 4.82311
N,Z= 17 16	2*J= 11	N= 1	P= 1	E= -274.59569	EXC= 4.84231
N,Z= 17 16	2*J= 7	N= 2	P= 1	E= -274.24925	EXC= 5.18875
N,Z= 17 16	2*J= 7	N= 3	P= 1	E= -274.08126	EXC= 5.35674
N,Z= 17 16	2*J= 3	N= 7	P= 0	E= -274.05353	EXC= 5.38447
N,Z= 17 16	2*J= 1	N= 5	P= 0	E= -274.03967	EXC= 5.39833
N,Z= 17 16	2*J= 3	N= 3	P= 1	E= -273.98248	EXC= 5.45552
N,Z= 17 16	2*J= 5	N= 6	P= 0	E= -273.85074	EXC= 5.58726
N,Z= 17 16	2*J= 7	N= 4	P= 1	E= -273.68585	EXC= 5.75215
N,Z= 17 16	2*J= 3	N= 4	P= 1	E= -273.67771	EXC= 5.76029
N,Z= 17 16	2*J= 9	N= 2	P= 0	E= -273.6599	EXC= 5.7781
N,Z= 17 16	2*J= 7	N= 5	P= 0	E= -273.51514	EXC= 5.92286
N,Z= 17 16	2*J= 5	N= 4	P= 1	E= -273.50026	EXC= 5.93774
N,Z= 17 16	2*J= 5	N= 7	P= 0	E= -273.46217	EXC= 5.97583
N,Z= 17 16	2*J= 1	N= 6	P= 0	E= -273.45636	EXC= 5.98164
N,Z= 17 16	2*J= 9	N= 3	P= 0	E= -273.31264	EXC= 6.12536
N,Z= 17 16	2*J= 7	N= 5	P= 1	E= -273.28369	EXC= 6.15431
N,Z= 17 16	2*J= 3	N= 5	P= 1	E= -273.14322	EXC= 6.29478
N,Z= 17 16	2*J= 11	N= 2	P= 1	E= -273.06251	EXC= 6.37549
N,Z= 17 16	2*J= 9	N= 4	P= 0	E= -273.04522	EXC= 6.39278
N,Z= 17 16	2*J= 9	N= 3	P= 1	E= -272.98637	EXC= 6.45163
N,Z= 17 16	2*J= 5	N= 8	P= 0	E= -272.94349	EXC= 6.49451
N,Z= 17 16	2*J= 1	N= 3	P= 1	E= -272.90259	EXC= 6.53541
N,Z= 17 16	2*J= 11	N= 1	P= 0	E= -272.80373	EXC= 6.63427
N,Z= 17 16	2*J= 11	N= 3	P= 1	E= -272.76705	EXC= 6.67095
N,Z= 17 16	2*J= 13	N= 1	P= 1	E= -272.69003	EXC= 6.74797
N,Z= 17 16	2*J= 11	N= 2	P= 0	E= -272.41012	EXC= 7.02788
N,Z= 17 16	2*J= 1	N= 7	P= 0	E= -272.21327	EXC= 7.22473

Continued on following page

## A. Shell Model Calculations

Table A.2, continued

PSDPF for level scheme in $^{33}\text{S}$					
N,Z= 17 16	2*J= 11	N= 4	P= 1	E= -272.17488	EXC= 7.26312
N,Z= 17 16	2*J= 15	N= 1	P= 1	E= -271.79485	EXC= 7.64315
N,Z= 17 16	2*J= 13	N= 2	P= 1	E= -271.75657	EXC= 7.68143
N,Z= 17 16	2*J= 11	N= 3	P= 0	E= -270.82834	EXC= 8.60966
N,Z= 17 16	2*J= 15	N= 2	P= 1	E= -270.72704	EXC= 8.71096
N,Z= 17 16	2*J= 13	N= 1	P= 0	E= -270.55799	EXC= 8.88001
N,Z= 17 16	2*J= 13	N= 2	P= 0	E= -269.78062	EXC= 9.65738
N,Z= 17 16	2*J= 17	N= 1	P= 1	E= -269.09826	EXC= 10.33974

## A.2. Transition Strength B(L)

PSDPF Calculations for B(M1) and B(E2) values in  $^{33}\text{P}$ , using SM-code NATHAN [40], with parameters from [78]:

Table A.3.: PSDPF calculations for B(E2) in  $^{33}\text{P}$  for spin states up to  $11/2_1^-$ .

PSDPF for B(E2) in [ $e^2 fm^4$ ]				
***** INI *****	2*J= 3	P= 0	N= 1	EXC= 1.44057
FIN 2*J= 1	P= 0	N= 4	DE= -4.60456	B(E2)= 2.552408749
FIN 2*J= 1	P= 0	N= 3	DE= -4.38949	B(E2)= 3.339914201
FIN 2*J= 1	P= 0	N= 2	DE= -2.95075	B(E2)= 3.889146706
FIN 2*J= 1	P= 0	N= 1	DE= 1.44057	B(E2)= 38.226649422
***** INI *****	2*J= 3	P= 0	N= 2	EXC= 2.67883
FIN 2*J= 1	P= 0	N= 4	DE= -3.36630	B(E2)= 0.122971959
FIN 2*J= 1	P= 0	N= 3	DE= -3.15123	B(E2)= 3.892444107
FIN 2*J= 1	P= 0	N= 2	DE= -1.71249	B(E2)= 0.219998805
FIN 2*J= 1	P= 0	N= 1	DE= 2.67883	B(E2)= 6.531304448
FIN 2*J= 3	P= 0	N= 1	DE= 1.23826	B(E2)= 48.775476158
***** INI *****	2*J= 3	P= 0	N= 3	EXC= 3.43276
FIN 2*J= 1	P= 0	N= 4	DE= -2.61237	B(E2)= 0.000053047
FIN 2*J= 1	P= 0	N= 3	DE= -2.39731	B(E2)= 0.315516139
FIN 2*J= 1	P= 0	N= 2	DE= -0.95856	B(E2)= 14.297335642
FIN 2*J= 1	P= 0	N= 1	DE= 3.43276	B(E2)= 0.978372341
FIN 2*J= 3	P= 0	N= 2	DE= 0.75393	B(E2)= 5.223921605
FIN 2*J= 3	P= 0	N= 1	DE= 1.99219	B(E2)= 3.945669931
***** INI *****	2*J= 5	P= 0	N= 1	EXC= 1.90493
FIN 2*J= 1	P= 0	N= 4	DE= -4.14020	B(E2)= 1.485460457
FIN 2*J= 1	P= 0	N= 3	DE= -3.92514	B(E2)= 0.377952059
FIN 2*J= 1	P= 0	N= 2	DE= -2.48639	B(E2)= 2.910624318
FIN 2*J= 1	P= 0	N= 1	DE= 1.90493	B(E2)= 35.367936718
FIN 2*J= 3	P= 0	N= 4	DE= -3.17021	B(E2)= 0.508422431
FIN 2*J= 3	P= 0	N= 3	DE= -1.52783	B(E2)= 0.179002330
FIN 2*J= 3	P= 0	N= 2	DE= -0.77390	B(E2)= 3.611608222
FIN 2*J= 3	P= 0	N= 1	DE= 0.46436	B(E2)= 5.205250307
***** INI *****	2*J= 5	P= 0	N= 2	EXC= 3.50815

Continued on following page

# A. Shell Model Calculations

Table A.3, continued

PSDPF for B(E2) in [ $e^2 fm^4$ ]				
FIN 2*J= 1	P= 0	N= 4	DE= -2.53698	B(E2)= 0.070740616
FIN 2*J= 1	P= 0	N= 3	DE= -2.32191	B(E2)= 0.637630478
FIN 2*J= 1	P= 0	N= 2	DE= -0.88317	B(E2)= 0.202086854
FIN 2*J= 1	P= 0	N= 1	DE= 3.50815	B(E2)= 6.457011063
FIN 2*J= 3	P= 0	N= 4	DE= -1.56699	B(E2)= 2.327622539
FIN 2*J= 3	P= 0	N= 3	DE= 0.07539	B(E2)= 1.804874379
FIN 2*J= 3	P= 0	N= 2	DE= 0.82932	B(E2)= 72.959854386
FIN 2*J= 3	P= 0	N= 1	DE= 2.06758	B(E2)= 25.432269930
FIN 2*J= 5	P= 0	N= 1	DE= 1.60322	B(E2)= 1.197516340
***** INI *****	2*J= 5	P= 0	N= 3	EXC= 3.97065
FIN 2*J= 1	P= 0	N= 4	DE= -2.07448	B(E2)= 0.165216976
FIN 2*J= 1	P= 0	N= 3	DE= -1.85941	B(E2)= 3.724524262
FIN 2*J= 1	P= 0	N= 2	DE= -0.42067	B(E2)= 0.030494458
FIN 2*J= 1	P= 0	N= 1	DE= 3.97065	B(E2)= 0.744634663
FIN 2*J= 3	P= 0	N= 4	DE= -1.10448	B(E2)= 10.464769097
FIN 2*J= 3	P= 0	N= 3	DE= 0.53790	B(E2)= 1.043931345
FIN 2*J= 3	P= 0	N= 2	DE= 1.29182	B(E2)= 2.822076901
FIN 2*J= 3	P= 0	N= 1	DE= 2.53008	B(E2)= 5.206187688
FIN 2*J= 5	P= 0	N= 2	DE= 0.46250	B(E2)= 0.001360035
FIN 2*J= 5	P= 0	N= 1	DE= 2.06573	B(E2)= 5.458642058
***** INI *****	2*J= 7	P= 0	N= 1	EXC= 3.77787
FIN 2*J= 3	P= 0	N= 4	DE= -1.29727	B(E2)= 0.096639155
FIN 2*J= 3	P= 0	N= 3	DE= 0.34511	B(E2)= 1.003152375
FIN 2*J= 3	P= 0	N= 2	DE= 1.09904	B(E2)= 0.506560816
FIN 2*J= 3	P= 0	N= 1	DE= 2.33730	B(E2)= 58.315048363
FIN 2*J= 5	P= 0	N= 4	DE= -1.23424	B(E2)= 0.295524882
FIN 2*J= 5	P= 0	N= 3	DE= -0.19279	B(E2)= 6.122103730
FIN 2*J= 5	P= 0	N= 2	DE= 0.26972	B(E2)= 36.767427894
FIN 2*J= 5	P= 0	N= 1	DE= 1.87294	B(E2)= 21.199539806
***** INI *****	2*J= 7	P= 0	N= 2	EXC= 5.91183
FIN 2*J= 3	P= 0	N= 4	DE= 0.83670	B(E2)= 4.031385945
FIN 2*J= 3	P= 0	N= 3	DE= 2.47908	B(E2)= 6.483884235
FIN 2*J= 3	P= 0	N= 2	DE= 3.23300	B(E2)= 3.286604539
FIN 2*J= 3	P= 0	N= 1	DE= 4.47126	B(E2)= 0.002281470
FIN 2*J= 5	P= 0	N= 4	DE= 0.89973	B(E2)= 0.207042037
FIN 2*J= 5	P= 0	N= 3	DE= 1.94118	B(E2)= 24.442886682
FIN 2*J= 5	P= 0	N= 2	DE= 2.40368	B(E2)= 6.447331058
FIN 2*J= 5	P= 0	N= 1	DE= 4.00691	B(E2)= 0.112334818
FIN 2*J= 7	P= 0	N= 1	DE= 2.13397	B(E2)= 1.099005422
***** INI *****	2*J= 9	P= 0	N= 1	EXC= 5.47021
FIN 2*J= 5	P= 0	N= 4	DE= 0.45810	B(E2)= 0.694954931
FIN 2*J= 5	P= 0	N= 3	DE= 1.49956	B(E2)= 0.806613145
FIN 2*J= 5	P= 0	N= 2	DE= 1.96206	B(E2)= 0.000139271
FIN 2*J= 5	P= 0	N= 1	DE= 3.56528	B(E2)= 45.757688542
FIN 2*J= 7	P= 0	N= 2	DE= -0.44162	B(E2)= 0.017721192
FIN 2*J= 7	P= 0	N= 1	DE= 1.69234	B(E2)= 0.408304094
***** INI *****	2*J= 9	P= 0	N= 2	EXC= 6.50959

Continued on following page

# A. Shell Model Calculations

Table A.3, continued

PSDPF for B(E2) in [ $e^2 fm^4$ ]				
FIN 2*J= 5	P= 0	N= 4	DE= 1.49748	B(E2)= 11.495317554
FIN 2*J= 5	P= 0	N= 3	DE= 2.53893	B(E2)= 7.333573627
FIN 2*J= 5	P= 0	N= 2	DE= 3.00144	B(E2)= 0.297727038
FIN 2*J= 5	P= 0	N= 1	DE= 4.60466	B(E2)= 5.494465188
FIN 2*J= 7	P= 0	N= 2	DE= 0.59775	B(E2)= 5.822075535
FIN 2*J= 7	P= 0	N= 1	DE= 2.73172	B(E2)= 0.031148027
FIN 2*J= 9	P= 0	N= 1	DE= 1.03938	B(E2)= 0.021198923
***** INI *****	2*J= 7	P= 1	N= 1	EXC= 4.47049
FIN 2*J= 3	P= 1	N= 4	DE= -1.77673	B(E2)= 2.686693037
FIN 2*J= 3	P= 1	N= 3	DE= -1.48851	B(E2)= 1.575426879
FIN 2*J= 3	P= 1	N= 2	DE= -1.01956	B(E2)= 3.223687145
FIN 2*J= 3	P= 1	N= 1	DE= -0.63978	B(E2)= 16.804071677
FIN 2*J= 5	P= 1	N= 3	DE= -1.44468	B(E2)= 0.042420408
FIN 2*J= 5	P= 1	N= 2	DE= -1.08962	B(E2)= 3.040889428
FIN 2*J= 5	P= 1	N= 1	DE= -0.69612	B(E2)= 8.505692378
***** INI *****	2*J= 9	P= 1	N= 1	EXC= 5.69591
FIN 2*J= 5	P= 1	N= 3	DE= -0.21926	B(E2)= 2.271595289
FIN 2*J= 5	P= 1	N= 2	DE= 0.13580	B(E2)= 0.407648240
FIN 2*J= 5	P= 1	N= 1	DE= 0.52931	B(E2)= 2.549281570
FIN 2*J= 7	P= 1	N= 3	DE= -0.29452	B(E2)= 3.260009189
FIN 2*J= 7	P= 1	N= 2	DE= 0.05687	B(E2)= 5.463403271
FIN 2*J= 7	P= 1	N= 1	DE= 1.22542	B(E2)= 18.867091310
***** INI *****	2*J= 11	P= 1	N= 1	EXC= 5.81242
FIN 2*J= 7	P= 1	N= 3	DE= -0.17801	B(E2)= 9.576827069
FIN 2*J= 7	P= 1	N= 2	DE= 0.17338	B(E2)= 0.090071934
FIN 2*J= 7	P= 1	N= 1	DE= 1.34193	B(E2)= 5.194772454
FIN 2*J= 9	P= 1	N= 2	DE= -0.30569	B(E2)= 0.006811573
FIN 2*J= 9	P= 1	N= 1	DE= 0.11651	B(E2)= 5.268325488

Table A.4.: PSDPF calculations for B(M1) in  $^{33}\text{P}$  for spin states up to  $11/2_1^-$ .

PSDPF for B(M1) in [ $u_N^2$ ]				
***** INI *****	2*J= 1	P= 0	N= 2	EXC= 4.39133
FIN 2*J= 1	P= 0	N= 1	DE= 4.39132	B(M1)= 0.286148081
***** INI *****	2*J= 1	P= 0	N= 3	EXC= 5.83003
FIN 2*J= 1	P= 0	N= 2	DE= 1.43874	B(M1)= 0.006827456
FIN 2*J= 1	P= 0	N= 1	DE= 5.83006	B(M1)= 0.114130622
***** INI *****	2*J= 1	P= 0	N= 4	EXC= 6.04513
FIN 2*J= 1	P= 0	N= 3	DE= 0.21507	B(M1)= 0.145426046
FIN 2*J= 1	P= 0	N= 2	DE= 1.65381	B(M1)= 0.002451433
FIN 2*J= 1	P= 0	N= 1	DE= 6.04513	B(M1)= 0.168453718
***** INI *****	2*J= 3	P= 0	N= 1	EXC= 1.44053
FIN 2*J= 1	P= 0	N= 4	DE= -4.60456	B(M1)= 0.000110201
FIN 2*J= 1	P= 0	N= 3	DE= -4.38949	B(M1)= 0.003366842
FIN 2*J= 1	P= 0	N= 2	DE= -2.95075	B(M1)= 0.001133333

Continued on following page

# A. Shell Model Calculations

Table A.4, continued

PSDPF for $B(M1)$ in $[u_N^2]$				
FIN 2*J= 1	P= 0	N= 1	DE= 1.44057	B(M1)= 0.004104441
***** INI *****	2*J= 3	P= 0	N= 2	EXC= 2.67883
FIN 2*J= 1	P= 0	N= 4	DE= -3.3663	B(M1)= 0.068279364
FIN 2*J= 1	P= 0	N= 3	DE= -3.15123	B(M1)= 0.000897125
FIN 2*J= 1	P= 0	N= 2	DE= -1.71249	B(M1)= 0.069954086
FIN 2*J= 1	P= 0	N= 1	DE= 2.67883	B(M1)= 0.092576472
FIN 2*J= 3	P= 0	N= 1	DE= 1.23826	B(M1)= 0.129684614
***** INI *****	2*J= 3	P= 0	N= 3	EXC= 3.43273
FIN 2*J= 1	P= 0	N= 4	DE= -2.61237	B(M1)= 0.08082769
FIN 2*J= 1	P= 0	N= 3	DE= -2.39731	B(M1)= 0.01582251
FIN 2*J= 1	P= 0	N= 2	DE= -0.95856	B(M1)= 0.02250102
FIN 2*J= 1	P= 0	N= 1	DE= 3.43276	B(M1)= 0.006868949
FIN 2*J= 3	P= 0	N= 2	DE= 0.75393	B(M1)= 0.000298812
FIN 2*J= 3	P= 0	N= 1	DE= 1.99219	B(M1)= 0.002115943
***** INI *****	2*J= 5	P= 0	N= 1	EXC= 1.90493
FIN 2*J= 3	P= 0	N= 4	DE= -3.17021	B(M1)= 0.129877091
FIN 2*J= 3	P= 0	N= 3	DE= -1.52783	B(M1)= 0.04512377
FIN 2*J= 3	P= 0	N= 2	DE= -0.7739	B(M1)= 0.128705458
FIN 2*J= 3	P= 0	N= 1	DE= 0.46436	B(M1)= 0.004781283
***** INI *****	2*J= 5	P= 0	N= 2	EXC= 3.50813
FIN 2*J= 3	P= 0	N= 4	DE= -1.56699	B(M1)= 0.009136546
FIN 2*J= 3	P= 0	N= 3	DE= 0.07539	B(M1)= 0.011982069
FIN 2*J= 3	P= 0	N= 2	DE= 0.82932	B(M1)= 0.006685454
FIN 2*J= 3	P= 0	N= 1	DE= 2.06758	B(M1)= 0.113786808
FIN 2*J= 5	P= 0	N= 1	DE= 1.60322	B(M1)= 0.272947565
***** INI *****	2*J= 5	P= 0	N= 3	EXC= 3.97063
FIN 2*J= 3	P= 0	N= 4	DE= -1.10448	B(M1)= 0.00027832
FIN 2*J= 3	P= 0	N= 3	DE= 0.5379	B(M1)= 0.271023425
FIN 2*J= 3	P= 0	N= 2	DE= 1.29182	B(M1)= 0.076896565
FIN 2*J= 3	P= 0	N= 1	DE= 2.53008	B(M1)= 0.104755069
FIN 2*J= 5	P= 0	N= 2	DE= 0.4625	B(M1)= 0.04030582
FIN 2*J= 5	P= 0	N= 1	DE= 2.06573	B(M1)= 0.002713869
***** INI *****	2*J= 7	P= 0	N= 1	EXC= 3.77783
FIN 2*J= 5	P= 0	N= 4	DE= -1.23424	B(M1)= 0.00012459
FIN 2*J= 5	P= 0	N= 3	DE= -0.19279	B(M1)= 0.006489346
FIN 2*J= 5	P= 0	N= 2	DE= 0.26972	B(M1)= 0.008068235
FIN 2*J= 5	P= 0	N= 1	DE= 1.87294	B(M1)= 0.000024854
***** INI *****	2*J= 7	P= 0	N= 2	EXC= 5.91183
FIN 2*J= 5	P= 0	N= 4	DE= 0.89973	B(M1)= 0.00242147
FIN 2*J= 5	P= 0	N= 3	DE= 1.94118	B(M1)= 0.040387939
FIN 2*J= 5	P= 0	N= 2	DE= 2.40368	B(M1)= 0.00559959
FIN 2*J= 5	P= 0	N= 1	DE= 4.00691	B(M1)= 0.059903524
FIN 2*J= 7	P= 0	N= 1	DE= 2.13397	B(M1)= 0.000258156
***** INI *****	2*J= 9	P= 0	N= 1	EXC= 5.47023

Continued on following page

# A. Shell Model Calculations

Table A.4, continued

PSDPF for $B(M1)$ in $[u_N^2]$				
FIN 2*J= 7	P= 0	N= 2	DE= -0.44162	B(M1)= 0.19221503
FIN 2*J= 7	P= 0	N= 1	DE= 1.69234	B(M1)= 0.004239684
***** INI *****	2*J= 9	P= 0	N= 2	EXC= 6.50963
FIN 2*J= 7	P= 0	N= 2	DE= 0.59775	B(M1)= 0.000014089
FIN 2*J= 7	P= 0	N= 1	DE= 2.73172	B(M1)= 0.337094089
FIN 2*J= 9	P= 0	N= 1	DE= 1.03938	B(M1)= 0.241216669
***** INI *****	2*J= 7	P= 1	N= 1	EXC= 4.47053
FIN 2*J= 5	P= 1	N= 3	DE= -1.44468	B(M1)= 0.002215613
FIN 2*J= 5	P= 1	N= 2	DE= -1.08962	B(M1)= 0.155944357
FIN 2*J= 5	P= 1	N= 1	DE= -0.69612	B(M1)= 0.007697199
***** INI *****	2*J= 7	P= 1	N= 2	EXC= 5.63903
FIN 2*J= 5	P= 1	N= 3	DE= -0.27613	B(M1)= 0.000147395
FIN 2*J= 5	P= 1	N= 2	DE= 0.07893	B(M1)= 0.061725007
FIN 2*J= 5	P= 1	N= 1	DE= 0.47243	B(M1)= 0.029228474
FIN 2*J= 7	P= 1	N= 1	DE= 1.16855	B(M1)= 0.010569573
***** INI *****	2*J= 7	P= 1	N= 3	EXC= 5.99043
FIN 2*J= 5	P= 1	N= 3	DE= 0.07527	B(M1)= 0.011905542
FIN 2*J= 5	P= 1	N= 2	DE= 0.43032	B(M1)= 0.019865789
FIN 2*J= 5	P= 1	N= 1	DE= 0.82383	B(M1)= 0.013511275
FIN 2*J= 7	P= 1	N= 2	DE= 0.35139	B(M1)= 0.056532489
FIN 2*J= 7	P= 1	N= 1	DE= 1.51994	B(M1)= 0.11097844
***** INI *****	2*J= 9	P= 1	N= 1	EXC= 5.69593
FIN 2*J= 7	P= 1	N= 3	DE= -0.29452	B(M1)= 0.017523691
FIN 2*J= 7	P= 1	N= 2	DE= 0.05687	B(M1)= 0.003313093
FIN 2*J= 7	P= 1	N= 1	DE= 1.22542	B(M1)= 0.004439641
***** INI *****	2*J= 9	P= 1	N= 2	EXC= 6.11813
FIN 2*J= 7	P= 1	N= 3	DE= 0.12768	B(M1)= 0.001612274
FIN 2*J= 7	P= 1	N= 2	DE= 0.47908	B(M1)= 0.011306733
FIN 2*J= 7	P= 1	N= 1	DE= 1.64763	B(M1)= 0.006756998
FIN 2*J= 9	P= 1	N= 1	DE= 0.42221	B(M1)= 0.673997699
***** INI *****	2*J= 11	P= 1	N= 1	EXC= 5.81243
FIN 2*J= 9	P= 1	N= 2	DE= -0.30569	B(M1)= 0.079635081
FIN 2*J= 9	P= 1	N= 1	DE= 0.11651	B(M1)= 0.237707393

## B. Mapping and technical drawing of LYCCA FEE-mezzanine

Since the arrangement of ASIC channels on FEE-mezzanine is neither orderly serial nor identical to the physical position of LYCCA-DSSSD channels, the channel mapping was determined. Table B.1 indicates the correct assignment. The schematics of FEE-mezzanine are shown in Fig. B.1, B.2, B.3, B.4, B.5. The physical position of LYCCA-DSSSD channels is illustrated by the following figure (adopted from [97]):

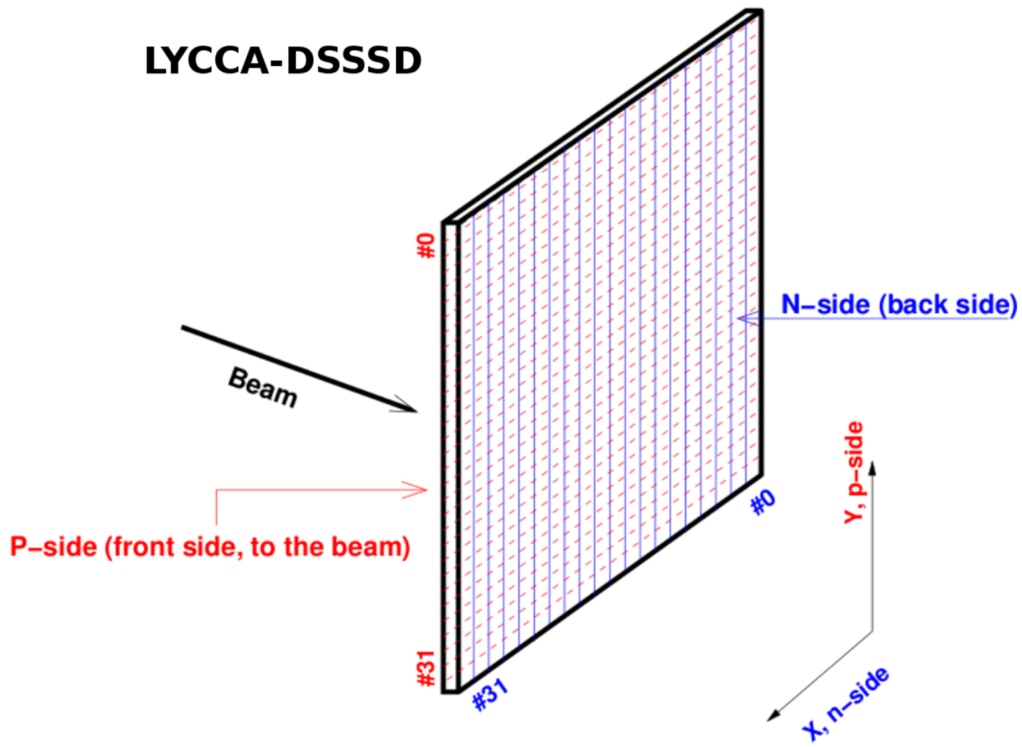


Table B.1.: ASIC channel mapping. The assignment is according to the physical position of p- and n-side on each DSSSD (cf. Fig. 5.4) and the ASIC channel number.

p-side (ASIC3 & ASIC4)			n-side (ASIC1 & ASIC2)		
Phys. pos.	AISC channel	AISC3/ASIC4 (0-15)	Phys. pos.	AISC channel	AISC1/ASIC2
0	32	AISC3/0	0	1	ASIC1/1
1	35	ASIC3/3	1	0	ASIC1/0
2	34	AISC3/2	2	4	ASIC1/4
3	33	ASIC3/1	3	3	ASIC1/3
4	39	ASIC3/7	4	2	ASIC1/2
5	38	ASIC3/6	5	7	ASIC1/7
6	37	ASIC3/5	6	6	ASIC1/6
7	36	ASIC3/4	7	5	ASIC1/5
8	42	ASIC3/10	8	11	ASIC1/11
9	41	ASIC3/9	9	10	ASIC1/10
10	40	ASIC3/8	10	9	ASIC1/9
11	46	ASIC3/14	11	8	ASIC1/8
12	45	ASIC3/13	12	14	ASIC1/14
13	44	ASIC3/12	13	13	ASIC1/13
14	43	ASIC3/11	14	12	ASIC1/12
15	49	ASIC4/1	15	18	ASIC2/2
16	48	ASIC4/0	16	17	ASIC2/1
17	47	ASIC3/15	17	16	ASIC2/0
18	62	ASIC4/14	18	15	ASIC1/15
19	52	ASIC4/4	19	21	ASIC2/5
20	51	ASIC4/3	20	20	ASIC2/4
21	50	ASIC4/2	21	19	ASIC2/3
22	59	ASIC4/11	22	25	ASIC2/9
23	56	ASIC4/8	23	24	ASIC2/8
24	53	ASIC4/5	24	23	ASIC2/7
25	63	ASIC4/15	25	22	ASIC2/6
26	60	ASIC4/12	26	28	ASIC2/12
27	57	ASIC4/9	27	27	ASIC2/11
28	54	ASIC4/6	28	26	ASIC2/10
29	61	ASIC4/13	29	31	ASIC2/15
30	58	ASIC4/10	30	30	ASIC2/14
31	55	ASIC4/7	31	29	ASIC2/13



## B. Mapping and technical drawing of LYCCA FEE-mezzanine

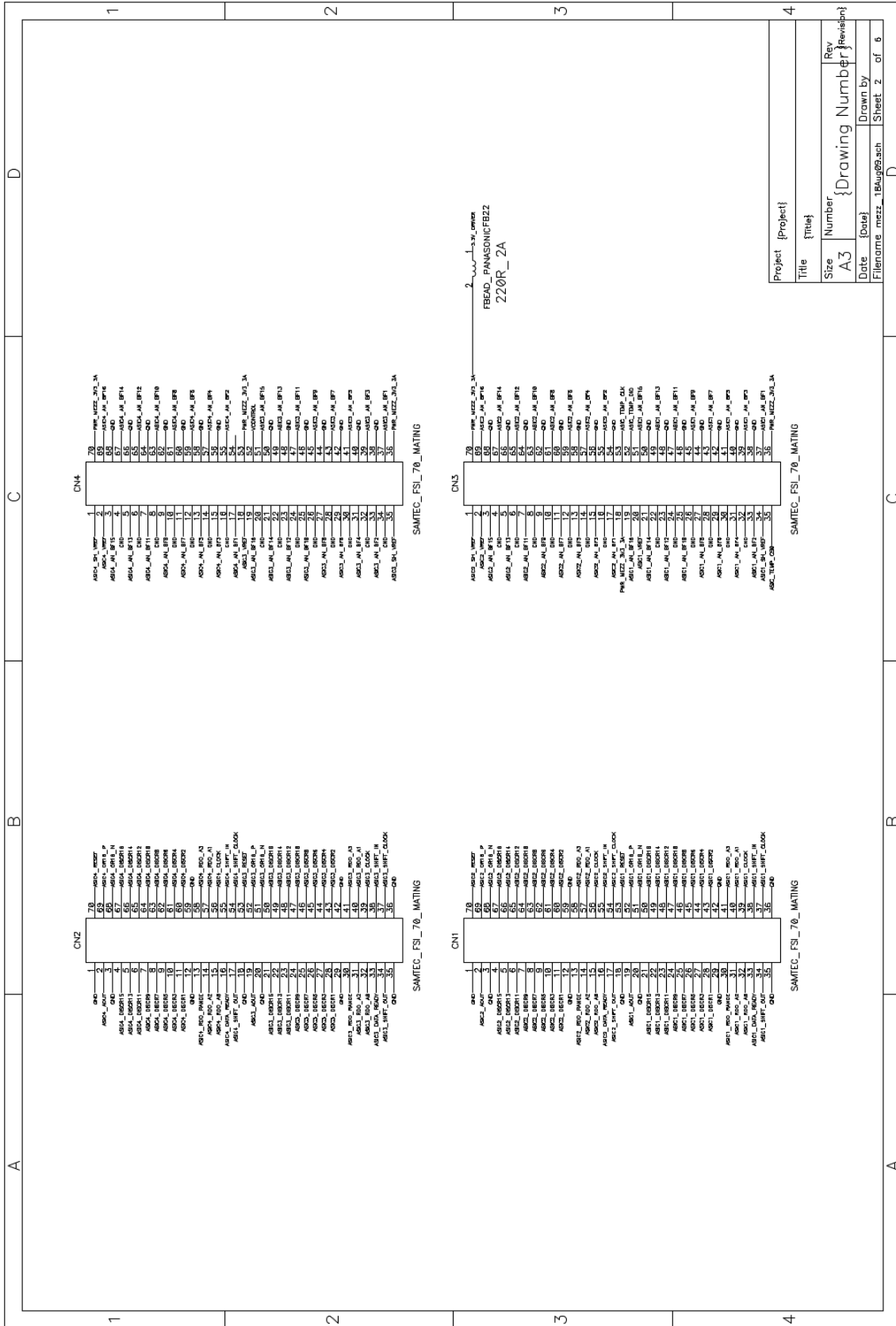


Figure B.1.: Schematic of four ASIC connectors on FEE-board.

AS1

Capacitor Multilayer Ceramic X7R 15v 10%

Resistor Thin Film Zippac C 0.1% 330K

Capacitor Multilayer Ceramic X7R 50v 10%

Project {Project}

Title {Title}

Size Number

A3

Date {Date}

Filename mezz\_18Aug05.sch

Sheet 3 of 6

148

## B. Mapping and technical drawing of LYCCA FEE-mezzanine

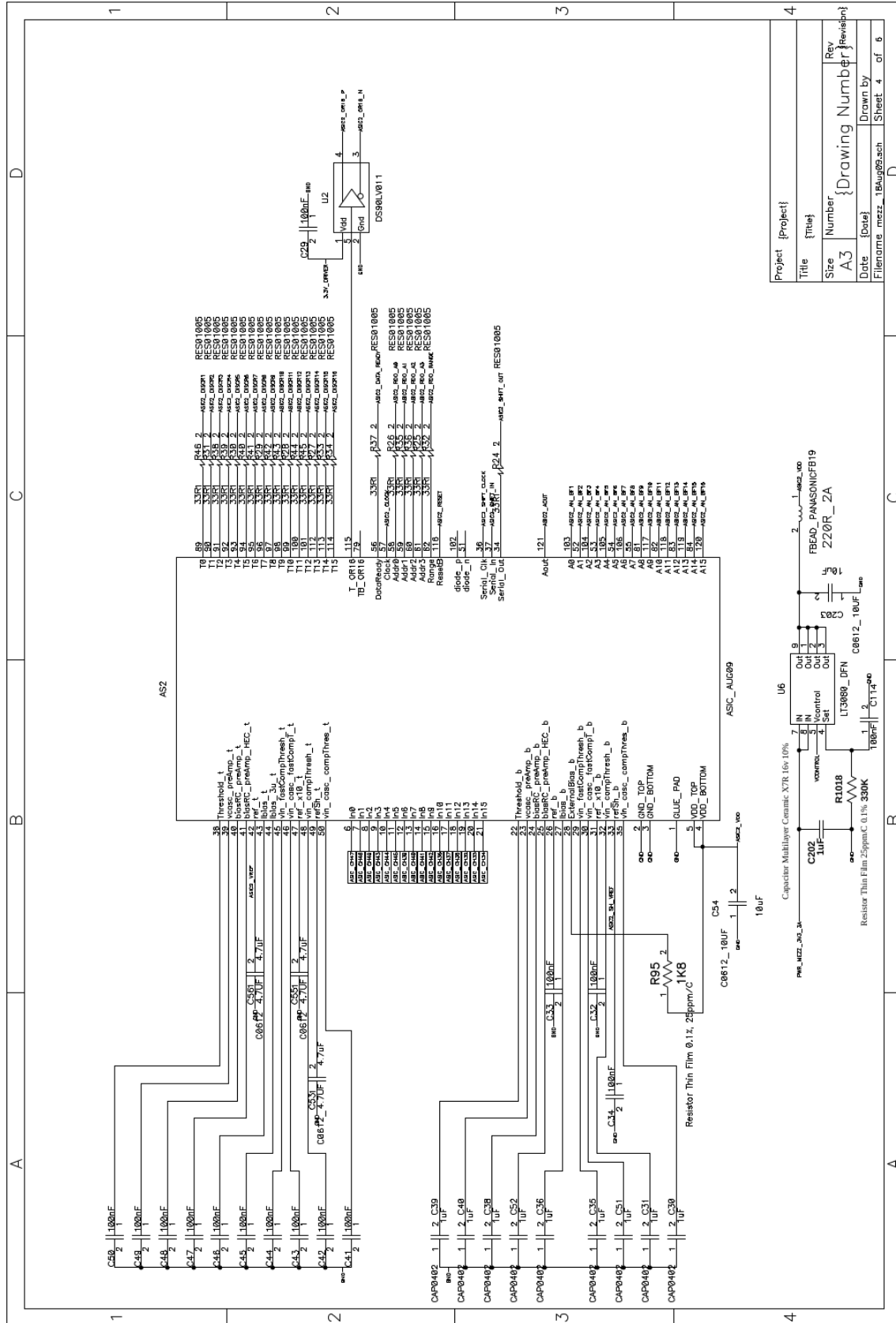
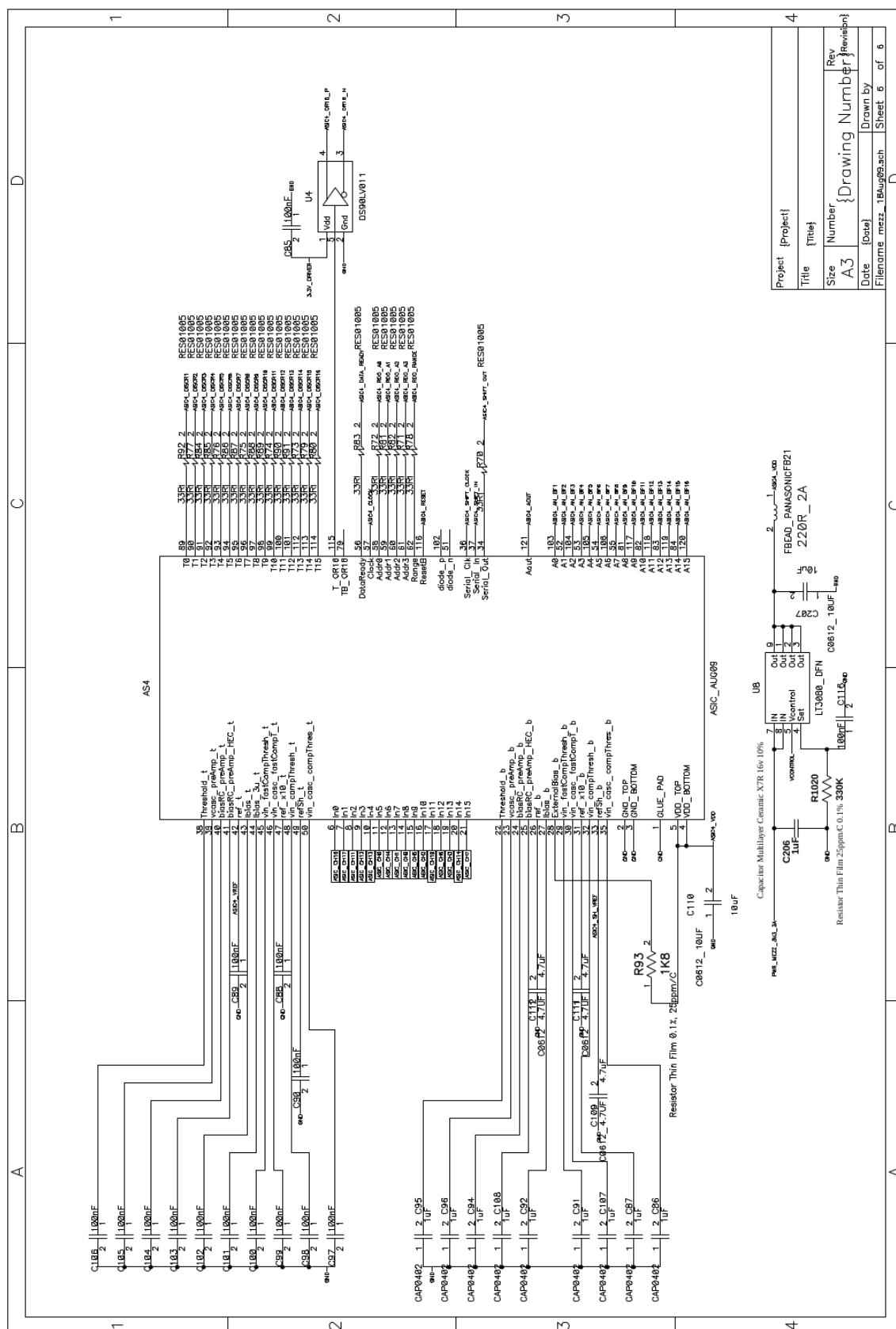


Figure B.3.: Schematic of ASIC2.

150

Figure B.5.: Schematic of ASIC4.





# List of Tables

1.1. Single Particle Energies (SPE) in MeV for the PSDPF interaction. . .	30
2.1. Summary of experimental results for $^{33}\text{P}$ . . . . .	41
2.2. Summary of experimental results for $^{33}\text{S}$ . . . . .	46
2.3. Extreme values of the multipole mixing ratio $\delta$ . . . . .	49
2.4. $\gamma\gamma$ angular-correlation groups by HORUS . . . . .	53
3.1. Comparison between experimental and calculated states in $^{33}\text{P}$ . . . .	60
3.2. Comparison between experimental and theoretical values of $B(M1)$ and $B(E2)$ in $^{33}\text{P}$ . . . . .	70
3.3. Comparison between experimental and calculated states in $^{33}\text{S}$ . . . .	71
3.4. [Comparison between experimental and theoretical values of $B(M1)$ and $B(E2)$ in $^{33}\text{S}$ . . . . .	72
5.1. Overview of LYCCA-DSSSD characteristics . . . . .	87
5.2. Overview of LYCCA-CsI(TI) characteristics . . . . .	90
6.1. Result of Pulser test . . . . .	111
6.2. Information of the employed triple-alpha source . . . . .	112
6.3. Decomposition of the triple-alpha spectrum . . . . .	114
A.1. PSDPF calculations for level scheme in $^{33}\text{P}$ . . . . .	137
A.2. PSDPF calculations for level scheme in $^{33}\text{S}$ . . . . .	139
A.3. PSDPF calculations for $B(E2)$ in $^{33}\text{P}$ . . . . .	140
A.4. PSDPF calculations for $B(M1)$ in $^{33}\text{P}$ . . . . .	142
B.1. ASIC channel mapping . . . . .	146

# List of Figures

1.1. Schematic illustration of the nucleon-nucleon potential . . . . .	16
1.2. Single-particle potentials . . . . .	17
1.3. Single-particle states in the shell model . . . . .	18
1.4. Comparison of experimental to calculated microscopic energies . . . .	19
1.5. Two-neutron separation energies $N = 42$ to $65$ . . . . .	19
1.6. Comparison of the one-particle and one-hole states in nuclei around $^{16}\text{O}$ . . . . .	20
1.7. Number of energy states used for the USD Hamiltonian for each nucleus	24
1.8. Number of energy states used for the USDA and USDB Hamiltonian for each nucleus . . . . .	24
1.9. Difference between experimental and theoretical ground-state binding energies . . . . .	25
1.10. Schematic presentation of the configuration of nuclei in island of in- version . . . . .	27
1.11. Chart of $sd$ -shell nuclei with known negative-parity states . . . . .	29
1.12. Chart of $sd$ -shell nuclei included in the fit of $1\hbar\omega$ states . . . . .	30
1.13. Comparison of the experimental and calculated excited states in $N =$ $18$ and $19$ isotones . . . . .	31
1.14. Level scheme of $^{33}\text{P}$ from previous work . . . . .	32
1.15. Level scheme of $^{33}\text{S}$ from previous work . . . . .	33
2.1. Schematic drawing of the HORUS $\gamma$ -ray spectrometer . . . . .	36
2.2. Projection spectrum of the $^{13}\text{C} + ^{26}\text{Mg}$ fusion-evaporation reaction .	37
2.3. $\gamma\gamma$ -coincidence spectra in $^{33}\text{P}$ . . . . .	38
2.4. Level scheme of $^{33}\text{P}$ from present work . . . . .	40
2.5. $\gamma\gamma$ -coincidence spectra in $^{33}\text{S}$ . . . . .	43
2.6. Level scheme of $^{33}\text{S}$ from present work . . . . .	45
2.7. Angular distribution of $ X_1^{0,\pm 1}(\theta) ^2$ . . . . .	50
2.8. Correlation of two coincident $\gamma$ rays . . . . .	51
2.9. $\gamma\gamma$ angular correlation for 2378/1848 keV cascade . . . . .	54
2.10. $\gamma\gamma$ angular correlations for known states . . . . .	55



## List of Figures

2.11. $\gamma\gamma$ angular correlations for 6936-keV state . . . . .	56
2.12. $\gamma\gamma$ angular correlations for new energy levels . . . . .	57
3.1. Detailed comparison between experimental and calculated levels in $^{33}\text{P}$	62
3.2. Detailed comparison between experimental and calculated levels in $^{33}\text{S}$	66
4.1. Chart of Nuclides . . . . .	75
4.2. Structure of Super-FRS . . . . .	76
4.3. AGATA detector . . . . .	77
4.4. LYCCA detector system . . . . .	78
4.5. LYCCA setup in PreSPEC campaign . . . . .	80
5.1. Plot of $\Delta E - E$ relationship . . . . .	82
5.2. Band structure of p-n junction . . . . .	84
5.3. Schematic of the double sided silicon strip detector . . . . .	85
5.4. A view of the LYCCA-DSSSD . . . . .	86
5.5. A block of LYCCA-CsI scintillators . . . . .	87
5.6. Band structure in a scintillation crystal . . . . .	88
5.7. CsI crystal . . . . .	89
5.8. Technical drawing of a LYCCA $\Delta E - E$ telescope . . . . .	91
5.9. Connection of CsI block . . . . .	92
5.10. View of the charge-sensitive preamplifier . . . . .	92
5.11. View of the AIDA ASIC . . . . .	93
5.12. Simplified diagram of the AIDA preamplifiers . . . . .	94
5.13. Schematic diagram of the functionality of one ASCII channel . . . . .	95
5.14. View of a FPGA board . . . . .	96
5.15. Front End Electronics (FEE) concept . . . . .	98
5.16. Adapter boards for FEE modules . . . . .	99
5.17. View of LYCCA-electronic system . . . . .	100
5.18. Connection of MACB units . . . . .	100
5.19. Front panel of MACB . . . . .	101
5.20. Technical drawing of LYCCA chamber . . . . .	103
5.21. Technical drawing of the new mechanical structure of LYCCA chamber	104
5.22. Illustration of the LYCCA chamber with the new beam pipe . . . . .	104
5.23. Complete LYCCA setup at IKP Cologne . . . . .	105
6.1. LYCCA Experiment Control window . . . . .	106
6.2. Window of AIDA Hardware Control . . . . .	107
6.3. Example of a correctly started DAQ Run . . . . .	108

## List of Figures

6.4. Monitoring of hardware temperatures . . . . .	108
6.5. View of the Configuration of ASICs . . . . .	109
6.6. View of statistics of ASICs . . . . .	110
6.7. View of MERGE Control for LYCCA setup . . . . .	110
6.8. Spectra of pulser test . . . . .	111
6.9. Illustration of the location of 14 installed telescopes . . . . .	113
6.10. Triple-alpha spectra from DSSSD . . . . .	114
6.11. Decomposition of the triple-alpha spectrum . . . . .	115
6.12. Two-dimension plot of $\alpha$ energy to ASIC channels . . . . .	116
6.13. Illustration of the double-peak structure on strip Back6 and Back7 . .	117
6.14. Correction of spectrum for p-side strips . . . . .	118
6.15. Correlation of adjoining strips on DSSSD . . . . .	119
6.16. Energy correlation of p- and n-side . . . . .	120
6.17. Location of the 10 DSSSDs in the in-beam experiment . . . . .	121
6.18. Calibrated energy spectra of $^{12}\text{C}$ -beam . . . . .	121
6.19. Calibrated in-beam energy spectra . . . . .	122
6.20. Comparison of the 50 MeV energy spectra of the p-side and n-side strip	123
6.21. PN-correlation of telescopes $T5$ and $T24$ . . . . .	124
6.22. PN-correlation of $T3$ , $T6$ , $T22$ and $T25$ . . . . .	125
6.23. PN-correlation of $T4$ , $T9$ , $T23$ and $T26$ . . . . .	126
6.24. Angular distribution of elastically scattered $^{12}\text{C}$ -particles . . . . .	128
6.25. Energy spectra of $^{12}\text{C}+^{12}\text{C}$ scattering from telescope $T5$ . . . . .	130
6.26. Angular distribution of $(0^+, 0^+)$ state of $^{12}\text{C}+^{12}\text{C}$ scattering . . . .	131
6.27. Energy spectra of $^{12}\text{C}+^{12}\text{C}$ scattering from telescopes $T22$ and $T23$ .	132
7.1. New design of the LYCCA chamber . . . . .	134
7.2. New LYCCA chamber with DSSSDs installed . . . . .	135
B.1. Schematic of FEE connector . . . . .	147
B.2. Schematic of ASIC1 . . . . .	148
B.3. Schematic of ASIC2 . . . . .	149
B.4. Schematic of ASIC3 . . . . .	150
B.5. Schematic of ASIC4 . . . . .	151

# Bibliography

- [1] J. W. Holt, N. Kaiser, and W. Weise, *Progress in Particle and Nuclear Physics* **73**, 35 (2013).
- [2] B. Loiseau and Y. Nogami, *Nucl. Phys. B* **2**, 470 (1967).
- [3] H. Witała *et al.*, *Phys. Rev. Lett.* **81**, 1183 (1998).
- [4] E. Epelbaum *et al.*, *Phys. Rev. C* **66**, 064001 (2002).
- [5] P. Mermod *et al.*, *Phys. Lett. B* **597**, 243 (2004).
- [6] G. Musiol, J. Ranft, R. Reif, and D. Seelinger, *Kern- und Elementarteilchenphysik* (Verlag Harri Deutsch, Thun, Frankfurt am Main, 2. Auflage 1995) p. 305.
- [7] O. Haxel, J. H. D. Jensen, and H. E. Suess, *Phys. Rev.* **75**, 1766 (1949).
- [8] M. G. Mayer, *Phys. Rev.* **75**, 1969 (1949).
- [9] P. Möller, W. Myers, W. Swiatecki, and J. Treiner, *Atomic Data and Nuclear Data Tables* **39**, 225 (1988).
- [10] P. Möller, A. Sierk, T. Ichikawa, and H. Sagawa, *Atomic Data and Nuclear Data Tables* **109-110**, 1 (2016).
- [11] G. Audi, A. Wapstra, and C. Thibault, *Nuclear Physics A* **729**, 337 (2003).
- [12] Y. Suzuki, *Progress of Theoretical Physics* **55**, 1751 (1976).
- [13] J. Chen and B. Singh, *Nuclear Data Sheets* **112**, 1393 (2011).
- [14] A. Ozawa *et al.*, *Phys. Rev. Lett.* **84**, 5493 (2000).
- [15] M. Freer, *Rep. on Prog. in Phys.* **70**, 2149 (2007).
- [16] A. Arima and F. Iachello, *Phys. Rev. Lett.* **35**, 1069 (1975).
- [17] J. E. García-Ramos *et al.*, *Phys. Rev. C* **89**, 034313 (2014).

## Bibliography

- [18] H. Hergert *et al.*, [Phys. Rev. Lett. \*\*110\*\*, 242501 \(2013\)](#).
- [19] D. Witthaut, S. Mossmann, and H. J. Korsch, [Jour. of Phys. A \*\*38\*\*, 1777 \(2005\)](#).
- [20] B. Wildenthal, [Prog. Part. Nucl. Phys. \*\*11\*\*, 5 \(1984\)](#).
- [21] B. A. Brown and B. H. Wildenthal, [Annu. Rev. Nucl. Part. Sci. \*\*38\*\*, 29 \(1988\)](#).
- [22] B. A. Brown and W. A. Richter, [Phys. Rev. C \*\*74\*\*, 034315 \(2006\)](#).
- [23] E. K. Warburton, J. A. Becker, and B. A. Brown, [Phys. Rev. C \*\*41\*\*, 1147 \(1990\)](#).
- [24] B. A. Brown, [Physics \*\*3\*\*, 104 \(2010\)](#).
- [25] E. Caurier, F. Nowacki, and A. Poves, [Phys. Rev. C \*\*90\*\*, 014302 \(2014\)](#).
- [26] E. K. Warburton, J. A. Becker, and B. A. Brown, [Phys. Rev. C \*\*41\*\*, 1147 \(1990\)](#).
- [27] J. B. McGrory, [Phys. Rev. C \*\*8\*\*, 693 \(1973\)](#).
- [28] D. Millener and D. Kurath, [Nuclear Physics A \*\*255\*\*, 315 \(1975\)](#).
- [29] K. Wimmer *et al.*, [Phys. Rev. Lett. \*\*105\*\*, 252501 \(2010\)](#).
- [30] J. Retamosa, E. Caurier, F. Nowacki, and A. Poves, [Phys. Rev. C \*\*55\*\*, 1266 \(1997\)](#).
- [31] E. Caurier, F. Nowacki, A. Poves, and J. Retamosa, [Phys. Rev. C \*\*58\*\*, 2033 \(1998\)](#).
- [32] S. Nummela *et al.*, [Phys. Rev. C \*\*63\*\*, 044316 \(2001\)](#).
- [33] A. Poves and A. Zuker, [Phys. Rep. \*\*70\*\*, 235 \(1981\)](#).
- [34] S. Kahana, H. C. Lee, and C. K. Scott, [Phys. Rev. \*\*180\*\*, 956 \(1969\)](#).
- [35] H. L. Crawford *et al.*, [Phys. Rev. C \*\*89\*\*, 041303 \(2014\)](#).
- [36] F. Nowacki and A. Poves, [Phys. Rev. C \*\*79\*\*, 014310 \(2009\)](#).
- [37] M. Bouhelal *et al.*, [Nucl. Phys. A \*\*864\*\*, 113 \(2011\)](#).
- [38] E. Courier and F. Nowacki, [Acta. Phys. Pol. \*\*30\*\*, 705 \(1999\)](#).

## Bibliography

- [39] Caurier *et al.*, *Phys. Rev. C* **59**, 2033 (1999).
- [40] E. Caurier and others, *Rev. Mod. Phys.* **77**, 427 (2005).
- [41] S. Cohen and D. Kurath, *Nuclear Physics* **73**, 1 (1965).
- [42] E. K. Warburton and B. A. Brown, *Phys. Rev. C* **46**, 923 (1992).
- [43] S. Aydin *et al.*, *Phys. Rev. C* **86**, 024320 (2012).
- [44] S. Aydin *et al.*, *Phys. Rev. C* **89**, 014310 (2014).
- [45] R. Chapman *et al.*, *Phys. Rev. C* **92**, 044308 (2015).
- [46] M. Bouhelal, F. Haas, E. Caurier, and F. Nowacki, *J. Phys.: Conf. Series* **580**, 012025 (2015).
- [47] R. C. Barse, D. H. Youngblood, and J. L. Yntema, *Phys. Rev.* **167**, 1043 (1968).
- [48] W. Davies, J. Hardy, and W. Darcey, *Nucl. Phys. A* **128**, 465 (1969).
- [49] E. Berkowitz, A. Rollefson, E. Berners, and C. Browne, *Nucl. Phys. A* **140**, 173 (1970).
- [50] W. R. Harris, K. Nagatani, and J. W. Olness, *Phys. Rev. C* **2**, 1412 (1970).
- [51] R. Chakrabarti *et al.*, *Phys. Rev. C* **80**, 034326 (2009).
- [52] N. Davis and J. Nelson, *J. Phys. G: Nucl. Phys.* **13**, 375 (1987).
- [53] W. Currie, L. Earwaker, J. Martin, and A. S. Gupta, *Physics Letters B* **28**, 480 (1969).
- [54] P. E. Carr *et al.*, *Journal of Physics A: Mathematical, Nuclear and General* **6**, 685 (1973).
- [55] A. R. Poletti, T. T. Bardin, J. G. Pronko, and R. E. McDonald, *Phys. Rev. C* **7**, 1433 (1973).
- [56] P. Wagner *et al.*, *Phys. Rev. C* **7**, 2418 (1973).
- [57] L. Sanin *et al.*, *Nucl. Phys. A* **245**, 317 (1975).
- [58] J. Halperin, C. H. Johnson, R. R. Winters, and R. L. Macklin, *Phys. Rev. C* **21**, 545 (1980).

## Bibliography

- [59] W. P. Abfalterer, R. W. Finlay, and S. M. Grimes, *Phys. Rev. C* **62**, 064312 (2000).
- [60] J. A. Becker, L. F. Chase, D. B. Fossan, and R. E. McDonald, *Phys. Rev.* **146**, 761 (1966).
- [61] J. Dubois, *Nucl. Phys. A* **117**, 533 (1968).
- [62] K. T. Knöpfle *et al.*, *Phys. Rev. C* **4**, 818 (1971).
- [63] A. Bisoi *et al.*, *Phys. Rev. C* **90**, 024328 (2014).
- [64] F. Pühlhofer, *Nucl. Phys. A* **280**, 267 (1977).
- [65] O. Tarasov and D. Bazin, *Nucl. Instr. Meth. Phys. Res. B* **266**, 4657 (2008).
- [66] L. Netterdon *et al.*, *Nucl. Instr. Meth. Phys. Res. A* **754**, 94 (2014).
- [67] B. Hubbard-Nelson, M. Momayezi, and W. K. Warburton, *Nucl. Inst. and Meth. in Phys. Res. Sec. A*: **422**, 411 (1999).
- [68] W. Skulski *et al.*, *ACTA PHYSICA POLONICA B* **31**, 47 (2000).
- [69] M. Elvers, *Investigation of Octupole Vibrations in the Rare-Earth Region with Different Experimental Probes and Implementation of a Multithreaded Evaluation Software for Double Coincidence Listmode Data*, Ph.D. thesis, Institut für Kernphysik, Universität zu Köln (2011), dissertation.
- [70] S. Raman *et al.*, *Phys. Rev. C* **32**, 18 (1985).
- [71] H. Morinaga and T. Yamazaki, *In-beam Gamma-ray Spectroscopy* (North Holland Publishing Company, Amsterdam, new York, Oxford, 1976).
- [72] K. S. Krane, R. M. Steffen, and R. M. Wheeler, *Nucl. Data Tab.* **11**, 351 (1973).
- [73] K. S. Krane and R. M. Steffen, *Phys. Rev. C* **2**, 724 (1970).
- [74] I. Wiedenhöver *et al.*, *Phys. Rev. C* **58**, 721 (1998).
- [75] A. Blazhev, “private communication: shell model calculations for *sd* shell nuclei,” (2015).
- [76] M. R. Nixon *et al.*, *Journal of Physics G: Nuclear Physics* **1**, 430 (1975).

## Bibliography

- [77] M. Bouhelal, “private communication: PSDPF calculations for *sd* shell nuclei,” (2017).
- [78] W. A. Richter, S. Mkhize, and B. A. Brown, *Phys. Rev. C* **78**, 064302 (2008).
- [79] J. Cummings and D. Donahue, *Nucl. Phys. A* **142**, 609 (1970).
- [80] “National nuclear data center,” <https://www.nndc.bnl.gov/chart/>.
- [81] M. Winkler *et al.*, *Nuclear Instruments and Methods B* **266**, 4183 (2008).
- [82] Z. Podolyak *et al.*, *Technical Proposal of HISPEC* (FAIR-NUSTAR, 2005).
- [83] S. Akkoyun *et al.*, *Nuclear Instruments and Methods A* **668**, 26 (2012).
- [84] R. Lozeva *et al.*, *Nucl. Instr. Meth. Phys. Res. A* **562**, 298 (2006).
- [85] P. Golubev *et al.*, *Nuclear Instruments and Methods A* **723**, 55 (2013).
- [86] D. Ralet *et al.*, *Nuclear Instruments and Methods A* **786**, 32 (2015).
- [87] A. Wendt *et al.*, *Phys. Rev. C* **90**, 054301 (2014).
- [88] K. Moschner *et al.*, *Phys. Rev. C* **94**, 054323 (2016).
- [89] G. Guastalla *et al.*, *Phys. Rev. Lett.* **110**, 172501 (2013).
- [90] K. Krane, *Introductory Nuclear Physics* (John Wiley and Sons, 3. edition 1988).
- [91] R. Hoischen *et al.*, *Nuclear Instruments and Methods A* **654**, 354 (2011).
- [92] H. Spieler, *Semiconductor Detector Systems*, Series on Semiconductor Science and Technology (Oxford University Press, Oxford, 2005).
- [93] A. Örbom *et al.*, *Medical Physics* **42**, 575 (2015).
- [94] J. Yorkston *et al.*, *Nuclear Instruments and Methods A* **262**, 353 (1987).
- [95] D. Torresi *et al.*, *Nuclear Instruments and Methods A* **713**, 11 (2013).
- [96] L. Grassi *et al.*, *Nuclear Instruments and Methods A* **767**, 99 (2014).
- [97] J. Taprogge, *First in-beam measurements with the  $\Delta E$ -E-TOF LYCCA-Array at relativistic energies*, Master’s thesis, Institut für Kernphysik, Universität zu Köln (2011).

## Bibliography

- [98] D. Rudolph *et al.*, *Technical Design Report of LYCCA* (FAIR-NUSTAR, 2008).
- [99] A. Wendt, *Isospin symmetry in the sd shell: Coulomb excitation of  $^{33}\text{Ar}$  at relativistic energies and the new Lund-York-Cologne-Calorimeter*, Ph.D. thesis, Institut für Kernphysik, Universität zu Köln (2012), dissertation.
- [100] T. Davinson *et al.*, *Technical Design Report of AIDA* (FAIR-NUSTAR, 2006).
- [101] D. Braga *et al.*, in *2009 IEEE Nuclear Science Symposium Conference Record (NSS/MIC)* (2009) pp. 1924–1928.
- [102] P. Coleman-Smith, “private communication: AIDA FEE specification,” (2015).
- [103] P. Coleman-Smith, “private communication: Specification for the MACB,” (2016).
- [104] “private communication with mechanics workshop: Drawing of LYCCA chamber with the new beam pipe,” (2016).
- [105] J. F. Ziegler, M. Ziegler, and J. Biersack, *Nucl. Inst. and Meth. in Phys. Res. B* **268**, 1818 (2010).
- [106] R. Brun and F. Rademakers, *Nucl. Inst. and Meth. in Phys. Res. A* **389**, 81 (1997).
- [107] *HDTV* (<http://www.ikp.uni-koeln.de/projects/hdtv>).
- [108] D. A. Bromley, J. A. Kuehner, and E. Almqvist, *Phys. Rev. Lett.* **4**, 365 (1960).
- [109] R. H. Davis, *Phys. Rev. Lett.* **4**, 521 (1960).
- [110] H. Emling, R. Nowotny, D. Pelte, and G. Schrieder, *Nucl. Phys. A* **211**, 600 (1973).
- [111] R. Wieland *et al.*, *Phys. Rev. C* **8**, 37 (1973).
- [112] D. Shapira, R. G. Stokstad, and D. A. Bromley, *Phys. Rev. C* **10**, 1063 (1974).
- [113] R. G. Stokstad *et al.*, *Phys. Rev. C* **20**, 655 (1979).
- [114] H. G. Bohlen *et al.*, *Z. Phys. A - Atoms and Nuclei* **308**, 121 (1982).
- [115] M. Buenerd *et al.*, *Phys. Rev. C* **26**, 1299 (1982).



## Bibliography

- [116] M. E. Brandan, *Phys. Rev. Lett.* **49**, 1132 (1982).
- [117] C. Perrin *et al.*, *Phys. Rev. Lett.* **49**, 1905 (1982).
- [118] H. G. Bohlen *et al.*, *Z. Phys. A - Atoms and Nuclei* **322**, 241 (1985).
- [119] W. E. Frahn, *Phys. Rev. Lett.* **26**, 568 (1971).
- [120] F. Hoyle, *Astrophys. J. Suppl. Ser.* **1**, 121 (1954).
- [121] M. Freer *et al.*, *Phys. Rev. C* **49**, R1751 (1994).
- [122] M. Itoh *et al.*, *Phys. Rev. Lett.* **113**, 102501 (2014).
- [123] L. Morelli *et al.*, *J. Phys. G: Nucl. Part. Phys.* **43**, 045110 (2016).



# Danksagung

Während meiner Arbeit haben viele Menschen mich unterstützt. Die Erstellung dieser Dissertation konnte nur durch die Hilfe von ihnen möglich sein. Bei folgenden Menschen möchte ich ganz herzlich bedanken:

Herrn Prof. Dr. Peter Reiter danke ich für die Vergabe des Themas, sowie die exzellente Betreuung meiner Arbeit. Die wissenschaftliche und persönliche Unterstützung von ihm bietet mir die Möglichkeit, mich weiter zu entwickeln.

Herrn Prof. Dr. Andreas Zilges danke ich ganz herzlich für die Übernahme des Ko-referats. Außerdem möchte ich Herrn Prof. Dr. Andreas Schadschneider und Herrn Dr. Christoph Fransen für ihre investierte Zeit als Mitglieder der Prüfungskommission danken.

Weiterhin möchte ich mich bei Herrn Dr. Michael Seidlitz für seine Betreuung und sinnvolle Diskussion, sowie sein sorgfältiges Korrekturlesen meiner Arbeit bedanken. Bei Frau Dr. Mouna Bouhelal und Herrn Prof. Dr. Florent Haas möchte ich herzlich für ihre Beitrag sowie die Unterstützung von PSDPF-Schalenmodellberechnung danken. Darüber hinaus danke ich Herrn Dr. Andrey Blazhev für seine Unterstützung von theoretischer Berechnung und die Zusammenarbeit bei der Erfassung der Publikation.

Herrn Kai Wolf danke ich für seine ausgezeichnete Mitarbeit bei dem Aufbau des LYCCA-Strahlrohrs sowie den Tests der LYCCA-Detektoren. Weiterhin möchte ich mich für die kooperative und effektive Zusammenarbeit bei der ganzen LYCCA-Kollaboration bedanken: Herrn Stefan Thiel und Herrn Christoph Görden von der Universität zu Köln, Herrn Patrick Coleman-Smith, Herrn Paul Morrall und Herrn Ian Lazarus von der STFC Daresbury Laboratory, Herrn Prof. Dr. Mike Bentley, Herrn Dr. Simon Fox und Frau Dr. Lianne Scruton von der University of York, sowie Herrn Prof. Dr. Dirk Rudolph, Herrn Dr. Pavel Golubev und Herrn Christian Lorenz von der Lund University.

Zuletzt möchte ich mich bei der gesamten Arbeitsgruppe für die enge Zusammenarbeit und vielfältige Unterstützung sowie die freundliche Arbeitsatmosphäre bedanken. Ganz besondere geht mein herzlicher Dank an Herrn Konrad Arnswald, Herrn Dr. Benedikt Birkenbach, Herrn Dr. Gunnar Friessner, Herrn Dr. Andreas

## *Bibliography*

Hennig, Herrn Dr. Herbert Hess, Herrn Robert Hetzenegger, Herrn Rouven Hirsch, Herrn Levent Kaya, Herrn Lars Lewandowski, Herrn Michael Queiser, Herrn Dawid Rosiak, Herrn D. Schneiders, Herrn Burkhard Siebeck, Herrn Tim Steinbach, Herrn Dr. Tim Thomas, Herrn Dr. Andreas Vogt, Herrn Dr. Andreas Wendt, und Herrn Dr. K.O. Zell. Weiterhin gilt mein Dank den Operateuren des Tandembeschleunigers des IKP, Herrn Frank Bielau, Herrn Victor Rehl, Herrn Otto Rudolph und Herrn Albert Wedel für die erfolgreich und reibungslos durchgeführte Strahlzeit sowie die Unterstützung bei meinem Experiment und Inbetriebnahme des LYCCA-Systems.

Zum Schluss möchte ich mich bei meiner ganzen Familie, meiner Eltern und meiner Schwester für die jahrelange bedingungslose Unterstützung und Ermutigung bedanken. Insbesondere danke ich meiner Frau Xiaorong, die immer hinter mir steht und mich mit ihrer Liebe und Leidenschaft motiviert und unterstützt.

# Erklärung

Ich versichere, dass ich die von mir vorgelegte Dissertation selbstständig angefertigt, die benutzten Quellen und Hilfsmittel vollständig angegeben und die Stellen der Arbeit – einschließlich Tabellen, Karten und Abbildungen –, die anderen Werken im Wortlaut oder dem Sinn nach entnommen sind, in jedem Einzelfall als Entlehnung kenntlich gemacht habe; dass diese Dissertation noch keiner anderen Fakultät oder Universität zur Prüfung vorgelegen hat; dass sie – abgesehen von unten angegebenen Teilpublikationen – noch nicht veröffentlicht worden ist sowie, dass ich eine solche Veröffentlichung vor Abschluss des Promotionsverfahrens nicht vornehmen werde. Die Bestimmungen dieser Promotionsordnung sind mir bekannt. Die von mir vorgelegte Dissertation ist von Prof. Dr. Peter Reiter betreut worden.

Köln, December 20, 2017

Bo Fu

## Teilpublikationen:

*$\gamma$ -ray spectroscopy of  $^{33}\text{P}$  and  $^{33}\text{S}$  after fusion-evaporation reactions*

B. Fu, M. Seidlitz, A. Blazhev, M. Bouhelal, F. Haas, P. Reiter, K. Arnswald, B. Birkenbach, C. Fransen, G. Friessner, A. Hennig, H. Hess, R. Hirsch, L. Lewandowski, D. Schneiders, B. Siebeck, T. Steinbach, T. Thomas, A. Vogt, A. Wendt, K. Wolf, and K. O. Zell

Physical Review C **94** (2016) 034318.



# Lebenslauf

## Persönliche Details

Name: Bo Fu  
Geburtsdatum: 30. September 1979  
Geburtsort: Nei Mongol, VR China  
Nationalität: chinesisch  
Familienstand: verheiratet

## Promotion

Seit 08/2014 **Promotion in der Fachrichtung Kernphysik**  
Institut für Kernphysik, Universität zu Köln  
Thema:  *$\gamma$ -ray spectroscopy of  $^{33}\text{P}$  and  $^{33}\text{S}$  & upgrade  
and commissioning of the Lund-York-Cologne CALorimeter*

## Schul- und Hochschulausbildung

10/2005 - 02/2014 **Diplomstudium der Physik an der Universität zu Köln**  
Thema: *Lebensdauermessung in  $^{33}\text{P}$*   
09/1998 - 07/2002 **Bachelorstudium der Physik**  
University of Lanzhou, VR China  
Thema: *The interacting filed under constraint conditions*  
09/1995 - 07/1998 **Zhengding-Gymnasium in Hebei, VR China**  
Abschluss: Gaokao (*Nationales Examen zur Hochschul-  
Immatrikulation*) (Punkte: 589 von 750)

## Arbeitsverhältnisse

08/2014 - 09/2017 **Wissenschaftlicher Mitarbeiter der Universität zu Köln**